ASTROCHEMICAL MODELING OF DUST GRAIN AND COMETARY ICES

Drew Anthony Christianson

Independence, Wisconsin

Bachelor of Science, University of Wisconsin – Eau Claire, 2018

A Dissertation submitted to the Graduate Faculty

of the University of Virginia in Candidacy for the Degree of

Doctor of Philosophy

Department of Chemistry

University of Virginia

August 2024

Robin T. Garrod, Advisor

Eric Herbst, Chair

L. Ilsedore Cleeves

Kateri DuBay

Anthony Remijan

Astrochemical Modeling of Dust Grain and Cometary Ices

Drew Anthony Christianson

(ABSTRACT)

Chemical models have long been useful tools to study various astronomical environments. These models can provide insight that can assist in both observations and experiments. One such instance is with interstellar dust grains and the effects of grain porosity. The degree of porosity in interstellar dust-grain material is poorly defined, although recent work has suggested that the grains could be highly porous. Aside from influencing the optical properties of the dust, porosity has the potential to affect the chemistry occurring on dust-grain surfaces, via increased surface area, enhanced local binding energies, and the possibility of trapping of molecules within the pores as ice mantles build up on the grains. Using the microscopic Monte Carlo chemical kinetics model *MIMICK*, we construct dust grains atom by atom and allow adsorption from the gas-phase to build up an ice layer. From this, we investigate the physical and chemical effects that a porous and a non-porous grain have on the composition and structure. Chemical models of cometary ices are also exceptionally rare. We build on previous work, using the rate-equation chemical kinetics model *MAGICKAL*, and improve on previous functions in an attempt to model more complex environments that a comet may experience. We start by modeling Comet Hale–Bopp, a long period comet. Here we include functions to model the active phase of a comet. Then we move onto a short period comet, 67P/Churyumov–Gerasimenko, allowing for more complex initial ices and including factors for solar UV and protons on the ice. Finally, we add in additional functions allowing for dust grain buildup on the

surface and add in a dust loss factor. Using this final model, we attempt to model the chemical effects highly energetic events external to the solar system, such as passing hot stars and nearby supernovae, have on the chemistry of cold storage comets.

Acknowledgments

I am not normally an overtly sentimental person. However, without the help of many people in my life over the past 5 years of graduate school, as well as the years leading up to it, I doubt I would have made it this far. Chief among everyone has to be my advisor and mentor Rob. I began graduate school with no experience in astrochemistry and only a surface level experience in coding. Now, thanks to his patience and guidance, I am much more confident and capable in academia than I ever was.

Thanks also to Eric Willis, a former member of the Garrod Group during my first year who was a great influence on me when I was just getting started, and for more than just that I took up his project. Eric was immeasurably helpful in not only getting me out of my shell and becoming familiar with the Charlottesville community, getting comfortable in the group, and also starting out as a graduate researcher. I would also like to thank all the members of the Garrod Group, both present and past, that I have had the pleasure of working with. I always appreciated your presence during work hours if I needed another person to be a sounding board or if I needed to voice one of my emphatic opinions on things just as the pronunciation of ".gif" and the inconsistent naming scheme of the planets, to name a few.

Thanks to all of my friends who supported me mentally and emotionally, despite being far away, over the years. Through all of the stress of classes and research, they all provided relief, be it through Dungeons & Dragons, video games, watching movies, and our rare physical get-togethers. Thanks to Daniel, who has been a constant for near a decade now and always having time for me. Thank you to my usual D&D groups for all the fun and surprising shenanigans. Also thanks to Chris, Connor, Lo-

gan, and Quin, friends and fellow scientists who despite attending different schools, were a constant help. Without them, I may not have even decided to attend graduate school in the first place. To Steve, my undergraduate research advisor, thank you for starting me on my research journey and being the one to help me ultimately find where I wanted get my PhD.

To my parents, sister, and grandma, thank you for being supportive of me throughout the years whether it be through pushing me to pursue my passions, being available if I was in need, teaching me to do laundry when I finally had to learn to take care of myself, or sending a near constant stream of cookies and strawberry jelly. Whenever I reached a milestone over the years, they have always been there, cheering me on. Perhaps they were even more excited for my publications than I was, despite not usually understanding the contents. A final big thank you everyone who helped me along the way, for keeping my head on straight, and allowing me to get to where I am.

Contents

List of Figures

List of Tables

Chapter 1

Introduction

1.1 A Brief Introduction to Astrochemistry

Astrochemistry, in its simplest form, can be concisely described as: the study of chemistry in space. More broadly, it is the study of chemical abundances, reactions, and conditions in non-terrestrial environments. The official advent of the astrochemistry field is typically cited as being in the 1930s. In 1937, methylidyne (CH) was detected for the first time in the interstellar medium, and subsequent studies confirmed this detection, making it the first ever molecule detected in space (e.g. Swings and Rosenfeld, 1937). Soon to follow was the cyano radical (CN) (McKellar, 1940) and the methylidyne cation (CH^+) (Douglas and Herzberg, 1941). Following this, it was not until further developments in radio astronomy that the next molecule, the hydroxyl radical (OH), was detected in 1963 (Weinreb et al., 1963). From there, more and more molecules have been detected each year.

Astrochemistry is distinguishable from its parent disciplines for a number of reasons. However, perhaps one of the most jarring distinction between it and chemistry is the level of molecular complexity. On Earth, chemists often deal with large complexes and proteins that can be made up of hundreds or even thousands of atoms. Among the many detected molecules in space, there is a category referred to as complex organic molecules (COMs), which is defined as any organic molecule containing

six or more atoms. It should now be clear the drastic disparity of what is considered 'complex' between the two disciplines. Much of this stems from the interstellar environments common in astronomy. Most extra-terrestrial environments are under extreme conditions, by Earth standards. Temperatures can range from as low as ∼2.725 K (Fixsen, 2009) into the thousands or higher near stars or other energetic events such as supernova. Pressures of most environments are also so low that there are no liquids.

To top it off, when looking at the atomic makeup of the universe, almost all of the baryonic matter is made up of the two smallest atoms. Approximately 74%, by mass, is composed of atomic hydrogen (H), and approximately 24% is composed of atomic helium (He), leaving less than 2% of matter made up of everything else. It is often in part for this reason that astronomers will call anything in this 2% simply as 'metals', much to a chemist's chagrin. As a result of these conditions, most of the detected molecules are relatively small, often being composed of thirteen atoms or less. There exist exceptions such as polycyclic aromatic hydrocarbons (PAHs), which are molecules composed of several ring structures, and fullerenes (e.g. Berné et al., 2013) colloquially referred to as 'buckyballs' which are named as such due to the spherical ball-like structure. Along with this, larger and more complex molecules tend to be more difficult to identify in space, between the complexity of their spectral profiles and disentangling them from observations to the sheer number of potential molecules to look for. Despite this, more and more molecules are being detected and confirmed every year.

1.2 Chemical Modeling

Modeling techniques are common throughout the sciences, and astrochemistry is no exception. Given the extreme conditions and far-off locations of the areas-of-interest within the field, it is unsurprising that modeling would become a common method of research. The entirety of the research performed herein was done using computational techniques which were then used to compare to previous observations and experiments. Two modeling techniques were primarily used during this work: Monte Carlo methods and Rate-Equation methods.

1.2.1 Monte Carlo models

In general, a model using a Monte Carlo method uses repeated random sampling to simulate probable outcomes. That is to say, if you have a set of possible actions and their likelihood, if you then randomly select from those actions weighted by their likelihood and repeat the process, you will end up with a likely solution. In terms of chemical modeling, this can be quite useful. Microscopic Monte Carlo techniques can explicitly keep track of the positions and conditions of individual particles in a model thus allowing for detailed mapping of a given chemical system. For example, this method can be used to simulate the motion of particles on a dust grain surface, how they react with other particles, and the resulting structure of ice build-up, as utilized in Garrod (2013b) using the model *MIMICK*.

The off-lattice chemical kinetics model *MIMICK* is utilized in Chapter 2 and presented in Christianson and Garrod (2021). The model was originally presented in Garrod (2013b) and has since been adapted and improved in various forms. Willis and Garrod (2017) originally incorporated the effects of "back-diffusion" or the idea

that a given particle may move back to a previously visited site. Meanwhile, Clements et al. (2018a) utilized the model to attempt to replicate experiments of amorphous solid water (ASW) under interstellar conditions. Despite the usefulness of Monte Carlo methods, they are also quite computationally expensive. It is therefore less useful for modeling large systems.

1.2.2 Rate-Equation models

Rate-equation methods involve using molecular and atomic concentrations and rate constants to predict chemical reactions and abundances as they change over time. Compared to the Monte Carlo methods briefly discussed in §1.2.1, it is less computationally intensive and much better suited for larger systems such as cloud models and hot cores. Herbst and Klemperer (1973) was the first to publish a rate equation method in the context of astrochemistry, and was used to model a dense interstellar cloud. More recent studies with rate-equation methods includes protoplanetary disk models (e.g. Waggoner and Cleeves, 2022).

The chemical kinetics model *MAGICKAL* is another such model first presented in Garrod (2013d) where it was used to model hot cores. This model also has been adapted to model interstellar clouds. Later, Garrod (2019) adapted the model for use on modeling cometary ice surfaces. This model is used extensively in Chapters 3-5. While generally useful in a large scope, these models can be somewhat limited by the fact that they do not discretely define positions and instead relies on bulk quantities and overall abundances. This model cannot therefore specifically distinguish sections of an ice surface. Other rate-equation models face similar limitations.

1.3 Astrochemical Environments

The universe is filled with myriad stars. Just as there are many stars, there are also many different environments that the study of astrochemistry hopes to explore. There are studies of protoplanetary disks, dark interstellar cloud, hot cores, galactic centers, terrestrial bodies, and many more. Here, we will focus specifically on two types of environments. The first one is interstellar dust grains. Dust grains are generally conglomerates of carbonaceous or siliceous material. While often approximated as being spherical, most are oddly shaped and quite porous. The exact structure isn't known due to how difficult it is to physically get to them. They are generally assumed to be less than a micron in size and even as small as a few Å(Weingartner and Draine, 2001).

Other molecules may adsorb from the gas-phase onto the surface which allows for an ice mantle to be gradually be built. This also facilitates chemical reactions that would otherwise be difficult in the gas-phase. Chemical processing may occur due to radiolysis caused by cosmic rays or UV impingement. Conditions within the dust grains environment may also allow for heating, sublimation, or even the entire ice mantles being stripped from the surface, returning the contents to the gas-phase. Fig. 1.1 shows a simple dust grain and ice mantle and some of the processes that may occur (Burke and Brown, 2010). Some species observed in the interstellar medium do not readily form in the gas-phase. Grain surfaces are one of the proposed mechanisms that could facilitate the formation of many of these species.

Over time as a star forms, dust grains may start to gather up, forming larger structures such as planetesimals and future comets. This leads to the second environment relevant to this work: comets. Comets are sometimes referred to as "dirty

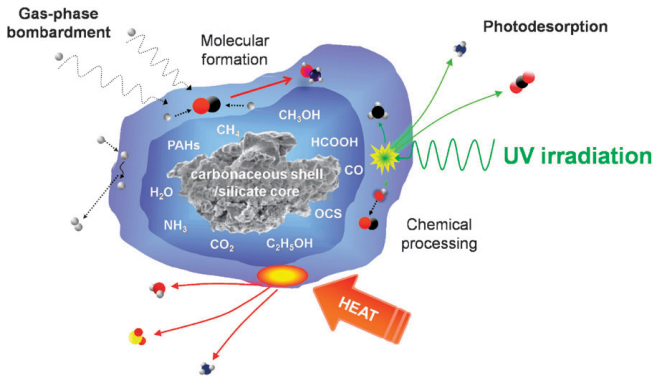

Figure 1.1: A pictorial schematic showing a dust grain as well as various processes that may occur in the ice. Image taken from Burke and Brown (2010).

snowballs" or "icy dirtballs" depending on who you ask. The point being that it is some amalgamation of ice and dust. Most comets formed with the formation of the solar system. They then rest out at various cometary reservoirs in the outer reaches of the solar system such as in the Kuiper Belt (Kuiper, 1951) and the Oort Cloud (Oort, 1950). Within these cometary reservoirs, they remain cold, as low as 5 K, and well preserved. This is why they are generally referred to as 'pristine' as much of the ice will remain unaltered. Comets therefore provide unique windows into the dearly solar systems conditions once they are perturbed into orbits to the inner solar system when we can observe them. Comets are also a potential origin for water and organics arriving on Earth. Though due to widely varying D/H ratios detected in comets, the actual contribution of comets in depositing water on the early Earth is still widely debated (Lis et al., 2019). However, recent studies of Xe isotope ratios in comet 67P, shown in Fig. 1.2 indicate that comets could have brought quantities of organic molecules greater than today's biomass to the early Earth (Altwegg, 2022).

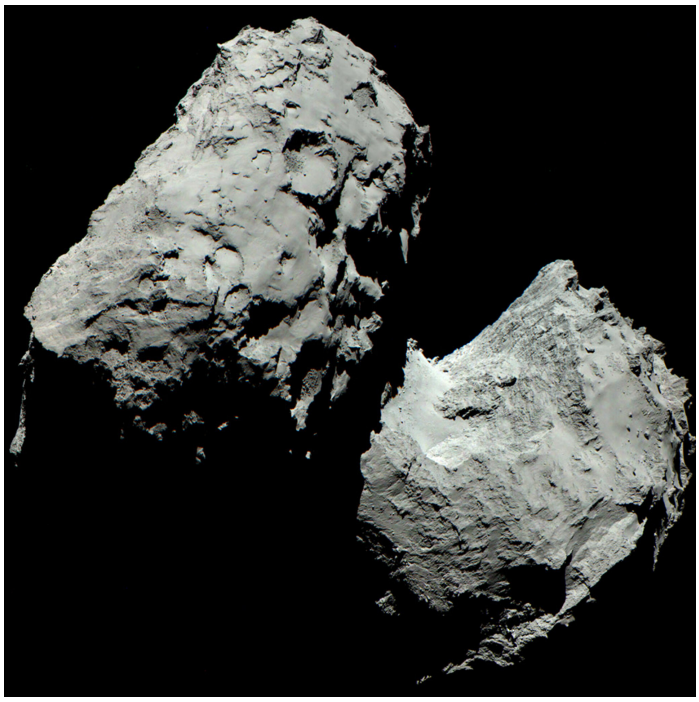

Figure 1.2: A true color image of Comet 67P/Churyumov–Gerasimenko taken on August 6th, 2014 during the ROSETTA mission. Credits: ESA/Rosetta/MPS for OSIRIS Team MPS/UPD/LAM/IAA/SSO/INTA/UPM/DASP/IDA

1.4 Dissertation Scope

This dissertation focuses on development of various existing models and expanding their capabilities to model specific sources or phenomena. These include both Monte Carlo and rate-equation models. The chapters are divided up as follows.

Chapter 2 utilized the Monte Carlo model *MIMICK* originally presented in Garrod (2013c). This study models grains of various sizes and different porosity to model the chemical and physical effects on dust grain ices. A set of approximately spherical non-porous grains and porous grains are created and gas-phase species are allowed to adsorb onto the surface, diffuse, and react.

Chapter 3 was in part covered within the Dissertation Defense of Eric R. Willis,

but has since been expanded upon and completed. This study utilizes the comet version of the chemical kinetics model *MAGICKAL* which was presented in Garrod (2019). This model is rate-equation based and has had multiple improvements to its modeling capabilities. Previously only used to model cold storage comets, this work presents results on the active phase chemistry of Comet Hale–Bopp.

Chapter 4 continues on the work of Chapter 3, also utilizing the *MAGICKAL* model. Model capabilities were improved to consider the effects of solar UV and solar protons on cometary ices, which were previously ignored, as well as tests the effect of varying the initial chemical composition. This is used to assess the validity of claims such as Drozdovskaya et al. (2019) on whether comets are required to inherit their initial ices directly from the interstellar or protostellar conditions. The primary target for this study is Comet 67P/Churyumov–Gerasimenko, however, additional models using Comet Hale–Bopp with the updated model are also included.

Chapter 5 utilizes model improvements of *MAGICKAL* and attempts to test the effect of extrasolar energetic events such as passing hot stars and nearby supernovae can significantly impact the cometary ice chemistry in both the short term and the long term. Active comets like Comet 67P are expected to have this dusty outer shell as well as to experience significant mass loss. The model now has additional capabilities of building up a pure dust grain shell on the surface and allows for dust loss, which was not previously possible.

Chapter 2

Interstellar Dust Grain Porosity

The work presented in this chapter has been published in Frontiers in Astronomy and Space Sciences with Robin T. Garrod (Christianson and Garrod, 2021).

2.1 Introduction

Dust grains are known to play a major role in the chemical evolution of interstellar clouds and star-forming regions. Of critical importance is the production of molecular hydrogen on grain surfaces, through the reactions of hydrogen atoms adsorbed from the gas phase (e.g. Gould and Salpeter, 1963; Hollenbach and Salpeter, 1971); much of the H_2 produced in this way desorbs again, to become the dominant component of the gas in dense, dark clouds. In clouds of sufficient visual extinction, the dust grains may build up ice mantles composed mostly of water, but with substantial amounts of CO, CO_2, NH_3 and several other simple species (Boogert et al., 2015). Much of the chemistry that produces these grain-surface molecules involves the surface diffusion of atomic hydrogen, which is understood to be mobile even under the cold ($\sim$ 10 K) conditions of dark clouds (Senevirathne et al., 2017). By repetitive thermal hopping between surface potential minima (binding sites), H atoms may meet other reactive species, such as atomic O or N, and react. The adsorption of atoms, as well as molecules such as CO, from the gas phase and their subsequent hydrogenation leads

to the buildup of ice mantles many monolayers in thickness (Cuppen et al., 2017).

Interstellar dust grains are typically considered to be composed of either carbonaceous or silicaceous material, both of which populations may be identified in the interstellar medium. By fitting observational extinction values to models that consider the optical properties of dust grains, Mathis et al. (1977) provided a grain-size distribution for the Milky Way of $dn \propto a^{-3.5}da$, valid for grains with radii in the range 50 Å$< a < 0.25$ μm. Weingartner and Draine (2001) produced more detailed expressions using more recent observational data, providing distinct distributions for carbon versus silicate grains, as well as bringing the minimum size down to molecular scales (i.e. a few Å).

In chemical kinetic models of interstellar grain-surface chemistry, in which the grain-surface populations of various atomic and molecular species are traced over astronomical timescales, a canonical, spherical grain radius of 0.1 μm is typically chosen to represent all grains in the model. The grain surface is assumed to comprise around 1 million binding sites, based on a site density of $\sim 10^{15}$ cm^{-2} (Hasegawa et al., 1992a). Some chemical models of interstellar clouds have considered a distribution of grain sizes, each having their own independent chemistry (Acharyya et al., 2011; Pauly and Garrod, 2016, 2018). However, without the existence of a strong temperature gradient across the size distribution, the influence of the grain size on the surface chemistry in those models appears to be fairly limited.

Most such chemical kinetic models use the so-called "rate-equation" approach (see Garrod, 2008), in which the grain-surface population of each chemical species is traced over time; each chemical species is assigned a fixed binding energy and barrier against diffusion. While efficient, this technique is unable to treat the microscopic structure of either the ice mantle or the underlying dust grain itself, as the positions

of individual atoms or molecules on the grain are not considered. The dust grains in these models are thus implicitly smooth and spherical, as are the molecular ices that form on their surfaces. Most models therefore say nothing about the possible influence of grain morphology or porosity on interstellar molecular abundances, either on the grain surfaces or in the gas phase.

Experimental investigations of the direct deposition of interstellar ice analogs suggest the possibility for grain-surface ices to achieve substantial degrees of porosity (e.g. Raut et al., 2007), but no observational evidence has yet been found to indicate that true interstellar ices, which are formed primarily through surface chemistry rather than direct deposition, should be substantially porous; the dangling bond IR feature associated with porous ASW has not so far been detected in the ISM (Keane et al., 2001). Laboratory work indicates that the formation of ices through chemical reactions, rather than direct deposition from the gas phase, appears to be crucial to the degree of porosity. In experiments by Oba et al. (2009), hydrogen atoms and O_2 molecules were co-deposited onto Al and D_2O surfaces, leading to the buildup of water ice films through chemical reactions. Those authors found no dangling-bond features that would indicate porosity, and they suggested that the reaction energy could be responsible for the compactness of the ice. Similar work by Accolla et al. (2013) involving D and O_2 deposition likewise found no spectral identifiers of porosity.

Astrochemical models of interstellar ice formation by Garrod (2013b) used a microscopic Monte Carlo technique to trace the formation of water and several other chemical species through atomic addition reactions. Those authors found that the ability of oxygen atoms to diffuse on the grain/ice surface over long periods of time allowed them to find the strongest binding sites, prior to reaction with atomic H, so that the chemically-produced water molecules would automatically be formed in

strong binding sites that would otherwise correspond to nascent surface inhomogeneities, thus allowing the ice to form smoothly at microscopic scales. Whether the production of compact water ice is due to the thermal diffusion of atomic oxygen, or to non-thermal, reaction-induced diffusion of the water molecule itself, the chemical production of water on dust grains appears to lead to little or no porous structure, in agreement with the existing observational evidence (although it has also been suggested that the filling of water-ice pores with molecules such as CO could remove the dangling-bond feature; e.g. He et al., 2019).

Similarly, until recently there has been little direct evidence to indicate either the degree or the precise form of porosity, if any, that interstellar dust-grains themselves might assume; however, some indirect evidence suggests that interstellar dust grains could be highly porous. While models of scattering by dust typically assume optical properties corresponding to spherical or spheroidal dust grains of uniform composition, Mathis (1996) tested models using composite dust grains, whose volume could also be composed of some fraction of empty space, f_{vac}. Mathis found that models using grains with $f_{vac} = 0.45$ could be successful in reproducing observational extinction curves (although see also Weingartner & Draine 2001); this vacuum fraction, which we identify with the porous structures that we model here (Sec. 2.3), was assumed in those models to be present equally in grains of all sizes.

Dust grains detected in the comae of comets may also be porous, based on analysis of the range of grain sizes and densities. In the case of comet 67P, these grains appear to be loose aggregations of low density (0.1 – 1 g cm^{-3}) and mean size around 10μm that are made up of smaller sub-units (Agarwal et al., 2007). The sub-units themselves are of sizes more appropriate to interstellar grains, on average around 0.1μm, and are thought to be closer in density to the native material from which they are composed

(Mannel et al., 2019), indicating a low degree of porosity on those size scales. It is unclear, however, whether those sub-units could themselves be formed from smaller structures.

Dust-grain coagulation models appropriate to star- and planet-forming environments (Ossenkopf, 1993; Ormel et al., 2009) indicate that large, micron-scale grains can become porous, but their smallest sub-units are of similar size to the typical interstellar dust grains, and therefore do not indicate whether any porosity may exist in those smaller grains. Other dust models (Jones et al., 2014) have considered the accretion of carbon atoms onto existing grains in the outer regions of molecular clouds, as a mechanism to replenish the dust destroyed through energetic processes such as interstellar shocks, in order to explain the apparent imbalance between dust formation and destruction in the ISM. This accretion process, which would necessarily occur at low dust temperatures (no greater than around 30 K under typical interstellar conditions), could plausibly introduce irregularities to the grain surfaces, or, with a sufficient degree of accretion, outright porosity in the outer layers of the grain material.

Most recently, Potapov et al. (2020) carried out experiments in which interstellar dust-grain analog particles composed of amorphous carbon were formed and deposited onto a substrate. Ices of water, CO, and other molecular species were then deposited onto the grains, and their temperature-programmed desorption profiles analyzed. The authors reported behavior indicating that the ices were spread over very large surface areas, indicating an extreme degree of porosity. They proposed that interstellar grains may have surface areas enhanced by factors of several hundred, producing maximal ice thicknesses on the order of 1 monolayer in interstellar clouds. However, we note that the degree of porosity in interstellar grains themselves would be dependent on

the precise mechanism and environment of their formation.

Here, we investigate the influence of interstellar dust porosity on the chemistry and composition of ices that form on the dust-grain surfaces. Dust porosity has the potential to affect the chemistry occurring on dust-grain surfaces, via increased surface area, enhanced local binding energies, and the possibility of trapping of molecules within the pores as ice mantles build up on the grains.

Garrod (2013b), mentioned above, introduced a microscopic Monte Carlo chemical kinetic model for interstellar grain-surface chemistry that was capable of simulating diffusive chemistry on fully three-dimensional surfaces. The model uses an off-lattice treatment, allowing surface particles to assume positions that are determined entirely by their interactions with nearby binding partners. In that study, the model was used to simulate the production of water and several associated molecules over astronomical timescales; an important effect noted by Garrod was the formation of porosity in the ices, which was dependent on both the temperature of the dust grain and the rate of accretion of gas-phase atoms onto the grain, as controlled by the gas density; under the dark-cloud conditions used in those models, the ices produced were found to be non-porous. Here, we use an updated version of the model with a larger chemical network, such that all of the main interstellar ice components may be modeled. The structure of the underlying dust grain may be directly controlled by the placement of the (carbon) atoms from which it is constructed, meaning that any structure can in principle be used; this includes the possible variation of both the large-scale morphology of a grain and its microscopic surface roughness. We run chemical models on both porous and non-porous grains of a selection of sizes, using broadly spherical large-scale structures. These models represent the first such attempt to model explicitly the effects of dust-grain porosity on interstellar grain-

surface chemistry.

2.2 Methods

The model results presented here make use of the off-lattice microscopic Monte Carlo chemical kinetics code *MIMICK* (Model For Interstellar Monte Carlo Ice Chemical Kinetics), developed by Garrod (2013b). This model uses an exact description of a dust grain in which the positions of all of its constituent atoms are explicitly described. The model traces the chemistry occurring on the dust-grain surface by similarly tracking the positions and movements of the atoms and molecules that are adsorbed onto the surface from the gas phase. The positions of those species on the surface correspond to local potential minima (binding sites), as determined by the strength of the pairwise potentials experienced by each surface particle. Positions may change when mobile species make thermal hops between adjacent binding sites.

All of the various physical and chemical processes occurring on the grain, namely adsorption/accretion, thermal desorption, thermal hopping and reaction, are treated as a sequence of consecutive events. The Monte Carlo treatment used here follows that of Gillespie (1976), in which random numbers are used to determine (i) which process occurs next and (ii) the time increment between each such event, based on the calculated rates of every possible process at that moment in time. In the case of thermal diffusion, each individual hop from one binding site to another is treated as a distinct event. Standard rate formulations are used for each of the various processes for each individual atom/molecule on the surface; thus, those rates are dependent not only on the type of atom/molecule in question but on the number, type, and spatial arrangement of its binding partners.

The model employed here uses a somewhat more advanced treatment for the calculation of surface binding energies and diffusion barriers than that of Garrod (2013b). Clements et al. (2018b) provide an outline of this treatment, which is described in detail by Garrod & Deselm (*in prep.*). In brief, each pairwise interaction between atoms, molecules or surface particles is treated as a Lennard-Jones (6–12) van der Waals potential, with a defined optimal separation, σ, and a potential well depth, ϵ. When an atom or molecule arrives on the surface through adsorption from the gas phase, its position is optimized by minimization of the sum of all pairwise potentials that it experiences (while the positions of the individual binding partners are assumed to be fixed). The 6–12 potentials are tuned to have a cutoff separation of $r = 2.5\sigma$; any nearby species that fall within this cutoff distance are termed "binding partners", and thus contribute to the total binding energy of the adsorbed species. Any binding partners that fall within a distance $r = 1.5\sigma$ are termed "contiguous", and may be considered to be in direct contact with the species in question.

The process of diffusion may occur in multiple possible directions for a given surface atom/molecule, with each direction having its own associated energy barrier. Firstly, the model determines which directions are possible. To do this, all viable diffusion pathways are assumed to pass through saddle-points in the local surface potential; due to the spherical symmetry of the pairwise potentials, each saddle-point falls approximately between adjacent pairs of binding partners that are immediately contiguous to the diffuser (see Garrod, 2013b, for a diagram of such an arrangement). Diffusion through that saddle-point may be imagined as a rotation of the diffuser about the axis that joins two of those contiguous binding partners to each other; those binding partners are termed the "saddle-point pair". Each saddle-point pair can be identified geometrically, and has a unique diffusion pathway associated with

it. (Garrod, 2013b, also provides a more detailed description of the geometric considerations involved in identifying the saddle-point pairs). As an example, one may imagine an atom sited atop a triangular arrangement of three contiguous binding partners. Any given pair of those binding partners would constitute a saddle-point pair, with rotation around each such pair providing a unique direction of diffusion through a potential saddle point.

For every atom or molecule on the surface at a given moment, the model holds a list of saddle-point pairs (i.e. diffusion directions), for each of which a diffusion barrier is also defined. A diffusion barrier consists of the energy required to break or stretch each surface bond to the furthest distance the diffuser could reach as a result of rotation around the axis defined by the saddle-point pair. Some existing bonds would be entirely broken by such a procedure, while others would merely be stretched, while still remaining within the cut-off distance of the van der Waals interaction. The calculation excludes any bonds that would be shortened in this procedure. The bonds between the diffuser and the binding partners that comprise the saddle-point pair also do not contribute to the diffusion barrier, as the rotation around the saddle-point pair occurs at constant radial distance from each. The diffusion barriers are therefore always lower than the total binding energy, and they vary depending on the direction of diffusion; diffusion events that require the breaking or stretching of stronger pairwise potentials have higher barriers and are therefore less likely to occur. (The key difference between the present treatment and that of Garrod, 2013b, is that the older model only considered contiguous binding partners as contributors to the diffusion barriers and binding energies). If and when a particular diffusion event is selected by the Monte Carlo routine according to its barrier-defined rate, the diffusing particle is allowed to rotate around the saddle-point pair until it encounters another

particle on the other side; its position is then re-optimized based on all of the pairwise potentials experienced in its new location.

The full diffusion procedure described above, while being approximate in the determination of diffusion barriers and prescriptive in the choice of available directions, obviates the need to evaluate directly the potential energy surface involved in every possible diffusion event of every surface species; such a simplification is essential to allow this kinetic model to run on manageable timescales.

All surface diffusion considered in this model is based on thermal rates (as defined by the barriers described above); no tunneling contributions to diffusion rates are considered. At the 10 K temperature used in the models presented here, tunneling is not expected to contribute significantly to the diffusion rates of hydrogen atoms; quantum calculations by Senevirathne et al. (2017) indicate a crossing temperature (i.e. the temperature at which tunneling begins to dominate) of $T_C(\mathrm{H}) = 9.7$ K for H atoms on amorphous water ice. T_C values for other species that could plausibly diffuse via tunneling, e.g. H_2, should be expected to be substantially lower, due to the larger mass involved; the same authors found $T_C(\mathrm{D}) = 6.9$ K on amorphous water ice.

In the present version of the *MIMICK* model, all surface particles, whether atoms or molecules (or atoms comprising the dust grain itself) are considered to be spherical, with a radius of 1.6 Å, such that the optimal separation used in the pairwise potentials is $\sigma = 3.2$ Å. This size is chosen to ensure that the physical size of the ice formed on the grains is representative of water ice, which is the dominant constituent. Variable values of σ will be introduced in future work.

Importantly, as in the models of Clements et al. (2018b), the thermal desorption

of a surface particle follows a specific trajectory, which is defined by the vector sum of the pairwise potentials at the starting position. The desorbing particle incrementally traces out this trajectory until it reaches the edge of the calculation-space used in the model. If the trajectory intersects with other particles then the desorbing particle may be re-accreted. This eventuality is especially important in cases where enclosed surfaces exist within the porous structures of the grain. Note that the present model does not use the treatment presented by Clements et al. for the gradual relaxation of a newly-adsorbed particle. Atoms and molecules accreted from the gas phase are assumed to thermalize immediately on the surface.

Only surface particles that are considered "free" are allowed to diffuse or to desorb. Free particles are defined as those that have available at least one surface diffusion pathway, as determined by their local geometry. Particles that are completely enclosed by contiguous binding partners (as would be the case for molecules within the bulk ice) have no such pathways. Thus, any particle that is capable of diffusion also has some probability of thermal desorption. Counting the number of free particles also provides a determination of the number of particles present in the surface layer of the ice.

Reactions between surface species are allowed to occur when the reactants become contiguous, whether that be through diffusion, adsorption, or as the result of an earlier reaction. Once contiguous, that reaction between specific particles is considered as a process that competes with all others to be the next event in the sequence. If the reaction has no activation energy barrier, then it is assigned a rate equal to the sum of the characteristic vibrational frequencies of the reactants. The rates of reactions that have activation energy barriers are further moderated by an efficiency factor representing the faster of either the thermal reaction probability (Boltzmann factor)

or a probability based on tunneling through a rectangular barrier, as is typically employed in the usual rate-equation based models (e.g. Hasegawa et al., 1992a).

Many typical (non-MC) kinetic models of grain-surface chemistry include a chemical desorption (CD) mechanism, whereby the energy released in the formation of a molecule via a surface reaction is sufficient to allow the molecule–surface bond to be broken and the reaction product to desorb into the gas phase (Garrod et al., 2007). This mechanism is usually assumed to occur with an efficiency of approximately (or sometimes precisely) 1%; in the remainder of cases, the reaction energy would be lost through vibrational interactions with the surface and the product would remain on the grain. Experimental studies (Minissale et al., 2016) have confirmed that this process can occur, typically with greater probability on bare-grain analogs than on the amorphous water ice that is expected to build up on the grain surfaces. For most reactions, those experiments obtained only upper limits to the efficiency, on the order of 10%. Recent *ab initio* molecular dynamics studies of the H + CO $\rightarrow$ HCO reaction system on crystalline water ice indicate that energy loss to the surface occurs too rapidly to allow product desorption (Pantaleone et al., 2020). In most kinetic models that include the CD mechanism, while its inclusion may be important to the abundances of certain gas-phase species (such as methanol) that do not apparently have a viable gas-phase formation mechanism, the influence on the abundances of surface species is relatively minor. We therefore leave the inclusion of this desorption mechanism in the *MIMICK* model to future work.

2.2.1 Construction of the dust grains

Three sizes of non-porous grain are constructed for use in the chemical model, with radii of approximately 50, 75, and 100 Å. In each case, this begins with the generation of a spherical grain composed of atoms in a simple cubic arrangement, placed at their optimal separations, σ. Because the chemical model *MIMICK* requires only the surface of the grain to be defined, a sphere of material is removed from the center, leaving a shell that is substantially thicker than the cutoff distance of the potentials used by *MIMICK*. The process up to this point is identical to that used by Garrod (2013b), albeit with much larger grains in the present case.

To produce an amorphous surface structure, the simple-cubic grain is first compressed in all three dimensions by a factor 0.75. The position of each atom is then offset in a randomized direction, by a random distance ranging from $0 - \sigma$. These two procedures randomize the positions of the atoms sufficiently to remove all trace of the original simple cubic micro-structure, while retaining the spherical shape. Each atom in the grain is then allowed to relax, according to a randomized sequence, using Lennard-Jones type potentials of arbitrary, uniform strength. This ensures that all of the atoms in the grain are at appropriate distances from each other. The upper row of Fig. 1 shows the non-porous grains produced in this way; the surface of each is amorphous, while retaining a well defined spherical morphology at large scales.

To produce a porous grain, a smaller grain core is initially created using the method described above. The largest porous grain uses the smallest non-porous grain as its core, while the medium-sized porous grain uses a core of radius 25 Å. The chemical model is then employed to deposit more (carbon) atoms from the gas phase onto this core surface. The trajectories of the incoming atoms are entirely

randomized. Upon landing, no chemistry or surface diffusion is allowed, but the positions of the accreting atoms are optimized, again using Lennard-Jones potentials. This hit-and-stick type approach results in open, porous structures. The accretion of atoms is halted when the maximum radial position of any atom (centered on the zero-position of the grain core) is equal to the maximum radial position of atoms in either the intermediate- or the large-sized non-porous grain; the resulting porous portions of each grain have a maximum thickness $\sim$50 Å, but the average is closer to 40 Å. The porosity of the porous portions of both grains is measured to be $\sim$64 %. Taking into account the non-porous core of each grain, this produces overall porosities of 61 % and 53 % for the medium and large grains, respectively. The latter is not far from the value used by Mathis (1996).

The five different grains created for the chemical simulations range in size from 50 – 100 Å in radius. This is smaller than the typical value of 0.1 μm (1000 Å) used in chemical models, although smaller grains such as these would be more numerous in the distribution and should provide a larger fraction of the available surface area for accretion, assuming non-porous, spherical grains. Smaller grains are also more computationally favorable using the microscopic Monte Carlo kinetics approach, as larger grains generate larger ices composed of greater numbers of atoms and molecules, each of which must be handled individually.

During the main chemical simulations, the atoms comprising the dust grains are fixed in place and do not participate in any chemical reactions, either directly or as a catalyst. Their main function is to define the physical surface of the grain.

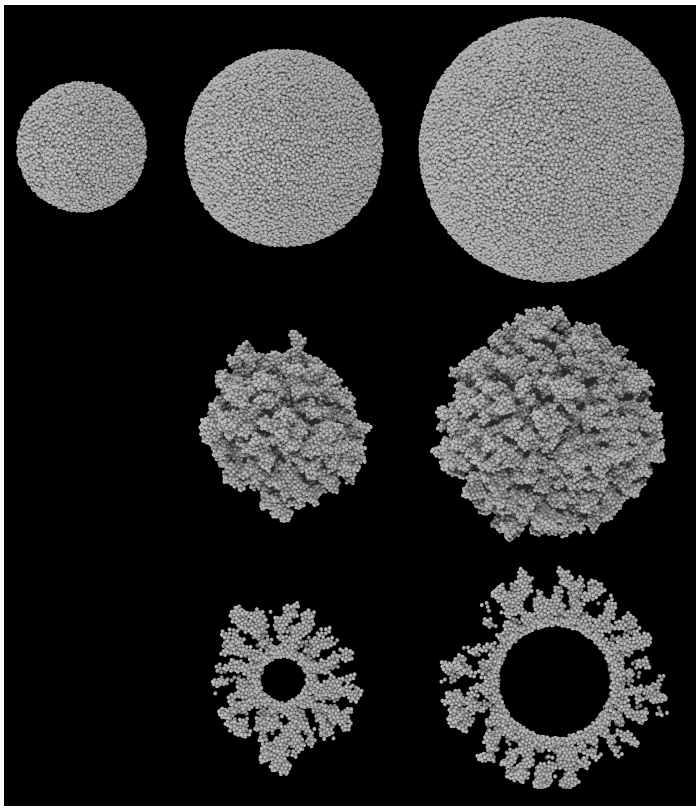

Figure 2.1: Ray-traced images of the five grain types used in the chemical models. All grains are composed of a collection of spheres representing carbon atoms. Top row: the three non-porous grains; middle row: the two porous grains, of comparable size to the two largest non-porous grains; bottom row: the cross sections of the two porous grains. From left to right, grains have a radius approximately 50, 75, and 100 Å. Note that the inner portions of the grains are removed to simplify the chemical kinetics calculations; the inner void is completely inaccessible to surface atoms and molecules.

2.2.2 Physical and chemical conditions

To represent a dark interstellar cloud (or, more precisely, a dark cloud core), the gas density is set to $n_{\rm H} = 2 \times 10^4$ cm^{-3} and both the grain and gas temperatures are set to 10 K (e.g. Bergin and Tafalla, 2007); similar conditions have been used in past models of dark cloud chemistry (e.g. Hasegawa et al., 1992a; Garrod et al., 2007). Although no gas-phase chemistry is included in these models, the gas density and

temperature determine the rates of accretion of gas-phase species onto the grain.

The gas-to-dust ratio by number is tailored for the specific grain size used in each model run, to maintain a consistent mass ratio of 100:1 appropriate to the Milky Way. This influences the total number of atoms initially available in the gas phase in our models. The chosen grain size used in each model run is assumed to be representative of the entire dust population, assuming a mass density of 3 g cm^{-3} for grain material. As grain size increases, the number of representative dust grains must decrease, thus increasing the amount of gas per dust grain. For the large grain, a gas-to-dust ratio by number of 10^{10} is used, which corresponds specifically to the number of hydrogen atoms present in either H or H_2 at the start of the models. The medium and small grains use lower values, as scaled by volume. For comparability between the chemical models, the gas-to-dust ratios used for the large- and medium-sized porous grains are the same as those of their non-porous equivalents.

The total budget (i.e. number of atoms) of each element used in the model is generated based on the gas-to-dust ratio and the abundance of each, relative to total hydrogen. The assumed gas-phase composition at the beginning of each model is shown in Table 2.1, based on the initial gas-phase elemental abundances used by Garrod (2013d). The grains in our models begin with no ice mantles. To better represent the composition of ices in dark clouds, a proportion of the carbon and oxygen budgets is incorporated into CO. Most of the hydrogen budget is assumed to be in the form of molecular hydrogen, with the atomic H abundance also chosen to represent typical dark cloud values. Gas-phase H_2 is not allowed to adsorb onto the grains, following Garrod (2013b); this simplification is necessary to allow the models to run on manageable timescales.

As the models progress, atoms and molecules in the gas accrete onto the grain

surface, depleting the gas-phase budget of each and thus reducing the amount still available for the further growth of the ice mantles. However, an exception is made in the treatment of the atomic H budget. To ensure that its rate of adsorption is always appropriate to dark cloud values, its abundance in the gas phase is held steady at its initial value. In full gas-grain models of dark cloud chemistry, gas-phase processes such as cosmic-ray induced dissociation allow the gradual release of some hydrogen locked up in H_2 back into atomic form, meaning that the fractional abundance of H is maintained at some base value, even though other species may become strongly depleted from the gas phase over time. This simple fix to the code avoids having explicitly to model the gas-phase chemistry.

Table 2.1: Initial gas-phase abundances as a fraction of total hydrogen.

Chemical species	Fractional abundance
H_2	0.4999
H	2.0×10^{-4} (fixed)
O	2.7×10^{-4}
C	9.0×10^{-5}
N	7.5×10^{-5}
CO	5.0×10^{-5}

The model assumes that the sticking coefficient for all species is unity, following typical assumptions used in other models. Experimental work by He et al. (2016b) indeed found a sticking coefficient of 1 for CO (the only adsorbing molecule in our model), although their low-temperature value for H_2 was in the 0.6–0.7 range. The sticking coefficient for atomic H on an amorphous water surface was calculated to be 0.980 by Dupuy et al. (2016) at dust/gas temperatures of 10 K. Sticking coefficients for H on amorphous carbon surfaces are not well defined, although Pirronello et al. (1997) suggest it could be appreciably less than one. Experiments by Chaabouni et al. (2012) find a value of 1 for silicate surfaces, however.

The model includes 39 chemical species and 70 different reactions, allowing C, O, N and CO to be hydrogenated all the way to CH_4, H_2O, NH_3 and CH_3OH. Molecules such as H_2, C_2, O_2, N_2 and CO may also be formed on the grain surfaces, along with various others. Table 2.2 details each of the reactions included in the model, with the assumed activation energy barriers and barrier widths indicated; this network is a simplified version of that presented by Garrod (2013d). Most of the reactions occurring on the grains are initiated by the diffusion of atomic H to meet its reaction partners, although reactions may occur in any situation in which two reactants come into contact. Table 2.3 provides a selection of important pair-wise potentials used in the model, which determine both the binding energies and diffusion barriers experienced locally by surface species. The potentials are somewhat lower than those used by Garrod (2013b), which reflects the fact that contributions to the binding of all local species within the cutoff distance are now considered, not only those species that are contiguous to the particle in question, which was the previous method. As described by Garrod (2013b), the pairwise potentials are intended to reproduce the overall binding energies of the species in question on surfaces of, for example, pure amorphous water.

The barriers against diffusion in any direction are always lower than the corresponding binding energies for a particular particle in a particular binding site, although different directions of diffusion typically have different values. The models produce as an output the distribution of the ratios of diffusion barrier versus binding energy for each chemical species in the network (in increments of 0.05), which are calculated at every output time in the model. In around 99% of atomic-H surface diffusion events, the barrier of the successful diffusion direction lies in the range 0.25–0.7 times the local binding energy, with around 18-20% of those barriers falling in

the 0.4-0.45 range, which is the most populous bin. The average binding energy of an H atom on the final (outer) surface of the ice mantles is approximately 460 K. This compares well with the value used in many past gas-grain models (e.g. Garrod, 2013d) of 450 K; DFT calculations by Wakelam et al. (2017b) indicate values of 400 K and 680 K for H on water, dependent on the method used. Using our model's average binding energy of 460 K, the diffusion barriers in the above fractional range produced by the model provide absolute values in the range 115–322 K, with the most common falling in the 184–207 K bin. Senevirathne et al. (2017), based on their calculations for H on amorphous water ice, recommended a representative ratio of diffusion barrier to binding energy for H of 0.37; combined with their representative binding energy of 661 K (57 meV), this suggests a diffusion barrier of 243 K. This latter value in particular seems fairly consistent with our range of values, in spite of the higher overall binding energy. Indeed, looking at the actual distribution of diffusion barriers produced by those authors, their most common diffusion barriers lie in the $\sim$175 – 230 K range, which coincides well with our most common bin.

For H_2, the model produces average binding energies of around 380–395 K; Garrod (2013d) use a value of 430 K. The calculations of Wakelam et al. (2017b) for the H_2–H_2O dimer suggest a binding energy of 800 K, but full cluster calculations by Ferrero et al. (2020) for amorphous solid water give a value in the range 226–431 K, in keeping with our model values. The experimental measurements of He et al. (2016a) indicate binding energies in a range between 322 and 505 K, with the former corresponding to high H_2 coverage and the latter to low coverage. Our models produce binding energies for CO and O_2 of around 1015 K and 1240 K, respectively; these are somewhat higher and somewhat lower, respectively, than the calculations by Ferrero et al. (2020) although our values fall comfortably within the range of experimental values quoted

by those authors (870–1600 K for CO and 914–1520 K for O_2).

For H_2O, the model produces an average binding energy around 4,750 K. The outer ice surface contains a selection of molecules besides water, so the effective binding energy of a water molecule is somewhat lower than might be expected on a pure water ice; a common value used in rate-equation models is 5,700 K (Garrod, 2013d). The calculations of Wakelam et al. (2017a) indicate values of 4800 or 5300 K based on water dimers or clusters, while Ferrero et al. (2020) obtain a range of 3605–6111 K. Experiment also provides a range of values, although Sandford and Allamandola (1990) obtain 4815 K for unannealed water ice that is very close to our value. Again, we note that our value is produced with a water-dominated ice mixture that includes all of the typically observed interstellar solid-phase species, rather than pure water. In practice, at the low temperatures used in the present models, the rates of diffusion and desorption of water molecules are negligible.

The model does not consider the influence of the condensation energies of adsorbed species, the energy released by chemical reactions, nor the effects of high-energy photons on the overall temperature of the grain/ice. Although the associated temperature fluctuations could be substantial for very small grains (e.g. Cuppen et al., 2006), they are beyond the scope of the present model. The recent modeling simulation of water-ice deposition by Clements et al. (2018b) included a treatment for the non-thermal diffusion of newly-adsorbed molecules, caused by the excess energy gained as they are accelerated into the surface potential. That treatment was tuned specifically for water molecules, and we do not extend it here to other species. In any case, the ability of the adsorbed atoms in the present model to exhibit some degree of thermal diffusion following adsorption makes this simplification less important under the conditions tested here.

The models are run for simulated times on the order of tens of thousands of years, and by the end of each model run around half of the heavy atoms have been depleted from the gas phase, forming ices on the grain surfaces. By the end of its run-time, each model is thus on the cusp of experiencing strong gas-phase depletion which would slow the further growth of the ice mantle. The time taken to build up an ice mantle of a particular size is dependent on the cross-sectional area presented by the combined grain and ice mantle, averaged over all solid angles (the details of the accretion process are described in detail by Garrod, 2013b). The different sizes and morphologies of the grains thus affect the cross-sectional area presented to gas phase species, while those cross sections also rise as the ice mantles grow over time. For purposes of comparison between models, it is therefore helpful to define output times in relative terms, corresponding to the amount of depletion from the gas phase. This measure is more instructive than, for example, a determination of the number of ice molecules on the grains or the thickness of the ice, as it makes no assumptions about the chemical or physical form that the ice mantles take. Each model is set up to produce outputs for 1000 different time values, which here we will refer to as "intervals". Those intervals are evenly spaced in the amount of O, C, N and CO that have been accreted from the gas phase as a fraction of the initial amount (which varies depending on the size of the grain, via the gas-to-dust ratio). Each interval corresponds to a roughly equivalent amount of ice build-up, but as time goes on and depletion from the gas phase increases, the timescale required to complete one interval lengthens. The final populations of the grain-surface molecules achieved in each grain-size model scale roughly with the volume ratio of the underlying grains.

The run-time (wall time) of the models ranges from a few days to two weeks, depending on the size of the dust grain.

For each grain size and morphology used in the models, a total of three physically and chemically identical runs are carried out, with the only difference being the initial random number seed used in the Monte Carlo algorithm. This ensures that the model results are reproducible, and to some extent demonstrates the degree of random variation in the chemical abundances.

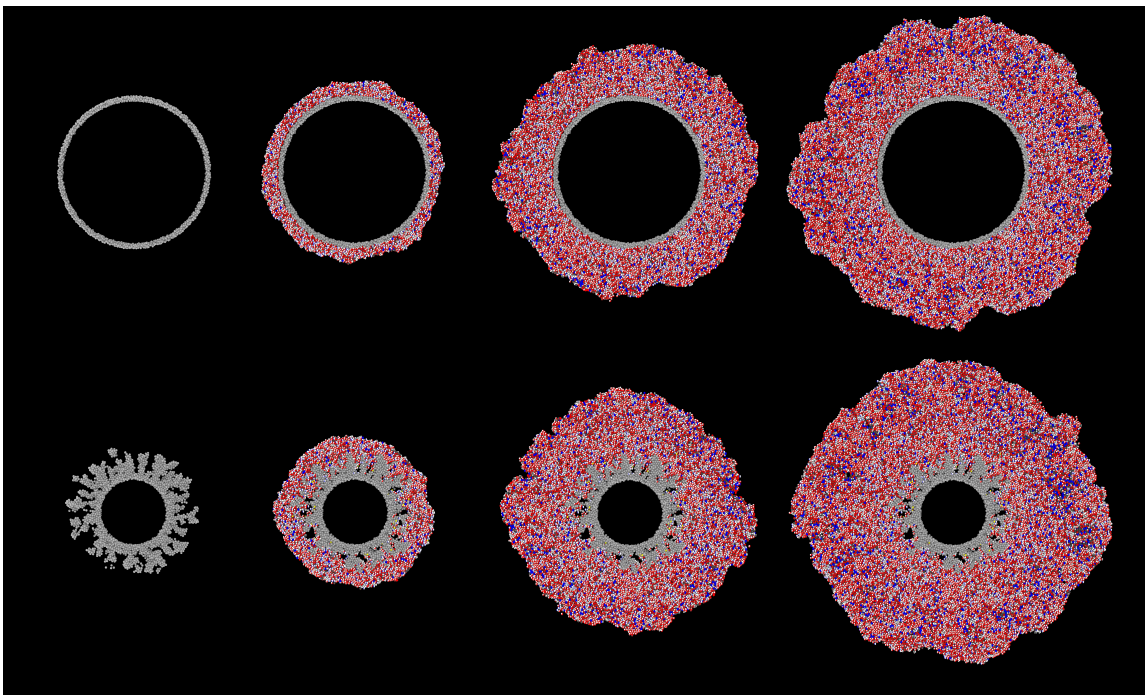

Figure 2.2: Ray-traced, cross-sectional images of the large (100 Å radius) non-porous (top) and large porous (bottom) grain types at different stages of ice build-up; left to right: interval 0, interval 100, interval 500, interval 1000. Gray spheres represent the carbon atoms composing the dust grain. Grain-surface atoms are represented by spheres of white (H), red (O), black (C) and blue (N). Molecules are similarly represented as collections of such atoms in appropriate structures. H_2 molecules are colored yellow for ease of identification.

2.3 Results

Fig. 2.2 shows ray-traced images of the cross-sections through the large porous and non-porous grains, at selected points in the model runs. From left to right, the images depict the growth of the ice mantles at comparable moments (based on the degree of gas-phase depletion of heavy species). For the non-porous grain, the material from the gas phase builds up relatively uniformly over the entire surface. There is also no indication of empty pockets. Based on the results of the hydrogen/oxygen system modeled by Garrod (2013b), the ice produced on dust grains under dark-cloud physical conditions should be non-porous, as heavy atoms accreted from the gas phase would have ample time to diffuse on the surface, finding and filling any nascent surface inhomogeneities, which tend to manifest initially as stronger binding sites due to their local curvature.

For the porous dust grains, after a sufficient amount of ice mantle has been built up (interval 100), the surface appears to be relatively uniform as well. However, looking below the surface, there are some differences. Firstly, rather than filling up the pores in the grain material, the ice fills them only partially, with some porosity remaining as the ice builds up over the top, leaving empty pockets that are not present in the non-porous grains. Secondly, there appears to be a collection of molecular hydrogen gathered in those remaining porous structures.

Fig. 2.3 shows cross-sectional close-up images of the large porous grain at early times in the ice-mantle evolution. Porous structures are gradually filled, sometimes leaving voids in the ice. While much of the volume of the pore voids present in the original grain is filled, some of the bare grain surface remains and there are internal ice surfaces formed where the pores are not completely filled. H_2 molecules, marked

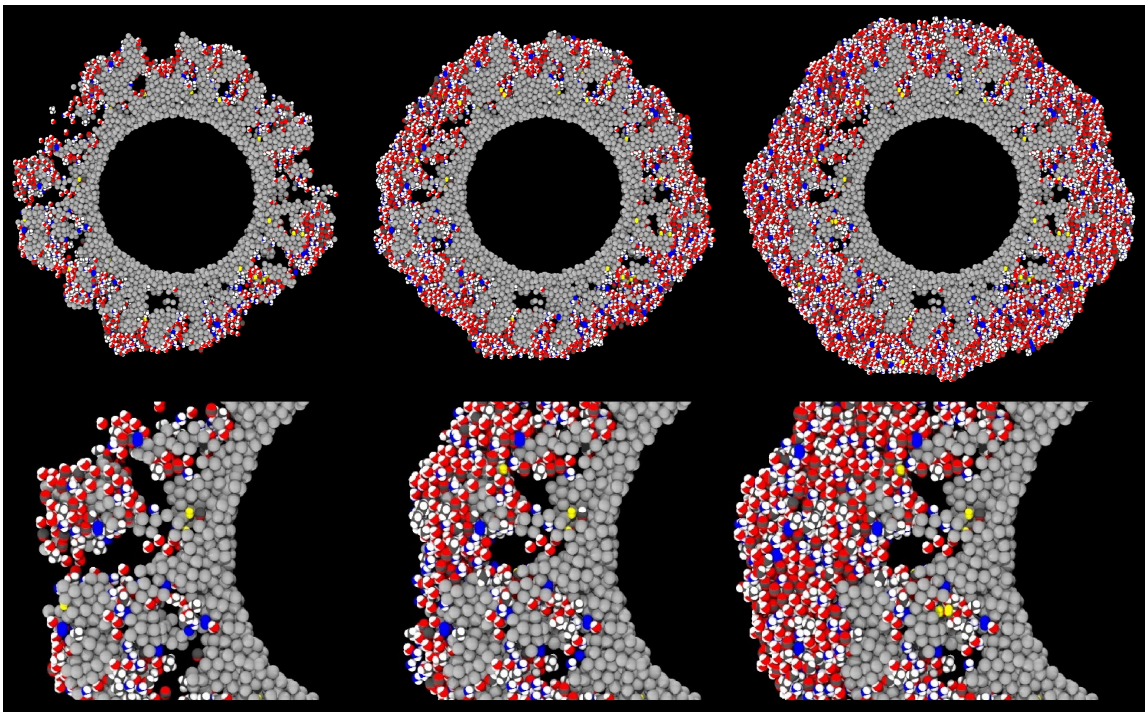

Figure 2.3: Ray-traced, cross-sectional images of the large (100 Å radius) porous grain type at the early stages of ice build-up, corresponding to the grain shown in the bottom row of Fig 2.2; here, the cross-section at a different angle is shown. Left to right: interval 25, interval 50, interval 100. The three upper panels show the full cross-section, while the lower panels show close-up images of the same small region of the grain at each of the three intervals. Gray spheres represent the carbon atoms composing the dust grain. Grain-surface atoms are represented by spheres of white (H), red (O), black (C) and blue (N). Molecules are similarly represented as collections of such atoms in appropriate structures. H_2 molecules are colored yellow for ease of identification.

in yellow, can also be seen more clearly in Fig. 2.3; some are apparently bound directly to the grain material itself, while others are embedded in the ice. Notably, the H_2 molecules present at interval 25 (left-most images) seem mostly to retain their positions at later intervals, indicating that they are well fixed into those structures. It may be noted that the ices that form once the pores in the grain material are covered over are themselves non-porous; as found by Garrod (2013b), under dark-cloud conditions, oxygen and other atoms have long enough pre-reaction lifetimes

before they react with the more mobile H atoms (producing e.g. water), that they may diffuse enough to find strong surface binding sites, leading to a smoothing of the ice surface. The porosity that is present in the ice by the end of the model runs is due to the initial presence of porosity in the grain material. The final grain/ice does not retain that same degree of porosity, as the ice partially fills the original voids, and then forms non-porous ice once those are fully enclosed.

Table 2.4 shows the absolute number of atoms and molecules resident on the grain surfaces at the end of each model. Values shown are the mean final populations of the three random number-seed runs for each setup. The final time in each model is also indicated. Table 2.5 shows the same population data given as a fraction of the total water on the grains, which allows an easier comparison between models. The porous grains take a little longer to reach their final state (i.e. the same amount of ice) as, compared with their non-porous equivalents, the porous grains present slightly smaller accretion cross sections.

Comparing between models, firstly we may consider the effect of grain size, by contrasting the relative abundances achieved in each of the three non-porous grain models. The abundance data suggest that variation in size has little effect on the relative abundances of the main ice constituents, such as CO, CO_2, and other stable molecules. CO reaches a population a little over 4% of total water, while CO_2 is at around 49%. In comparison to observational values toward background stars, the latter is a little high, while the former is a little low; observational lower and upper values are 9–67% and 14–43%, respectively (Boogert et al., 2015). This may be explained by our use of static physical conditions throughout the model run, combined with the lack of gas-phase chemistry. The initial chemical abundance of CO is representative of a somewhat evolved gas-phase chemistry, while that of atomic

oxygen is more appropriate to early times; this combination therefore leads to a somewhat higher degree of conversion of CO to CO_2 than observations would suggest.

The fractional abundances of volatile species on the grains do not scale so well with grain size; C, O, N and OH are seen to fall with increasing grain size. The absolute abundances of these species increase with greater grain radii, but not at the r^3 ratio seen for stable species. However, these values are likely reflective of the lifetime of such species against reaction with a newly-accreted H atom on the grain surface, which is more dependent on grain surface area than on total volume. The differences between grain-size models do not otherwise seem to affect the resultant chemical compositions of stable molecules.

The two porous grains may also be compared. Fractional abundances between the medium- and large-sized porous grains are again similar for stable species, while the atoms and radicals show somewhat less variation; indeed, the fractional abundance of atomic H is identical between the two. We note also that the quantities of atomic H shown in the Table correspond largely to H trapped within the bulk ice; the total, instantaneous population of free (surface) H atoms on the grains in any of the models hovers around one.

Comparison of the abundances of each chemical species between the porous and non-porous models of the same grain size demonstrates an interesting outcome. Beginning with the medium grains, the final fractional abundances are fairly consistent with one another for most species, especially stable molecules. The one molecular abundance that stands out in comparison between porous and non-porous grains is that of molecular hydrogen, which is about two times greater in the porous cases than it is in the non-porous cases, by the end of the model runs. The absolute numbers of H_2 on the grains are on the order of hundreds, so the differences cannot be due to

random small-number fluctuations. Consideration of the large porous and non-porous grains shows similar behavior for all species, while the discrepancy in the absolute abundance of H_2 is further exacerbated. Atomic H also shows a much stronger variation than the other atoms when comparing between porous and non-porous grains.

In order to pinpoint the cause of this, the time-dependence of the H_2 population may be examined. Fig. 2.4 shows the absolute populations of H_2 for the large porous and non-porous grains, averaged over the three random number-seed runs for each case; each of the individual runs is close to its mean curve. For most intervals, the porous and non-porous grains show almost identical trends, except that the porous-grain model has a very rapid up-tick at early times – times at which the porous grain-surface is still exposed. Ignoring this offset, there is otherwise convergence in behavior after that initial jump. It is evident that the enhancement in H_2 population at those early stages becomes a permanent feature of the ice, as the offset is retained right until the end of the models. The growth in the H_2 populations toward the end of both sets of models is caused by the falling rates of accretion of heavy species from the gas phase, as their limited budgets run out, while H atoms remain plentiful throughout, increasing the probability of H_2 production (the same effect is seen in Fig. 2.5).

There are several possible explanations for the larger population of H_2 on the porous grains. We propose the following as the most likely: (i) the porous surface enhances the overall conversion of H into H_2, with mobile H_2 formed in the pores diffusing away to be incorporated into the general bulk ices; (ii) the porous surface enhances production rates locally within the pores, leading to the build-up of H_2 where it is formed; (iii) H_2 that is formed anywhere on the grain surface may diffuse into the pores, where it becomes trapped.

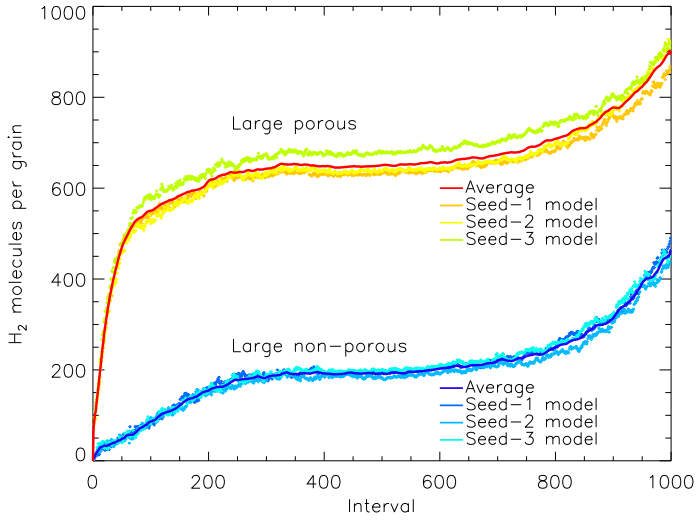

Figure 2.4: The amount of molecular hydrogen present on the grain versus relative time intervals, for the large porous and non-porous grain models. The solid lines show a moving average (of period 10) over the three runs for either grain type, with the data from the individual runs plotted as individual points. Interval 1000 corresponds to the end time of the models shown, which are shown individually for each model in Table 2.4.

Fig. 2.5 shows the total number of H_2 molecules formed throughout each model; the plot shows all of the three runs for both the large porous and large non-porous grains. The overall production of H_2 is extremely similar between models and grain sizes, including at the early times when the effects of the porosity manifest. Any difference may be accounted for by slight variations in the sizes of the porous and non-porous dust grains. We can therefore rule out a difference in the production efficiency of H_2 on the porous grain as the cause of its greater H_2 retention.

It is instructive also to consider the amount of "free" H_2 throughout each model, shown in Fig. 2.6 (large grains). This is a measure of the number of H_2 molecules that are capable of undergoing diffusion or desorption, at whatever rate, and which may therefore be classified specifically as surface species. Molecules that are not "free" are necessarily trapped under other species. The behavior of the free H_2 is qualitatively

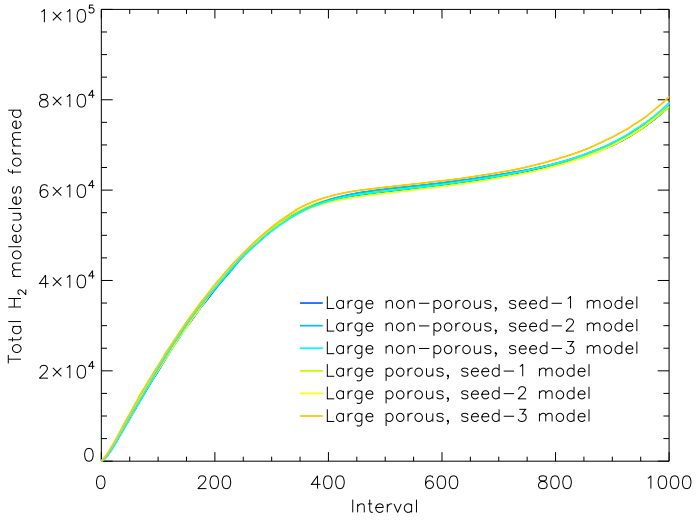

Figure 2.5: The total count of hydrogen molecules formed in the model up to a given moment, versus relative time intervals. All H_2 formed is shown, regardless of whether it is trapped in the ice, desorbed into the gas phase, or destroyed by chemical reactions. Data from the three runs for the large porous and non-porous grain models are shown. Interval 1000 corresponds to the end time of the models shown, which are shown individually for each model in Table 2.4.

similar to that of the total H_2 population, and it also grows strongly at early times in the porous grain models. The absolute number of free H_2 molecules in the porous model reaches a peak of around 45 until late times, which is a factor $\sim$15 lower than the total H_2 on the grain at that time. Over the same period in the non-porous case, there is only a few free H_2 molecules at any one time, corresponding to roughly one in fifty of the total H_2 on that grain.

Clearly, the much greater absolute numbers of surface H_2 on the porous grain indicates that those particular molecules at least are stored on the surfaces of the open porous structures that become closed off to outside chemical influence by around interval 100. With such a build-up in surface H_2 abundances in the pores, it is natural that some H_2 should become incorporated into the ice mantles that form specifically within the pores (i.e. no longer free). Fig. 2.7 shows an image of the H_2 present on

the large porous grain at the end of one of the runs, with no other atoms, molecules, or grain material depicted. The image includes all H_2 molecules present in three dimensions, not just a cross-section. The distribution of H_2 clearly favors the pore structures, although some H_2 is still present in the outer mantles.

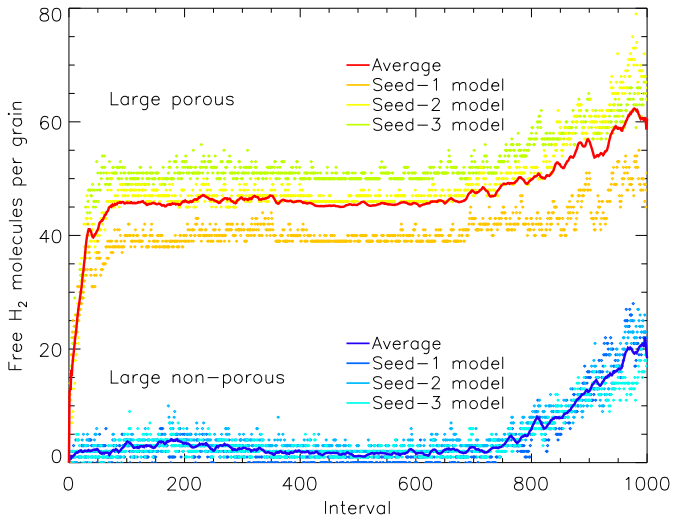

Figure 2.6: The amount of free molecular hydrogen present on the grain plotted versus relative time interval, for the large porous and non-porous grain models. Free species are able to undergo surface diffusion and desorption, but may reside on enclosed surfaces within pores. The solid lines show a moving average (of period 10) over the three runs for either grain type, with the data from the individual runs plotted as individual points. Interval 1000 corresponds to the end time of the models shown.

We again consider the feature seen in Figs. 2.4–2.6 in which the amount of H_2 (whether the amount on the grain, the number of free molecules, or the total formed) increases over the last few hundred intervals. This effect is the result of the run-down in the gas-phase budget of species other than hydrogen, i.e. the depletion of those species. While, for example, atomic O becomes less and less abundant in the gas phase over time, due to its adsorption and incorporation into the ice mantle, the amount of gas-phase H stays the same; this means that for any one adsorbed H atom, its surface reaction partner is increasingly likely to be another H atom, which drives up the H_2 production rate. Meanwhile, the time required for a fixed number of gas-phase atoms

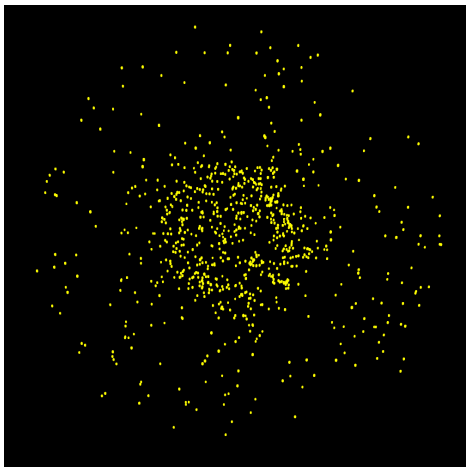

Figure 2.7: Ray-traced image of the large porous grain type at the final stage of ice build-up showing only the H_2 molecules and excluding the grain and all other ice species.

(or CO) to be adsorbed from the gas phase also rises, due to their smaller remaining budgets. The amount of time associated with each interval therefore lengthens (see Sec. 2.2), making the increase in H_2 molecules appear more dramatic.

Fig. 2.8 shows the amount of free H_2 on the grain, just as in Fig. 2.6, but is shown here as a percentage of the total population of free species. Note that the number of free species in this model corresponds approximately to the number of species (atoms or molecules) present in the surface of the ice or on the surface of the grain (during the early stages before a mantle has built up). This count of surface species includes not only the outer surface but any enclosed surfaces that remain within the pores. As a fraction of the total, we see initially that the difference between the porous and non-porous grains is quite stark, as the pores in the grain material retain a substantial amount of H_2. The difference gently declines for later intervals for two reasons: (i) much of the porous structure within the grain material becomes filled up and smoothed out, so that some of the surface H_2 trapped there is locked into the bulk ice that resides in the grain pores, and (ii) the outer surface of the ice

mantle grows, so that the enclosed surfaces that remain deep down in the grain/ice account for a smaller fraction of the total surface available. By the end of the two runs, the percentage of surface coverage by H_2 is similar (within a factor of 2); the difference that remains nevertheless corresponds to the H_2 that is trapped within porous structures, residing on their enclosed surfaces and unable to escape. Plotted as a percentage of total coverage, the apparently dramatic rise in free H_2 (seen in Fig. 2.6) is far more subdued in both models.

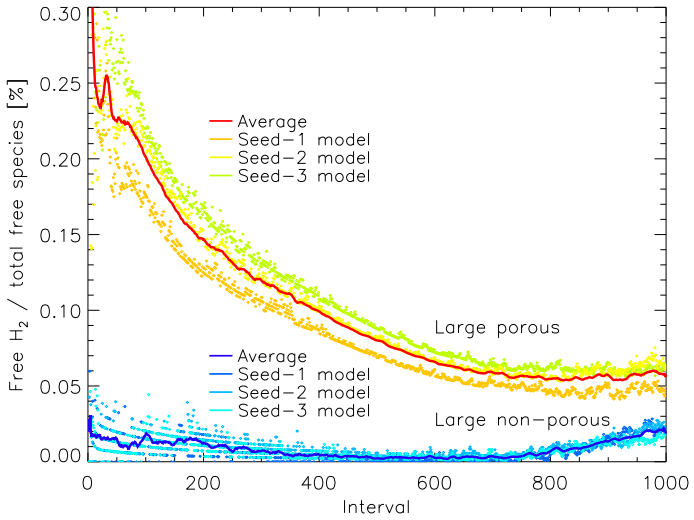

Figure 2.8: The percentage of free molecular hydrogen present on the grain as a function of all free species, plotted versus relative time interval for the large porous and non-porous grain models. Free species are able to undergo surface diffusion and desorption, but may reside on enclosed surfaces within pores. The solid lines show a moving average (of period 10) over the three runs for either grain type, with the data from the individual runs plotted as individual points. Interval 1000 corresponds to the end time of the models shown.

2.4 Discussion

Aside from some small variations in fractional abundances, neither the grain size nor porosity appear to have a major effect on the grain-surface ice composition, except in

the case of H_2. Atomic H is also retained to a somewhat higher degree on the porous grains, but the absolute numbers are relatively small compared with H_2.

Porous grains retain molecular hydrogen uniquely, either in the ice mantles that form within the pores, or on the surfaces of the pore mantles, in cases where voids exist within the icy pores (having been partially filled and then closed over by ice). The porosity does not induce any greater production of H_2 (or other stable molecules) on the grains; rather it acts simply to trap those molecules. However, even if the total H_2 produced is essentially unchanged, it is a different question to ask whether the presence of pores affects where on the grain that fixed amount of H_2 is formed. Trapping of atomic hydrogen on pore surfaces could lead to local production of H_2 that may likewise become trapped; alternatively, H_2 produced elsewhere on the grain could also become trapped, following surface diffusion into the pores. Both are plausible explanations for the excess of trapped H_2 in the pores and pore ices.

As described by Garrod (2013b) in the case of porous ices produced on smooth grains, the reason molecular hydrogen becomes trapped in pores at all has to do with the effect of surface structure on binding energies. The surface of a smooth grain is flatter; thus, fewer grain-surface binding partners maintain close proximity to a given hydrogen molecule at any time. However, the interior of the pores is more irregular and concave on very small scales, allowing more grain atoms or bulk-ice molecules to contribute to the binding energies and diffusion barriers experienced by a particle within that structure. The resulting stronger binding site allows for the molecular hydrogen to be held within the pore for long enough for other ice material to cover it up, or at least to seal over the pore before it is able to escape. The larger proportion of "free" H_2 molecules in the porous, versus non-porous, grain models indicates that the sealing of porous voids is a non-negligible effect, although the complete incorporation

of excess H_2 into the pore ices is the primary cause of retention.

Atomic hydrogen is mobile on the grain surfaces, but upon entering a pore it may encounter a strong binding site and be retained there for a longer period than if it were in a weak binding site. The arrival of another H atom would convert it to H_2, allowing that molecule to be trapped in that site. It may be seen, though, that other molecules – whose progenitor-atoms such as O, C and N are much less mobile on the grains – can also fill up the pores; the pores are not filled solely or even predominantly with H_2. Also, the overall ice structure outside of the grain-pores does not become porous itself once the underlying pores are covered over. This is because the heavier atoms in the model are still sufficiently mobile to find strong binding sites for themselves, including those located within the pores, prior to being hydrogenated by atomic H (which leads to a stronger surface bond and much lower mobility, at which point that species becomes fixed).

Why, then, should H_2 be uniquely affected by the presence of many strong binding sites within the pores? H_2 is unique also in being a mobile surface species that is largely unreactive. It may react indeed with OH, for example, but all of its few reactions have an activation energy barrier. On the other hand, atoms like H, O, C, and N, even though reasonably mobile, will react immediately upon meeting some other reactive species, ending their diffusion. Their diffusion path length on the surface is therefore limited by meetings with potential reaction partners, as well as by their somewhat slower diffusion rates (versus their main reaction partner, atomic H). An H_2 molecule, however, has the chance to sample a much larger fraction of the grain surface, seeking out strong binding sites, with its main loss route ultimately being desorption into the gas phase rather than reaction. As well as having a greater chance to find those strong sites, the lifetime against desorption of an H_2 molecule

will be substantially increased if it does find one.

Given a large selection of strong binding sites on the grain, due to their high mobility H_2 molecules are most likely to fill them. The availability of a larger number of strong sites in the porous case therefore invites the retention of H_2. When strongly bound species are formed on top of the H_2, or in close quarters, that H_2 becomes trapped. The disappearance of strong binding sites as the ices build up and become more uniform in structure removes this effect.

While the numbers of H_2 being trapped in the present models are on the order of hundreds, larger grains would likely store proportionately more. Also, the model specifically leaves out the accretion of H_2 directly from the gas phase; all of the trapped H_2 in the models must first be formed on the grains through chemical reactions. In reality, grains would be under a constant flood of H_2 adsorption, even if the individual lifetimes of those molecules were short. We should expect that any strong binding sites in the grain pores would be rapidly and comprehensively filled by H_2 in that case. The potential for trapping could therefore be much higher in a more realistic simulation. Unfortunately, as the H_2 abundance in the gas phase is around 1000 times higher than the other species collectively, at current computational speeds those simulations would take years rather than weeks.

Similarly to molecular hydrogen, the trapping of other unreactive, volatile species such as helium could also be important. Interstellar He abundances are around 10% with respect to total H (by number), and could therefore similarly flood the surface. Neon, as the next inert element, might also be sufficiently mobile on the grain surfaces to find strong binding sites and therefore experience trapping. If these or other inert species could be trapped in the deepest layers of the ices, close to the grain surfaces themselves, then they could be retained on the grains long into the star

formation process, even under warm conditions where much of the ice material might have already desorbed. Such a mechanism may be contrasted with the ice annealing process explored by, e.g., Bar-Nun et al. (1987), whereby highly-porous water ice was used to trap Argon gas, with the pores being closed over through a diffusive creeping mechanism of the ice at the pore openings.

It should be noted that it is specifically the microstructure of the porous grains that is most important to the retention of H_2, or other volatiles similarly affected, in the models presented here. The coagulation of large, smooth grains would not likely produce such an effect. However, the presence of an icy coating on the grain pore surfaces may be just as effective as the bare grain itself in trapping H_2, so long as the build-up of the ice within those pores allows the underlying microporous and/or irregular structure to be retained.

The release of the chemical energy of surface reactions has been suggested as a mechanism for both the general heating of a dust grain and the non-thermal desorption of H_2 in particular (see e.g. the review of Wakelam et al., 2017a). Calculations of the heating effect of H_2 production on silicate grains through the addition of H atoms by Navarro-Ruiz et al. (2014) suggested a strong influence on the temperatures of very small grains. Scaling their calculations to the size of our "large", 100 Å radius grains, the expected change in temperature would be less than 0.1 K per H_2 production event, with a time constant for the radiation of the excess energy of less than 1 μs, i.e. much faster than the rate of H_2 production. The whole-grain effect of chemical heating (at least via H_2 formation) is therefore unlikely to have a significant influence on our models, although the somewhat smaller local structures produced in our porous grains could be more strongly affected. Chemical heating could affect the local structure of the ice also; however, Oba et al. (2009) suggest that in the case

of amorphous ice formation through surface chemical reactions, the structure is not influenced by this mechanism, in line with calculations by Kouchi et al. (1994).

The chemical energy of reactions could allow H_2 formed on the grains to desorb through direct chemical desorption, although in our models the desorption process follows explicit trajectories, so that an H_2 molecule desorbed in this way could certainly be re-adsorbed. However, if the surface of the grain is indeed flooded with H_2 molecules (see above), the influence explicitly of the H_2 formation process should be far less important than the diffusion of H_2 into the pores. Indeed, the models presented here show that the H_2 does not need to be formed *in situ* within the pore structures to become trapped there.

The kinetic models used here sample only a small region of parameter space in terms of grain size, porosity and small-scale structure/roughness. The simulated dust-grains are constructed crudely to produce high degrees of porosity. A more detailed determination of the precise microstructures of interstellar dust grains is therefore necessary to constrain the proposed effect using chemical kinetic models. It is also the case that the carbon atoms that constitute the grain material in our treatment are not allowed to participate in any way in the surface reactions; we do not, for example, consider chemisorption in the production of H_2 or other species. As discussed by Wakelam et al. (2017a), reactions between physisorbed H atoms are likely to be the dominant H_2 formation mechanism under translucent and dark cloud conditions, while substantial water or other ice mantles are not expected to build up before visual extinctions greater than around 3 magnitudes (i.e. translucent) are achieved (Whittet et al., 2001).

Our model also uses only a simple, static treatment of the physical conditions of dark clouds, ignoring the lower density and visual extinction that would pertain

at early times, and which could lead to a somewhat higher dust temperature. The initial chemical conditions are also quite simple, with CO and H_2 assumed already to have formed in substantial quantities at the time the models begin. The lack of a gas-phase chemistry could also affect the results; it is possible, for example, that the gas-phase production of water would lead to some component of the surface water ice originating through direct deposition from the gas phase; such conditions would be a little closer to those frequently employed in the laboratory for the study of porous amorphous water ices, and might therefore lead to a higher degree of porosity in the ices themselves that would not be associated directly with the grain material's porosity. However, past dark-cloud gas-grain chemical models by our group (e.g. Garrod and Pauly, 2011) have not found any substantial contribution from gas-phase water in the build-up of the ice mantles, even under conditions of low extinction and elevated dust-grain temperatures.

The possibility of thermal desorption and re-deposition of water ice onto the dust grains in protoplanetary disks, however, might provide a regime in which ices of substantial porosity could be formed, through direct deposition rather than chemical formation on the grain surfaces. H_2 or other volatiles might be expected to be trapped in such structures also.

2.5 Conclusion

Our chemical kinetic models of interstellar grain-surface chemistry indicate that, given a highly porous dust grain, molecular hydrogen may be trapped in strong binding sites caused by the irregular surface structure of the pore surfaces. The coating of those pore surfaces with water and other common dust-grain ice mantle constituents locks

the H_2 into the ice, although the irregular surface structures of the ice itself continue to allow trapping until the pores are completely filled and the grain/ice takes on a more regular, spherical morphology. The closing over of the pores, creating voids, is only a small part of the trapping effect, but a fraction of the trapped H_2 is found to be free on the surfaces of those enclosed voids. A full-scale treatment of H_2 adsorption onto the grains using this microscopic treatment might be expected to exhibit even greater degrees of trapping. The trapping effect could provide a means for other volatile and relatively inert species to be retained on the grains, enclosed in the deepest ice layers. Such an effect would allow chemical species trapped under interstellar cloud conditions to be preserved in the ices into much later stages in the star- and planet-formation process.

Chapter Acknowledgements

DAC ran computational models, analyzed the data, and co-wrote the manuscript. RTG wrote the *MIMICK* computational code, helped analyze the data and co-wrote the manuscript. We thank the anonymous referees for comments and suggestions that improved this paper. This work was funded by the NASA Astrophysics Research and Analysis program, through grant number NNX15AG07G.

Table 2.2: The reaction network used in MIMICK. Activation barriers, where present, are in units of Kelvin, with barrier widths in Angstrom.

Reaction	E_a (K)	Width (Å)	Reaction	E_a (K)	Width (Å)
$H + H \rightarrow H_2$	-	-	$O + CH \rightarrow HCO$	-	-
$H + O \rightarrow OH$	-	-	$O + CH_2 \rightarrow H_2CO$	-	-
$H + OH \rightarrow H_2O$	-	-	$O + CH_3 \rightarrow CH_3O$	-	-
$H + O_2 \rightarrow O_2H$	-	-	$O + CO \rightarrow CO_2$	1000	1.27
$H + O_2H \rightarrow H_2O_2$	-	-	$O + HCO \rightarrow H + CO_2$	-	-
$H + O_3 \rightarrow OH + O_2$	-	-	$OH + OH \rightarrow H_2O_2$	-	-
$H + H_2O_2 \rightarrow OH + H_2O$	1800	1.00	$OH + CH_2 \rightarrow CH_2OH$	-	-
$H + C \rightarrow CH$	-	-	$OH + CH_3 \rightarrow CH_3OH$	-	-
$H + CH \rightarrow CH_2$	-	-	$OH + CH_3OH \rightarrow H_2O + CH_2OH$	359	1.00
$H + CH_2 \rightarrow CH_3$	-	-	$OH + CH_3OH \rightarrow H_2O + CH_3O$	852	1.00
$H + CH_3 \rightarrow CH_4$	-	-	$OH + CH_4 \rightarrow H_2O + CH_3$	1780	1.00
$H + N \rightarrow NH$	-	-	$OH + CO \rightarrow H + CO_2$	80	1.00
$H + NH \rightarrow NH_2$	-	-	$N + N \rightarrow N_2$	-	-
$H + NH_2 \rightarrow NH_3$	-	-	$CH_3 + CH_3 \rightarrow C_2H_6$	-	-
$H + CO \rightarrow HCO$	2320	1.35	$CH_3 + HCO \rightarrow CH_3CHO$	-	-
$H + HCO \rightarrow H_2 + CO$	-	-	$HCO + HCO \rightarrow HCOCHO$	-	-
$H + HCO \rightarrow H_2CO$	-	-	$CH_3 + CH_3O \rightarrow CH_3OCH_3$	-	-
$H + H_2CO \rightarrow CH_2OH$	4500	1.35	$CH_3 + CH_2OH \rightarrow C_2H_5OH$	-	-
$H + H_2CO \rightarrow CH_3O$	2320	1.35	$HCO + CH_3O \rightarrow HCOOCH_3$	-	-
$H + H_2CO \rightarrow H_2 + HCO$	2960	1.22	$HCO + CH_2OH \rightarrow HCOCH_2OH$	-	-
$H + CH_2OH \rightarrow CH_3OH$	-	-	$C + C \rightarrow C_2$	-	-
$H + CH_2OH \rightarrow H_2 + H_2CO$	-	-	$C + CH \rightarrow C_2H$	-	-
$H + CH_3O \rightarrow CH_3OH$	-	-	$C + CH_2 \rightarrow C_2H_2$	-	-
$H + CH_3O \rightarrow H_2 + H_2CO$	-	-	$C + CH_3 \rightarrow C_2H_3$	-	-
$H + CH_4 \rightarrow H_2 + CH_3$	5940	2.17	$CH + CH \rightarrow C_2H_2$	-	-
$H_2 + C \rightarrow CH_2$	2500	1.00	$CH + CH_2 \rightarrow C_2H_3$	-	-
$H_2 + CH_2 \rightarrow CH_3 + H$	3530	1.00	$CH + CH_3 \rightarrow C_2H_4$	-	-
$H_2 + CH_3 \rightarrow H + CH_4$	6440	1.00	$CH_2 + CH_2 \rightarrow C_2H_4$	-	-
$H_2 + NH_2 \rightarrow H + NH_3$	6300	1.00	$CH_2 + CH_3 \rightarrow C_2H_5$	-	-
$H_2 + OH \rightarrow H + H_2O$	2100	1.00	$H + C_2 \rightarrow C_2H$	-	-
$O + O \rightarrow O_2$	-	-	$H + C_2H \rightarrow C_2H_2$	-	-
$O + OH \rightarrow O_2H$	-	-	$H + C_2H_2 \rightarrow C_2H_3$	1300	1.00
$O + O_2 \rightarrow O_3$	-	-	$H + C_2H_3 \rightarrow C_2H_4$	-	-
$O + O_2H \rightarrow O_2 + OH$	-	-	$H + C_2H_4 \rightarrow C_2H_5$	605	1.00
$O + C \rightarrow CO$	-	-	$H + C_2H_5 \rightarrow C_2H_6$	-	-

Table 2.3: Pairwise potentials, ϵ (K), between selected surface species.

	Grain carbon	H_2O	CO
H	45	45	45
H_2	40	40	40
C	100	100	100
O	100	100	100
N	100	100	100
OH	300	450	120
CO	120	120	120
N_2	125	125	120
O_2	150	150	120
CO_2	280	280	120
CH_4	180	180	120
NH_3	520	700	120
CH_3OH	320	640	120
H_2O	350	700	120

Table 2.4: The total abundance of some notable ice species averaged over three runs. The final time of each model is also indicated, which corresponds to interval 1000 in each case.

	Non-Porous			Porous	
Species	Small (34,885 yr)	Medium (56,417 yr)	Large (71,851 yr)	Medium (66,636 yr)	Large (83,484 yr)
H	7	32	62	43	92
H_2	31	214	463	363	895
C	47	69	193	98	200
O	42	75	160	100	177
N	84	170	507	250	522
OH	116	109	338	205	341
CO	3,002	10,699	23,180	10,739	22,943
N_2	10,420	36,876	82,028	38,565	82,163
O_2	182	467	1,319	609	1,339
CO_2	33,240	121,364	263,505	122,636	262,636
CH_4	906	4,208	8,466	3,879	8,907
NH_3	16,560	63,815	134,897	62,443	134,043
CH_3OH	502	2,549	4,958	2,297	5,353
H_2O	67,187	247,960	533,161	249,904	534,938

Table 2.5: The fractional abundance of some notable ice species relative to the total water ice, averaged over three runs.

	Non-Porous			Porous	
Species	Small	Medium	Large	Medium	Large
H	1.09e-4	1.24e-4	1.16e-4	1.72e-4	1.72e-4
H_2	4.57e-4	7.09e-4	8.69e-4	1.45e-3	1.67e-3
C	6.99e-4	4.32e-4	3.63e-4	3.92e-4	3.74e-4
O	6.29e-4	4.71e-4	3.00e-4	4.00e-4	3.30e-4
N	1.25e-3	1.02e-3	9.52e-4	9.99e-4	9.76e-4
OH	1.72e-3	8.16e-4	6.33e-4	8.19e-4	6.38e-4
CO	4.47e-2	4.36e-2	4.35e-2	4.30e-2	4.29e-2
N_2	1.55e-1	1.54e-1	1.54e-1	1.54e-1	1.54e-1
O_2	2.71e-3	2.34e-3	2.47e-3	2.44e-3	2.50e-3
CO_2	4.95e-1	4.91e-1	4.94e-1	4.91e-1	4.91e-1
CH_4	1.35e-2	1.46e-2	1.59e-2	1.55e-2	1.67e-2
NH_3	2.46e-1	2.50e-1	2.53e-1	2.50e-1	2.51e-1
CH_3OH	7.47e-3	8.52e-3	9.30e-3	9.19e-3	1.00e-2

Chapter 3

Ice Chemistry of Comet Hale–Bopp

The work presented in this chapter has been published in Icarus in Astronomy and Space Sciences with Eric R. Willis and Robin T. Garrod (Willis et al., 2024), wherein I am the corresponding author.

3.1 Introduction

Cometary nuclei are believed to contain some of the most primitive and well-preserved material from the formation of the Solar System (Weissman et al., 2020). Generally, comets are stored in one of two regions of the Solar System – the Kuiper Belt (Kuiper, 1951) and the Oort cloud (Oort, 1950); from here, some gravitational perturbation may place a comet into an orbit that more closely approaches the Sun. The Kuiper Belt extends from the orbit of Neptune (∼30 AU) out to ∼50 AU, and has a mean temperature of ∼40 K (Hsieh and Jewitt, 2006). The Oort cloud is significantly larger and colder, with suggested inner and outer radii of 3000 and 50,000 AU, respectively, and a mean temperature of ∼10 K (Hsieh and Jewitt, 2006). Other estimates have placed the maximum radius of the Oort cloud at a value as large as 200,000 AU (Duncan et al., 1987).

Cometary ice is dominated by H_2O, yet complex organic molecules (COMs) – typically defined as organic species with 6 or more atoms – have also been detected in comets via remote observations, as well as from returned samples (Mumma and Charnley, 2011). The long-period comet C1/1995 (Hale–Bopp), which has an Oort cloud origin, was found to harbor an array of complex organics. Bockelée-Morvan et al. (2000) detected formamide (NH_2CHO) and methyl formate ($HCOOCH_3$) in the coma of Hale–Bopp using ground-based telescopes. In the same comet, Crovisier et al. (2004) detected ethylene glycol ($(CH_2OH)_2$), with a production rate from the cometary nucleus of around 0.25% that of H_2O, indicating a substantial quantity of this molecule in the ice. Observations of Hale–Bopp beginning in August 1995 detected outgassing of nine other molecular species, including methanol (CH_3OH), formaldehyde (H_2CO), and acetonitrile (CH_3CN) (Biver et al., 1997). Although the abundance of methanol – usually considered the simplest COM – that was detected toward Hale–Bopp (∼2.4% with respect to water) is not unusually high compared with other Oort Cloud comets, the brightness of Hale–Bopp allowed for the observational detection of an unusually broad range of larger, less abundant COMs. This great number of molecular data-points thus makes Hale–Bopp a good candidate for the modeling of possible COM chemistry in the comet nucleus.

Samples returned from the *Stardust* mission to comet 81P/Wild 2 (Brownlee et al., 2006) have also revealed significant chemical complexity. Glavin et al. (2008) utilized a combination of liquid chromatography and UV fluorescence to make detections of methylamine (CH_3NH_2) and ethylamine ($CH_3CH_2NH_2$) in the returned samples. Following on from that study, Elsila et al. (2009) studied the ^{13}C content of amino acids in the solid samples returned from Wild 2, reporting the first detection of a cometary amino acid, glycine (NH_2CH_2COOH).

More recently, Altwegg et al. (2016) used the ROSINA mass spectrometer (Balsiger et al., 2007) to detect glycine, methylamine, and ethylamine in the coma of Comet 67P/Churyumov–Gerasimenko. These detections, along with the simultaneous identifications of phosphorus-bearing molecules and other organics, have confirmed the discoveries made by the *Stardust* team, and highlighted the role that comets could have played in seeding the early Earth with organic molecular building blocks.

Many sulfur-bearing molecules have also been detected in the coma of Comet 67P/Churyumov–Gerasimenko, such as H_2S, SO, S_2, S_3, CH_3SH, and C_2H_5SH. Some sulfur-bearing species are used as bio-signatures in the search for life, and the presence of species like S_2 in Comet 67P indicates the ice mantles formed during or prior to the solar nebula and were, at least in part, maintained to this day, as opposed to being formed or reformed later in the solar systems lifetime (Calmonte et al., 2016). Additionally, many ammonium salts have been detected in cometary dust outbursts (Altwegg et al., 2020) including more recently detections of $NH_4^+SH^-$ by Altwegg et al. (2022) within the cometary dust specifically, while remaining more independently as NH_3 and H_2S within the cometary ice, both of which are some of the most abundant species within the ice.

Understanding the origin and evolution of COMs in cometary ices is of fundamental importance. Comets are thought to preserve much of their molecular content from the proto-solar nebula stage, and perhaps even earlier; Drozdovskaya et al. (2019) compared the composition of comet 67P with the abundances of gas-phase molecules detected toward the low-mass star forming region IRAS 16293-2422, finding correlations between their N-, S- and HCO-group-bearing species. However, the degree of processing that cometary ices may have undergone during later stages of evolution, including as fully-formed comets, is difficult to discern. The ongoing development of

detailed chemical kinetic models of cometary chemistry provides an opportunity to simulate the production, survival and/or destruction of molecules – including COMs – at these later stages.

Models of gas-phase chemistry in cometary comae have existed for some time (e.g. Irvine et al., 1998). Those models only included gas-phase processes in active comets, and were adapted from models constructed to simulate interstellar chemistry. One of the key questions motivating their use has been in distinguishing between those species formed in the cometary ice ("parent" species) and those formed via energetic processing in the coma ("daughter" species). However, in order to properly determine which species are produced in the coma, and which are inherited directly from the cometary nucleus, detailed models of the solid-phase chemistry in comets are needed.

Garrod (2019) (hereafter G19) published the first such computational model of solid-phase chemistry in cometary ice, which used an adapted version of the interstellar astrochemical code *MAGICKAL* (*Model for Astrophysical Gas and Ice Chemical Kinetics and Layering;* Garrod, 2013a). In the model of G19, the comet nucleus was constructed by extending the grain-surface and ice-mantle chemistry already included in *MAGICKAL*, while switching off the gas-phase chemistry. Although photochemistry was already present, new reactions were added to the network to take account of molecular dissociation induced by cosmic ray impacts. The nucleus material consisted of both ice material composed of various molecules and atoms, and a variable dust component that was chemically inert but capable of diminishing the impinging interstellar UV field. The physical structure of the comet was modeled by dividing the nucleus into 25 layers, each three times thicker than the last, beginning with a 1 monolayer-thick outer layer. The total depth into the nucleus was $\sim$136 m. Chemistry was studied for the "cold storage" phase of an Oort cloud comet's lifecycle, before

the onset of any activity caused by solar approach. Significant COM formation was observed to a depth of ∼15 m, due to processing of the ice by galactic cosmic rays, with the upper ∼1μm affected also by the penetration of UV photons.

Experimental work by Gronoff et al. (2020) and Maggiolo et al. (2020) also examined the effects of GCRs on cometary ices. While the effect of GCRs on isotopic ratios are negligible, the chemical processing is significant down to depths of tens of meters, although a more active collisional history between comets may lead to mixing of ices, allowing for processed, non-pristine, material to exist at greater depths. However, if a comet has no collisions, or even just a few soon after formation, then the ice should remain pristine below the tens of meters mark.

Furthermore, the material outgassed by a comet, either within a localized outburst or by sublimation, is highly dependent on its dynamical history. A comet on its first close solar approach will eject material that has been processed by GCRs, while much older comets that have had their surfaces significantly eroded away may instead eject more pristine ice. Both in intermediary stages, as well as in cases with more recent cometary collisions, it is likely to see some mixture of processed and pristine ice within outbursts which may be localized to certain parts of the comet.

Although comets spend the majority of their time in cold storage, either in the Kuiper Belt or the Oort Cloud, the solar approach of cometary bodies is very interesting from a chemical perspective. As noted above, cometary bodies eject material from their surfaces when approaching the Sun, and COMs have been detected in the resulting coma material. However, there have been no models of solid-phase cometary chemistry that consider solar approach.

In this paper, we present an updated version of the cometary ice chemistry model

of G19, in which we consider both the long, "cold-storage" phase in the Oort Cloud and the subsequent solar approach, following the orbital dynamics of comet C1/1995 (Hale–Bopp) as established in the literature. Based on distance-dependent solar irradiation, we solve the heat diffusion equation in one dimension, allowing time- and depth-dependent temperature profiles to be obtained, which are then incorporated into the chemical model. The model now incorporates a full range of non-thermal chemical reaction mechanisms (Jin and Garrod, 2020; Garrod et al., 2022), which allows bulk-ice reactions to be treated accurately, including reactions initiated by photodissociation or CR-induced dissociation of molecules. The model also includes a new treatment to take account of the back-diffusion effect, when calculating rates of bulk diffusion for specific chemical species between ice layers of different depths and thicknesses.

§3.2 describes the new mechanisms incorporated into the chemical model, as well as the heat transfer and back-diffusion simulations. §3.3 presents the results of the heat-transfer and back-diffusion simulations, as well as our chemical model results. §3.4 compares the results from these models with those of G19, as well as observations of Hale–Bopp. Conclusions follow in §3.5.

3.2 Methods

Here we build upon the model of ice chemistry in cometary nuclei introduced by G19. The initial model was adapted from the hot-core chemical kinetics model, *MAGICKAL* (Garrod, 2013a). The reader is referred to G19 for a full description of the comet chemical model. Below we outline basic elements of the model, along with the major updates that have been made to this new version.

The new comet model moves beyond the pure cold-storage treatment studied by G19, and presents several improvements. Firstly, we have incorporated a range of new non-diffusive ice chemistry mechanisms, following Jin and Garrod (2020) and Garrod et al. (2022) (see §3.2.2). A more accurate treatment of back-diffusion between ice layers within the comet, building on the work of Willis and Garrod (2017), is also included in the model (§3.2.3). In the models presented here, the cold-storage phase is followed by the solar approach of the comet (§3.2.4).

3.2.1 Basic model functions

The cometary solid-phase chemical kinetics model of G19 divided the comet into 25 distinct layers of ice/dust, each of thickness three times greater than the last, beginning with an upper layer one monolayer thick. These 25 layers collectively produced a thickness corresponding to ∼136 m; beneath this was an inert reservoir layer of indefinite thickness that would replenish any shortfall in the above layers.

Within each of the 25 regular ice/dust layers, the behavior of a set of chemical species was traced over time. The chemistry occurring in each layer included diffusive reactions between various species, photodissociation caused by Galactic UV photons, dissociation caused by Galactic cosmic-ray impingement, spontaneous reactions (i.e. "non-diffusive" reactions, see below) between newly-produced dissociation products and pre-existing local reaction partners, and – in the surface layer only – the thermal and non-thermal desorption of species according to their binding energies and the temperature of the comet. The temperature in the G19 models was assumed to be uniform through all layers and at all times in each model run. No adsorption of atoms or molecules from the gas-phase onto the surface was allowed, based on the

assumption of low local gas densities, and this assumption is retained in the present model.

Transfer of chemical species between the 25 layers was allowed in the G19 model, caused by diffusion of mobile species across layer boundaries. Transfer was also allowed as the result of losses induced in the upper layer (due to desorption), or of either losses or gains in the total amount of ice/dust in any of the layers, as the result of the chemistry. This transfer was monitored throughout the model, to ensure that the amount of material in all layers was held constant over time. Any additional material required in the deepest (25^{th}) layer was drawn from the reservoir beneath, which was assumed to retain a pristine ice composition throughout (based on the chosen starting composition in the model). Excess material in the deepest layer was likewise transferred into the reservoir. Figure 3.1 shows a simplified schematic of how the updated version of the *MAGICKAL* comet model presented here functions.

The chemical composition of the comet was assumed to include not only ice but also a dust component. Although the dust was treated as chemically inert, it was allowed to undergo transfer between layers according to losses or gains in other species; in this way, desorption of volatile material from the surface of the comet would lead to the enrichment of the dust component of the upper layers, as material (both ice and dust) from the next layer down replaced the lost material from the surface. The effect of the attenuation of the UV photon field by the dust was also considered, meaning that the dust enrichment of the upper layers would also serve to reduce somewhat the rates of UV photodissociation in the layers beneath.

Although the model has several mechanisms for the loss of atoms/molecules from the surface layer (e.g. thermal sublimation), it does not include any means for the ejection of dust from the surface. Dust loss from a comet could occur either through

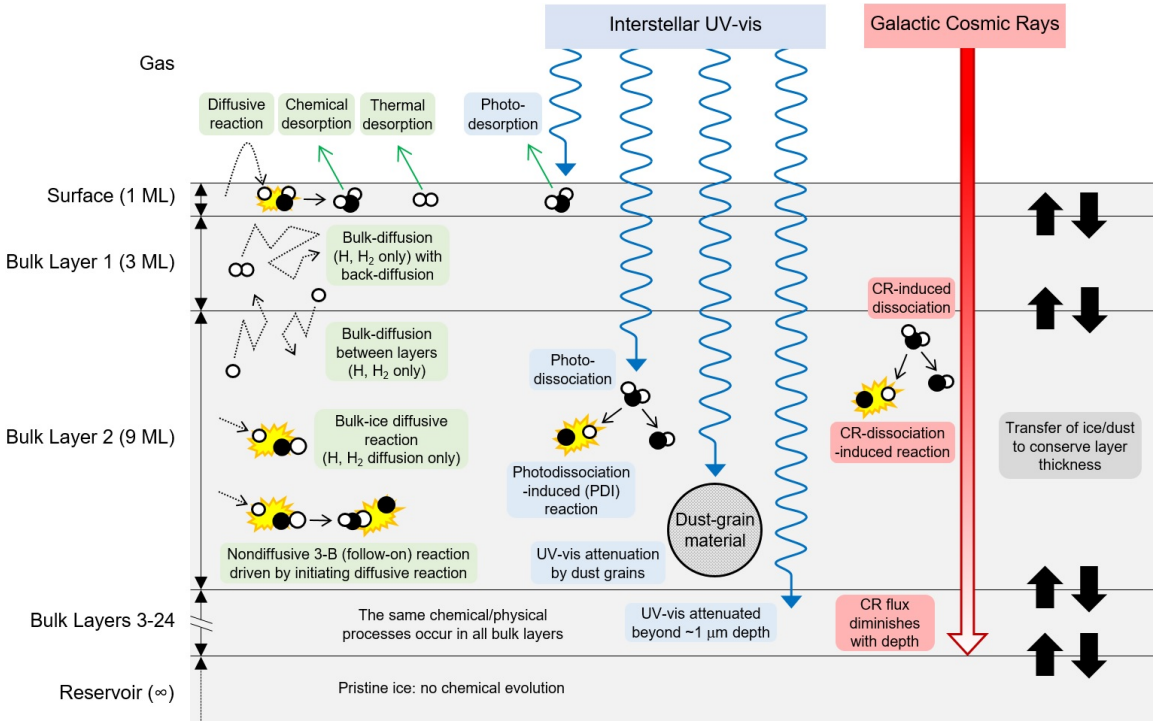

Figure 3.1: A simplified pictorial schematic of some of the physical processes modeled by *MAGICKAL*. Each bulk (i.e. sub-surface) layer is three times thicker than the last. Dotted arrows indicate surface or bulk-ice diffusion. Solid black arrows indicate the products of reaction or dissociation. Each ice/dust layer is assigned its own local temperature, while molecular dissociation rates (induced by UV–Vis photons and Galactic cosmic rays) are also locally determined. The same chemical reactions and physical processes are allowed in the surface layer and all bulk layers, except for desorption processes, which only occur in the surface layer. Aside from H and H_2, molecular shapes shown are intended only to be representative of generic structures. Some processes have been omitted for clarity.

local outburst events or as the result of sublimation of icy molecular material; however, the inclusion of rates for these mechanical dust-loss processes in the chemical model is non-trivial and is thus left for future investigation.

Here we make a point of clarifying our definitions of two important mass-loss processes: (i) outbursts, which are characterized by a sudden and brief increase in brightness sometimes attributed to the sudden local ejection of dust and trapped volatiles, and (ii) outgassing, which is a continuous process of sublimation of ices

that is dependent on heliocentric distance via temperature. While our model does not include the localized and brief events associated with cometary outbursts, it does consider outgassing through the continuous process of sublimation (although, as noted above, without any concomitant dust loss).

The initial fractional composition of the comet was set to be the same as in G19. As water is the most abundant ice species, other fractional abundances are set with respect to water ice. CO and CO_2 are each set to 20%, Methanol is set to 5%, and methane, formaldehyde, and ammonia are each set to 1%. These fractional abundances are based on the dominant components of interstellar ices. We also start with an initial dust content equal to 111% with respect to water ice. These initial ice fractions apply to the surface layer as well as all bulk ice layers including the reservoir. As the chemical model progresses, we also allow a maximum dust content per layer of ∼74% of the total composition. This value is based on the maximum space-filling factor for identically sized spheres (e.g. Hales, 2005).

The G19 chemical models were applied only to static physical conditions intended to represent the cold-storage phase of cometary evolution. The present models include both cold storage and a solar approach phase, described in detail below.

Here we also employ an expanded chemical network based on that of Willis et al. (2020), with all species that contain more than 5 carbon atoms removed to make the integration of the chemical equations more easily manageable.

Other changes to the modeling treatment of G19 as applied to the present model are described below. A list of reactions with activation energies and barrier widths used in the model is available online (https://garrodgroup.as.virginia.edu/resources).

3.2.2 Non-diffusive chemical mechanisms

In most prior gas-grain astrochemical kinetics models, the production of COMs has relied on diffusive chemistry occurring between functional-group radicals on interstellar dust-grain surfaces or within the ices that build up on those surfaces (e.g., Hasegawa et al., 1992b; Garrod et al., 2008; Garrod, 2013c). These mechanisms generally require the dust grains to reach temperatures at which larger radical species can become mobile, which may easily be reached in the star-forming cores where many COMs are found. However, recent gas-phase detections of COMs in cold environments (e.g., Bacmann et al., 2012; Cernicharo et al., 2012; Bergner et al., 2017) indicate that, if such molecules are indeed formed on the grains, then formation mechanisms must be operative that can occur at much lower temperatures, at which large radicals remain thermally immobile. The implications of these findings extend also to cometary ice chemistry, as comets in the Oort cloud exist at very low temperatures ($\sim$10 K) for very long time periods.

In the comet model presented by G19, chemistry was assumed to occur both through diffusive meetings of reactants, as well as through a novel, non-diffusive photodissociation-induced mechanism, whereby reactive radicals produced by photolysis in the ice could spontaneously react with nearby reaction partners. A similar non-diffusive mechanism was also included to account for reactions induced by direct cosmic-ray impingement, following the production of reactive radicals deep within the ice via radiolysis.

Subsequent interstellar gas-grain chemistry models by Jin and Garrod (2020) and Garrod et al. (2022) further refined the formulation of the non-diffusive photodissociation-induced reactions, and generalized it to allow similar formulations for other non-

diffusive reaction processes. The new comet models presented here incorporate these and other recent advances in surface/solid-phase interstellar chemistry.

Firstly, the "photo-dissociation induced" (PDI) mechanism of non-diffusive reactions has been updated as described by Jin and Garrod (2020) and Garrod et al. (2022); the latter authors took into consideration the efficiency at which photo-products would recombine with each other if no other reaction partner were immediately present. The effect of this change was to reduce somewhat the production of unreacted radicals in the bulk ice. All changes to the photon-induced mechanisms are mirrored precisely in the corresponding cosmic-ray induced processes.

An additional non-diffusive chemical mechanism is added to the model: the so-called "three-body" (3-B) reaction mechanism, described in detail by Jin and Garrod (2020) and Garrod et al. (2022). In this mechanism, a preceding surface or bulk-ice reaction may lead to a follow-on reaction if some third reactive body happens to be in close proximity to the site of the first reaction. The follow-on reaction could involve an activation energy barrier, and the follow-on reaction therefore need not occur immediately following the initiating reaction, so long as the reactants remain undisturbed for long enough for the barrier to be eventually overcome. The initiating reaction could be a diffusive process, a PDI (or similar cosmic ray-induced) process, or another three-body reaction. Following Garrod et al. (2022), we allow a total of three cycles of 3-B reactions to occur. Within the scheme of the 3-B process, our model also includes adjustments to permit a sufficiently exothermic initiating reaction to allow the activation energy barrier of the follow-on reaction to be instantaneously overcome, as described by Jin and Garrod (2020) and formulated by Garrod et al. (2022). A form of the 3-B process was initially included in the gas-grain model of Garrod and Pauly (2011) that was used to explain the production of interstellar solid-phase CO_2.

The generic form for calculating the rates of non-diffusive processes, between two species A and B, is given by

$$R_{AB} = f_{act}(AB)R_{comp}(A)\frac{N(B)}{N_M} + f_{act}(AB)R_{comp}(B)\frac{N(A)}{N_M}, \tag{3.1}$$

where f_{act} is an efficiency related to the activation energy barrier (between 0 and 1), R_{comp} is the "completion rate" for species A or B, $N(A)$ and $N(B)$ are the abundances of species A and B in a particular layer, and N_M is the total abundance of all species in that layer (see Jin and Garrod, 2020).

The "completion rate" of some species A, involved in reaction with species B, depends on two quantities; the appearance rate of A (for example, the total rate at which species A is produced by photodissociation, in the case of a PDI process), along with an adjustment that takes account of any delay in the follow-on reaction related to the presence of an activation energy barrier. Again, Jin and Garrod (2020) provides a detailed description of the formulation of the non-diffusive reaction rates.

Finally, following Garrod et al. (2022), diffusion within the bulk ice in the new comet models is prohibited for species other than H and H_2 (surface diffusion by all species is nevertheless allowed as before). This is in line with experimental and modeling evidence (e.g. Ghesquière et al., 2018; Shingledecker et al., 2019) that indicates that heavier radicals do not diffuse rapidly, and as such that bulk diffusion may not be the main mechanism by which bulk-ice chemistry is driven. It is assumed here that bulk diffusion by H/H_2 involves movement between interstitial sites in the ice matrix (Chang and Herbst, 2014). In the present comet models, this restriction means that diffusive reactions in the bulk ice may only occur if they involve either

H or H_2. Furthermore, diffusion between bulk-ice layers is also restricted to those two species. The outcome of this change on the interstellar chemical model results is described by Garrod et al. (2022).

It should be noted that all of the chemical reactions included in the network may occur through any of the diffusive or non-diffusive mechanisms used in the models, so long as one or other of the reactants is allowed to diffuse (according to the above stipulation), or that one or other reactant may be formed by some preceding mechanism (e.g. photodissociation, or another reaction), in the case of non-diffusive processes.

3.2.3 Back-diffusion between layers

Back-diffusion is the phenomenon by which particles diffusing in/upon a lattice undergo a random walk, such that they may re-visit lattice sites that they have already diffused away from.[1] This effect has been shown to impact reaction rates on the surfaces of interstellar dust grains of various morphologies. In the study of back-diffusion on interstellar dust grains by Willis and Garrod (2017), the authors used kinetic Monte Carlo models to demonstrate that the surface reaction rate for the simple chemical system of H + H $\rightarrow$ H_2 is decreased when back-diffusion is considered, compared with the typical rate-equation chemical kinetics approach. The magnitude of this effect was observed to be inversely proportional to the surface coverage of the diffusing particle. Thus, when the surface was mostly covered with diffusers, the effect was negligible, whereas with just two diffusers a maximum back-diffusion factor of $\sim$5 was observed, diminishing the reaction rates by this factor.

[1] §3.2.3 and the research outlined within were completed primarily by Eric R. Willis.

While the latter study considered the effect of back-diffusion on diffusive chemical reaction rates on grain surfaces, similar effects in three dimensions may affect both the rates of diffusive reactions in the bulk-ice layers and the rates at which diffusers may pass between the layers; the comet model includes terms that allow diffusers in one layer to pass upward or downward to an adjacent layer. As discussed above, in the models presented here, diffusion within the bulk ice is limited to H and H_2 and is assumed to involve movement between interstitial sites within the ice structure.

In the comet models of G19, the rate of bulk diffusion at which some species i diffuses into the surface layer from the thicker mantle layer below, $R_{\mathrm{diff},m}(i)$, was defined according to

$$R_{\mathrm{diff},m}(i) = k_{\mathrm{diff}}(i) N_m(i) \frac{N_S}{6 N_M}. \tag{3.2}$$

$$k_{\mathrm{diff}}(i) = \nu_0(i) \exp[-E_{\mathrm{diff}}(i)/T], \tag{3.3}$$

where $N_m(i)$ corresponds to the population of species i within a particular mantle layer, N_S and N_M are the total number of available sites that can be occupied in the surface and bulk, respectively, $k_{\mathrm{diff}}(i)$ is the diffusion rate coefficient, $\nu_0(i)$ is the characteristic frequency of species i, $E_{\mathrm{diff}}(i)$ is the barrier to bulk diffusion of species i, and T is the temperature of the ice layer.

G19, following Garrod (2013a), considered bulk diffusion to be a "swapping" process, but the same formulation is applicable to the present assumption that diffusion of H and H_2 occurs between interstitial sites. Similar expressions were used by G19 to describe the rates of diffusion across the interfaces of all 25 layers in the comet model.

Eq. (3.2) describes a situation in which there is a high degree of occupation by diffusers of the available sites in the ice. Thus, there is always a substantial number of

diffusers directly adjacent to the interface between layers, such that any one of them might cross with a single "hop" (i.e. diffusion event); the overall rate of diffusion across the interface is therefore dominated by the diffusion rates of those interface-adjacent diffusers. Eq. (3.2) is composed of: the total rate at which any diffuser of type i in the ice layer makes a single hop in any direction, given by $k_{\rm diff}(i)N_m(i)$; the fraction of all diffusers that are adjacent to the interface, N_S/N_M; and a factor 6 that comes from the six diffusion directions available to a particle at the interface between the surface and the mantle ice layer, on the assumption of a cubic ice structure.

Unfortunately, since the abundances of the diffusing H and H_2 particles in the comet models could fall far short of maximum occupation, back-diffusion could have a significant impact on the rates of transfer between layers, with diffusers having to undergo multiple hops within the bulk before reaching the interface, including many hops that might lead them away from the interface in question. Eq. (3.2) in that case could be highly inaccurate.

Garrod et al. (2017) considered such a situation in the context of bulk-diffusion in interstellar dust-grain ice mantles, which involves ices with a maximum thickness around a few hundred monolayers. Those authors used a simple three-dimensional kinetic Monte Carlo model to determine the average number of diffusion events (denoted by $N_{\rm move}$) required for a lone diffuser to reach the top layer of a monolithic ice mantle of finite thickness from some arbitrary starting point. (Note that escape from the lowest monolayer is blocked by the presence of the dust grain itself). The following relationship was found to provide an excellent fit to the data:

$$N_{\rm move} = 2(N_{\rm th} + 1/2)^2, \tag{3.4}$$

where $N_{\rm th}$ is the thickness of the ice in monolayers (equal to N_M/N_S). This expression indicates that, with increasing thickness, the number of diffusion events needed to reach the interface between the surface and the mantle increases rapidly. Eq. (3.4) describes an extreme case, in which there is only one diffuser present. In the other extreme case, provided by Eq. (3.2), in which diffusers are very abundant, $N_{\rm move} = 6N_{\rm th} = 6N_M/N_S$.

As noted by Willis and Garrod (2017) in the context of surface diffusion, the strength of the back-diffusion effect is dependent on the abundance of the diffusers. Furthermore, the degree of back-diffusion indicated by Eq. (3.4) should become extremely large when dealing with ice layers of macroscopic size, leading to a large divergence between the two extreme cases. In order to provide an accurate picture of diffusion between the layers in the comet model, a treatment is thus required that can account for back-diffusion anywhere between the two extreme cases corresponding to "many" or "few" diffusers.

As part of this paper, we present the results of a three-dimensional Monte Carlo (MC) model that explicitly simulates the back-diffusion effect in a bulk ice, for a wide range of conditions relevant to comets.

A number of three-dimensional Monte Carlo simulations were also run that considered the back-diffusion effect on *reaction rates* in a bulk-ice layer (as opposed to diffusion between layers), for reactions between like species (e.g. H+H). However, in this case the standard reaction rates were found to be consistent with the Monte Carlo simulations; back-diffusion reduced the reaction rates by a maximum factor around 1.5 for all except very thin ices (a few monolayers), for which the effect reached a factor of a few. For high occupation of reactants, the effect was removed entirely. These MC results, presented briefly in Appendix A.1, indicate that back-diffusion

has only a weak effect on the rates of bulk-ice reactions driven by three-dimensional diffusive processes. Furthermore, the inclusion of alternative reaction partners (e.g. O, OH, etc.) would be expected to reduce the effect again, even in thin ices.

Considering that the effects on rates are so small, we choose not to include any kind of parameterization of the bulk-ice back-diffusion effect on chemical reactions in the present models. For chemical reactions occurring in the surface layer of the comet, the back-diffusion correction of Willis and Garrod (2017) was implemented.

Monte Carlo simulations of back diffusion between layers

The ultimate goal of the MC simulations of bulk diffusion is to determine a parameter representing the average number of diffusion events ("hops") undertaken by all diffusers of a particular chemical species, in a layer of chosen thickness, to produce the escape of *one* of those diffusers, either to the layer above or the layer below.[2] We label this quantity the "back-diffusion factor", θ, and it is involved in determining the rates of diffusive transfer of H and H_2 between layers in the comet model according to the expression

$$R_{\mathrm{diff},m}(i) = k_{\mathrm{diff}}(i) N_m(i)/\theta, \tag{3.5}$$

with quantities defined as in Eqs. (3.2) and (3.3). These rates should be divided by 2 when implementing separate upward and downward diffusive escape rates.

The MC model is functionally similar to that described by Garrod et al. (2017), except that it has now been extended to many diffusers (which requires the ice to have an explicitly defined lateral size), and that it allows diffusers to escape from both the top and bottom interfaces (in the case of dust-grain ices, escape from the lower

[2] §3.2.3 and the research outlined within were completed primarily by Eric R. Willis.

interface was blocked). The interstitial sites in the ice that the diffusers may occupy are assumed to take a simple cubic arrangement. For most of the MC simulations, we limit the maximum thickness to 30 monolayers (i.e. 30 sites), for computational efficiency. A lateral width of $N_{\text{lat}} = 15$ (i.e. 15 sites wide) is used for both lateral dimensions, with periodic boundary conditions applied across the four lateral surfaces to simulate a much larger ice. No periodicity is included for the vertical dimension.

Diffusion is simulated for a range of ice thicknesses up to the pre-defined maximum of 30 ML. The model begins by creating an ice with a thickness of 1 ML, and depositing one diffuser in a randomly-chosen site. This diffuser is then allowed to hop (i.e. diffuse), with an equal probability of choosing any of the available directions. The number of hops taken is recorded until that diffuser leaves the ice, by hopping out of either the top or bottom monolayer. The diffuser is then replaced in another randomly-chosen site, and the process is repeated 500,000 times to ensure a good statistical sample, from which the mean value is recorded. Then a second diffuser is added and the simulations are re-run, and so on. For simulations with multiple diffusers, the *total* number of hops of all diffusers is recorded, and all diffusers are replaced randomly in the ice once a single diffuser leaves. If a diffuser attempts to hop into a site that is already occupied, a swapping event occurs in which the two particles exchange places. This is counted as two hops, one for each particle.

Once the maximum number of diffusers (i.e. $N_{\text{lat}}^2 N_{\text{th}}$) has been reached in a given thickness, the model adds another layer onto the ice, and starts over again at one diffuser. This way, the maximum amount of coverage space is properly sampled, and a relationship detailing the magnitude of the back-diffusion effect as a result of both thickness (N_{th}) and number of diffusers (N_d) can be determined. In order to derive expressions to parameterize the data, we make use of the `Eureqa` modeling engine

(Schmidt and Lipson, 2009, 2014). §3.3.1 details the results of the simulations and their parameterization.

3.2.4 Heat transfer and solar approach

G19 presented detailed models of the cold-storage phase of Oort cloud comets. In this work[3], we go beyond this, by modeling the chemistry during several solar orbits subsequent to cold storage; this requires knowledge of, in particular, the temperature behavior of the comet as a function of time. In order to calculate this behavior, the orbits of a comet of interest must first be calculated, which requires knowledge of its orbital elements. We used the `PyEphem` package (Rhodes, 2011) to load these orbital elements from the IAU Minor Planet Center[4]. The orbital positions of the comet of interest (in this case, comet Hale–Bopp) were then calculated for one solar orbit, using the most recently-known orbital elements, which were originally downloaded in January 2020. These orbital elements were then assumed to be unchanged for subsequent orbits of the comet in this model.

Hale–Bopp has a semi-major axis of 181 AU, an inclination of 89 degrees, and an eccentricity of 0.99. This results in a perihelion distance of 0.92 AU, an aphelion distance of 360 AU, and an orbital period of 2429 years. Detailed values are included in Table 3.1. With the orbits of the comet calculated, the chemical model requires that the heat transfer throughout the cometary ice be calculated, in order to obtain temperatures at each layer, for each time point. This was done following the method of Herman and Podolak (1985), in which the heat diffusion equation is solved in a one-dimensional fashion. The heat diffusion equation is given by

[3] §3.2.4 and the research outlined within were completed in collaboration with Eric R. Willis.
[4] https://www.minorplanetcenter.net/data

Parameter	Value
Inclination	88.9912°
Longitude of Ascending Node	283.3585°
Argument of Perihelion	130.6487°
Semi-Major Axis	180.7048 AU
Mean Daily Motion	0.0004057° day^{-1}
Eccentricity	0.99492735
Mean Anomaly	0.0000° from perihelion
Epoch Date	03/29.6285/1997
Equinox Year	2000
Perihelion Distance	0.917867899 AU
Aphelion Distance	360.4929504 AU
Orbital Period	2429 years

Table 3.1: Physical parameters used to model the orbit of the comet. All parameters obtained from the IAU Minor Planet Center database, or calculated from them.

$$\rho c(T)\frac{\partial T}{\partial t} = \nabla[\kappa \nabla T], \tag{3.6}$$

where ρ is the material density, $c(T)$ is the specific heat, κ is the thermal conductivity, and T is the temperature. In the heat diffusion simulations presented here, we assume that the comet is spherical and uniformly illuminated by the Sun. Boundary conditions at the surface and the interior edge of the comet nucleus must be defined in order to obtain a solution. At the surface, the boundary condition is defined by conservation of energy:

$$\frac{\partial T}{\partial r}|_{r=R} = \epsilon\sigma T^4 - \frac{(1-A)S}{d_H^2}\langle cos\,\xi\rangle - F_{\mathrm{ISRF}}. \tag{3.7}$$

R is the radius of the comet, ϵ is the emissivity, σ is the Stefan-Boltzmann constant, T is the temperature of the cometary surface, A is the surface albedo, S is the solar constant, d_H is the heliocentric distance (which changes in time), $\langle cos\,\xi\rangle$ is the

Parameter	Value	Ref.
ϵ	0.5	Whipple and Huebner (1976)
A	0.04	Mason et al. (2001)
$\langle cos\,\xi \rangle$	0.25	Uniform illumination
$F_{\rm ISRF}$	2.67×10^{-2} erg s^{-1} cm^{-2}	Mezger (1990)
ρ	1 g cm^{-3}	Guilbert-Lepoutre and Jewitt (2011)
c_w	$7.4 \times 10^4\,T + 9.0 \times 10^5$ erg g^{-1} K^{-1}	Herman and Podolak (1985)
c_d	1.2×10^7 ergs g^{-1} K^{-1}	Guilbert-Lepoutre and Jewitt (2011)
h	0.1	Guilbert-Lepoutre and Jewitt (2011)
κ_w	$7.1 \times 10^{-3}\,T$ erg s^{-1} cm^{-1} K^{-1}	Kouchi et al. (1994)
κ_d	4.2×10^5 erg s^{-1} cm^{-1} K^{-1}	Ellsworth and Schubert (1983)
ψ	0.3	Guilbert-Lepoutre and Jewitt (2011)

Table 3.2: Physical parameters used in the heat diffusion model.

average value of the local solar zenith angle, and $F_{\rm ISRF}$ is the mean intensity of the interstellar radiation field. The first term on the right-hand side of Eq. 3.7 corresponds to the radiative cooling from the surface of the comet, while the second and third terms correspond to the incoming solar and interstellar radiation, respectively. Note that, in this formulation, we ignore the cooling effects of sublimation from the cometary surface, as well as thermal effects of phase changes within the nucleus (although sublimation is still included in the chemical model itself. These effects are left for future studies.

The boundary condition in the interior of the comet is defined thus:

$$\frac{\partial T}{\partial r}|_{r=0} = 0, \tag{3.8}$$

indicating that the heat flux becomes 0 at the center of the comet. Table 3.2 shows the values of the parameters used in the heat diffusion simulations and their literature references.

As noted in Eq. 3.6, $c(T)$ is a function of temperature. The specific heat is

defined as

$$c(T) = X_w\, c_w + X_d\, c_d, \tag{3.9}$$

where X_w and X_d are the mass fraction of water (as a proxy for the total ice) and dust, respectively, and c is the specific heat of each component. For these simulations, we assume that $X_w = X_d = 0.5$, following Guilbert-Lepoutre and Jewitt (2011). The expressions for c_w and c_d are given in Table 3.2.

Similarly, κ is also a function of temperature. In the simulations presented here, it is defined as

$$\kappa = \phi h \kappa_s, \tag{3.10}$$

following Guilbert-Lepoutre and Jewitt (2011). In Eq. 3.10, h is the Hertz factor, which scales the conductivity to account for reduced contact area between grains within the solid matrix. We set h to 0.1. κ_s is the conductivity of the cometary ice matrix, which is calculated as

$$\kappa_s = x_w \kappa_w + x_d \kappa_d, \tag{3.11}$$

where x_w and x_d are the volume fractions of water and dust, respectively, and κ_w and κ_d are the conductivities of amorphous water and dust, respectively. Table 3.2 shows their values. Note that, in this formulation, we assume that all ice in the comet is amorphous in nature. This is likely to be the case when the comet is in cold storage, but there will be phase changes when solar approach begins. However, our chemical model does not currently have the functionality to account for these phase changes,

so we save their study for future work.

Finally, ϕ is a correction factor, first developed by Russell (1935), which accounts for the effect of pores on the thermal conductivity of a solid matrix. Its formula is given by

$$\phi = \frac{\psi^{2/3} f + (1 - \psi^{2/3})}{\psi - \psi^{2/3} + 1 - \psi^{2/3}(\psi^{1/3} - 1) f}, \tag{3.12}$$

where ψ is the porosity (assumed to be 0.3, following Guilbert-Lepoutre and Jewitt, 2011), and f is the ratio of the conductivity of pores to the solid matrix, κ_p/κ_s. The conductivity of the pores is calculated by

$$\kappa_p = 4 r_p \epsilon \sigma T^3, \tag{3.13}$$

where $r_p = 10^{-4}$ cm (the mean radius of a pore) and $\epsilon = 0.9$ (Guilbert-Lepoutre and Jewitt, 2011).

Once the boundary conditions and parameters are defined, the heat diffusion equation can be solved through time. Firstly, to do this the physical space over which to solve Eq. 3.6 must be defined; we chose $R = 30$ km (Hale–Bopp; Fernández, 2000). Within this range, specific depth points must be defined, as well as the initial temperatures at those depths. In our temperature calculations, the ice is divided into 250 depth points, such that the final depth point ends at 30 km. The surface is considered its own layer, with a thickness of 1 cm, while the layers after that are spaced logarithmically in depth. Once the depths are set, the initial temperature is defined at each point. For this model, we simply assume a uniform temperature of 10 K throughout the ice at the initial time point of the simulation, corresponding

approximately to Oort cloud conditions.

Other heating effects, such as that produced by the radioactive decay of species including ^{26}Al, are not considered in the present model. Heating by radioactive decay is primarily a deep mantle effect, in that greater heating occurs deeper into the comet. Our chemical model primarily considers surface and outer mantle chemistry where radioactive heating is weakest. It is possible that the addition of such effects could cause a stratification of volatiles (e.g. Prialnik et al., 2008). Such might be noticeable after significant mass loss, but would have a relatively minor effect on the present model, which ignores outbursts that could be a major mass-loss contributor.

Once the initial conditions have been defined, the orbital position is allowed to evolve in time according to the specified cometary orbit. The impinging flux at the surface changes according to the heliocentric distance d_H, and the change in temperature is first calculated at the surface. Derivatives $\partial T/\partial r$ are then calculated throughout the ice. Once these derivatives have been calculated, the second derivatives are computed, and the temperatures at each depth in the ice are integrated using Gear's method. Once the temperatures are calculated for a full orbit, and the calculations are done again, continuing from those input conditions. Here, we calculate 5 orbits using Hale–Bopp's orbital parameters. §3.3.2 presents the results from these simulations, and discusses their inclusion in the cometary ice chemistry model.

3.3 Results

Results are divided into three subsections, corresponding to the back-diffusion calculations that are incorporated into the comet chemistry model (§3.3.1), the heat transfer calculations that determine the time- and depth-dependent temperature of

the comet during solar approach (§3.3.2), and the results from the cold storage and solar approach comet chemical kinetics models (§3.3.3) that make use of the results of §3.3.1 and §3.3.2.

3.3.1 Back-diffusion between layers

To determine the behavior of the back-diffusion factor, θ, the three-dimensional Monte Carlo model described in §3.2.3 was run.[5] The model provides the average total number of hops, N_{hops}, by all diffusers in the system, required for a single diffuser to leave the ice. Although N_{hops} is precisely the quantity that we wish to express with our final formulation for θ, we use the former label exclusively for the data produced by the MC models. The number of diffusers in the ice, N_d, is also equivalent to the quantity $N_m(i)$ in Eq. (3.5).

Figure 3.2 shows the raw data for selected ice thicknesses, N_{th}, between 1 and 30 ML. The intermediate thicknesses, although not shown, display similar behavior. The data range from $N_d = 1$ (a single diffuser) up to $N_d = N_{\text{lat}}^2 N_{\text{th}}$ (full occupation).

Fig. 3.2 shows that, for ice thicknesses greater than one, N_{hops} falls with an increasing number of diffusers in the ice, N_d, until some lower limit is reached. This makes intuitive sense, as the more diffusers that are present in the ice, the greater the probability that some particles will randomly be placed initially close to the top or bottom interface of the ice. It may also be reasoned that, beyond some threshold in occupation, increasing the number of diffusers should no longer reduce the number of hops required; many of the additional diffusers would be sited deep within the ice, increasing the number of total hops without increasing the rate of successful exit from

[5] §3.3.1 and the research outlined within were completed primarily by Eric R. Willis.

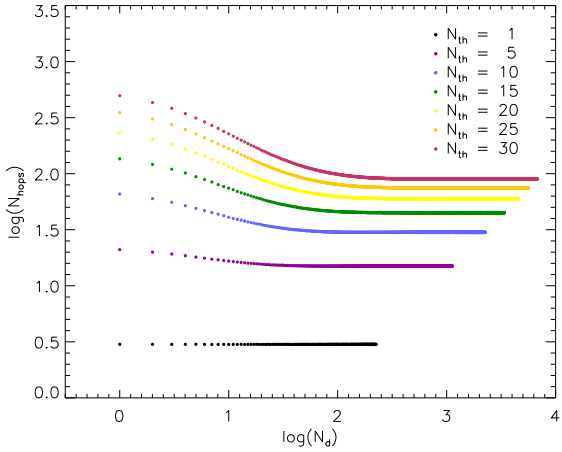

Figure 3.2: Raw data from 3D back-diffusion Monte Carlo code, using $N_{\text{lat}} = 15$. Data are color-coded according to thickness. The x-axis indicates the number of diffusers, while the y-axis displays the number of hops executed by all diffusers in the ice until one of the diffusers exits from the upper or lower layer of the ice.

the interfaces.

It can also be seen from Fig. 3.2 that N_{hops} is constant for $N_{\text{th}} = 1$, taking a value of 3. For thicker ices, the number of hops required to escape is always greater than for thinner ices for any given value of N_d.

It is possible, without the need for a simulation, to derive the back-diffusion factor when the ice has the maximum number of diffusers (high occupation), meaning that back-diffusion will be at its minimum:

$$\theta_{\text{hi}} = 3N_{\text{th}}, \tag{3.14}$$

This expression is derived from the consideration that, if all sites are occupied, there is a total of $N_{\text{lat}}^2 N_{\text{th}}$ diffusers that could diffuse, while only those in the upper or lower monolayers, a total of $2N_{\text{lat}}^2$, could successfully diffuse out of the ice at either interface. Considering finally that one of these may only successfully exit with a probability of

1/6, Eq. 3.14 becomes self-evident. The expression matches perfectly with the data in Fig. 3.2, using the right-most point for each value of $N_{\rm th}$, corresponding to full occupation. The same expression gives a perfect match also to all of the data-points for the $N_{\rm th} = 1$ case, in which any upward or downward hop leads to the escape of the diffuser, meaning that back-diffusion is again minimized, regardless of the degree of occupation of sites.

At the other extreme, an expression for the single-diffuser case (low occupation) may be derived from the models. Based on the data partially shown in Fig. 3.2, for the points $\log(N_d) = 0$, the single-diffuser back-diffusion factor relevant to the comet models is well fit by the expression

$$\theta_{\rm lo} = 0.5N_{\rm th}^2 + 1.5846N_{\rm th} + 0.699, \tag{3.15}$$

which is assigned a minimum value of 3, to ensure that the $N_{\rm th} = 1$ case is accurately reproduced. Fig. 3.3 shows the fit for Eq. 3.15 with the full set of single-diffuser data ($N_{\rm th} = 1 - 30$). Note that the single-diffuser expression shown in Eq. (3.4), for a monolithic dust grain-surface ice mantle, as determined by Garrod et al. (2017), corresponds to escape only from the upper layer. It is to be expected that the outcome in that scenario will be different from the case of two interfaces, when occupation is low and back-diffusion is significant.

For larger values of $N_{\rm th}$, the behavior as a function of N_d is more complicated. An example is shown in Fig. 3.4, for $N_{\rm th} = 20$, where it is apparent that the data can be described by a function that converges to Eq. (3.14) at high numbers of diffusers and Eq. (3.15) at low numbers of diffusers.

In order to parameterize this relationship, we introduce the following simple func-

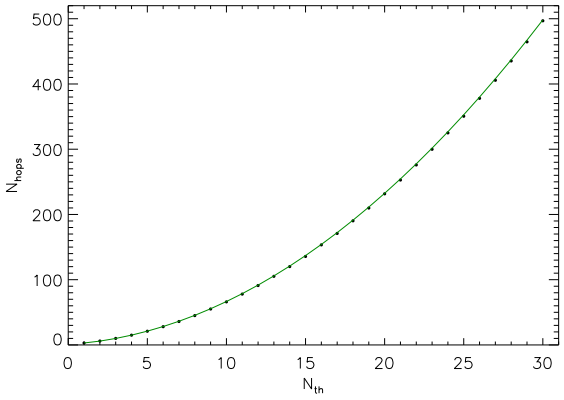

Figure 3.3: Monte Carlo data for single diffusers, using $N_{\rm lat} = 15$, fit to Eq. 3.15.

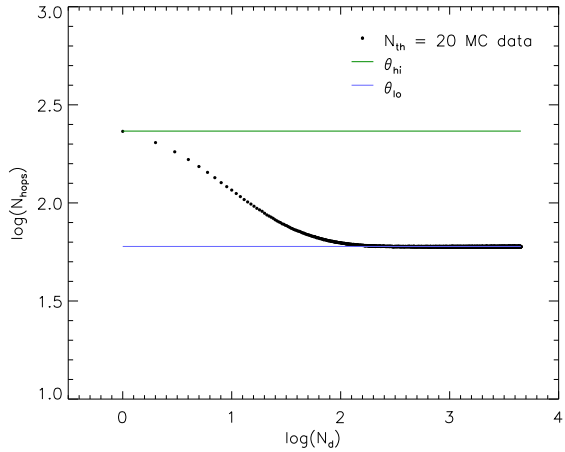

Figure 3.4: Data for back-diffusion simulations with $N_{\rm th} = 20$, with maximum and minimum values obtained from Eq. (3.14) and Eq. (3.15).

tion for the total back-diffusion factor, as a function of θ_{lo} and θ_{hi}:

$$\log_{10}(\theta) = a \log_{10}(\theta_{\text{lo}}) + (1 - a) \log_{10}(\theta_{\text{hi}}), \tag{3.16}$$

where a is a yet-to-be-defined switching function that describes the transition between the low- and high-occupation regimes. This function should depend on N_d and N_{th}.

We use the aforementioned `Eureqa` modeling software (Schmidt and Lipson, 2009, 2014) to derive a relationship for a from our MC model data. `Eureqa` utilizes genetic programming to test several functional relationships between variables, attempting to find minima corresponding to the user's chosen error metric. For these data, we have chosen to minimize the weighted mean absolute error (WMAE). Most data-points are assigned a weight of 1. However, in order to ensure the proper behavior at both extremes (one diffuser, and maximum diffusers), we give a weight of 100 to each data point in our data set that corresponds to $N_d = 1$ or $N_d = N_{\text{lat}}^2 N_{\text{th}}$.

We also give a weight of 10 to those data points with N_d =2 – 10, as this parameter space is expected to be most important for simulations of cometary ice chemistry, based on test chemistry simulations. In addition, because we can theoretically calculate θ_{lo} and θ_{hi} for any thickness, we create dummy data corresponding to the single- and maximum-diffuser case for each ice thickness up to N_{th}=10,000.

Using these input data, `Eureqa` provides the following function for a,

$$a = N_d^{-0.418\sqrt{\frac{N_d}{N_{\text{th}}}}},$$

which achieves a WMAE of ∼6e-5. With this basic relationship established, we

conducted a further parameter search using the expressions

$$a = (N_d)^b \tag{3.17}$$

$$b = -f_1 \left(\frac{N_d}{N_{\text{th}}} \right)^{f_2}. \tag{3.18}$$

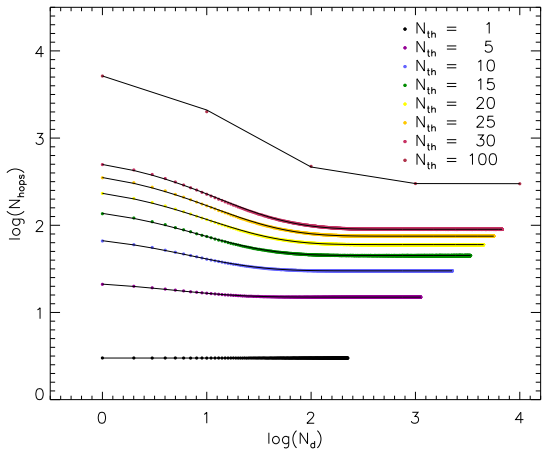

Figure 3.5: Data for back-diffusion simulations up to $N_{th} = 100$; black lines indicate the fitted values, θ.

Values $f_1 = 0.4051$ and $f_2 = 0.390$ were found to provide the best match, attaining a maximum fractional error per data point of ∼2% for the entire dataset, with an average error of ∼0.2% for each N_{th} value. Note also that a certain degree of computational error exists in the MC data, meaning that a perfect match to all datapoints is not achievable.

Eqs. (3.17) and (3.18) can be inserted into Eq. (3.16) to calculate the back-diffusion factor for any arbitrary N_d and N_{th} values.

Figure 3.5 displays the Monte Carlo data along with the curves produced by the fit. In addition to the $N_{\text{th}} = 1 - 30$ data, we also ran the Monte Carlo diffusion model with $N_{\text{th}} = 100$, to test the relationship at greater thicknesses, also shown in Figure

3.5. Due to computational costs, the $N_{\rm th} = 100$ model was run for five values of N_d, ranging logarithmically from 1 to 10^4. An excellent match is produced in this case also.

To ensure no dependence on the chosen lateral size of the ice used in the MC simulations, $N_{\rm lat}$, we also ran the models for the $N_{\rm lat} = 8$ and 10 cases. The model fit obtained from the $N_{\rm lat} = 15$ data works equally well for the other two cases, demonstrating that the lateral size of the periodically bounded ice is not a significant parameter in the back-diffusion.

Incorporation of Eqs. (3.5) and (3.14) – (3.18) into the rate-equation treatment for diffusion between layers in the cometary ice model is simple. Abundances of species within the ice layers in the comet model are given in units of ML. These abundances must first be converted into a raw number of diffusers, N_d, in order to calculate the value of θ. To do this, the volume of 1 ML of ice must be calculated. Here we make a simple approximation, by calculating the surface area of the comet given its radius R (30 km for Hale–Bopp; Fernández, 2000) and multiplying that by the thickness of 1 ML. In our treatment, 1 ML is equivalent to 3.215×10^{-10} m, given that cometary ice may be well represented by amorphous solid water ice (Brown et al., 1996). In reality, the comet will include various phases of water ice, and would be porous in nature; we omit these considerations in this simple calculation. Once the volume of a monolayer is determined, it is divided by the volume of one H_2O molecule to obtain the number of molecules in one ML of ice. From this, N_d for the diffuser of interest (H or H_2) can be calculated. The same modification is made for the calculations of the diffusion rates between all layers in the cometary ice.

Complementing the results presented above, we conducted similar MC models and analysis to parameterize θ for all values of N_d and $N_{\rm th}$ for the case of interstellar dust

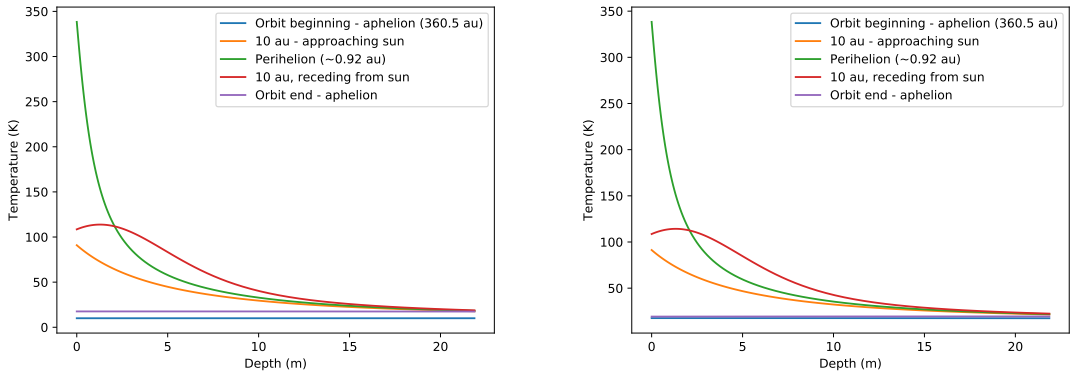

Figure 3.6: Temperature through the first ∼20 m of ice for the first (left panel) and second (right panel) orbital evolution of Hale–Bopp, based on the model of §3.2.4. The plots are color-coded for each orbital position. Subsequent orbits are very similar in behavior to the second orbit.

grain ices, using a monolithic ice mantle with only an upper interface. Parameters $f_1 = 0.3126$ and $f_2 = 0.390$ were obtained in that case; this new treatment should supersede that presented by Garrod et al. (2017) for use in interstellar astrochemical models.

3.3.2 Heat transfer simulations

The method outlined in §3.2.4 was used to solve the temperature evolution of Hale–Bopp ($R = 30$ km) for 5 orbits.[6] Fig. 3.6 (left panel) shows the results for the first orbit, at five different radial distances from the sun. The maximum temperature for this first orbit, attained at perihelion, is ∼338 K, achieved in the surface layer. As the comet recedes from the sun, it cools from the surface first, leading to peak temperatures that occur a few meters into the ice. By the time the orbit is complete, the temperature is mostly uniform throughout the first 20 m, slightly elevated from the initial value of 10 K, at a temperature of ∼18 K. Temperatures greater than 15 K

[6] §3.3.2 and the research outlined within were completed primarily by Eric R. Willis.

are maintained to a depth of ∼88 m (not shown here, in order to concentrate on the heating at the surface). The shapes of these temperature profiles are qualitatively similar to the one-dimensional calculations of Herman and Weissman (1987) (see their Fig. 2), although their methods were slightly more complicated, as they included a crystalline component to their ice, as well as sublimation in their version of Eq. 3.7.

The remaining four orbits look qualitatively similar to Figure 3.6, and are very similar to each other; the right panel of Figure 3.6 shows the temperature behavior during the second orbit. The maximum temperature achieved at perihelion is ∼338 K for each orbit. One difference between orbits is that the temperature evolves slightly further down into the cometary ice for each evolution, though this effect is small. For example, the temperature at a depth of 20 m is 18 K at the end of the first orbit, whereas at the end of the fifth orbit it is ∼21 K. Thus there is some small hysteresis in the ice temperature.

The time- and depth-dependent results of these simulations are read into the model of cometary ice chemistry at run time, to be converted into temperatures representative of the 25 chemically distinct ice layers. The layer widths in the heat transfer simulations are not the same as those in the chemical model. The first 16 layers in the comet chemistry model all fall within the 1 cm-thick surface layer of the heat-transfer model; thus those first 16 layers all have the same temperature throughout the evolution. The deeper, thicker layers in the chemical model sometimes intersect multiple depths whose temperatures are calculated independently in the heat-transfer model. In these cases, the temperature used for each chemical-model layer is the depth-weighted average of the calculated values from the heat-transfer model.

3.3.3 Results of updated chemical models

The basic chemical model of G19, outlined in §3.2.1 and §3.2.2, was updated to include the back-diffusion treatment of §3.3.1, along with updates to the chemical network and the inclusion of non-thermal chemical mechanisms. These additions and alterations to the model produce significant variations in the chemical behavior of the cold storage phase, compared with G19, as described below in §3.3.3. The chemical behavior during the new dynamical phase, occurring after the cold storage and using temperature profiles obtained in §3.3.2, is described in §3.3.3.

Cold storage phase

The previous chemical model presented by G19, which was compared with data for comet Hale–Bopp, had a different endpoint than the updated version presented here, running to 5 Gyr as opposed to the 4.5 Gyr in the updated model. The latter value was chosen to provide a slightly more accurate value for the age of the Solar System. Thus, data from the G19 model was re-plotted at 4.5 Gyr so as to compare directly with the new model endpoint for the cold storage phase. The plots in our Figure 3.7 show results at 10^6 yr into the cold storage phase, and may be compared with those of G19, in their Figure 12, panels d–f. Figure 3.8 shows abundances at the end-time of the model, with Figure 3.9 showing the re-plotted data at the equivalent time in the G19 model. Species shown in the left panels of Figs. 3.7–3.9 are those that are present in the ice at the beginning of the models. Species in the middle panels are exclusively products; the right panels show some of the more complex product species.

At 10^6 years into the cold storage phase (Fig. 3.7), the upper 1 μm of material shows the most variation in chemical composition, as was the case in the G19 models.

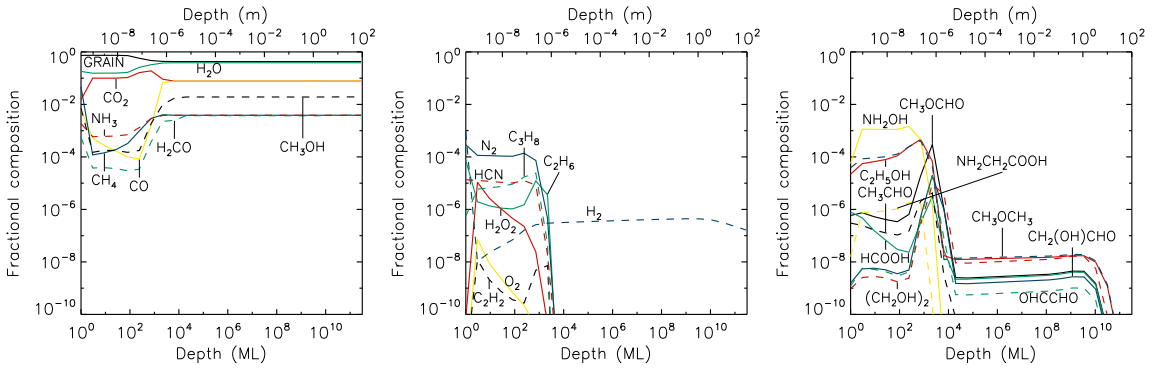

Figure 3.7: Fractional abundances of selected ice species at 10^6 years into the cold storage phase of the updated model, plotted with respect to depth into the comet surface; the surface (outermost) layer is at the left in each panel. The x-axes show the depth into the comet in units of monolayers (ML), shown on the bottom, and meters (m), shown on the top. The left panel shows species that are initially present in the ice, while species in the middle and right panels are products of the chemistry during cold storage.

Aside from in the very surface layer, most of the species that are initially present in the ice (left panel) see a drop in their fractional abundances by this time. The only exception to this is CO_2, which is instead enhanced at the expense of H_2O and CO; photodissociation of water produces an OH radical that may immediately react with nearby CO in the ice (via the PDI mechanism). It is also notable that while H_2O fractional abundance drops in the upper micron, it remains the dominant molecule at all depths and times. The fraction of dust grains in the upper micron is also increased, although it only reaches its maximum allowed value ($\sim$74%) in the upper 10^{-8} m or so. The lower abundance of H_2O and other species in the upper layers is partly due to this crowding out by dust grains. The increased dust concentration is ultimately caused by the destruction and/or sublimation of volatile species at the surface, while the dust grains are left in place.

The production of new species in the upper $\sim$1 μm is dominated by photodissociation by interstellar UV; chemistry in the deeper layers is dominated by the dissociative

action of cosmic rays, which have a substantial effect to depths on the order of around 10 m.

The product-species H_2O_2, N_2, HCN, and some hydrocarbons reach fractional abundances of around 10^{-6}–10^{-4} down to $\sim$1 μm depth. Much of the hydrogen peroxide is formed through photodissociation-induced (PDI) association reactions between OH radicals, while molecular nitrogen is formed through a similar reaction between NH radicals, which are the product of ammonia photodissociation. Dissociation of CO produces carbon atoms that may react with the dissociation products of ammonia, ultimately forming HNC and HCN. Atomic oxygen and OH may combine in the ice to form O_2H, which can be photodissociated or react with atomic H to produce O_2. Hydrocarbons of various hydrogenation states may be formed via the recombination of the dissociation products of methane (CH_4), while diffusive atomic H may also hydrogenate these species or abstract a hydrogen atom from them.

Some COMs, such as ethanol (C_2H_5OH) and dimethyl ether (CH_3OCH_3) also reach similar abundances down to $\sim$1 μm depth; however, they also maintain fractional abundances of up to 10^{-8} down to depths greater than 1 m or so. In the upper micron, these species are primarily formed via PDI reactions, and they reach something close to their peak abundances in less than 1000 yr. Ethanol and dimethyl ether in particular may build up their abundances by photodissociation of methanol to produce one of the radicals CH_2OH or CH_3O, which can combine with a methyl (CH_3) radical originating from photodissociation of methane or methanol. Photodissociation of methane may also produce the diradical methylene (CH_2), which can react directly with methanol to form dimethyl ether or ethanol. In the deeper layers, dissociation caused by cosmic rays results in similar production routes.

Other COMs, such as ethylene glycol ($(CH_2OH)_2$) and glycolaldehyde ($CH_2(OH)CHO$)

maintain abundances below 10^{-6} before abruptly spiking up by roughly two orders of magnitude at a depth of 1 μm and then immediately falling to abundances of 10^{-8} similar to the COMs previously mentioned. These species are primarily formed via three-body (3-B) reactions, i.e. the mechanism by which the product of a preceding reaction reacts immediately with some other nearby species. More specifically, mobile atomic H may react with methanol (CH_3OH) in the ice, abstracting a hydrogen atom to produce the CH_2OH radical, which can immediately react with some other nearby CH_2OH to form ethylene glycol. Although direct photodissociation of methanol to produce CH_2OH does occur, the H-abstraction reaction provides more CH_2OH, due to the high rate of H production as the result of water photodissociation.

Repetitive H-abstraction from ethylene glycol by other H atoms can lead directly to glycolaldehyde and glyoxal (OHCCHO); ethylene glycol production is the main route into the formation of all three of these molecules in the upper 1 μm. In the deeper layers, 3-B radical-recombination reactions produce each of the three molecules directly, i.e. through the addition of HCO radicals to produce glyoxal, the addition of HCO to CH_2OH to produce glycolaldehyde, or CH_2OH radicals combining to form ethylene glycol. HCO itself is mostly formed by the reaction of mobile H with CO, while CH_2OH is again mainly produced by H-abstraction from methanol by H atoms.

The spike effect in certain COM abundances around the 1 μm mark is caused by the competing formation and destruction produced by interstellar UV photons, which penetrate only to this limited depth. The photons enhance the production of COMs by producing radicals from simpler species, which then react together; but the UV also directly dissociates the product COMs, especially in the layers closest to the surface, where there is less absorption by the dust. The H atoms that are the product of photodissociation also abstract H from existing COMs, resulting in

further destruction and conversion to other products. In this way, while the overall production of COMs like methyl formate (CH_3OCHO) via radical addition falls with depth into the ice, the coincident drop in H production from all sources results in yet slower destruction, pushing up the abundance toward the 1 μm threshold. Beyond this point, the production of reactive radicals and of destructive atomic H relies solely on GCR-induced dissociation. Over time, the much lower rates involved with this mechanism gradually allow COMs to grow to substantial abundances in the deeper layers.

For some species, abundances drop dramatically in the uppermost (i.e. surface) layer, as compared with the layers directly beneath, or in some cases may instead be enhanced in that surface layer. This effect is caused by a combination of the ability of surface species to freely diffuse (with rates dependent on the temperature), and thus react, while volatile species may also desorb entirely from the surface layer, which is also not possible for species in the deeper layers.

While a number of more chemically complex species begin to reach substantial abundances to depths >1 m by 10^6 yr, as the result of cosmic ray-induced chemistry, some of the more intermediate-size ice species remain at low abundances at depths greater than one micron. However, by the end of the model run most species have reached more substantial abundances at these depths.

It is worth noting that the fractional molecular hydrogen abundance is relatively stable right through the ice, which is due to its ability to diffuse, allowing it to reach the very deepest layers. The H_2 abundance at all depths increases further by the end-time of 4.5 Gyr.

As may be expected, by 4.5 Gyr the chemical enhancement throughout the ice is

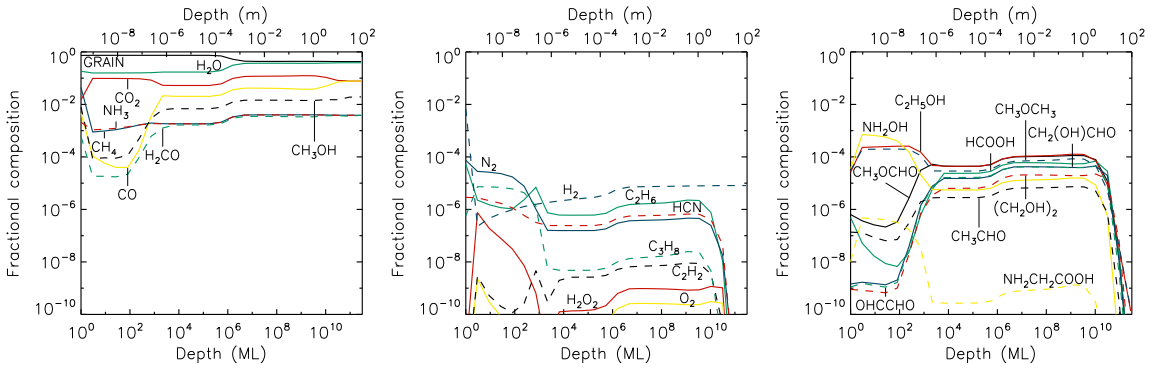

Figure 3.8: Fractional abundances of selected ice species at 4.5×10^9 years into the cold storage phase of the updated model, plotted with respect to depth into the comet surface; the surface (outermost) layer is at the left in each panel. The x-axes show the depth into the comet in units of monolayers (ML), shown on the bottom, and meters (m), shown on the top.

much more far-reaching than at 1 Myr, as shown in Figure 3.8; the longer timescale allows the slow cosmic ray-driven chemistry to convert more of the simple species into COMs, while also enhancing some other species that are formed by the destruction of those COMs themselves. Although in general the fractional abundances of ice species within the first micron have decreased somewhat compared to Figure 3.7, some species such as ethane and propane do not experience much change at all in the upper layers, instead only exhibiting differences in the deeper layers. In those deeper layers, below the first micron, the abundances of most product species shown in the middle and right-hand panels in Fig. 3.8 have increased by the end of the cold storage phase.

It may be noted also that the concentration of dust-grain material extends yet deeper at the end of the model run, achieving its maximum allowed value down to as deep as 100 μm. In the G19 model, shown in Figure 3.9, this enhancement reaches deeper, to around 1000 μm, due to the different diffusion behavior of volatiles combined with the weaker overall dissociation rates (due to recombination between

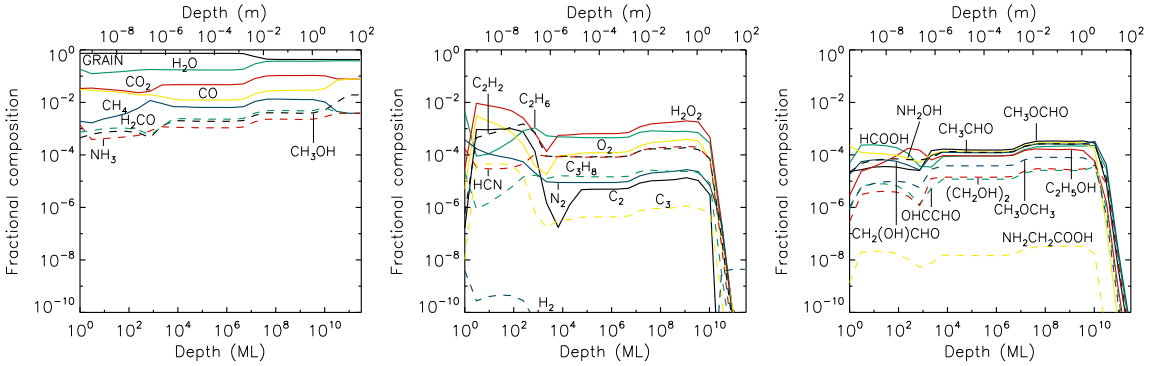

Figure 3.9: Fractional abundances of selected ice species at 4.5×10^9 years into the old G19 simulation, for comparison with the new data in Figure 3.8.

heavy photoproducts). In both models, a slight depression may be observed in the abundances of other species down to this depth, caused again by the crowding effect of the dust grains (rather than any explicit chemical effect). The further concentration of dust abundances in the upper layers by the end of the model also induces a slight shift in the reach of interstellar UV to somewhat shallower layers (compared with earlier times), as the photons are less able to penetrate, leading to lower dissociation rates and a less active photon-induced chemistry. Again, while the larger COMs show a closer correspondence between the new model and the G19 model, intermediate-sized hydrocarbon species, and some others, are generally lower in the new models. Interestingly, in the new model, glycine (NH_2CH_2COOH) shows a somewhat stronger production in the upper micron than was found in the G19 model, while at greater depths it is rather weaker than in G19; the G19 model produced glycine at a fairly stable value of around 10^{-8} at all depths. As noted by G19, even those values are insufficient to explain the presence of glycine in cometary ices, indicating that the glycine in e.g. 67P likely has a more primordial origin, rather than it being formed in situ during cold storage.

Comparing the old and new models more broadly, the most notable differences can

be found in the upper micron. Below these depths, the general order-of-magnitude behavior remains the same between the models for simple species (left panels in Figs. 3.7–3.9) at 10^6 years, and for both simple and complex molecules (right panels), as well as some intermediate-size species (middle panels) at $4.5x10^9$ years. Additionally, while in G19, H_2 had mostly been depleted in the bulk ice by 4.5 Gyrs, the updated model maintains a steady level and even increased fractionally from the previous milestone at 10^6 years.

Within the upper micron of the ice, most species have decreased in fractional abundance compared to the results in G19. Notable exceptions to this are CO_2, H_2, N_2, NH_2OH, and NH_2CH_2COOH. Meanwhile, C_2 and C_3 abundances are significantly lower at all depths and fall below the lowest shown fractional abundances. As a result, C_2H_4 and C_3H_6 were chosen as substitutes for illustrative purposes. At 10^6 years there is a spike in fractional abundance right at the one micron barrier while maintaining similar abundance values on either side of the peak, while others simply decrease in abundance below the one micron threshold.

An important divergence between the new models and the G19 models at 10 K is that most molecules produced in the upper micron are unable to diffuse deeper into the ice in the new treatment, which now only allows bulk diffusion for H and H_2. Although molecular diffusion on internal pore surfaces, which is a different process, may be plausible in the case of cometary ices, such behavior is beyond the scope of the present model. The G19 treatment assumed that bulk diffusion in the ice was a swapping process, which is now deprecated. The reasons for limiting bulk diffusion in this way are explained in more detail by Garrod et al. (2022), for the case of interstellar ices.

Another difference in the chemical treatment between the new and old models,

noted in § 2.2, involves the outcome of photodissociation events, in the case that one or other of the photoproducts does not immediately react with some other species already present in the ice via the nondiffusive PDI mechanism. In such cases, the new treatment allows these (trapped) photoproducts immediately to recombine (except in cases where H or H_2 are produced, as these are free to diffuse within the bulk ice). The same change is made also for the equivalent radiolysis-induced dissociation that has greater influence in the deeper layers. The change results in a rather lower rate of radical production in the ice overall. Consequently, a number of the intermediate-size radicals shown in the middle panels of Figure 3.7 (and Figure 3.8) achieve different abundances than in the G19 models. A specific example is the photodissociation of methanol (CH_3OH) in the upper layers; while the ejection of an H atom from methanol may produce a free CH_3O or CH_2OH radical in the ice, the branch that produces CH_3 + OH will in most cases result in recombination of these two radicals, as the chances of some other reactive radical being available nearby are much less than unity (although generally on the order of 1% or less). Methanol therefore serves as a much weaker source of the CH_3 radical than in the G19 models. This reduces the production of ethane (C_2H_6) in the ice, as well as other simple hydrocarbons to which it is chemically related, when comparing with the G19 results. The larger COM species, such as ethylene glycol, $(CH_2OH)_2$, are formed from methanol radicals such as CH_2OH, so their production is less strongly affected by the change.

Solar approach phase

Here the simulated comet was allowed to follow the projected orbital path of comet Hale–Bopp; the chemical model results are shown in Figures 3.10-3.12. As C_2 and C_3 are not nearly as abundant in the new model as in G19, and the solar approach

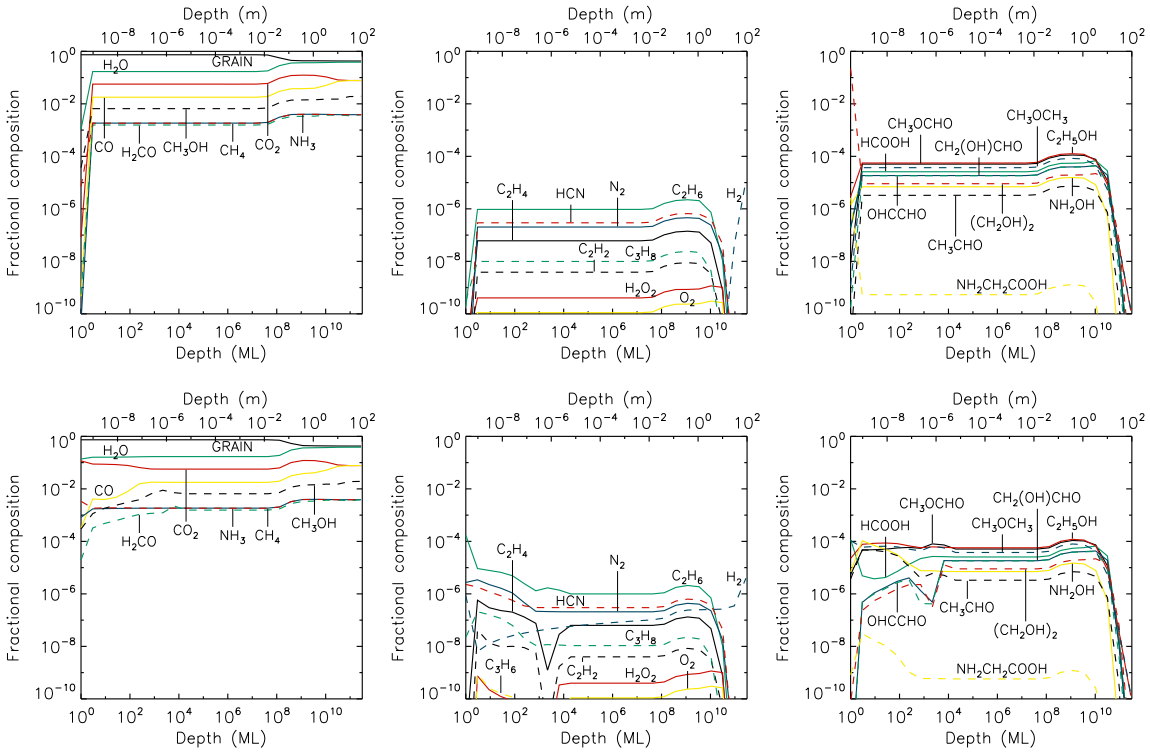

Figure 3.10: Fractional abundances of select ice species for the *first* of five solar approaches; Top: Abundances at first perihelion. Bottom: Abundances at first aphelion after starting point. The y-axis of each plot corresponds with the ice surface. The x-axis is the depth, from the surface, in terms of monolayers (ML) shown on the bottom and meters (m) shown on the top. Each column represents a different subset of species grouped based on size and relevance.

phase does not appear to change this, two other species (C_2H_4 and C_3H_6) are plotted instead. The species shown were similarly divided up into three different sets. Five sequential orbits for the comet were simulated (beginning at aphelion), based on the comet composition starting from that produced at the end of cold storage. Plots show the fractional abundances throughout the ice at perihelion and at the subsequent aphelion. "First aphelion" refers to the end of the first orbit rather than the starting point, and therefore "fifth/final aphelion" corresponds to the final time point.

The first species set (left panels) are most useful for seeing the effects on the ice as a whole. At perihelion (upper panels), excluding the low abundances within the first few monolayers, the abundance profiles are very flat out to depths of 10^8 monolayers. Come aphelion (lower panels), some variation reminiscent of its cold storage phase appears again. With each subsequent orbit, the flat portion of the abundance profile edges further right, or deeper into the ice, decreasing in value for the ice and increasing for the grains. This general behavior, in which the dust becomes more concentrated in the upper layers while the surrounding ice becomes richer in the simple/primordial species stored deeper in the ice, is a direct result of the ice loss as a result of sublimation caused by close solar approach. The molecular content that was built up in those upper layers during the entirety of the cold storage phase has been lost, to be replaced (i.e. at the same position relative to the new outer surface) by material originating deeper down.

Similar to the cold storage phase, by the time of the first aphelion (following the first solar approach), CO_2 is enhanced while all other species in the set are diminished. This is refreshed each perihelion, whereby the profile flattens out before returning to a similar shape the following aphelion. While each individual cycle still seems to enhance CO_2, throughout the ice as a whole it is actually decreasing. In its place,

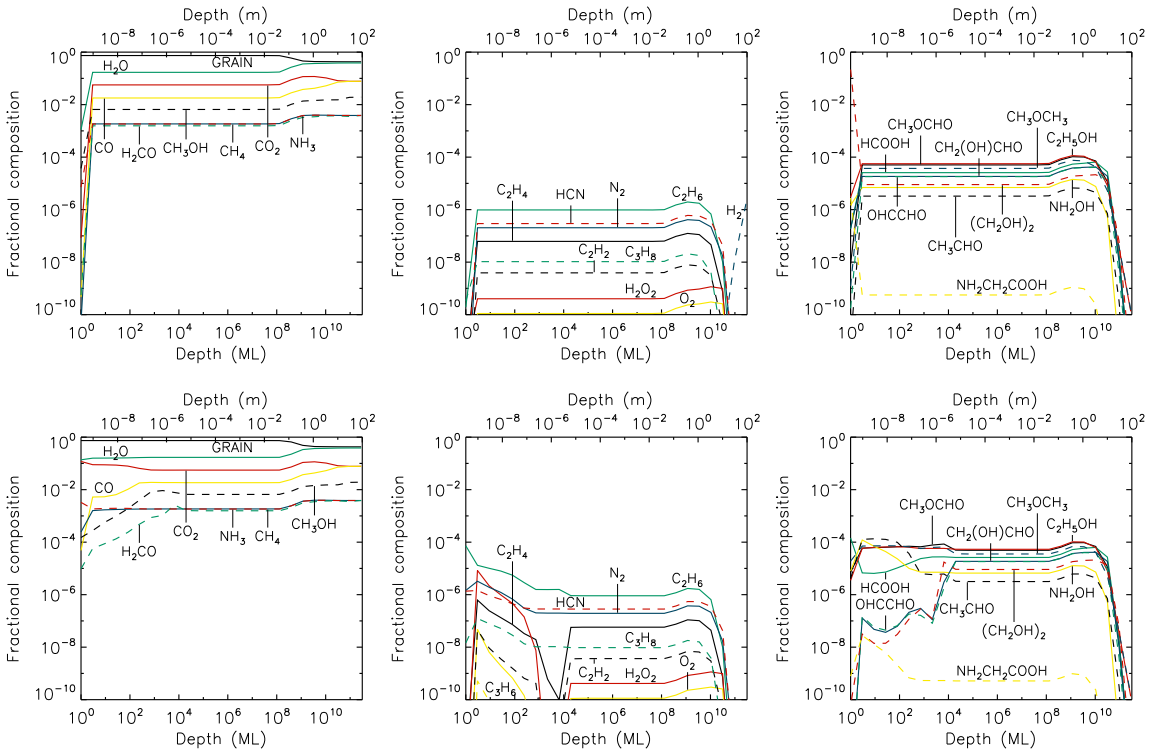

Figure 3.11: Fractional abundances of select ice species for the *second* of five solar approaches; Top: Abundances at second perihelion. Bottom: Abundances at second aphelion after starting point. Other information as per Fig. 3.10

the CO abundance increases.

Most other species tend overall to decrease over each subsequent orbit. The notable exceptions to this are O_2 and H_2O_2 which increase slightly each perihelion. The overall fractional abundances of these two species increase over time, although their surface (upper layer) values at perihelion decrease instead. Some other species exhibit the opposite, with a net decrease in abundance deeper than 1 μm depth, yet a slight increase in the upper layers at aphelion. Examples of this include C_2H_6, N_2, HCN, NH_2OH, CH_3CHO, and HCOOH. It is also worth noting that the first two orbits sometimes have species that do not follow a specific pattern, but in subsequent orbits seem to have adjusted and remain consistent.

The third and fourth Solar Approach orbits are not shown in the figures, due to their similarity to the results to the fifth orbit, which is shown in Fig. 3.12. In orbits 1 and 2 (Figs. 3.10 and 3.11), some species show irregular behavior, such as the low abundance of C_2H_2 and O_2 in the upper micron during the first aphelion, which is then restored by the second aphelion, and the sudden dip of C_2H_4 at 1 μm during the second aphelion. By the third orbit, the cometary ice abundances remain consistent between comparable points in the orbits. While changes are still evident between perihelion and aphelion, as shown in Figure 3.12, the differences in abundances between perihelion three to five, as well as aphelion three to five, are negligible. This trend would presumably continue if further orbits were run.

Most COMs are formed in the cold storage phase through gradual hydrogenation and dehydrogenation of smaller species, followed by radical addition. During the active phase, COMs broadly maintain similar abundances throughout the ice. Following the first perihelion, most of the COMs in the outer layers of the comet are originally from deeper layers of the comet, having been formed originally during the cold storage

phase by cosmic-ray radiolysis, and were left closer to the surface due to the mass-loss experienced during the comet's close solar passage. However, some COMs still form during the active phase, being driven by thermally activated reactions in response to the elevated temperatures. For example, methyl formate (CH_3OCHO) production is somewhat enhanced by the reaction $CH_3O + CO \rightarrow CH_3OCO$, which is mediated by an activation-energy barrier of ∼33 kJ/mol (4000 K) as determined by gas-phase data (Huynh and Violi, 2008). The addition of atomic H to the CH_3OCO radical completes the formation of methyl formate.

Regarding smaller species, H_2 and H are the only species with mobility in the ice mantle within this model. By the second aphelion, the majority of the H_2 budget has either reacted or moved to the surface and evaporated away. At all depths, O_2 ice is primarily formed from dissociation of O_2H, as well as the direct addition of oxygen atoms following dissociation of species such as OH, which originate mostly from water.

Once the inbound comet reaches about 5 AU it begins to experience significant loss of surface material due to thermal desorption, which outpaces all other formation and destruction routes. Similarly, once the outbound comet reaches 5 AU again, the surface loss has decreased below the other formation and destruction routes. Although there is indeed chemical activity within the ice during close solar approach, it is this mass loss, and the associated shift of deeper material toward the surface, that defines the major changes in chemical composition during the active-phase simulations. Post perihelion, the upper 1 μm of material again shows the effects of UV photo-processing. Given that much of this chemistry requires on the order of 1000 yr to reach maturity, as noted in § 3.3.3 above, the ∼2500 yr orbital period is sufficient for much of the same upper-layer composition to be re-formed by the return to aphelion.

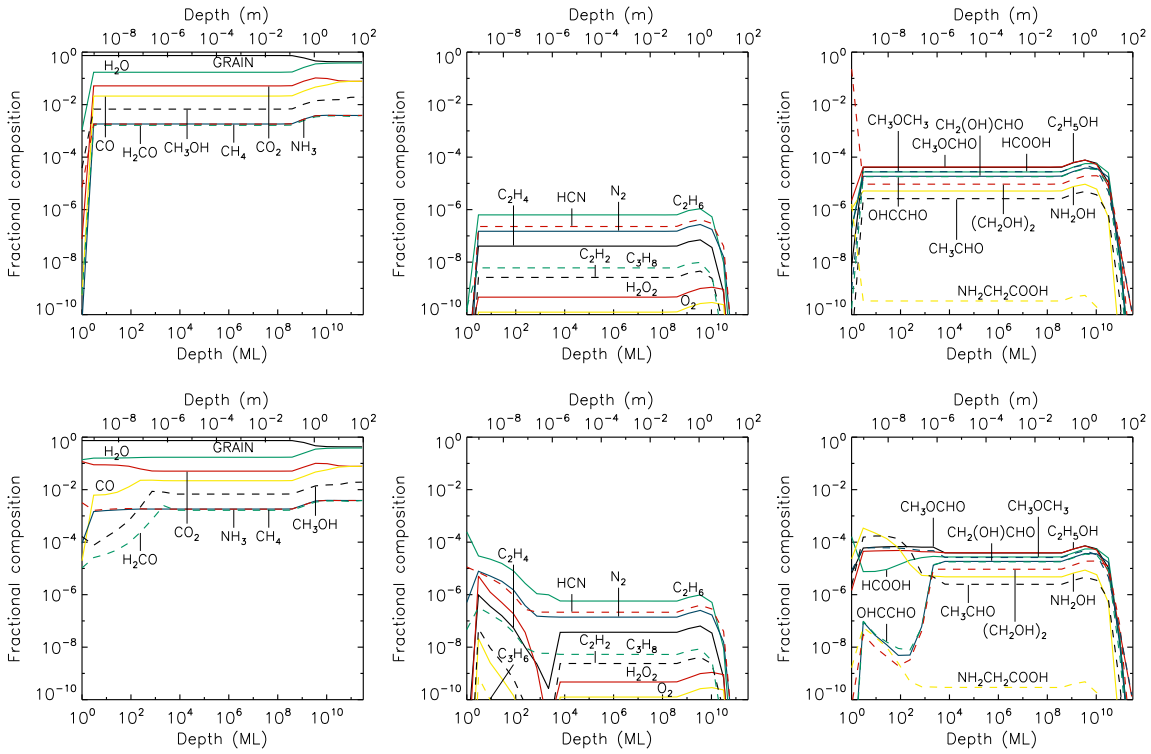

Figure 3.12: Fractional abundances of select ice species for the *final* of five solar approaches; Top: Abundances at fifth (final) perihelion. Bottom: Abundances at fifth (final) aphelion after starting point. Other information as per Fig. 3.10

3.4 Discussion

Before coming to the results of the chemical models, some discussion of the orbital parameter information for Hale–Bopp is warranted. As previously mentioned, the chemical model uses temperature profiles based on the heliocentric distance of comet Hale–Bopp over five orbits. Due to the uncertainty in the orbital behavior prior to its most recent solar approach, it was necessary to use the orbital parameters from the most recent orbit repetitively. Each of the five orbits in our model therefore uses this same set of positional data, corresponding to an orbital period of ∼2400 yr. However, there is evidence that Hale–Bopp's period has changed in the past; the previous apparition may have occurred ∼4200 yr before its most recent (Marsden, 1997). Assuming that the previous apparition was not its first, it is plausible that Hale–Bopp's prior orbital behavior could have been quite different from those two estimates as well.

While it is therefore unlikely, given the uncertainties, that our use of current orbital parameters is fully representative of Hale–Bopp's complete orbital history, the present, well-defined orbital parameters serve as a basis for obtaining from the model the broad chemical effects that Hale–Bopp is likely to have experienced over repeated active-phase orbits (assuming that it has indeed done so), or that it would do in future. It also serves as a basis for exploring the chemical behavior of the model itself under more stable conditions, before moving to models with more complex orbital dynamics in future work.

§ 3.3.3 makes note of chemical changes that occur at a depth of ∼1 μm into the ice. This can also be seen in many of the plots in Figures 3.7-3.12. The interstellar UV field has a significant effect on the upper layers of the ice, but quickly tapers

off at depths greater than about 1 μm. The significance of this particular depth is not arbitrary, but exists as a result of the limited UV penetration into the dust–ice mixture due to dust absorption. As a result, chemical changes are much more pronounced and diverse in these upper layers even from relatively early times in the models, allowing for the more varied and diverse complexity of molecules produced. The spikes and dips in the abundances mentioned throughout §3.3.3 are a direct result of the decreasing influence of UV photons with depth.

Furthermore, many species also fall off in abundance at a depth of ∼10 m. This is a result of the limited penetration of Galactic cosmic rays, which induce their own chemistry to greater depths than UV, but with lower dissociation rates and thus a slower effect that requires the long period of the cold storage phase to produce significant amounts of product molecules. Beyond the penetration depth of GCRs, there remain pristine ice layers, which ultimately include the reservoir of material explained in detail in §3.2.1. A slight bump in many abundances occurs at the deepest abundances, peaking a little beyond the 1 m mark. This is caused by the slightly elevated dissociation rates caused by GCR activity (see G19, Fig. 11), which are in turn related to the shape of the GCR energy spectrum.

The models produce a range of interesting results. First of all, even though the models start off with no complex molecules, significant COM abundances ($\sim 10^{-5}$ with respect to water ice) can be formed during the cold-storage stage alone. These COMs are formed primarily as a result of (>GeV) Galactic cosmic rays penetrating deep into the ice, which are present whether the comet is in the outer or the inner solar system. Galactic UV is also sufficient to enhance some complex ice species in the upper layers, while destroying others.

These CR and UV effects persist throughout the solar approach phase as well,

though now in tandem with a varying temperature profile driven by the solar heating. At the surface layers, many species notably drop in abundance during solar approach. This is not the case with some hydrocarbon abundances, which reach a peak in the upper layers. Some even grow in abundance with each subsequent orbit, indicating a gradual surface buildup of these hydrocarbons.

Interestingly, molecular hydrogen abundances seem to fall off quickly after the comet enters the active phase. It takes only two active-phase orbits for H_2 to have completely fallen off the scale at all layers of the ice (i.e. several orders of magnitude below a fraction 10^{-10} of total ice composition), and it never recovers. H_2 and atomic hydrogen are the only bulk ice species allowed mobility within the ice. By this point, the entire budget of trapped H_2, formed largely by the production of atomic H by GCR dissociation of stable species and the subsequent recombination of those H atoms, has gone: used up either by its involvement in reactions or – following accelerated diffusion through the ice driven by the higher temperatures – desorption from the surface of the comet.

One of the most notable molecules in the chemical network is the amino acid glycine (NH_2CH_2COOH), due to its significance to life, as well as recent cometary detections. Despite the ability of *MAGICKAL* to generate significant COM abundances within the simulated cometary nucleus, glycine still remains at relatively low abundances (versus the $\sim$1% with respect to water observed in comet 67P). Somewhat higher abundance can be seen in the upper micron, which reaches a peak during the cold storage phase. However, much of this upper-layer abundance is lost during solar approach.

As noted earlier, in §3.3.3, comparison of the same points in the first two orbits does not demonstrate a clear trend in the evolution of all chemical species at all

Species	CS	Peri1	Ap1	Peri2	Ap2	Peri3	Ap3	Peri4	Ap4	Peri5	Ap5	Observational
CO	1.7(-1)	1.7(-1)	1.7(-1)	1.7(-1)	1.7(-1)	1.7(-1)	1.7(-1)	1.7(-1)	1.7(-1)	1.7(-1)	1.8(-1)	1.2-2.3(-1)
CO_2	2.4(-1)	2.4(-1)	2.4(-1)	2.4(-1)	2.4(-1)	2.4(-1)	2.3(-1)	2.3(-1)	2.3(-1)	2.3(-1)	2.3(-1)	6(-2)
CH_4	1.0(-2)	1.0(-2)	1.0(-2)	1.0(-2)	1.0(-2)	1.0(-2)	1.0(-2)	1.0(-2)	1.0(-2)	1.0(-2)	1.0(-2)	1.5(-2)
H_2CO	9.7(-3)	9.7(-3)	9.7(-3)	9.7(-3)	9.7(-3)	9.7(-3)	9.7(-3)	9.7(-3)	9.7(-3)	9.7(-3)	9.7(-3)	1.1(-2)
CH_3OH	3.9(-2)	3.9(-2)	4.0(-2)	4.0(-2)	4.0(-2)	4.0(-2)	4.0(-2)	4.0(-2)	4.0(-2)	4.0(-2)	4.0(-2)	2.4(-2)
NH_3	1.0(-2)	1.0(-2)	1.0(-2)	1.0(-2)	1.0(-2)	1.0(-2)	1.0(-2)	1.0(-2)	1.0(-2)	1.0(-2)	1.0(-2)	7(-3)
C_2H_2	4.7(-9)	4.5(-9)	4.2(-9)	4.0(-9)	3.7(-9)	3.5(-9)	3.3(-9)	3.1(-9)	2.9(-9)	2.8(-9)	2.6(-9)	1-3(-3)
C_2H_6	1.1(-6)	1.1(-6)	9.9(-7)	9.4(-7)	8.7(-7)	8.2(-7)	7.6(-7)	7.2(-7)	6.7(-7)	6.3(-7)	5.9(-7)	6(-3)
HCOOH	1.1(-4)	1.1(-4)	1.0(-4)	1.0(-4)	1.0(-4)	1.0(-4)	9.8(-5)	9.7(-5)	9.5(-5)	9.3(-5)	9.1(-5)	9(-4)
CH_3CHO	6.4(-6)	6.2(-6)	6.0(-6)	5.8(-6)	5.5(-6)	5.4(-6)	5.2(-6)	5.0(-6)	4.8(-6)	4.7(-6)	4.5(-6)	2(-4)
CH_3OCHO	1.0(-4)	9.8(-5)	9.4(-5)	9.2(-5)	8.8(-5)	8.5(-5)	8.2(-5)	8.0(-5)	7.6(-5)	7.4(-5)	7.1(-5)	8(-4)
CH_3OCH_3	6.2(-5)	6.0(-5)	5.7(-5)	5.5(-5)	5.2(-5)	5.1(-5)	4.8(-5)	4.7(-5)	4.4(-5)	4.3(-5)	4.1(-5)	<5(-3)
$(CH_2OH)_2$	4.4(-5)	4.3(-5)	4.3(-5)	4.2(-5)	4.2(-5)	4.1(-5)	4.1(-5)	4.0(-5)	3.9(-5)	3.9(-5)	3.8(-5)	2.5(-3)
HCN	5.1(-7)	5.0(-7)	4.8(-7)	4.6(-7)	4.4(-7)	4.3(-7)	4.1(-7)	3.9(-7)	3.7(-7)	3.6(-7)	3.5(-7)	2.5(-3)
HNC	1.2(-8)	1.2(-8)	1.2(-8)	1.2(-8)	1.2(-8)	1.1(-8)	1.1(-8)	1.1(-8)	1.1(-8)	1.1(-8)	1.1(-8)	4(-4)
HNCO	3.4(-6)	3.4(-6)	3.4(-6)	3.4(-6)	3.4(-6)	3.3(-6)	3.3(-6)	3.3(-6)	3.3(-6)	3.3(-6)	3.2(-6)	1(-3)
CH_3CN	6.6(-15)	6.2(-15)	5.7(-15)	5.3(-15)	4.7(-15)	4.4(-15)	3.9(-15)	3.6(-15)	3.3(-15)	3.0(-15)	2.7(-15)	2(-4)
HC_3N	5.8(-19)	5.6(-19)	5.3(-19)	5.1(-19)	4.8(-19)	4.7(-19)	4.4(-19)	4.2(-19)	4.0(-19)	3.8(-19)	3.6(-19)	2(-4)
NH_2CHO	2.7(-7)	2.7(-7)	2.7(-7)	2.7(-7)	2.6(-7)	2.6(-7)	2.6(-7)	2.6(-7)	2.6(-7)	2.5(-7)	2.5(-7)	1.5(-4)

Table 3.3: Integrated fractional abundances (with respect to water) of selected chemical species, to a depth of 15 m, for various times in the models. Gas-phase observational values, shown for comparison, are taken from Mumma and Charnley (2011). Values are indicated in the form $A(B) = A \times 10^B$. 'CS' denotes the end of the cold storage phase (4.5 Gyr); 'Peri' stands for perihelion, and 'Ap' for aphelion, with the orbit number also indicated.

depths, and some species seem somewhat unstable in those earlier orbits, particularly when comparing between aphelions. It is not until the third orbit that the ice abundances seem to stabilize and follow a slow and steady trend over time. Each individual orbit is identical in terms of orbital parameters, and while the temperature profiles have small variations between orbits that are essentially gone after the second orbit, these variations are small enough not to be a likely cause for substantial chemical variation between orbits.

What may be seen, however, between the end-time abundance profiles of the cold-storage model and the perihelion and aphelion profiles for the first orbital model, is the extension of the deep-ice abundances (of COMs and other species) toward the upper layers (i.e. shifting from right to left); the desorption of material from the surface during the extreme heating of the comet around the time of perihelion leads to the loss of much of the material in at least the upper 1 cm, to be replaced at those depths with material that was heavily processed by GCRs during cold storage, but which was not subject to UV processing. Following the loss of what were previously the upper layers, the remaining material is now exposed to interstellar UV, so that by aphelion it has undergone some of the same processing as the original material did.

When the model comet embarks on its second passage toward the sun, the new set of upper layers that were revealed by solar processing in the previous orbit, and that were chemically processed by interstellar UV, are then subject to the same thermally induced loss. They are then replaced by new material that is subsequently processed in the same way. This new material will be much more similar in its initial composition to the material that it directly replaced, as compared with the upper-layer material that was directly inherited from the cold storage phase. Subsequent solar orbits would bring new material to the surface that shows the same behavior.

It can therefore be seen that, in these models, the material that is distinctly associated with interstellar UV during cold storage is lost to space during the first solar approach. However, the material that will be lost during the second solar approach will be material produced by GCRs at much greater depths (up to around 10 m or so). Furthermore, the subsequent passages do not remove enough material to deplete this GCR-processed material. Based on the total loss of ice material in units of monolayers, the comet loses ∼19.1 cm of ice from its surface per solar orbit, which remains consistent within a few percent for each orbit. For comparison, the total ice lost during the full cold storage phase is ∼19.3 cm. Although this means that the upper micron of material is lost many times over during even the cold phase, the loss rate of 1 μm per ∼23,000 yr means that the chemistry down to 1 μm is able to respond relatively rapidly, due to its characteristic timescale on the order of 1000 yr. The chemistry in those upper layers therefore remains quite stable during cold storage, in spite of the losses. The only substantial change in composition on long timescales is the gradual enrichment of the dust component.

It should be noted that the mass-loss discussed above corresponds specifically and uniquely to sublimation of the ice from the surface, and not from outbursts, which involves structural changes from cliff collapse and bursting of voids under pressure. The model is not presently capable of incorporating such a rapid and structurally complex occurrence. The ice that is modeled here should therefore be considered representative of regions of the comet that are left unaffected by any putative local outburst events.

3.4.1 Comparison with previous modeling techniques

In a broad sense, the new chemical results for cold storage are similar to those presented by G19; however, it should be noted that the G19 model with which we have compared our new data corresponds specifically to the 10 K case. As discussed in depth in that paper, the elevation of the temperature in the old model to 20 K (in all layers) induces bulk diffusion of large species that is not seen in the new models at any temperature, due to explicit changes in modeling techniques. Nevertheless, for comparable 10 K models, more appropriate to an Oort Cloud object, the differences in the chemistry between the new and old treatments are a matter of degree rather than a change in character.

Although not strongly manifested in the cold storage simulations, some of the updates to the chemical model are highly necessary in order to simulate the later solar approach. This is particularly true for the new treatment of back-diffusion within the ice when considering the rates of transfer between discrete layers. Although bulk diffusion in the new model is now strictly limited to H and H_2, these two species become highly diffusive in the bulk ice as temperatures increase. Meanwhile, as that diffusion occurs, these species will make their way to the surface of the comet more rapidly, allowing them to escape. The findings of the Monte Carlo simulations of three-dimensional random walk, and their parameterization into manageable expressions, indicate that the rates of transfer should be strongly affected by the back-diffusion effect – far more than any comparable effect related to reactions, either in the bulk ice or on the ice surface. The effect on these models is to allow the modest amounts of H and H_2 that exist in the deepest layers to be retained for longer, allowing, in particular, a somewhat more efficient process of H-abstraction and hydrogenation of radicals to occur deep in the ice. The adoption by G19 of simple

diffusion rates between layers, corresponding to the high-occupation case, is clearly inappropriate for the more typical low-occupation case for H and H_2. For example, in the deepest layer in the model, which has a thickness of $\sim 2.8 \times 10^{11}$ ML ($\sim$90 m), the low-occupation case provides a back-diffusion factor of around 10^{23}; an enormous modification to the rate of loss of H and H_2 by diffusion between layers compared with the simple, high-occupation rate.

It is indeed also notable that back diffusion has only a very limited effect on rates of reaction within the bulk ice; the effect is essentially negligible, being typically less than a factor 1.5, which is smaller than any uncertainty on the fundamental diffusion rates. Thus, while H and H_2 are much more effectively retained in the ice due to their large random walk, their efficiency in finding reaction partners in three dimensions is effectively unimpeded.

Our calculation of both these quantities for conditions appropriate to interstellar dust-grain ice mantles is also valuable, and allows the degree of occupation to be taken into account in the bulk-ice diffusion rates for those much thinner ices.

3.4.2 Comparison with Hale–Bopp abundances

Although we have adopted orbital parameters for the solar approach phase corresponding directly to Hale–Bopp, the chemical model outputs have not so far been directly compared with those of the comet itself. As noted in § 3.4, the present model cannot and does not attempt to simulate outburst events. However, following the approach of G19, it is useful to compare the solid-phase abundances produced by the model at various points in its dynamical/physical evolution with the gas-phase abundances determined for Hale–Bopp. To allow such a comparison, the fractional

Species	CS	Peri1	Ap1	Peri2	Ap2	Peri3	Ap3	Peri4	Ap4	Peri5	Ap5	Observational
CO	1.0(-1)	1.0(-1)	1.1(-1)	1.1(-1)	1.1(-1)	1.2(-1)	1.2(-1)	1.2(-1)	1.3(-1)	1.3(-1)	1.3(-1)	1.2-2.3(-1)
CO_2	3.3(-1)	3.3(-1)	3.3(-1)	3.2(-1)	3.2(-1)	3.1(-1)	3.1(-1)	3.0(-1)	3.0(-1)	3.0(-1)	2.9(-1)	6(-2)
CH_4	1.1(-2)	1.1(-2)	1.1(-2)	1.1(-2)	1.1(-2)	1.1(-2)	1.1(-2)	1.1(-2)	1.1(-2)	1.1(-2)	1.1(-2)	1.5(-2)
H_2CO	9.2(-3)	9.2(-3)	9.2(-3)	9.3(-3)	9.3(-3)	9.4(-3)	9.5(-3)	9.5(-3)	9.5(-3)	9.6(-3)	9.6(-3)	1.1(-2)
CH_3OH	3.8(-2)	3.9(-2)	3.9(-2)	3.9(-2)	3.9(-2)	3.9(-2)	3.9(-2)	3.9(-2)	4.0(-2)	4.0(-2)	4.0(-2)	2.4(-2)
NH_3	1.1(-2)	1.1(-2)	1.1(-2)	1.1(-2)	1.1(-2)	1.1(-2)	1.1(-2)	1.1(-2)	1.1(-2)	1.1(-2)	1.1(-2)	7(-3)
C_2H_2	2.4(-8)	2.3(-8)	2.2(-8)	2.1(-8)	1.9(-8)	1.8(-8)	1.7(-8)	1.6(-8)	1.5(-8)	1.4(-8)	1.3(-8)	1-3(-3)
C_2H_6	5.9(-6)	5.8(-6)	5.4(-6)	5.2(-6)	4.7(-6)	4.5(-6)	4.1(-6)	3.8(-6)	3.5(-6)	3.3(-6)	3.0(-6)	6(-3)
HCOOH	1.5(-4)	1.5(-4)	1.5(-4)	1.5(-4)	1.6(-4)	1.6(-4)	1.6(-4)	1.6(-4)	1.6(-4)	1.6(-4)	1.6(-4)	9(-4)
CH_3CHO	2.0(-5)	1.9(-5)	1.9(-5)	1.8(-5)	1.7(-5)	1.7(-5)	1.6(-5)	1.6(-5)	1.5(-5)	1.4(-5)	1.4(-5)	2(-4)
CH_3OCHO	3.0(-4)	3.0(-4)	2.9(-4)	2.8(-4)	2.7(-4)	2.6(-4)	2.5(-4)	2.4(-4)	2.3(-4)	2.2(-4)	2.1(-4)	8(-4)
CH_3OCH_3	2.2(-4)	2.2(-4)	2.1(-4)	2.0(-4)	1.9(-4)	1.9(-4)	1.7(-4)	1.7(-4)	1.6(-4)	1.5(-4)	1.4(-4)	<5(-3)
$(CH_2OH)_2$	5.3(-5)	5.3(-5)	5.4(-5)	5.4(-5)	5.4(-5)	5.4(-5)	5.5(-5)	5.5(-5)	5.4(-5)	5.4(-5)	5.4(-5)	2.5(-3)
HCN	1.8(-6)	1.7(-6)	1.7(-6)	1.6(-6)	1.6(-6)	1.5(-6)	1.4(-6)	1.4(-6)	1.3(-6)	1.2(-6)	1.2(-6)	2.5(-3)
HNC	7.2(-9)	7.3(-9)	7.5(-9)	7.7(-9)	8.1(-9)	8.3(-9)	8.6(-9)	8.8(-9)	9.1(-9)	9.3(-9)	9.5(-9)	4(-4)
HNCO	2.1(-6)	2.1(-6)	2.2(-6)	2.2(-6)	2.3(-6)	2.4(-6)	2.5(-6)	2.5(-6)	2.6(-6)	2.7(-6)	2.7(-6)	1(-3)
CH_3CN	4.6(-14)	4.5(-14)	4.2(-14)	3.9(-14)	3.5(-14)	3.2(-14)	2.9(-14)	2.6(-14)	2.3(-14)	2.1(-14)	1.9(-14)	2(-4)
HC_3N	2.4(-18)	2.3(-18)	2.3(-18)	2.2(-18)	2.1(-18)	2.0(-18)	1.9(-18)	1.8(-18)	1.7(-18)	1.6(-18)	1.5(-18)	2(-4)
NH_2CHO	2.2(-7)	2.1(-7)	2.1(-7)	2.2(-7)	2.2(-7)	2.2(-7)	2.3(-7)	2.3(-7)	2.4(-7)	2.4(-7)	2.4(-7)	1.5(-4)

Table 3.4: Integrated fractional abundances (with respect to water) of selected chemical species, to a depth of 1 m, for various times in the models. Gas-phase observational values, shown for comparison, are taken from Mumma and Charnley (2011). Values are indicated in the form $A(B) = A \times 10^B$. 'CS' denotes the end of the cold storage phase (4.5 Gyr); 'Peri' stands for perihelion, and 'Ap' for aphelion, with the orbit number also indicated.

abundances of selected ice species are integrated to a depth of ∼15 m into the model comet, corresponding to the maximum reach of GCR processing. These abundances are presented as a fraction of integrated water ice in Table 3.3, with values provided at the end of the cold storage phase and at each of the perihelion and aphelion points of the five simulated active-phase orbits. Observational abundances collated by Mumma and Charnley (2011) are also shown.

Three of the listed species, CH_4, H_2CO, and NH_3, which are those included in the initial composition of the comet at the beginning of the cold storage phase, remain consistent throughout the model runs. Two other species, CO and CH_3OH, increase slightly. All other species exhibit gradual decreases, yet at differing rates. It should be noted that all the species that either increase or remain constant are species in the initial set, and with the exception of CO_2 none of the initial species decrease. In each case, the fractional abundances are somewhat linear and experience no oscillatory behavior associated with varying orbital distance and the related temperature changes. Meanwhile, the effect of solar approach on COM abundances is a universal net negative. In the case of molecules not present in the initial, pristine ice composition, each solar approach reduces the overall inventory of all ice species.

When compared to the observational values, all of the starting species with the exception of CO_2 are within a factor of 2 or less. The CO_2 abundance is around 4x above the observed value. Most of the CO_2 in the ice derives from the initial abundance set at the beginning of the cold storage phase, although there is some conversion from CO and H_2O occurring mainly during cold storage. The discrepancy may therefore be due to the choice of initial abundance. Almost all other species shown in Table 3.3 appear to be several orders of magnitude below observational values. HCOOH and CH_3OCHO are the only ice species roughly within an order of

magnitude of the observational values, while CH_3CHO and $(CH_2OH)_2$ are roughly within two orders of magnitude. It is also worth mentioning that for CH_3OCH_3 there is only an observational upper limit, and our computational value lies roughly two orders of magnitude below this value.

It is interesting to note that the modeled ratios of the oxygen-bearing COMs HCOOH, CH_3OCHO and CH_3CHO relative to each other are reasonably consistent with the observed values, with the abundance of CH_3OCH_3 also being technically consistent with the observed upper limit. In contrast, the nitrogen-bearing molecules in the Table, aside from NH_3 (which is one of the initial ice species), are all underestimated by at least three orders of magnitude. Similarly, the organic molecules which do not contain oxygen similarly underestimate observational values by at least four orders of magnitude.

Overall, the disparity between the model and observational values is not significantly impacted by the processing from the solar approach phase. Despite the fact that all of the non-starting species decrease with time, the orders of magnitude differences between the model and observational values make this relatively insignificant. Even values from the end of the cold storage phase, when the fractional abundances of non-starting species are the highest, still notably underestimate all observational values.

The integration of local abundances to 15 m depth follows the approach of G19; however, it is noteworthy that in the present (cold storage) model, the abundances of some species begin to decline at depths less than this maximum value. In the G19 models, a small degree of thermal diffusion (even at 10 K) especially for small species may have allowed abundances to be smoothed out somewhat at around the integration threshold. Here, however, no such mechanism exists. Furthermore, due

to the exponentially increasing depth of each distinct chemical layer in the model, the abundances in deeper layers naturally contribute more to the integrated values than those of the upper layers. To ensure that the comparison with observational data is fair, we present in Table 3.4 the integrated values to a depth of 1 m total. This value also corresponds approximately to the total amount of material lost from the surface over the five orbits.

Using 1 m integration depth, most simple species nevertheless remain at fairly comparable values with the 15 m integration, although the changes are still significant, as the strongest depth-dependent variation for these species occurs at or around the 1 m mark. This is mainly because the loss of material extends to a depth of this order, becoming greater with each orbit (by around 19 cm). This means that the region of concentrated dust also extends to these depths.

For species not in the initial set, such as the hydrocarbons larger than methane, there is a modest increase in the ratio with respect to water. Much of this is caused by the drop in the integrated water content, by a factor 2.25 for the final aphelion. A number of species' abundances increase by a factor greater than this, indicating that they did not extend fully to 15 m. However, the changes are at most a further factor of around 2, and some species record a slight fall for the 1 m integration. In spite of this, a few of the COMs ultimately come a little closer to the observed values, e.g. methyl formate (CH_3OCHO); thus, according to the model, at least a substantial fraction of the methyl formate observed in the gas phase could plausibly have an origin in GCR-induced processing during the cold storage. But aside from dimethyl ether, the rest are rather too low.

Table 3.5 directly compares the updated model abundances versus those in G19. The table displays the abundances at the end-time of 4.5 Gyr for both models, using

an integration depth of 15m and 1m. Additionally, we identify the fractional change from G19 to the current model. Many ice species remain relatively consistent between the models, especially those included in our initial composition. Some undertake rather drastic decreases such as C_2H_2, CH_3CN, and HC_3N while some of the others have smaller, yet still significant, decreases. This general decrease in abundances can again be largely explained by the absence of bulk diffusion for species aside from atomic and molecular hydrogen as noted above.

Finally, it is instructive to consider how much of each molecule in the comparison has been ejected from the surface (intact) during each stage of the chemical evolution. This may be determined simply by summing the amounts of each molecule desorbed in various ways between each key time-point (e.g. perihelion to aphelion), as shown in Table 3.6. Here, we see that the material released into the gas phase during the solar approach phases is fairly consistent with the composition of the processed ice, more particularly with the upper 1 m integrated values. In general, the solar heating and desorption therefore appears to release the various ice components in a fairly uniform fashion. The surface temperatures achieved at peak should indeed be sufficient to allow the various species to desorb freely once they reach the upper surface layer. The exception is ethylene glycol, whose abundance in the gas with respect to water in each solar approach stage is a factor of $\sim$5 higher, and falls within an order of magnitude of the observed value. We note that our comparisons of course do not consider any gas-phase chemistry that could enhance or diminish molecular abundances following release either through the desorption mechanisms considered here or by localized outburst events.

It remains, however, a substantial challenge to construct a framework in which the outburst process may be meaningfully incorporated into this already quite complex

chemical treatment of comet nucleus chemistry. Similarly, it is by no means trivial to consider the process of diffusion on internal pore surfaces within the ice (to allow transport between different depths), nor to include the associated surface reactions and the growth (or collapse) of the pores over time.

Another aspect that is also not considered in the models is the possible loss of dust material as the result of gas drag from the continuous sublimation of volatiles over the entire surface. Modeling this process accurately would require a deeper analysis of the mechanics of dust loss than can be considered in the present work. However, dust loss through this mechanism could make a significant contribution to the overall mass loss from a comet, thus affecting our comparisons with observationally derived mass-loss estimates. There is thus room for further development of the model in this direction.

A more immediately tractable process for inclusion in the models that has not been considered here is the influence on the chemistry of UV photons and energetic protons originating from the Sun itself, which may be able to compete with interstellar photons in their processing of the upper ice layers for small heliocentric distances. The planned follow-up to the present publication (i.e. paper II) will address these additional drivers of chemical evolution. Also, the use of a more explicit calculation of initial ice abundances, derived from interstellar chemical models, may provide a more accurate starting point for the cold-storage ice composition, by including atoms, radicals, and sparse molecular components that could affect the later bulk-ice chemical behavior and physical structure. This would also provide a way to test more directly the survival of complex organic molecules inherited from earlier stages of solar-system evolution.

Based on these four methods of comparison of modeled ice abundances with

the available observational data, the quantities of product species, including COMs, produced during the cold storage and active phases are insufficient to account for the majority of observed abundances in the gas phase, excluding the simple, abundant ice constituents that are present in each layer from the beginning of the model. It is nevertheless interesting that certain quantities of COMs and other species, while not great enough to meet observational targets, are likely to be enhanced by the cold storage stage in particular, due to GCR processing.

The good match for the simpler species, such as CO, CH_3OH, etc., is a direct result of our choice of initial ice composition. The initial ice composition is already similar to interstellar ice compositions by design. All other species ultimately fail to be reproduced through methods currently implemented into the model. As noted by G19, for new comets the chemical signatures produced by the release of nucleus material could be somewhat different, and chemically richer, than those of comets that have undergone multiple passes and have thus already lost their outer $\sim$10 m of ice.

As to the origins of the observed COMs, given their abundances, these models would indicate that those molecules must have been incorporated into the comets from pre-existing material. This is a rather stronger conclusion than that provided by G19, who found some species could plausibly reach observable abundances to $\sim$15 m depths. However, as the present models do not yet include anything other than a limited selection of simple, initial species, it is unclear whether having a broader selection of initial species could still lead to some significant in situ production of larger species. It is also unknown to what degree any COMs inherited from primordial material might be diminished, rather than enhanced, by cosmic ray and/or UV processing.

3.4.3 Mass loss from Hale–Bopp

While not implemented as a function of the model, it is worth considering the effects of local outbursts of cometary nucleus material. Adding such effects into our models would cause further loss of ice species in the upper layers – including the dust itself, which is not allowed to leave the surface of the comet in the present model. As shown by Figs. 3.8–3.12, the abundances of complex ice species fall off drastically at depths greater than around 10–15 m. If, during the active phase, the comet were to lose its top 15 m of ice due to outbursts, the inventory of COMs formed during cold storage would be substantially depleted, replaced with ice material from the unprocessed core, and resulting in an almost completely pristine ice. From there, the remaining inventory could be entirely depleted following a second orbit, leaving behind a pristine ice.

It is worthwhile to consider the observational estimates of mass-loss from Hale–Bopp. Jewitt and Matthews (1999) measured the sub-mm dust continuum emission in the coma, determining the total dust-mass lost during the 1997 apparition to be $\sim 3 \times 10^{13}$ kg. Thence, they determined the ratio of dust- to water-mass production rates to be >5. Those authors then assumed that the water and dust loss could be attributed to active vents on the surface. Assuming a lower limit for the exposed area responsible for water production of 2800 km^2, and combining this with an assumed bulk density of 1 g cm^{-3}, they determined that the vent floors should have receded by a depth of $\sim$10 m per orbit.

As previously noted, our model displays a mass loss for Hale–Bopp of around 19 cm per orbit; with our adopted water-ice density of 0.9 g cm^{-3}, this corresponds to an ice-loss per orbit of 172 kg m^{-2}. The water-only mass loss is 112 kg m^{-2}.

If we allow, in our one-dimensional treatment, that all regions of the surface are actively able to sublimate, then a surface area of ∼11,300 km^2 (assuming $r = 30$ km) provides a total water-mass loss per orbit of 1.3×10^{12} kg and a total ice-mass loss per orbit of 1.9×10^{12} kg. On this basis, the model is reasonably consistent with the observationally determined total water loss of $< 6 \times 10^{12}$ kg.

Although our model does not currently implement dust loss mechanisms, we may further estimate how much dust might be lost along with the sublimating water. After the upper layers have been depleted of much of their ice content, which occurs even during the cold storage phase, our model produces a dust- to water-ice ratio of 5.37 by volume within the upper layers. Assuming that this ratio is maintained as dust and ice are lost from the surface, and assuming a dust density of 3 g cm^{-3}, our water-loss rate would indicate a total dust-loss per orbit of 2.3×10^{13} kg. Therefore, on the basis of a fully active surface for Hale–Bopp, both our explicit water-loss rate and the implied dust-loss rate align well with the values determined by Jewitt and Matthews (1999).

However, since this dust-loss process is not included in the model, a larger *depth* of material would be lost than our current model presumes. Since the maximum fractional dust content per layer allowed in our model (based on geometry) is ∼74%, approximately 73 cm of total material would be lost from the entire (non-localized) surface per orbit. While this is still a substantial difference, it is not sufficient to remove even the majority of the 10–15 m of processed ice over the five orbits tested here in our model. A less efficient removal of grains from the surface would also produce a smaller discrepancy in the depth of material lost between these two modeling cases, although this would inevitably lead to a poorer match to the dust-production rate.

Given that the approximate water-loss rate of the model corresponds to the observational value, we can examine two extreme scenarios regarding the active area of surface mass-loss. Jewitt and Matthews (1999) assume a very localized mass loss, corresponding to an active region of only a quarter of the available surface, based on a comet radius of 30 km. Under their scenario, the vent regions would go deep, exposing pockets of pristine ice. Meanwhile, the remaining regions of the surface with low activity would presumably still preserve the material that our models suggest to be enriched by UV and GCR processing during cold storage. In such a case, while our models would appear to underestimate the amount of material lost in those vent regions, they would overestimate the loss from the inactive region.

Alternatively, adopting the fully active surface implicitly considered by our model, while the upper micron of ice initially processed by the interstellar UV field is lost, a substantial amount of the ice processed by GCRs is retained even after five orbits. The reality, however, is likely some middle ground between these two scenarios. For example, our model cannot presently distinguish between surface regions that may experience different amounts of solar heating during the active phase. The lack of an explicit dust-loss mechanism is also an area where the model could be improved.

3.5 Conclusions

The model presented herein uses the first solid-phase chemical kinetics model adapted for cometary ices and adds in the capability of modeling the active phase as well as the earlier period of "cold storage" in the outer solar system. Previously, the model was limited to a constant set of physical conditions but is now capable of modeling changes in temperature due to changing radial distance from the sun as well as ice

Species	New (15m)	G19 (15m)	New/G19 (15m)	New (1m)	G19 (1m)	New/G19 (1m)
CO	1.7(-1)	1.5(-1)	1.1(+0)	1.0(-1)	7.8(-2)	1.3(+0)
CO_2	2.4(-1)	2.3(-1)	1.0(+0)	3.3(-1)	2.9(-1)	1.1(+0)
CH_4	1.0(-2)	1.8(-2)	5.6(-1)	1.1(-2)	3.5(-2)	3.1(-1)
H_2CO	9.7(-3)	1.2(-2)	8.1(-1)	9.2(-3)	1.3(-2)	7.1(-1)
CH_3OH	3.9(-2)	2.2(-2)	1.8(+0)	3.8(-2)	1.1(-2)	3.5(+0)
NH_3	1.0(-2)	9.0(-3)	1.1(+0)	1.1(-2)	6.1(-3)	1.8(+0)
C_2H_2	4.7(-9)	9.1(-5)	5.2(-5)	2.4(-8)	4.7(-4)	5.1(-5)
C_2H_6	1.1(-6)	3.8(-4)	2.9(-3)	5.9(-6)	2.0(-3)	3.0(-3)
HCOOH	1.1(-4)	2.5(-4)	4.4(-1)	1.5(-4)	5.9(-4)	2.5(-1)
CH_3CHO	6.4(-6)	2.5(-4)	2.6(-2)	2.0(-5)	7.1(-4)	2.8(-2)
CH_3OCHO	1.0(-4)	2.8(-4)	3.6(-1)	3.0(-4)	9.1(-4)	3.3(-1)
CH_3OCH_3	6.2(-5)	5.4(-5)	1.2(+0)	2.2(-4)	2.1(-4)	1.1(+0)
$(CH_2OH)_2$	4.4(-5)	4.6(-5)	9.6(-1)	5.3(-5)	7.7(-5)	6.9(-1)
HCN	5.1(-7)	9.9(-5)	5.2(-3)	1.8(-6)	5.5(-4)	3.3(-3)
HNC	1.2(-8)	7.4(-5)	1.6(-4)	7.2(-9)	1.6(-4)	4.5(-5)
HNCO	3.4(-6)	1.2(-5)	2.8(-1)	2.1(-6)	2.0(-5)	1.1(-1)
CH_3CN	6.6(-15)	1.2(-5)	1.7(-8)	4.6(-14)	2.3(-6)	2.0(-8)
HC_3N	5.8(-19)	5.2(-9)	1.1(-10)	2.4(-18)	2.2(-8)	1.1(-10)
NH_2CHO	2.7(-7)	2.2(-5)	1.2(-2)	2.2(-7)	4.4(-5)	5.0(-3)

Table 3.5: Comparison of the new results and the G19 model outputs at the endpoint of the cold-storage stage, based on the integrated fractional abundances of selected chemical species to a depth of 15 m and 1 m. The ratios of the new results versus G19 are also listed for each integration depth. Values are indicated in the form $A(B) = A \times 10^B$.

Species	ΔCS	ΔPeri1	ΔAp1	ΔPeri2	ΔAp2	ΔPeri3	ΔAp3	ΔPeri4	ΔAp4	ΔPeri5	ΔAp5	Observational
CO	4.1(-2)	1.1(-1)	1.0(-1)	1.1(-1)	1.1(-1)	1.1(-1)	1.1(-1)	1.2(-1)	1.2(-1)	1.2(-1)	1.3(-1)	1.2-2.3(-1)
CO_2	5.0(-2)	3.3(-1)	3.3(-1)	3.3(-1)	3.3(-1)	3.2(-1)	3.2(-1)	3.1(-1)	3.1(-1)	3.0(-1)	3.0(-1)	6(-2)
CH_4	1.5(-1)	1.1(-2)	1.1(-2)	1.1(-2)	1.1(-2)	1.1(-2)	1.1(-2)	1.1(-2)	1.1(-2)	1.1(-2)	1.1(-2)	1.5(-2)
H_2CO	4.1(-3)	1.1(-2)	1.1(-2)	1.1(-2)	1.1(-2)	1.1(-2)	1.1(-2)	1.2(-2)	1.2(-2)	1.2(-2)	1.2(-2)	1.1(-2)
CH_3OH	7.3(-2)	4.1(-2)	4.1(-2)	4.1(-2)	4.1(-2)	4.1(-2)	4.1(-2)	4.1(-2)	4.1(-2)	4.2(-2)	4.1(-2)	2.4(-2)
NH_3	7.0(-3)	1.1(-2)	1.1(-2)	1.1(-2)	1.1(-2)	1.1(-2)	1.1(-2)	1.1(-2)	1.1(-2)	1.1(-2)	1.1(-2)	7(-3)
C_2H_2	8.1(-13)	2.2(-8)	2.4(-8)	2.3(-8)	2.2(-8)	2.1(-8)	1.9(-8)	1.8(-8)	1.6(-8)	1.5(-8)	1.4(-8)	1-3(-3)
C_2H_6	2.5(-3)	5.5(-6)	5.9(-6)	5.8(-6)	5.5(-6)	5.1(-6)	4.8(-6)	4.4(-6)	4.0(-6)	3.7(-6)	3.4(-6)	6(-3)
HCOOH	2.9(-6)	1.5(-4)	1.5(-4)	1.5(-4)	1.5(-4)	1.6(-4)	1.6(-4)	1.6(-4)	1.6(-4)	1.6(-4)	1.6(-4)	9(-4)
CH_3CHO	4.8(-5)	1.9(-5)	2.0(-5)	1.9(-5)	1.9(-5)	1.8(-5)	1.7(-5)	1.7(-5)	1.6(-5)	1.5(-5)	1.5(-5)	2(-4)
CH_3OCHO	2.4(-4)	3.0(-4)	3.0(-4)	3.0(-4)	2.9(-4)	2.8(-4)	2.7(-4)	2.6(-4)	2.5(-4)	2.4(-4)	2.3(-4)	8(-4)
CH_3OCH_3	4.9(-3)	2.1(-4)	2.2(-4)	2.2(-4)	2.1(-4)	2.0(-4)	1.9(-4)	1.8(-4)	1.7(-4)	1.6(-4)	1.5(-4)	<5(-3)
$(CH_2OH)_2$	4.1(-8)	2.6(-4)	2.5(-4)	2.6(-4)	2.5(-4)	2.6(-4)	2.5(-4)	2.6(-4)	2.6(-4)	2.7(-4)	2.6(-4)	2.5(-3)
HCN	9.0(-6)	1.7(-6)	1.8(-6)	1.7(-6)	1.7(-6)	1.6(-6)	1.5(-6)	1.5(-6)	1.4(-6)	1.3(-6)	1.3(-6)	2.5(-3)
HNC	1.4(-10)	7.4(-9)	7.2(-9)	7.3(-9)	7.5(-9)	7.8(-9)	8.1(-9)	8.4(-9)	8.7(-9)	8.9(-9)	9.2(-9)	4(-4)
HNCO	8.0(-9)	2.2(-6)	2.1(-6)	2.1(-6)	2.2(-6)	2.3(-6)	2.3(-6)	2.4(-6)	2.5(-6)	2.6(-6)	2.6(-6)	1(-3)
CH_3CN	1.1(-9)	4.1(-14)	5.3(-14)	4.5(-14)	4.3(-14)	4.1(-14)	3.2(-14)	3.3(-14)	2.1(-14)	2.6(-14)	2.1(-14)	2(-4)
HC_3N	1.5(-20)	2.5(-18)	2.4(-18)	2.4(-18)	2.3(-18)	5.7(-18)	2.1(-18)	4.9(-18)	1.9(-18)	4.5(-18)	1.7(-18)	2(-4)
NH_2CHO	1.6(-10)	5.1(-7)	4.4(-7)	4.5(-7)	4.5(-7)	4.7(-7)	4.7(-7)	5.0(-7)	4.9(-7)	5.3(-7)	5.2(-7)	1.5(-4)

Table 3.6: The amount of material lost to the gas phase, with respect to the amount of water lost, for selected chemical species at various times/intervals in the models. Values are indicated in the form $A(B) = A \times 10^B$. 'ΔCS' corresponds to material the lost during the cold storage phase (4.5 Gyr); 'ΔPeri' corresponds to the loss from the previous aphelion to the current perihelion, and 'ΔAp' the loss from the previous perihelion to the current aphelion, with the orbit number also indicated.

depth. The model also includes a careful treatment for the effects of back-diffusion on H and H_2 mobility within the ice, as well as incorporating a selection of new nondiffusive processes based on recent interstellar-ice treatments. With these new adaptations, the model results may be more directly matched with observed gas-phase abundances from active-phase comets.

The application of the model firstly to 10 K cold storage conditions, representative of the Oort Cloud, produces a fairly rapid ($\sim$1000 yr) and rich chemistry in the upper $\sim$1 micron of the ice–dust mixture, caused primarily by interstellar-UV processing, as found by G19. In the deeper ice layers, to depths on the order of 10 m, Galactic cosmic-ray processing inducing a similar, but much slower chemistry that allows complex organic molecules (COMs) to build up in modest abundances. During the 4.5 Gyr of interstellar UV and GCR processing, around 19 cm of ice material is lost to space, leading to the concentration of the dust component down to a similar depth. Although the chemically rich upper micron of material is gradually lost over and over again, the chemistry is fast enough to maintain a fairly steady profile of molecular abundances over time.

The active-phase models, tailored for comet Hale–Bopp, consider five identical active-phase orbits immediately after exiting the cold storage phase. The orbital parameters for each orbit are based on the most recent observed orbit for this comet. Each solar approach phase leads to the loss of approximately 19 cm of ice from the surface, purely through sublimation over the whole comet surface (not localized outbursts). The modeled solid-phase chemistry is found to stabilize after two full orbits, such that the chemical composition as a function of depth is very similar when comparing the same point in each orbit. After this second orbit, chemical changes are much more gradual with time and trends are much more consistent.

Thus, the first solar approach is the most chemically unique, as it corresponds to the period when the outer layers of material, processed by UV during cold storage, is lost to space. Deeper material, processed by cosmic rays over billions of years, then becomes the de facto surface, which is itself then processed by UV in the upper micron of material. Further orbits release more surface material to reveal yet deeper ices. Within the five orbits modeled here, a substantial amount of material remains from the period of GCR processing. Although the chemical profiles remain qualitatively similar between orbits 2–5, dust concentration continues to greater depths each time.

As the chemistry has stabilized by this point and changes over time appear to be minimal, we can take the profile at any given point in the orbit and easily extrapolate to a larger number of orbits than the five performed with this model. Subsequent orbits should maintain comparable profiles at slightly reduced fractional abundances of non-pristine ice.

Compared to observations of comet Hale–Bopp, our fractional abundances of "pristine" ice (i.e. CO, CO_2, CH_4, NH_3, H_2CO and CH_3OH) as a fraction of water all match within an order of magnitude. However, all non-pristine ice species (i.e. product species) underestimate observations by at least one order of magnitude. Most remain within four orders of magnitude, but certain cases can underestimate observations by as much as fifteen orders of magnitude. In particular, the amino acid glycine is still produced in low abundance, below many other COMs. As a result, the current model and conditions still appear insufficient to replicate observed complexity within cometary ices.

It therefore seems essential to include an initially richer ice composition, to account for inherited primordial material. This supports work by Drozdovskaya et al. (2019), who found similar results for comet 67P in which the composition had simi-

larities with IRAS 16293 abundances for COMs and other molecules. More specific comet simulations based on 67P conditions, including the effects of differing initial ice compositions, would be necessary to confirm the significance of these findings to the present modeling treatment. We anticipate such a study in a follow-up paper. In such a context, not only the formation of COMs and other species but the destruction and/or survival of the same, through cold storage and ultimately solar approach, must also be considered.

Chapter Acknowledgements

This work was funded by the NASA Emerging Worlds Program, grant no. NNX17AE23G. DAC thanks the NASA FINESST program for a graduate fellowship. We thank the IAU Minor Planet Center for providing the orbital data necessary to run our models. We also thank our fellow research group member K. Stelmach for critical readings of the manuscript. We also thank our referees for their helpful comments in improving this paper.

Chapter 4

Ice Chemistry of Comet 67P/Churyumov–Gerasimenko

4.1 Introduction

Comets are often referred to as having pristine ice mantles. In this context, a pristine ice is one which is composed of material that has been well-preserved from the formation of the Solar System (Weissman et al., 2020). It is also suspected that cometary ices can be inherited directly from the proto-solar nebula or earlier. Comparisons made by Drozdovskaya et al. (2019) of bulk abundances in comet 67P/Churyumov–Gerasimenko with gas-phase molecular abundances detected toward the low-mass star forming region IRAS 16293-2422 showed correlations between their N-, S- and HCO-group-bearing species. Cometary studies are of interest as they can give us direct insight into the early solar system. Comets are made up of a mixture of dust and water ice along with lower abundances of other ice species such as carbon monoxide (CO), ammonia (NH_3, and an assortment of complex organic molecules (COMs), which are usually defined as organic molecules containing 6 or more atoms. The presence of COMs in cometary ices has been confirmed both from remote observations as well as return sample missions (Mumma and Charnley, 2011).

One of the reasons comets can remain so pristine is their current environment,

which is cold, far from the sun, and in a consistent orbit. During the cold storage phase of their lifetime, solar system comets typically exist in one of two reservoirs: the Oort Cloud (Oort, 1950) and the Kuiper Belt (Kuiper, 1951). The Oort Cloud is a roughly spherical shell surrounding the solar system. The predicted size of the Oort Cloud ranges from an inner radius of 3000 au to an outer radius of 50,000 au (Hsieh and Jewitt, 2006), with other estimates giving a maximum outer radius as high as 200,000 au (Duncan et al., 1987). As a result, the Oort Cloud has average temperatures of ∼10 K. The Kuiper Belt on the other hand is a more disk shaped body, similar to the asteroid belt, with an inner radius roughly from the orbit of Neptune (∼30 au) and an outer radius of ∼50 au. This cometary reservoir is notably warmer, with temperatures averaging ∼40 K (Hsieh and Jewitt, 2006). Due to their long lifetimes, comets may still undergo some degree of chemical processing due to cosmic rays and the interstellar UV field.

At some point during its cold storage lifetime, a comet may become perturbed from its stable orbit and enter an active phase as it approaches the sun. During this active phase, more significant chemical processing may occur due to thermal effects as well as influence from solar protons and UV irradiation. Oort Cloud comets can be influenced by gravitational effects of stars as they pass the solar system, often resulting in long-period comets, while Kuiper Belt comets are typically perturbed by collisions with other comets or gravitational effects from Neptune, often resulting in short-period comets. Of the short-period comets, a group referred to as a Jupiter Family Comet (JFC), which is a classification of comet orbiting the sun at a similar distance as Jupiter is (∼5 AU), is a common reservoir. Among this category is comet 67P/Churyumov–Gerasimenko.

The Rosetta mission launched in 2004 and was the first mission to have a space-

craft orbit, and even land on, a comet. This mission provided a wealth of information on the physical and chemical makeup of a comet. Comet 67P therefore becomes a nice reference point for chemical modeling. Matching data from computational studies to the information retrieved from the Rosetta mission will allow for the models to be fine-tuned, and therefore give a more accurate representation of other comets when using that model.

The chemical kinetics model *MAGICKAL* (Model for Astrophysical Gas and Ice Chemical Kinetics And Layering), first presented in Garrod (2013a), is a diverse model that was later adapted to model the chemistry of cometary ices in Garrod (2019), hereafter referred to as G19. Though models of comae (gas-phase models) have existed for some time (e.g. Irvine et al., 1998), *MAGICKAL* was the first computational model adapted to simulate the solid-phase chemistry of a comet.

Comets are suspects for the origin of some of Earth's water as well as potential carriers for simple molecules that could be a precursor to life, such as glycine. Therefore, understanding the chemical processes of cometary ices becomes vital to determine how valid claims such as these could be.

There is an abundance of chemical detections made of comet 67P. Data collected with the ROSINA mass spectrometer (Balsiger et al., 2007) was used to make many such detections, such as Altwegg et al. (2016) with the detection of glycine, methylamine, and ethylamine in the coma. They similarly reported detections of phosphorous-bearing molecules, which are vital to the formation of life. If these molecules were formed in the cometary nucleus, the presence of these species may indicate that comets could have been delivered to the early Earth through impacts and therefore may have had a hand in facilitating the formation of life. Similarly, Calmonte et al. (2016) detected various sulfur-bearing species as well, including H_2S,

SO, S_2, S_3, CH_3SH, and C_2H_5SH, some of which can be used as bio-signatures in the search for life. Additionally, the presence of species like S_2 indicates the ice mantle of comet 67P likely formed during or prior to the solar nebula, as opposed to a late-stage formation. This also supports the idea of comet 67P containing pristine ices. Altwegg et al. (2020) also detected ammonium salts in cometary outbursts of 67P, and more recently, Altwegg et al. (2022) detected $NH_4^+SH^-$ directly in the cometary dust formed directly from NH_3 and H_2S which are both abundant in the ice.

In this paper, we present updates to our previous model for cometary ice chemistry presented in Willis et al. (2024), hereafter referred to as Paper I. We examine the influences of solar effects on cometary ice chemistry, such as solar UV and high energy solar protons, that were ignored in previous models. The influence of interstellar/protostellar inheritance is also considered by incorporating a more rigorous set of initial abundances. Along with this, we also consider the addition of a broader range of chemical species such as sulfur (S) and sodium (Na) which have become relevant with the ammonium salt detection mentioned above as well as some notable findings presented here with the presence of sodium. Additional considerations of surface blockage via dust layer buildup is also discussed. Perhaps most importantly is the examination of comet 67P. As one of the best studied comets, there is a wealth of data from which to directly compare with our model. Updated models were also run for comet Hale–Bopp to compare previous data as well as to contrast short-period comets (67P) and long-period comets (Hale–Bopp).

§4.2 describes the new mechanisms incorporated into the chemical model, as well as the heat transfer and back-diffusion simulations. §4.3 presents the results of the heat-transfer and back-diffusion simulations, as well as our chemical model results. §4.4 compares the results from these models with those of G19, as well as observations

of Hale–Bopp, followed by conclusions in §4.5.

4.2 Methods

The model and process presented herein builds upon the one presented by Paper I. The model used in Paper I was, in turn, based on the model from G19, with various additions including a more comprehensive treatment of nondiffusive reactions (see Jin and Garrod, 2020; Garrod et al., 2022). Here, we start with the chemical kinetics model *MAGICKAL* which is presented in detail in G19. In addition to that, all of the updates and additions present within Paper I are present here unless noted otherwise. As in Paper I, the comet in the model is composed of 25 distinct layers that may be uniquely composed of ice and dust. From surface to interior, each layer is three times thicker than the last. The surface is set to be one monolayer thick, resulting in a total thickness of ∼136 m over all modeled layers. Below this depth is a reservoir that acts as both source and a sink. Material, be it ice or dust, can flow from the reservoir to replenish the layers above. Similarly, material can flow from the upper layers back into the reservoir if material is gained. Neither of these instances affect the fractional composition of the reservoir. As such, it acts as a constant source of pristine ice.

Within the model, some of the reaction barriers have been updated and some new sodium reactions were added in (§4.2.1). Comet 67P has many differences from comet Hale–Bopp which was the primary topic of Paper I. Some aspects, such as comet 67P being a short period comet, require additional detail and complexity to properly model their behavior (§4.2.2). Additional external effects originating from the sun, ultraviolet light and protons, were added in as well (§4.2.3). Finally, we use additional models to generate a more complex initial ice composition so that we may

compare it to the previously assumed simple composition (§4.2.4).

4.2.1 Model Updates

Various updates have been added from the version presented in Paper I and the version used to model comet 67P as well as updated versions of comet Hale–Bopp. Some of the changes are outlined in more detail within the following sections. MAGICKAL was improved in terms of its capabilities and efficiency. Some reaction energies were also updated. In particular, there was some necessary changes with the sodium chemistry treatment. In previous iterations of the comet model, treatment of the sodium chemistry was not an issue, as it ignored sodium as a component. However, with the updates outlined in §4.2.4, it became important to consider this. Certain model runs resulted in surface build up and blockage by sodium species Na, NaH, and NaOH. This made it apparent that proper treatment of the sodium chemistry was quite important when allowing some to exist in the initial ice. Therefore, additional formation and desorption reactions for NaOH were implemented.

4.2.2 Comets Hale–Bopp and 67P/Churyumov–Gerasimenko

Comet 67P is a very different type of comet from Comet Hale–Bopp and therefore cannot be treated in the same way. Hale–Bopp was an Oort Cloud comet that became a long period comet after being perturbed towards the inner solar system. As described in Paper I, the treatment included a Cold Storage phase, keeping the comet at a set distance of 1000 AU for a duration of 4.5 Gyr, followed by a Solar Approach phase, five subsequent orbits following given orbital parameters meant to represent its active phase. The comet itself has an approximate radius of 30 km, a porosity of 0.3,

and is assumed to have an equal amount of ice and dust content (Guilbert-Lepoutre and Jewitt, 2011).

67P on the other hand was originally a Kuiper Belt comet that eventually moved into becoming a Jupiter Family Comet (JFC), and therefore has a short orbital period. The treatment of the Cold Storage phase was nearly the same, with the only difference being the distance at which it was kept. To represent the cold storage phase of Comet 67P, the model uses a generic Kuiper Belt orbit at a radius of 43.75 AU, which results in a much warmer cold storage phase than in Paper I. Comet 67P currently has an orbital period of about 6-8 years and is a JFC. JFCs have frequent changes in their orbital parameters due to gravitational interactions with Jupiter. Due to these changes, the dynamical history of comet 67P is somewhat mysterious before the first observations in 1969. Models have been used to propose potential orbital histories for comet 67P (e.g. Krolikowska (2003)). Though beyond approximately 500 years the errors become too large to allow further extrapolation. For the purposes of our models, we make use of the JPL Horizons Web Application to generate the orbital positions over the last 500 years. This allows for a more dynamic, as well as accurate, orbit for the comet model than the method used in Paper I. This time frame covers the last 52 orbits of variable orbital periods of Comet 67P.

Due to its smaller aphelion owing to the fact it is a JFC, we also incorporated an additional phase between the cold storage and the active phase. This is nominally referred to as the Transition phase. This transition phase is an entirely arbitrary orbital shift. The path is calculated by connecting the designated Kuiper Belt orbit with the first time point of the active phase and using a simple Hohmann transfer orbit equation. The calculated transit time ends up coming out to approximately 42 years.

The modeled temperature of the comet was also matched to the temperature measured by Rosetta at a specific point in its orbit. Using an infrared sensor around mid July 2014, an average surface temperature of approximately 203 K was detected. Our initial simulations of 67P revealed it too cold to match observations. We then adjusted the value for the average solar zenith angle until the temperature at that time point matched the observation at that time point. Nicely, doubling the value from 0.25 to 0.5 yields an excellent match. A value of 0.25 is the case for a uniformly illuminated sphere. Therefore, given the odd lobed shape of comet 67P, such a value should be reasonable.

Some of the other input parameters, such as the comet size, the dust-to-ice ratio, and the porosity, were changed to replicate conditions of Comet 67P. This comet is much smaller that Hale–Bopp which was previously examined in Paper I, with a radius of less than a kilometer at its thinnest point. We therefore took this as our nominal comet radius for the purposes of our temperature profile calculations. The ice-to-dust ratio is also much different at 1:3, and it is also much more porous with an approximate value of 0.7 (Pätzold et al., 2019).

4.2.3 Solar Radiation Effects

In Paper I, effects of solar UV and energetic particles (i.e. protons) were deemed less important and excluded from the model for simplicity, due to the fact that even for the Solar Approach phase, the majority of its lifetime was spent far enough away from the sun where those effects were less important. For the majority of the comets lifetime, the interstellar UV field and the galactic cosmic rays (GCRs) were much larger contributors to the dissociation rates of molecules. Owing to the fact that

comet 67P is a JFC, and is thus closer to the sun even during its cold-storage stage, the same assumption could not be made when modeling the active phase for this comet.

Solar UV and solar proton fluxes are calculated in terms of their individual contributions to water ice photodissociation rates within each layer of the modeled comet. The first step is to find the radiance of the sun in relevant terms given by

$$I_{\odot} = \frac{I_0 a \pi \lambda}{hc} \tag{4.1}$$

where I_0 is the radiance of the sun at a given wavelength, obtained from Fig. 4 of Curdt et al. (2001) and taken to be 0.6 W sr^{-1} m^{-2} $\mathring{A}^{-1}$ (based on a wavelength of 1600 Å, i.e. the low photon-energy end of their dataset); a is a unit conversion factor equal to 10^5; λ is the specific wavelength in meters chosen at 1.6×10^{-7} m; h is the Planck constant in cgs units; and c is the speed of light also in cgs. We then find the interstellar UV intensity given by

$$\begin{aligned} I_{is} = 3.2028 \times 10^{12} \lambda_0^{-3} - 5.1542 \times 10^{14} \lambda_0^{-4} \\ +2.0546 \times 10^{16} \lambda_0^{-5} \end{aligned} \tag{4.2}$$

where λ_0 is the wavelength in Å, and is equivalent to Eq. 2 in Heays et al. (2017) except that it is in terms of Å rather than nm. From there we determine a scaling factor given by

$$f_{uvsol} = \frac{I_{\odot} R_{\odot}^2}{I_{is} D^2} \tag{4.3}$$

where $R_\odot$ is the radius of the sun and D is the distance to the comet in the same units. This gives us a scaling factor for the UV emitted by the sun for the dissociation reactions. Note that f_{uvsol} represents the scaling of the UV at the surface of the comet; the effect of UV absorption on the photodissociation rates is dealt with separately in each layer of the comet ice, based mainly on absorption by dust grains in the layers above. The rate of photodissociation in each comet layer represents the average value over all monolayers of ice within that layer, as per Garrod (2019).

To find the effects of solar protons, we use the energy delivery timescale data from Fig. 5 of Cooper et al. (2003) that provides the energy deposition rates from solar protons into water ice at two distances. In order to scale the proton effect with distance, we take the values at the two distances, scale them to 1 AU, and then average them to get a singular result. We can then find the water dissociation rate from solar protons given by

$$k_p = \frac{m_{water}}{2t_{year}E_{water}}\left(\frac{d_1^2}{t_1} + \frac{d_2^2}{t_2}\right) \tag{4.4}$$

where m_{water} is the mass of a water molecule in amu, t_{year} is the number of seconds in the Julian year, E_{water} is the water dissociation energy in eV, and the remaining components are an averaged value of the dose time taken at different distances and scaled to 1 AU. t_1 and t_2 are the electronic component of the dose times taken from Fig. 5 of Cooper et al. (2003), and d_1 and d_2 are the respective distances in AU from which the dose times are taken in order to scale the dose time to 1 AU. From there, the scaling factor for the solar protons is then given by

$$f_{psol} = \frac{k_p}{k_{cr}D^2} \tag{4.5}$$

where k_{cr} is the regular photon-driven water dissociation rate taken to be 3.28×10^{-10}. The rate of proton-driven dissociation for each chemical species in a particular layer is then based on the usual photodissociation rate multiplied by f_{psol}. The proton-driven dissociation is rate is assumed to remain flat to a depth of 1 micron and then sharply end. In a comet layer within which the proton flux reaches its maximum penetration of 1 micron, the dissociation rate for each species is pro-rated according to the number of monolayers that are within the 1 micron depth limit, as a fraction of the layer thickness. This depth corresponds to the sharp drop-off in the dose time in Fig. 5 of Cooper et al. (2003).

These factors are then added into the calculations scaling with distance to the sun and with depth into the cometary ice. UV photons are scaled by a blockage factor that drops sharply at around 1 micron. This is a similar depth to the penetration of solar protons, but the factors that scale it with depth are ultimately different. Finally, as with previous versions of the model (i.e. G19 and Paper I), the GCRs penetrate much deeper into the ice, reaching ∼15 m before dropping off. Aside from the addition of the solar UV and solar proton factors, this method is identical to previous iterations of the model.

4.2.4 Initial Ice Composition

In both G19 and Paper I, a rather simple initial ice composition was used for modeling the comet chemistry. These fractional abundances are based on the dominant components of interstellar ices. The ice was made up of seven simple molecules in a set number fraction. Water ice is the most abundant component, so all ice abundances are set with respect to water ice. Of the remaining initial components, CO

and CO_2 are each set to 20%, Methanol is set to 5%, and methane, formaldehyde, and ammonia are each set to 1%. We also include a dust component, and set the initial fraction to 111%. These abundances are the initial composition throughout all 25 layers and the reservoir. Both G19 and Paper I were unable to reproduce observations of complex organic abundances, implying the need for another source. A likely avenue to investigate is testing the effect that the initial ice composition has on the model.

Two different initial ice compositions were used and tested to determine the importance of initial abundances and the influences of inherited interstellar ices. The first composition we refer to as a *simple* ice. The *simple* ice is the same initial ice abundances outlined above, and the same ones used throughout G19 and Paper I. The second composition we refer to as an *interstellar* ice. This ice is created through a different version of *MAGICKAL* that is made to model dust and ice in interstellar clouds. This initial interstellar cloud model also includes atoms not present in the *simple* ice such as sulfur and sodium. This model is a cold collapse model and uses conditions typical of a dark cloud. Specific values are chosen somewhat arbitrarily based on these conditions.

Chemically, the model starts with atoms and ions as well as H_2. The initial abundances are shown in Table 4.1. The gas and dust temperature are both set to 10 K, the initial visual extinction is set to 3, and cosmic ray ionization rate is set to 1.3E-17. The cloud starts with a gas density of 3E+3 and the model runs until it reaches a density of 2E+8. The final abundances are taken and used as the initial ice composition of the comet model, simulating direct inheritance of ices from the interstellar cloud. Some ice species, such as ions, are excluded when transferring over abundances from the interstellar cloud model to the comet model for the sake

Species	Initial Abundance
H_2	0.499
H	2E-3
He	9E-2
O	3.2E-4
C	1.4E-4
N	2.14E-5
S^+	8E-8
Si^+	8E-9
Fe^+	3E-9
Na^+	2E-8
Mg^+	7E-9
P^+	3E-9
Cl^+	4E-9

Table 4.1: The initial abundances of species in the dark cloud model. Abundances are given with respect to total hydrogen.

of consistency. Some of the initial abundances and how they compare are shown in Fig. 4.1.

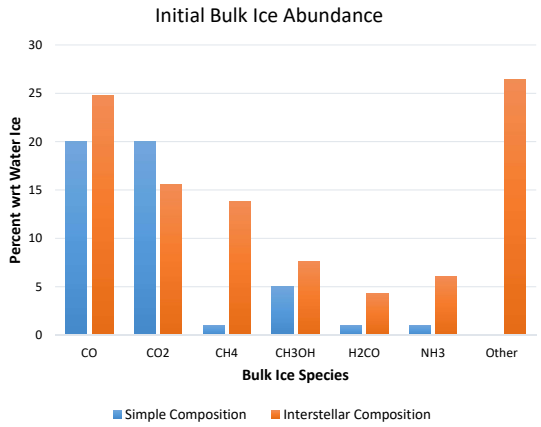

Figure 4.1: Comparison between the initial fractional abundances of ice species with respect to water ice. The *simple* ice composition is in blue (left columns) while the *interstellar* ice composition is in orange (right columns). The final category, "Other", is a sum of all ice species not listed. It is therefore nominally composed of 266 ice species.

As the initial *interstellar* ice was derived from a chemical model, it is significantly

more complex than the previously used *simple* ice. There are 273 ice species in the comet chemical network. The seven ice species used as the initial ice composition of the *simple* ice are still the most abundant within the *interstellar* ice. While the other 266 ice species overall make up a significant fraction of the ice ($\sim$26% wrt water ice), each individual component is small compared to the more abundant ice species previously mentioned. Among this "Other" category includes larger hydrocarbons, amines, and other organic molecules. In addition, more atoms have been added to the mix in the form of S, Si, Fe, Na, Mg, P, and Cl. G19 and Paper I, along with the *simple* ice, do not have any of these atoms included as they only start with the most abundant molecules.

These changes also affect the treatment of the reservoir of pristine ice below the bottom layer. Previously, the reservoir fractional abundances were set to constant values outlined above regardless of the stage of the model (i.e. Cold Storage or Solar Approach). However, with the addition of interstellar inheritance in our model, what constituted "pristine ice" changed as well. The interstellar abundances obtained from the previous model were used as the baseline for our pristine ice composition. Rather than maintaining a pre-specified value, the model instead references the fractional ice composition used at the beginning of the Cold Storage model, and maintains those values within the reservoir. This is done irrespective of the stage, so even during the later Solar Approach stage, the reservoir abundances are those from the beginning of the Cold Storage stage.

4.3 Results

Results are divided into three subsections, corresponding to the mass loss rate comparisons resulting in multiple renditions of the model (§4.3.1), the results from the comet chemical kinetics model for Comet 67P/Churyumov–Gerasimenko (§4.3.2) and subsections for the cold storage, transition, and solar approach phases of the model, and the results for the updated versions of the cold storage and solar approach for the Comet Hale–Bopp chemical kinetics models (§4.3.3).

4.3.1 Mass Loss Rates

The mass loss rate reported by Vincent et al. (2021) for comet 67P is approximately 50 cm per orbit, assuming mass loss is spread evenly across the surface. Realistically, mass loss can be heavily driven by outgassing events. However, as our models cannot currently take such events into consideration, we can instead take the reported value to be an upper limit. The mass loss rate changes not only throughout any given orbit, but also from one orbit to the next, given that the orbit of comet 67P changes its orbital parameters frequently. The most notable change was back in 1969 when it was first discovered. Comet 67P had been perturbed from a perihelion out around the orbit of Jupiter to a much closer approach of 1.2 au, where we have made our observations. We therefore can take the mass loss rates for our models only from the last few orbits of the comet to make reasonable comparisons.

While mass loss will be affected by changes in the photon flux and the addition of high energy protons, we found the largest changes come about as a result of differing ice compositions. Changes in the mass loss due to additional solar UV and solar protons is found to be negligible. When using the *simple* ice, used in previous iterations,

we find that the mass loss rate overestimates observations by 2-3 orders of magnitude. However, when we use the generated *interstellar* ice, the mass loss underestimates the observation by 2 orders of magnitude. This was a drastic difference between the two ice compositions. Further investigation showed a large number of sodium-bearing species pooling in the surface layers of the *interstellar* ice models. As sodium is not present in the *simple* ice models, this could have been a reason for the drastic change in the mass loss, as sodium species could cause a blockage of the surface.

In order to investigate this, two more model types were run. One excluded any sodium from the model, while another kept the sodium abundances but we added additional sodium reactions. The model that excluded sodium had a mass loss rate slightly higher than observations. While above our maximum value, it was nowhere near as high as the *simple* ice. Other ice species, especially longer hydrocarbons, were also in significant abundances at the upper layers. Meanwhile, adding the additional sodium chemistry to the *interstellar* ice model resulted in an even lower mass loss rate, underestimating observations by about 3 orders of magnitude.

4.3.2 Comet 67P/Churyumov–Gerasimenko

The orbital path comet 67P follows is depicted in Fig. 4.2. Chemical abundances are presented similar to those in G19 and Paper I. Chemical species are divided into three groups: simple species (e.g. H_2O, CO_2, CH_4, etc.), intermediate species (e.g. O_2, HCN, hydrocarbon chains, etc.), and large species (e.g. COMs). Each will be referred to as Set 1-3 respectively. The species in Set 1 are notably those that the initially *simple* ice model begins with. Various conditions were used for the comet 67P models. The values for the abundances in these plots are fractional with respect to water ice.

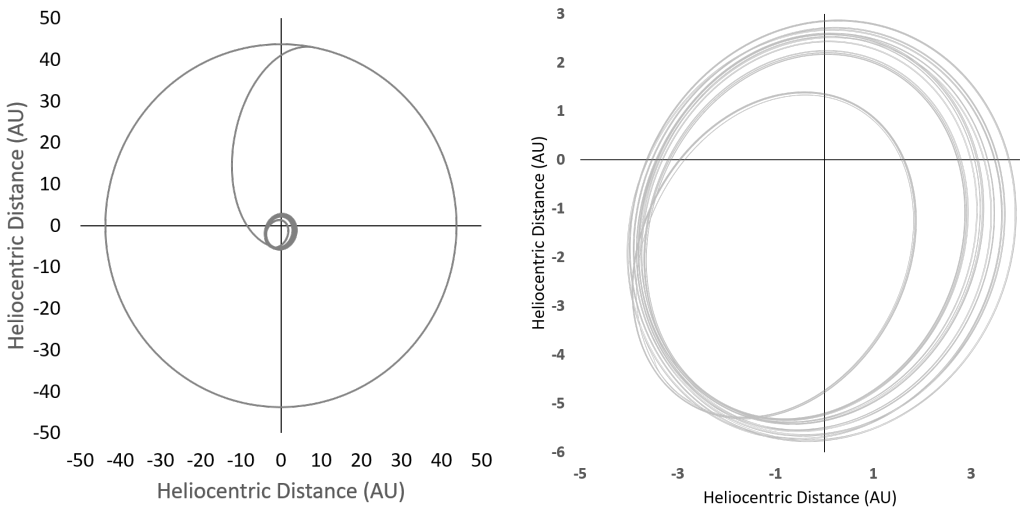

Figure 4.2: The orbital path of comet 67P/Churyumov–Gerasimenko used in our model. Left: The entire orbit, including Cold Storage, Transition, and Solar Approach phases. Right: Only the Solar Approach phase, data obtained from JPL Horizons Web Application. Z-axis data was transposed onto the xy-plane to better represent the radial distance. The Sun is centered on (0,0).

A model similar to that done in Paper I was run for comet 67P with an initially *simple* ice, but with physical parameters representative of comet 67P. A second model was run with the only difference being the incorporation of a more complex initial ice obtained by running an interstellar cloud model version of *MAGICKAL*. The third model was identical to the second model except it took into consideration the solar UV effects which had previously been ignored for Comet Hale–Bopp. The fourth model built upon the third model and also included the effects of solar protons. The fifth model used the initially *simple* ice but added in the solar UV and proton effects. The sixth model used a new *interstellar* ice abundance that excluded any sodium from the model. The seventh and final model used the previous interstellar initial abundance while making more consideration of the sodium chemistry. Each of these models was run in three stages: the Cold Storage phase, the Transition phase, and the Solar Approach phase.

Cold storage phase

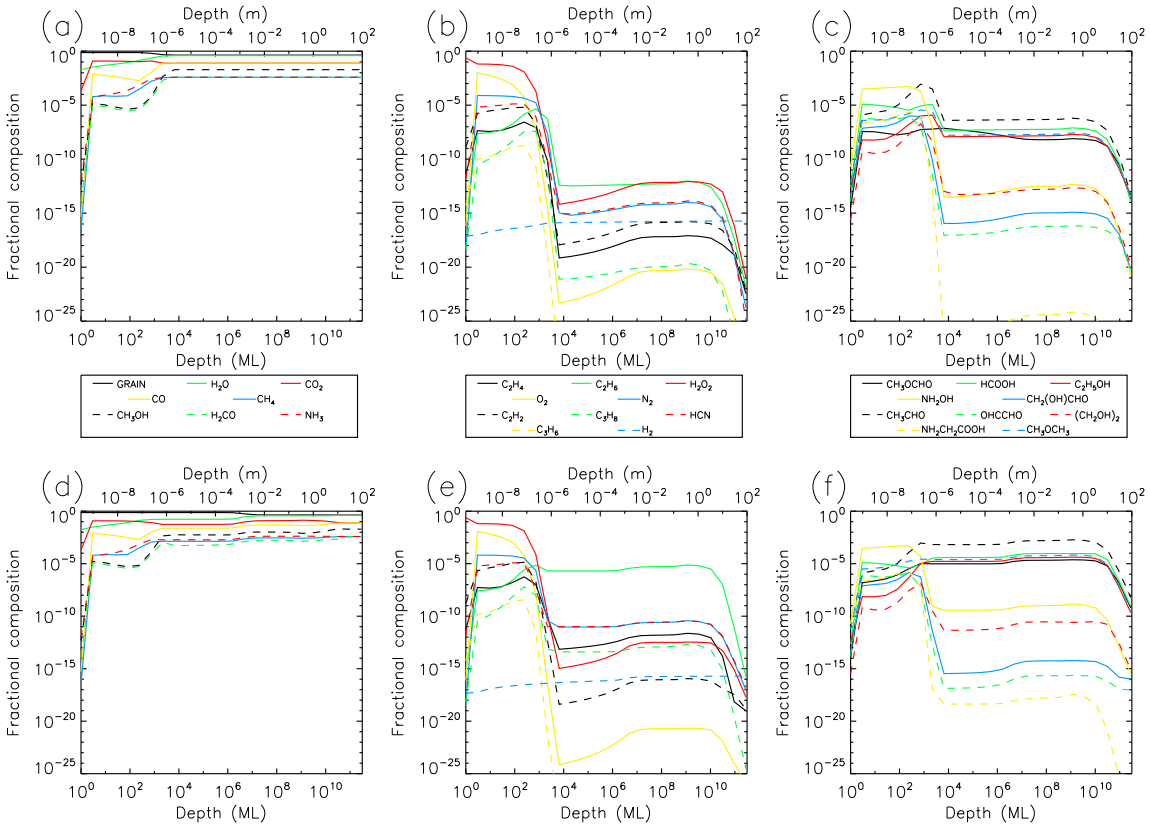

Figure 4.3: Fractional abundances of select ice species for the cold storage of comet 67P with initially *simple* ice abundances; Top: Abundances at 10^6 years. Bottom: Abundances at 4.5×10^9 years. The y-axis of each plot corresponds with the ice surface. The x-axis is the depth, from the surface, in terms of monolayers (ML) shown on the bottom and meters (m) shown on the top. Each column represents a different subset of species grouped based on size and relevance.

The Cold Storage is similar to that done in Paper I. The comet remains in a consistent orbit for 4.5 Gyr. Figs. 4.3 and 4.4 as well as Figs. C.1-C.5 show the abundances at 1 Myr and 4.5 Gyr. The primary difference with Paper I is that this Cold Storage is set to be a Kuiper Belt orbit, due to that being the presumed reservoir for comet 67P. An arbitrary orbital distance of 43.75 AU was used here. In Fig. 4.2, this stage is represented by the outermost circle on the left plot.

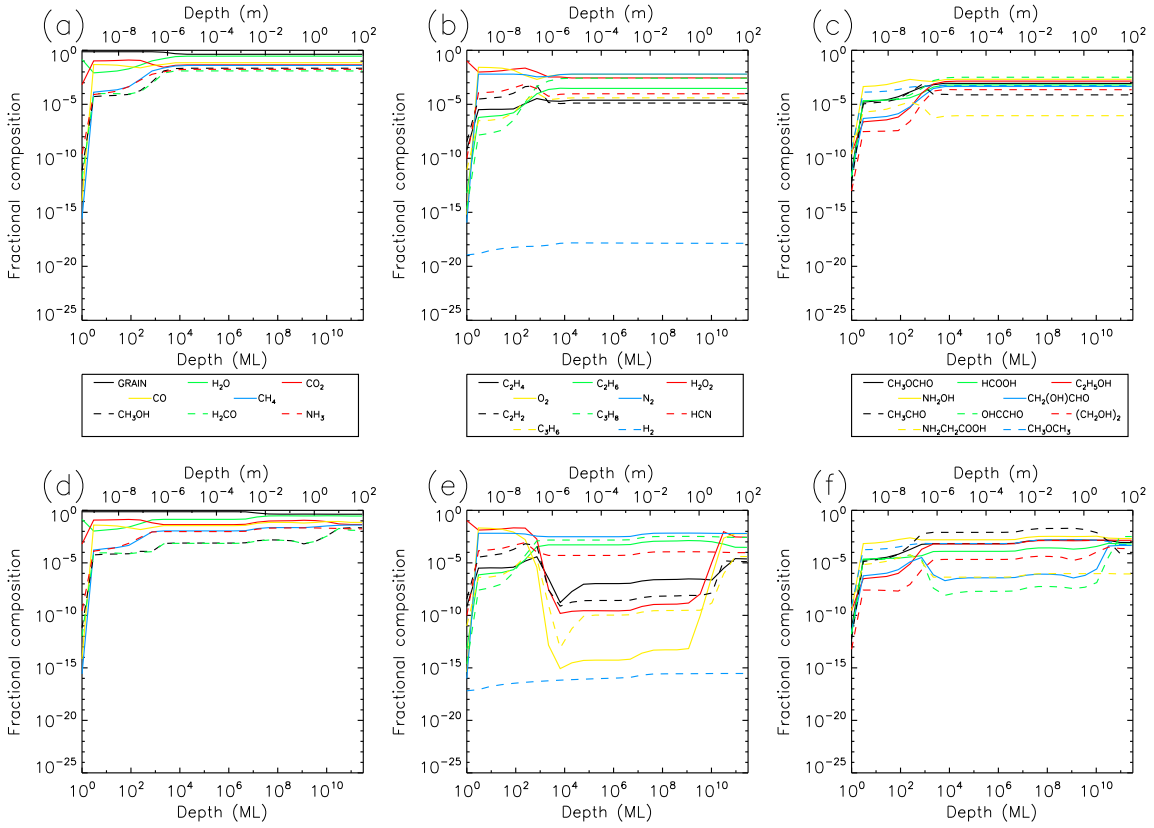

Figure 4.4: Fractional abundances of select ice species for the cold storage of comet 67P with initially *interstellar* ice abundances; Top: Abundances at 10^6 years. Bottom: Abundances at 4.5×10^9 years. The y-axis of each plot corresponds with the ice surface. The x-axis is the depth, from the surface, in terms of monolayers (ML) shown on the bottom and meters (m) shown on the top. Each column represents a different subset of species grouped based on size and relevance.

The first model is shown in Fig. 4.3. By 1 Myr we begin seeing changes in the upper micron of the ice. Of the initial ice species, shown in Set 1, only CO_2 shows an increase in fractional abundance, while the others decrease. Meanwhile, many other more complex species, in Set 2 and Set 3, have already begun to appear in high abundances as well in the upper micron. Most of these species reach from $10^{-}10$ to $10^{-}5$, while H_2O_2, O_2, and NH_2OH are even greater. The exception to the above is the surface layer where most species exhibit a sharp drop in abundance with exceptions being H_2O and H_2O_2. H_2 also does not have a sharp dip at the surface,

however its overall abundance throughout the ice is relatively low. The fraction of grain content also has an increase in this upper micron due to mass loss of ice in the comet. Beyond the micron mark, the Set 1 species show few changes from the initial abundances as noted by their flat profile. Meanwhile, more complex species also exist in lower abundances beyond the micron threshold and exhibit a stepladder-like trend around 1 micron and 10 meters. The deep layer abundances vary wildly between species, but generally the COMs of Set 3 reach higher abundances than the species of Set 2. By 4.5 Gyr, we see very similar trends. Within Set 1, there is still most deviation from the initial abundances, but it is apparent with the increase in fractional abundance of grain material being higher deeper into the ice that more ice has been affected and sublimated. Set 2 looks largely identical to the 1 Myr time-point with the largest difference being a much higher methane (C_2H_6) abundance below the 1 micron threshold. Meanwhile, for Set 3, most species see an increase in abundance below 1 micron, with some even surpassing the upper layer abundances.

The second model is shown in Fig. 4.4. Set 1, both at the 1 Myr time-point and the 4.5 Gyr time-point, is very similar to the first model. Beyond those species is where things begin to diverge. The first and most consistent thing of note for Set 2 and 3 is how all ice species have high abundances at the deepest layers. The abundances in the upper micron are comparable to their counterparts in the first model, but below that depth the difference is drastic. At 1 Myr, those in Set 2 maintain consistent abundances at all depths of the ice. Within the upper micron there is some variance, with some abundances increasing and others decreasing, Set 3 is similar in this way, except that abundances are consistently a bit lower in the upper micron. Once the model reaches 4.5 Gyr, we can see a dip in the range of 1 micron to 10 meters for many species in Set 2 and 3. This dip is largest for unsaturated hydrocarbons as well

as O_2 and H_2O_2. We see similar, albeit smaller, dips in OHCCHO, glycolaldehyde ($CH_2(OH)CHO$), and glycine (NH_2CH_2COOH). On the other hand, acetaldehyde (CH_3CHO) notably increases in abundance within this range. Most other species remain relatively consistent over time.

For the third and fourth models, shown in Figs. C.1 and C.2 respectively, the abundances do not diverge significantly from those in the second model. The same can be said for the fifth model, shown in Fig. C.3, with abundances mostly similar to those in the first model. In all three cases, the largest variance can be seen for some species in the upper 1 micron that have abundances differing by up to an order of magnitude. The sixth and seventh models are similar as well, but most notably they are each nearly identical to the fourth model, with only minor differences barely able to be identified from the figures.

Transition phase

The Transition phase is a new stage of the model incorporated specifically for comet 67P or comets like it. Due to the frequent changes in orbit (e.g. Krolikowska (2003)), much of the distant history of comet 67P is shrouded in uncertainty. We therefore assumed a simple Hohmann transfer directly from our Kuiper Belt orbit directly to the beginning of our active phase approximately 500 years ago. This decision was entirely arbitrary and was based purely on the availability of reliable data. It could be that comet 67P had a much longer active phase or a much more complex transition from cold storage, but taking those considerations would go well beyond the scope of this work. The assumed transition takes approximately 42 years. This phase contains a drastic change in orbital distance, moving from approximately 44 AU to 5 AU. The top panels of Figs. 4.5-4.7 as well as Figs. C.6-C.9 show the abundances at the end

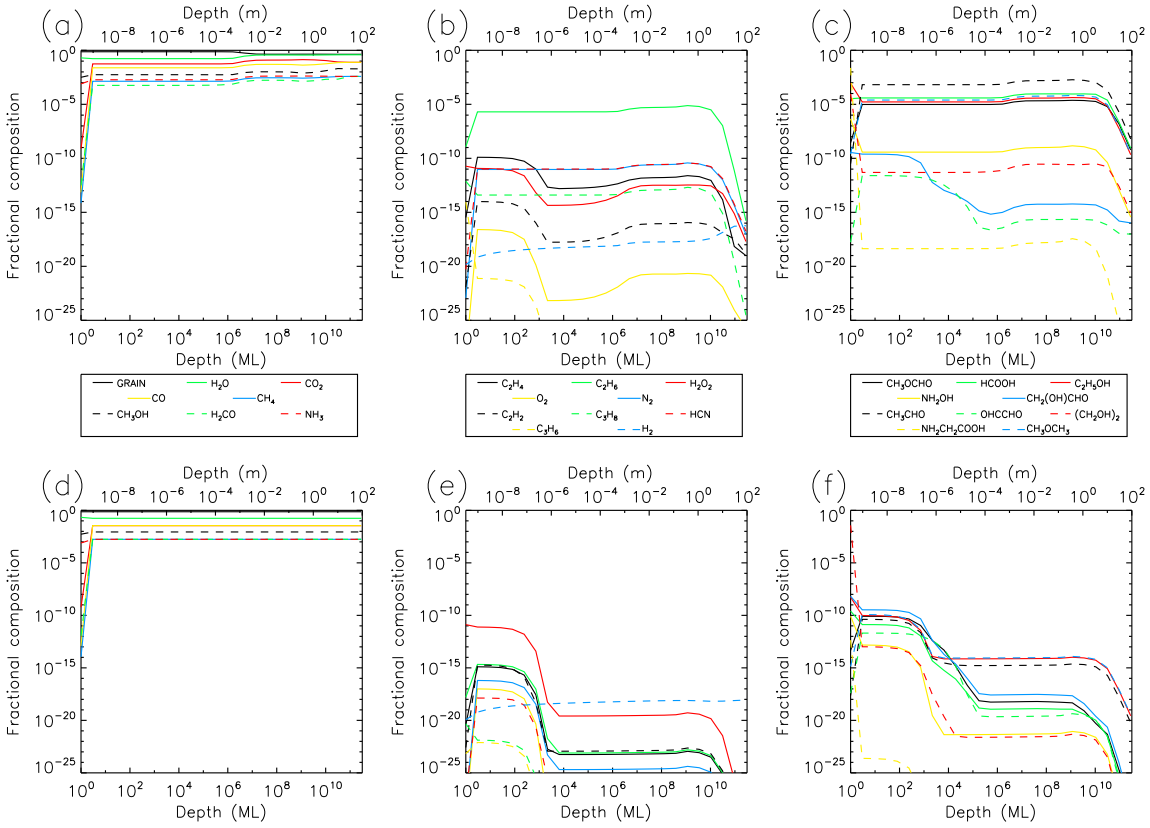

Figure 4.5: Fractional abundances of select ice species for the transition phase (Top) and active phase (Bottom) of comet 67P with initially *simple* ice abundances. The y-axis of each plot corresponds with the ice surface. The x-axis is the depth, from the surface, in terms of monolayers (ML) shown on the bottom and meters (m) shown on the top. Each column represents a different subset of species grouped based on size and relevance.

of this period directly before beginning the Solar Approach phase outlined in §4.3.2. In Fig. 4.2, this stage is represented by the half-ellipse connecting the outer circle to the inner section on the left plot.

The first model is shown in the top panels of Fig. 4.5. The first trend of note is within Set 1, most abundances have flattened out again. While there are some minor fractional differences at different depths, most notably at the 1 mm mark, the values are otherwise similar at all depths. Set 2 shows a marked decrease in the fractional

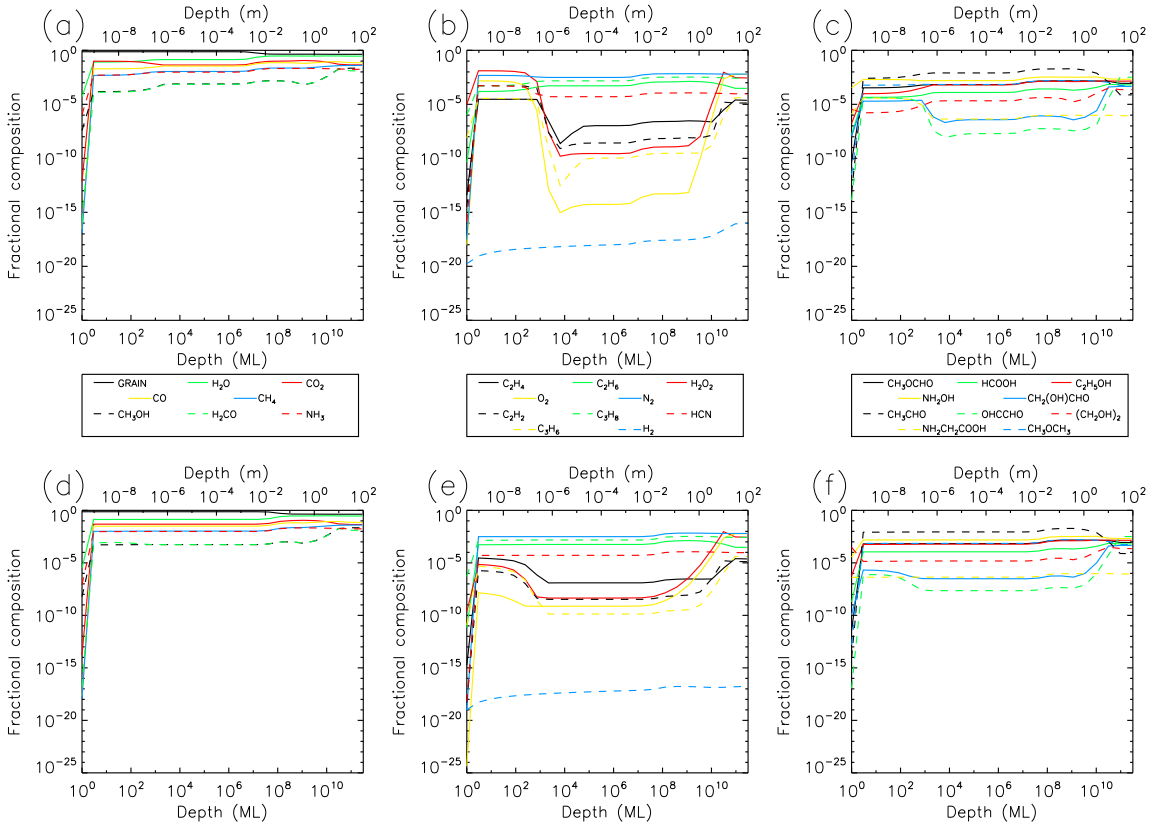

Figure 4.6: Fractional abundances of select ice species for the transition phase (Top) and active phase (Bottom) of comet 67P with initially *interstellar* ice abundances. The y-axis of each plot corresponds with the ice surface. The x-axis is the depth, from the surface, in terms of monolayers (ML) shown on the bottom and meters (m) shown on the top. Each column represents a different subset of species grouped based on size and relevance.

abundances of the upper micron, usually making the abundances of each respective ice species consistent within a few orders of magnitude from the surface to about 10 meters, with most variance being seen in species that already had low abundances. Set 3 is similar, with most of the profiles flattening out and remaining more consistent than those in Set 2. Notably, OHCCHO and glycolaldehyde ($CH_2(OH)CHO$) are exceptions to this and have gradually increasing abundances above 1 mm as you get closer to the surface.

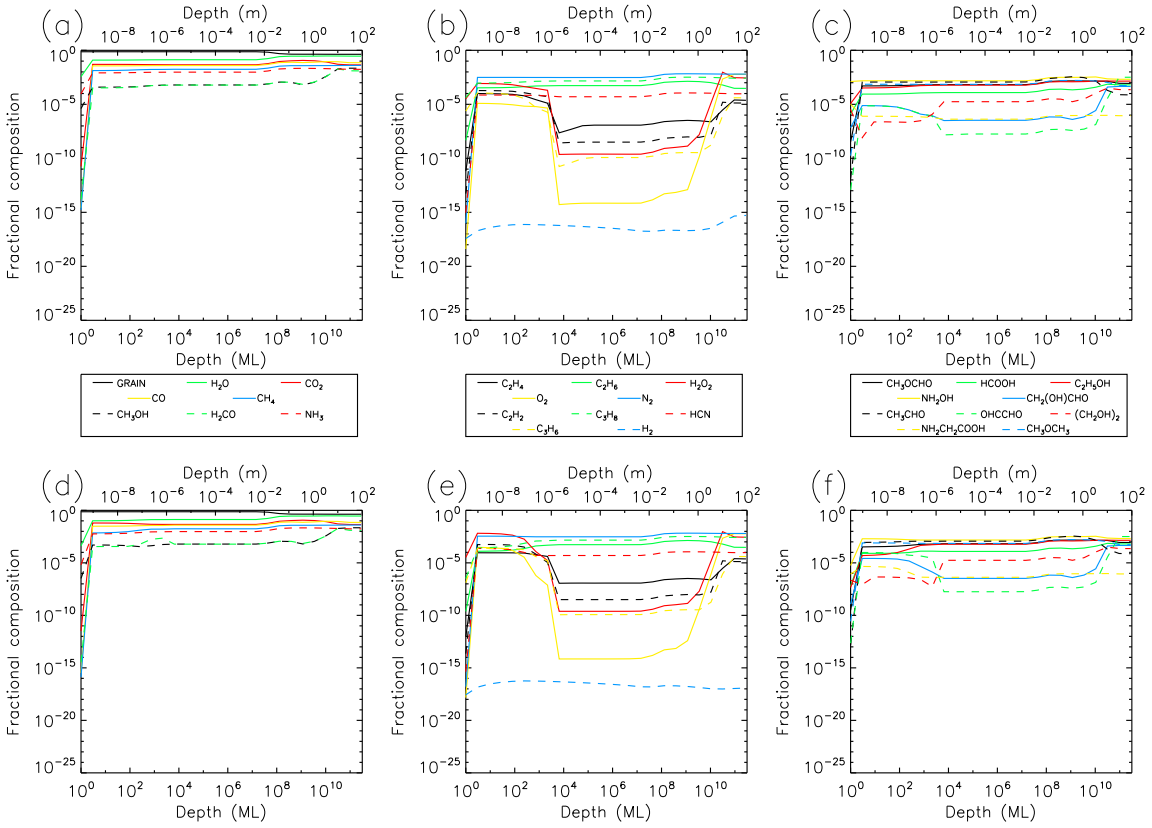

Figure 4.7: Fractional abundances of select ice species for the transition phase (Top) and active phase (Bottom) of comet 67P with initially *interstellar* ice abundances, solar protons and UV, and additional sodium chemistry. The y-axis of each plot corresponds with the ice surface. The x-axis is the depth, from the surface, in terms of monolayers (ML) shown on the bottom and meters (m) shown on the top. Each column represents a different subset of species grouped based on size and relevance.

The second model, shown in the top panels of Fig. 4.6, shows some similar trends. Set 1 has also started to flatten out the profile in the upper micron, leading to a relatively consistent abundance at all depths. For Set 2 and 3, the ice abundances in the upper micron also change. Ice species such as ethane (C_2H_6) and acetaldehyde (CH_3CHO) which had consistently high abundances at depths of 1 micron and below have their upper micron abundances increased to have values similar to lower depths. Meanwhile for species such as H_2O_2 and glycolaldehyde, which had significant dips in abundance below 1 micron, the abundances within the upper micron show slight

decreases.

The third and fourth models, shown in the top panels of Figs. C.6 and C.7 respectively, are once again very similar to the second model, with the primary differences being in the upper micron. Both of these models show a slightly lower fractional abundance here for most species within Set 2 and 3. There is also a much sharper shift at 1 micron within the fourth model most apparent in Set 2. The fifth model, shown in the top panels of Fig. C.8, is also similar to the first model. However, here we see some even more drastic differences limited to the upper micron. The abundances of unsaturated hydrocarbons as well as O_2 and H_2O_2 show significantly higher abundances around five orders of magnitude. OHCCHO, glycolaldehyde (CH_2(OH)CHO), and glycine (NH_2CH_2COOH) also show a couple order of magnitude increase at this depth. Finally, the sixth and seventh models, shown in the top panels of Figs. C.9 and 4.7 respectively, are very similar to the fourth model, with the only notable differences being slightly lower abundances in the upper micron of a few species in Set 2 and 3.

Solar approach phase

The Solar Approach phase is the active phase of the comet. This orbit was much more complex and subject to change, due to it being a JFC, than a long period comet like Hale–Bopp. Therefore, unlike Paper I, each orbit in the Solar Approach is different. Similarly, due to it being a short period comet, we model approximately 50 orbits with periods ranging from around 6-8 years. The perihelion and aphelion distances also periodically change, especially the former. As a result, when presenting results, we opted to show only the endpoint rather than each perihelion and aphelion of each orbit. The bottom panels of Figs. 4.5-4.7 as well as Figs. C.6-C.9 show the

abundances at the end of the active phase of our models, approximately 500 years after the previous stage. In Fig. 4.2, this stage is represented by the innermost section on the left plot and the entirety of the right plot. About 50 years ago, comet 67P had a drastic change in its orbit, resulting in a much closer perihelion that is represented in the inner set of circles.

The first model, shown in the bottom panels of Fig. 4.5, already shows significant deviation from the previous stage. Not only was the upper micron affected, but the abundance of complex molecules has been significantly depleted down to over 10 m. Within Set 1, we can see the flattening of the profile has reached all the way across the plot for all species, meaning the fractional abundances have become uniform throughout the different ice layers. For both Set 2 and Set 3, all species have experienced decreases in abundances, with the most abundant reaching to around $10^{-}10$. Specifically, many COMs as well as H_2O_2 have abundances here, while hydrocarbons, diatomics, and glycine all fall below $10^{-}15$. However, some variation remains. The upper micron tends to have a higher abundance of species in both sets which are reduced again between 1 micron and 10 m.

The second model, shown in the bottom panels of Fig. 4.6, also changes quite a bit from the previous stage, though not to the same degree as the first model. The uniform abundances of species in Set 1 has reached down to 0.1 m. In Set 2, within the upper micron, abundances of O_2, H_2O_2, and unsaturated hydrocarbons has decreased, while their abundances between 1 micron and 10 meters has increased. On the other hand, the remaining species stay fairly consistent. Within Set 3, the abundances maintain their abundances below 1 micron, but they vary in the upper micron. Glycolaldehyde, OHCCHO, and glycine decrease in abundance while most others increase in abundance.

The third and fourth models, shown in the bottom panels of Figs. C.6 and C.7 respectively, are mostly similar to the second model, but with increased abundances of O_2, H_2O_2, unsaturated hydrocarbons, glycolaldehyde, OHCCHO, and glycine in the upper micron and actually only have minor changes from the previous stage in the upper micron. The fifth model, shown in the bottom panels of Fig. C.8, is once again similar to the first model with the exception that within the upper micron abundances of most species within Set 2 and 3 are around five orders of magnitude higher. The values within the upper micron are similar to those from the previous stage. However, the abundances below 1 micron are lower for a few species, such as H_2O_2 and glycolaldehyde, than those in the first model.

The sixth model, shown in the bottom panels of Fig. C.9, is similar to the second model. The upper micron has not changed significantly from the previous stage, but from 1 micron to 10 m the abundances have increased even more drastically than in previous models. Many other species, including those COMs within Set 3, have much flatter, and therefore more consistent, abundances throughout the ice down to 10 m. The seventh model, shown in the bottom panels of Fig. 4.7, is the most different from the other models in how little has changed from the previous stage. Overall, the profiles are strikingly similar to its equivalent at the end of the Transition phase. Some slight deviations are an increase in the upper micron of O_2, H_2O_2, OHCCHO, and HCOOH by around an order of magnitude each.

4.3.3 Comet Hale–Bopp

Here we present new results for comet Hale–Bopp based on the updates and additions made since the work presented in Paper I. Chemical abundances are presented the

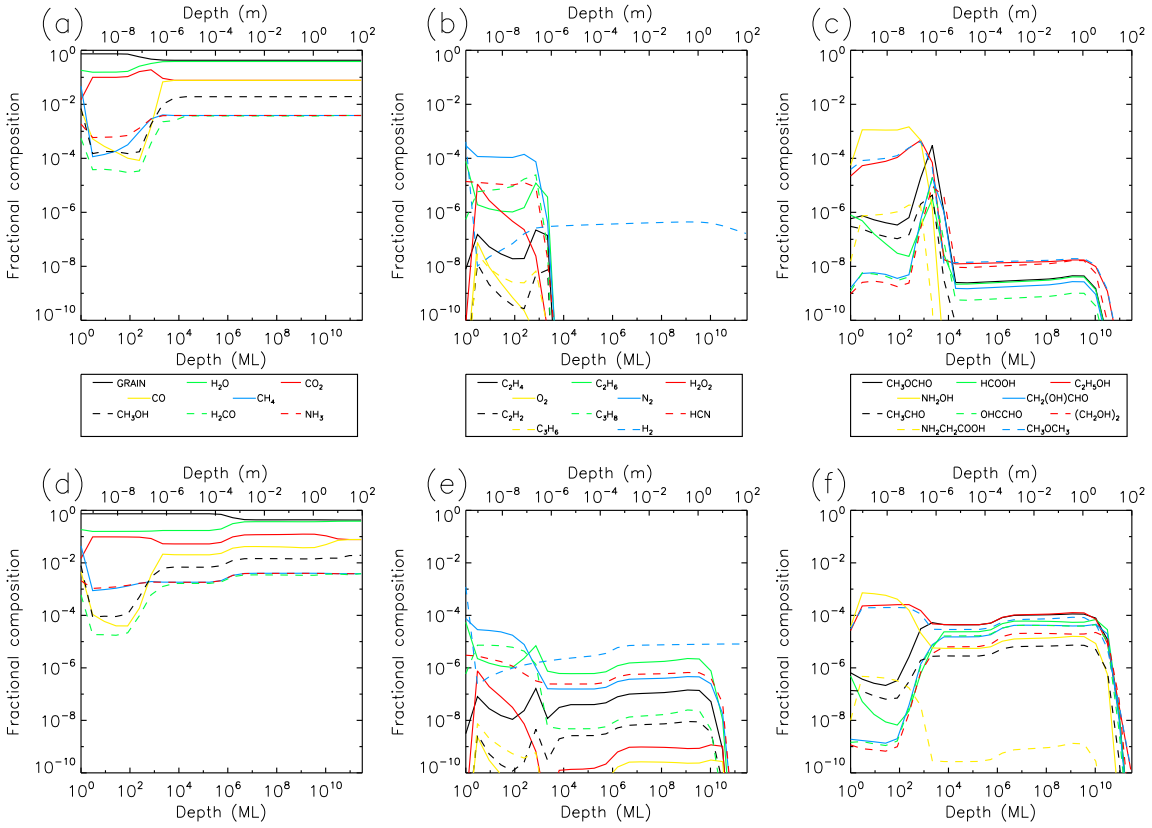

Figure 4.8: Fractional abundances of select ice species for the cold storage of comet Hale–Bopp with initially *simple* ice abundances and solar UV; Top: Abundances at 10^6 years. Bottom: Abundances at 4.5×10^9 years. The y-axis of each plot corresponds with the ice surface. The x-axis is the depth, from the surface, in terms of monolayers (ML) shown on the bottom and meters (m) shown on the top. Each column represents a different subset of species grouped based on size and relevance.

same as those outlined in §4.3.2. In comparison to the seven model types depicted for comet 67P, only three of them were chosen for Hale–Bopp. The first model uses the initially *simple* ice while taking into consideration the solar UV effects. The second model is identical to the first model except is also considers solar protons. The final model is equivalent to the final model for comet 67P and uses the *interstellar* ice with the solar UV and proton effects as well as the additional sodium chemistry. The plots are presented in a similar way to those shown in Paper I, where we depict the Cold Storage abundances at 1 Myr and 4.5 Gyr and then the perihelion and aphelion

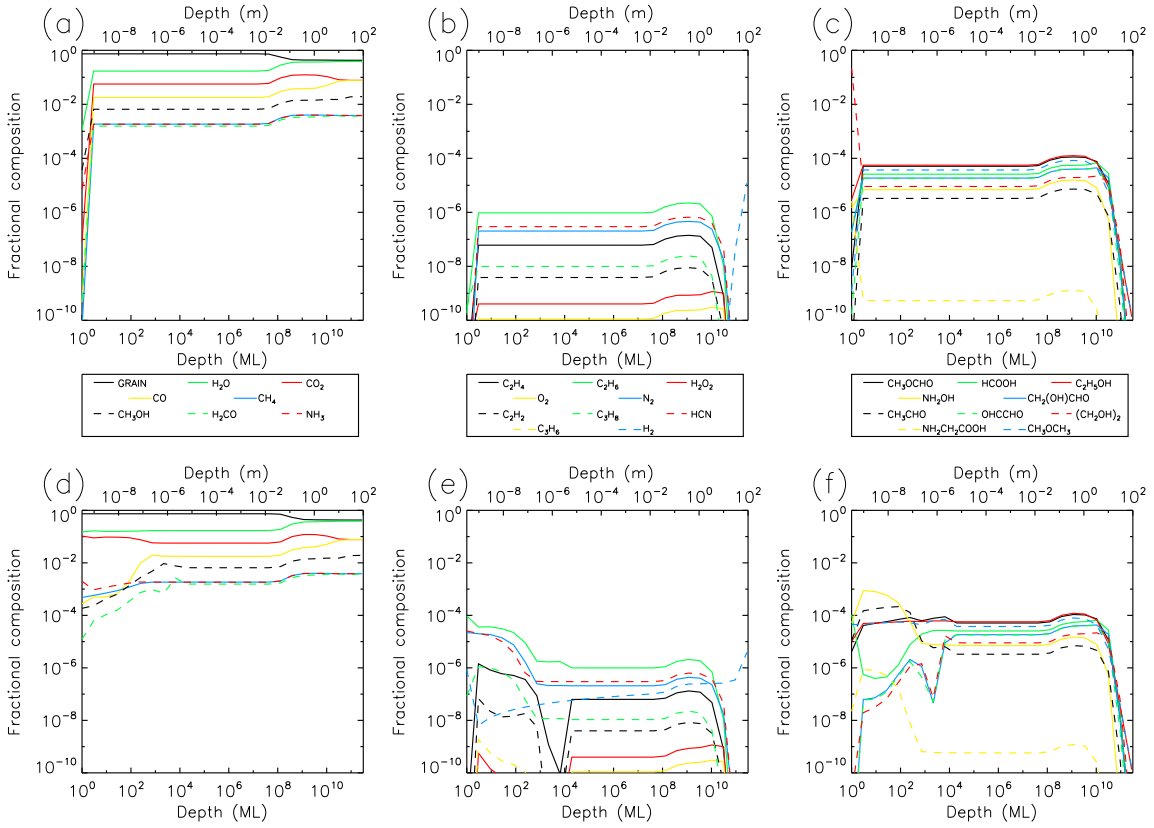

Figure 4.9: Fractional abundances of select ice species for the *first* of five solar approaches of comet Hale–Bopp with initially *simple* ice abundances and solar UV; Top: Abundances at first perihelion. Bottom: Abundances at first aphelion after starting point. The y-axis of each plot corresponds with the ice surface. The x-axis is the depth, from the surface, in terms of monolayers (ML) shown on the bottom and meters (m) shown on the top. Each column represents a different subset of species grouped based on size and relevance.

of the five Solar Approach orbits. As in Paper I, orbits 3 and 4 of the five are not shown due to being similar to the final orbit.

The first model, shown in Figs. 4.8-4.11, and the second model, shown in Figs. 4.12-4.15, both overall have nearly identical abundance profiles to those presented in Paper I. Meanwhile, the third model, shown in Figs. 4.16-4.19, is naturally quite different. Initially, by 1 Myr, the abundance of many species in Set 2 and 3 have dropped significantly within the upper micron while maintaining higher abundances

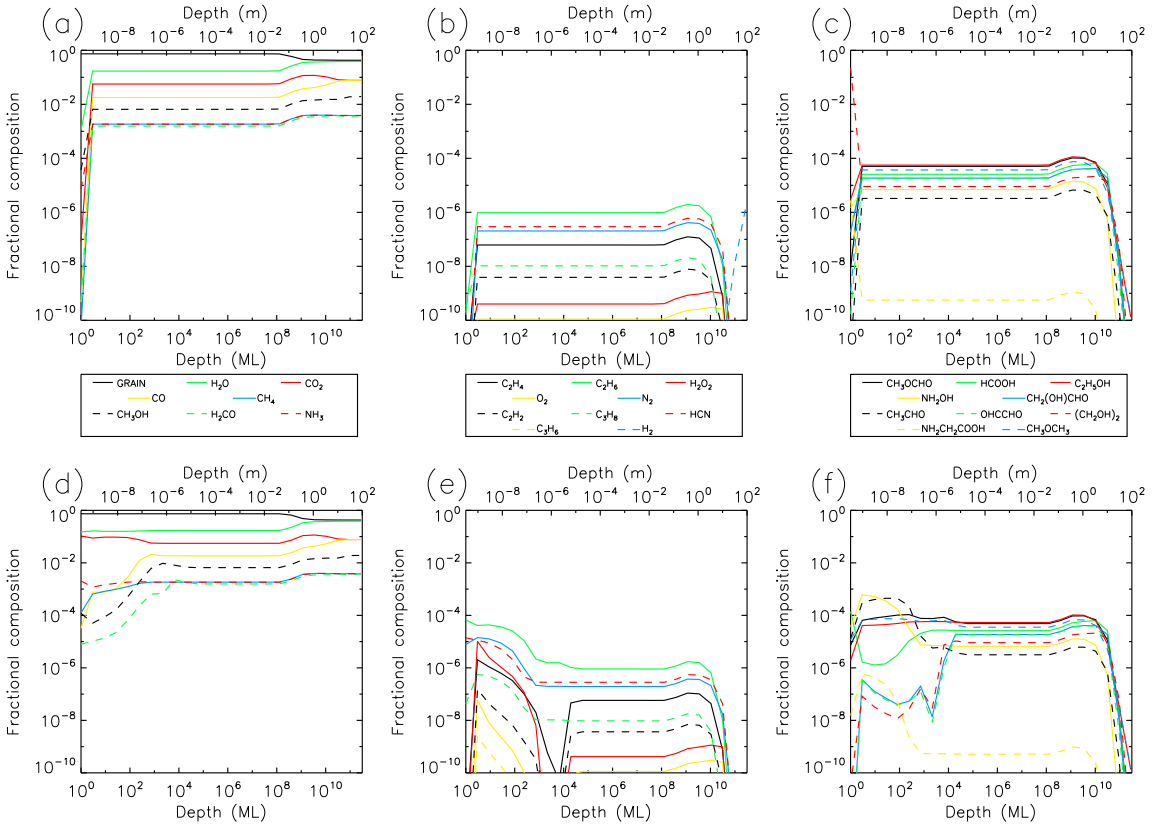

Figure 4.10: Fractional abundances of select ice species for the *second* of five solar approaches of comet Hale–Bopp with initially *simple* ice abundances and solar UV; Top: Abundances at second perihelion. Bottom: Abundances at third aphelion after starting point. The y-axis of each plot corresponds with the ice surface. The x-axis is the depth, from the surface, in terms of monolayers (ML) shown on the bottom and meters (m) shown on the top. Each column represents a different subset of species grouped based on size and relevance.

below. Notable exceptions include N_2, HCN, and NH_2OH. However, by 4.5 Gyr this has changed significantly. While some COMs still decrease in the upper layers of the ice compared to the lower layers, the values of some, such as glycolaldehyde, have increased by two orders of magnitude within the upper micron compared to the previous time-point. Additionally, many of the species within Set 2 have comparatively uniform abundances at all depths by this point. The exceptions to this are HCN, O_2, and H_2O_2. While the fractional abundance within the upper micron reached about

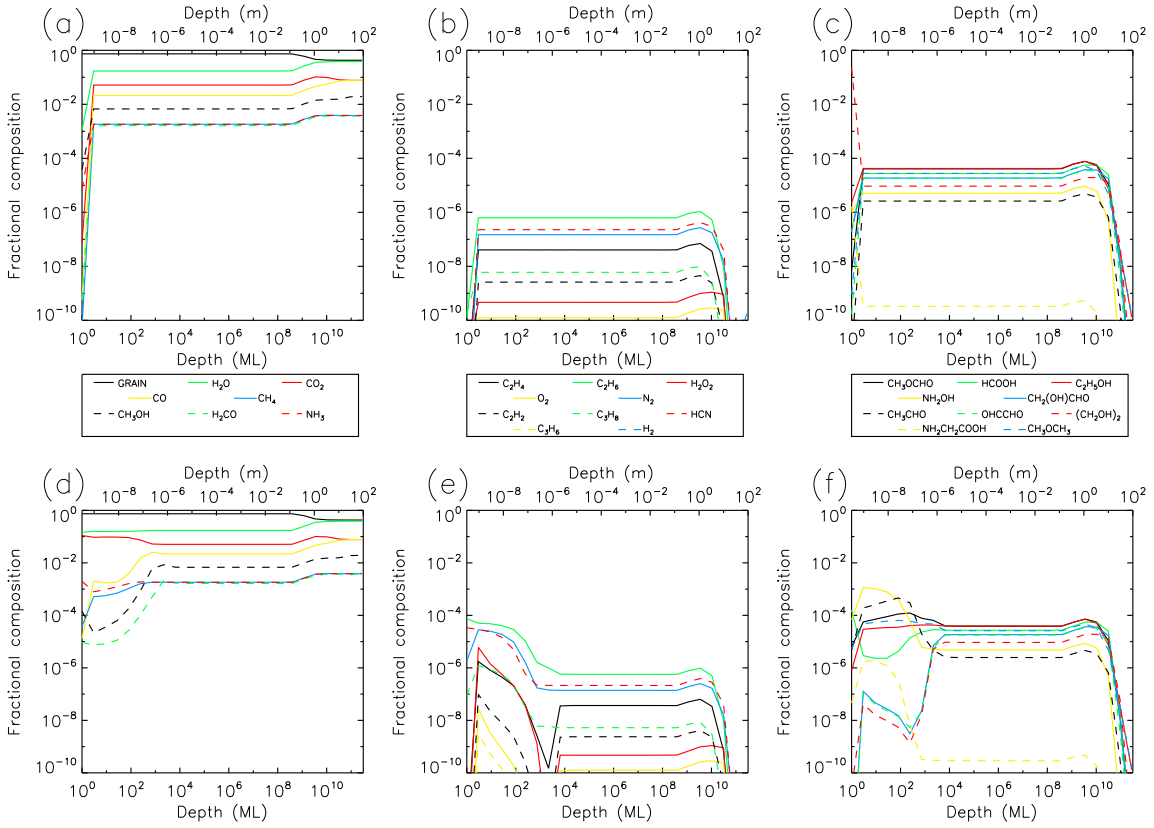

Figure 4.11: Fractional abundances of select ice species for the *fifth* of five solar approaches of comet Hale–Bopp with initially *simple* ice abundances and solar UV; Top: Abundances at fifth perihelion. Bottom: Abundances at fifth aphelion after starting point. The y-axis of each plot corresponds with the ice surface. The x-axis is the depth, from the surface, in terms of monolayers (ML) shown on the bottom and meters (m) shown on the top. Each column represents a different subset of species grouped based on size and relevance.

$10^{-}3$ for HCN and about $10^{-}5$ for the other two with respect to water ice, between 1 micron and 10 m, all three are significantly depleted.

Upon making its first solar approach, the ice below one micron shows only minute changes. However, there are significant changes within the upper micron. During aphelion, most of the ice species within Set 2 and 3 have increased in abundance, the exceptions being C_2H_6, C_3H_6, C_3H_8, and C_2H_5OH. The O_2 and H_2O_2 abundances have also drastically increased by three orders of magnitude. On the other hand,

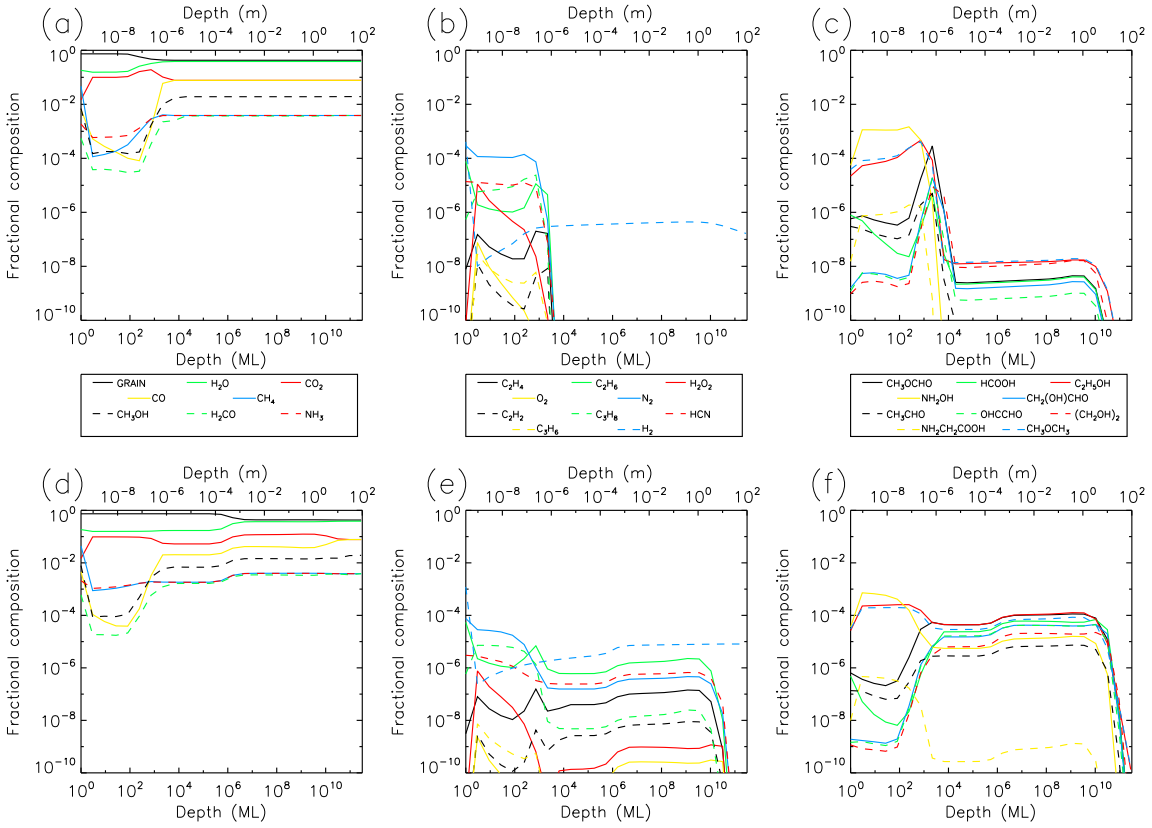

Figure 4.12: Fractional abundances of select ice species for the cold storage of comet Hale–Bopp with initially *simple* ice abundances and solar protons and UV; Top: Abundances at 10^6 years. Bottom: Abundances at 4.5×10^9 years. The y-axis of each plot corresponds with the ice surface. The x-axis is the depth, from the surface, in terms of monolayers (ML) shown on the bottom and meters (m) shown on the top. Each column represents a different subset of species grouped based on size and relevance.

during perihelion, these values are reduced back to approximately $10^{-}4$ for H_2O_2 and $10^{-}7$ for O_2. Meanwhile, the other ice species in Set 2 and 3 increase in abundance in the upper micron at perihelion, matching the abundances below 1 micron. Beyond the first solar approach, we can see that there is not much change even by the fifth solar approach. While the profiles adjust based on heliocentric distance, the first aphelion is very similar to the fifth aphelion, and so on.

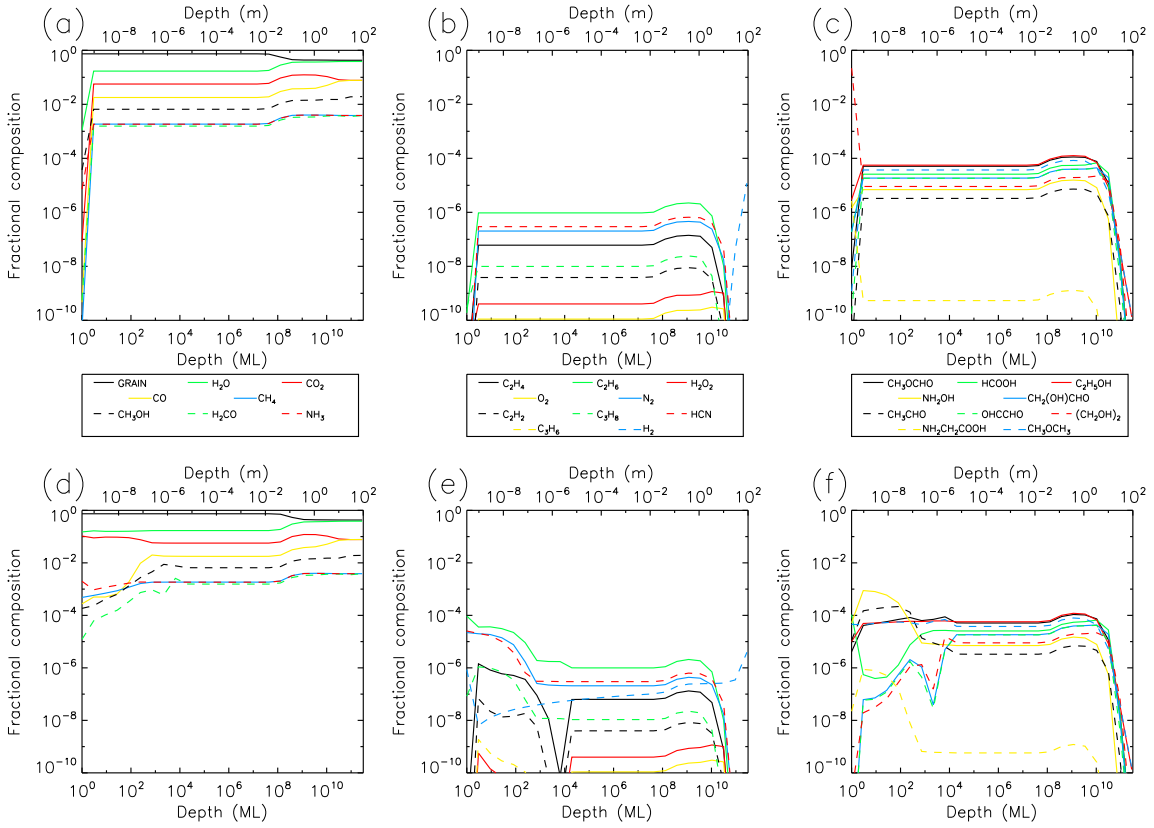

Figure 4.13: Fractional abundances of select ice species for the *first* of five solar approaches of comet Hale–Bopp with initially *simple* ice abundances and solar protons and UV; Top: Abundances at first perihelion. Bottom: Abundances at first aphelion after starting point. The y-axis of each plot corresponds with the ice surface. The x-axis is the depth, from the surface, in terms of monolayers (ML) shown on the bottom and meters (m) shown on the top. Each column represents a different subset of species grouped based on size and relevance.

4.4 Discussion

When considering the validity of the model results, it is important to discuss the assumptions made of the comets orbit. Comet 67P was first observed in 1969 following a notable perturbation in its orbit. There are no direct observations of the comet prior to this time. Calculations mapping back the orbit prior to discovery can initially be quite reliable, but will quickly deteriorate the farther back we try to project. This is

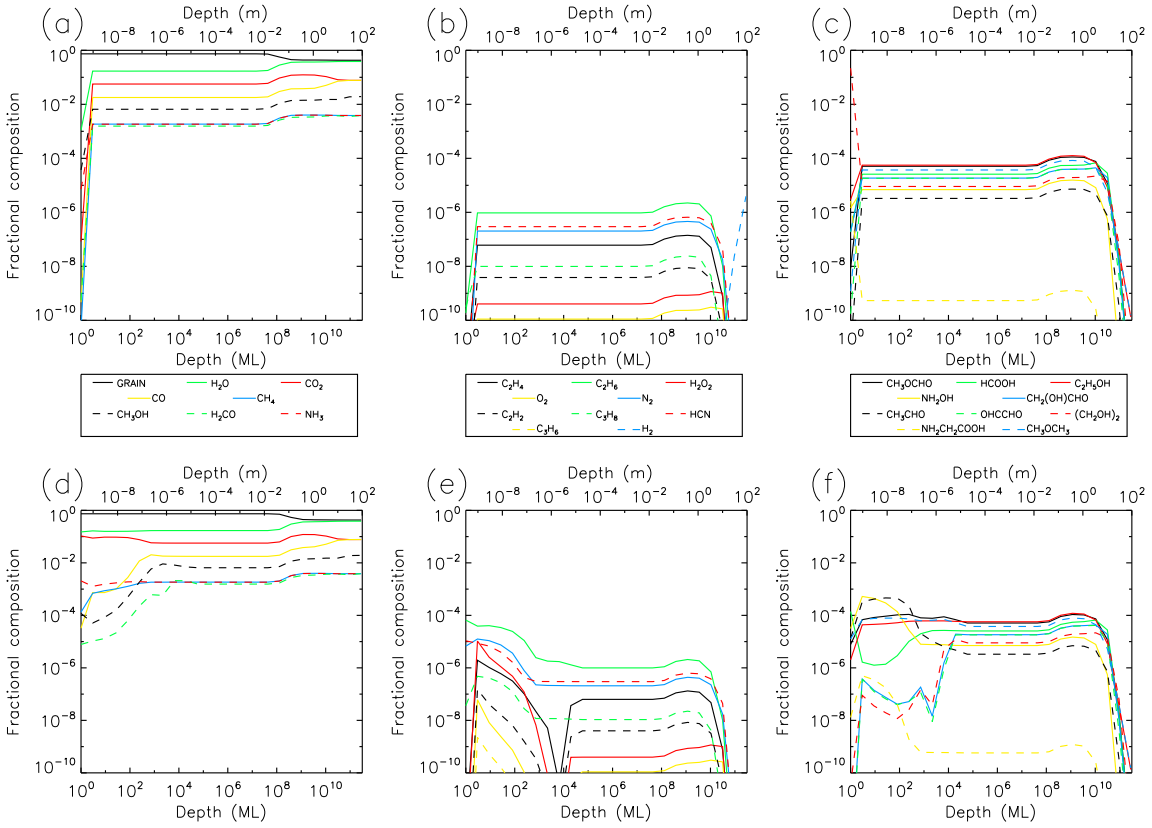

Figure 4.14: Fractional abundances of select ice species for the *second* of five solar approaches of comet Hale–Bopp with initially *simple* ice abundances and solar protons and UV; Top: Abundances at second perihelion. Bottom: Abundances at third aphelion after starting point. The y-axis of each plot corresponds with the ice surface. The x-axis is the depth, from the surface, in terms of monolayers (ML) shown on the bottom and meters (m) shown on the top. Each column represents a different subset of species grouped based on size and relevance.

especially true for a JPC like Comet 67P, as the frequent interactions with Jupiter have caused numerous shifts in its orbital parameters over a relatively short period of time. It is for this reason that current predictions beyond roughly 500 years in the past are largely unreliable.

As a result, this work made the assumption that immediately before this time, Comet 67P was in the Kuiper Belt and in a single orbit moved to the predicted orbit 500 years ago. While it is within the realm of possibility that this is exactly

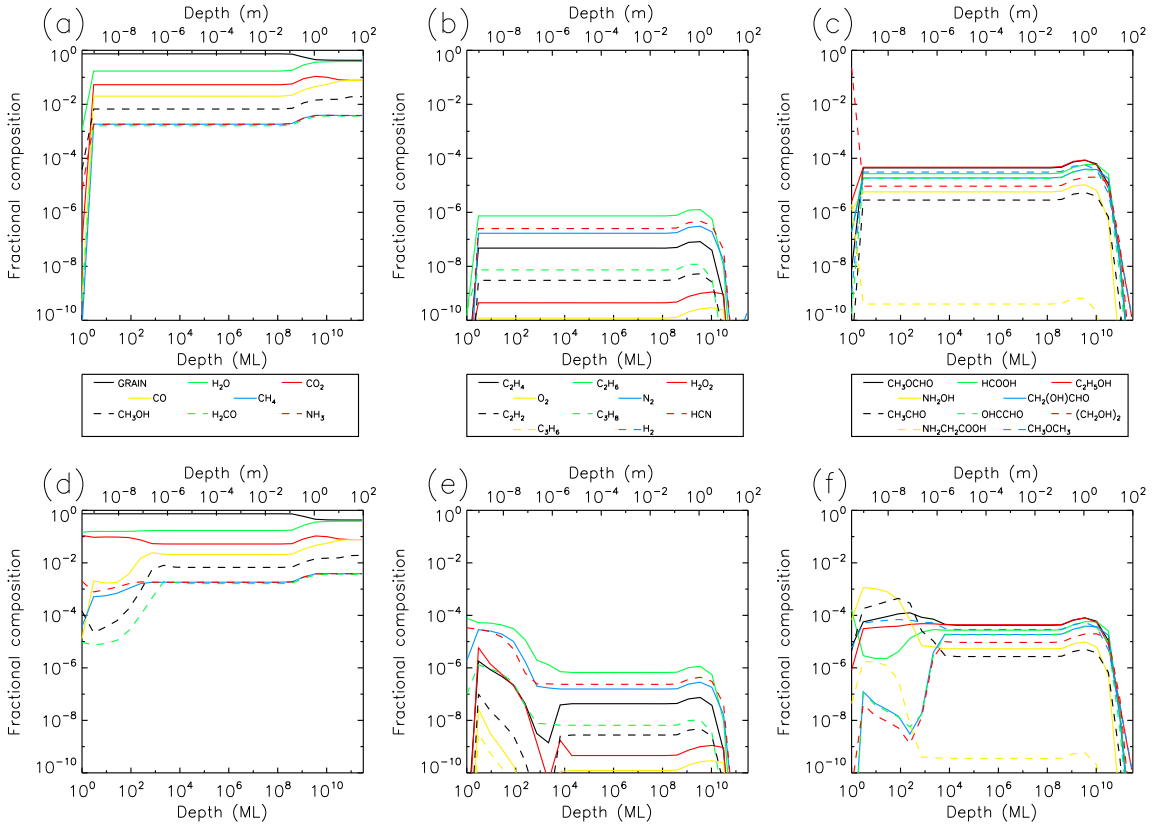

Figure 4.15: Fractional abundances of select ice species for the *fifth* of five solar approaches of comet Hale–Bopp with initially *simple* ice abundances and solar protons and UV; Top: Abundances at fifth perihelion. Bottom: Abundances at fifth aphelion after starting point. The y-axis of each plot corresponds with the ice surface. The x-axis is the depth, from the surface, in terms of monolayers (ML) shown on the bottom and meters (m) shown on the top. Each column represents a different subset of species grouped based on size and relevance.

what happened, there are any number of ways in which the comet could realistically have gotten there. Rather than an immediate shift, Comet 67P could have slowly shifted its orbit inward over a long period of time, gradually pushed further into the inner solar system by gravitational perturbations of the gas giants. That is to say nothing of where within the Kuiper Belt it could have been during its cold storage. The temperature of a comet in the Kuiper Belt could notably vary depending on its composition from as much as ∼30 to 60 K, potentially having a significant impact

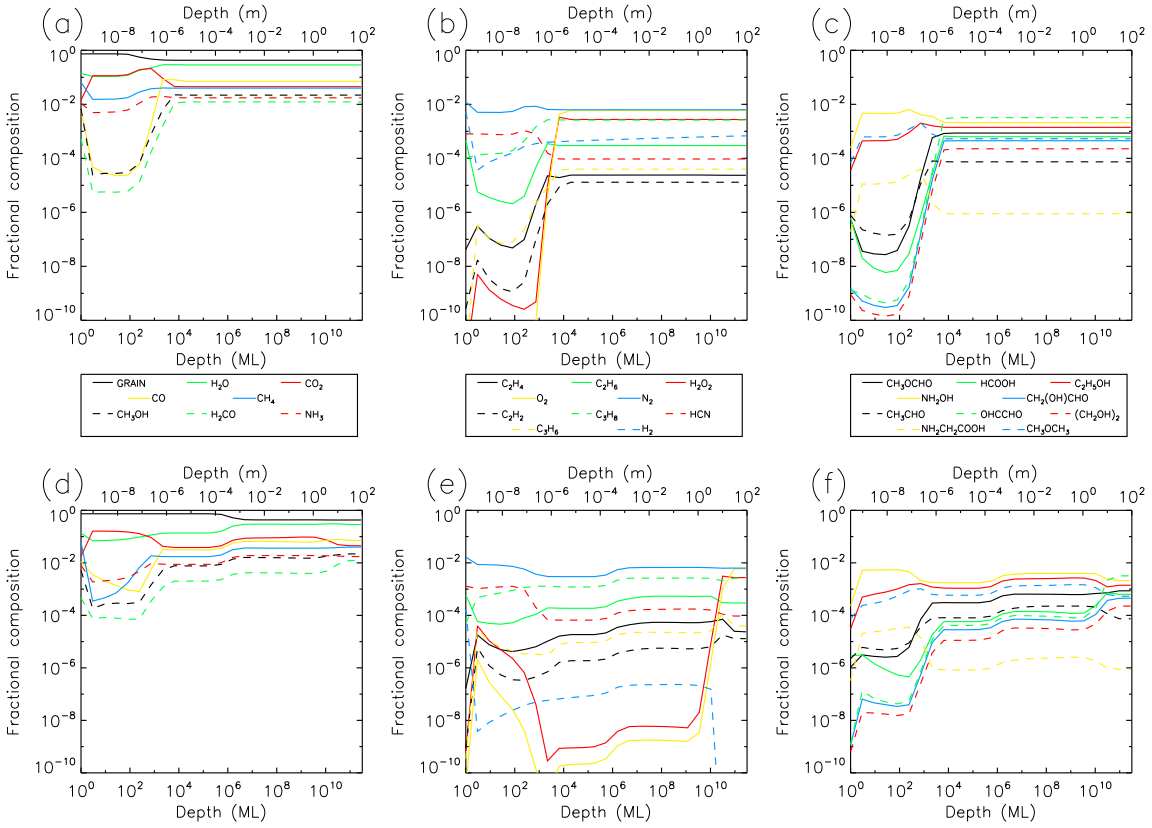

Figure 4.16: Fractional abundances of select ice species for the cold storage of comet Hale–Bopp with initially *interstellar* ice abundances, solar protons and UV, and additional sodium chemistry; Top: Abundances at 10^6 years. Bottom: Abundances at 4.5×10^9 years. The y-axis of each plot corresponds with the ice surface. The x-axis is the depth, from the surface, in terms of monolayers (ML) shown on the bottom and meters (m) shown on the top. Each column represents a different subset of species grouped based on size and relevance.

on the cold storage ice processing. Ultimately, there is little we can say about what Comet 67P actually experienced prior to this time for certain.

However, as a result of using direct calculations of orbital positions, as opposed to static orbital parameters as in Paper I, the resulting changes over the past ∼500 years should retain their credibility. On top of this, if we consider the expected mass loss per orbit as quoted by Vincent et al. (2021) and by all versions of our current model for Comet 67P, it may not be unreasonable to say that whatever journey the

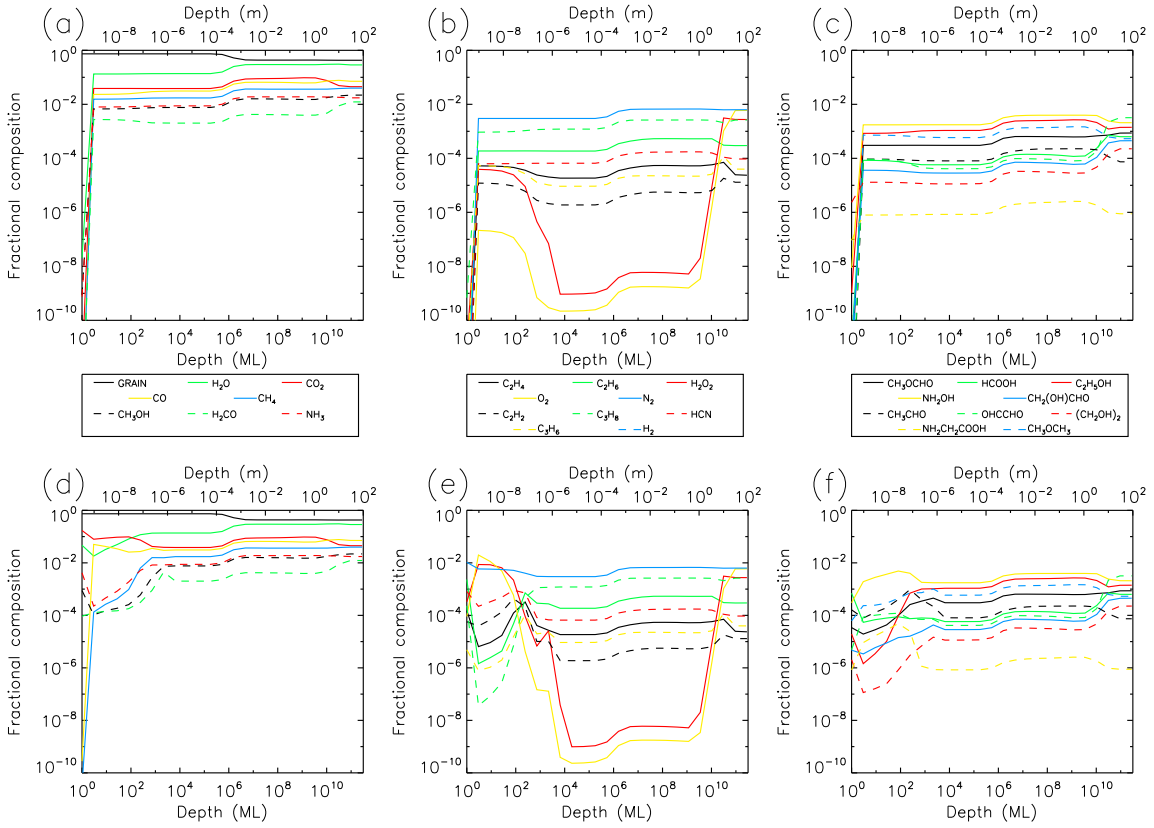

Figure 4.17: Fractional abundances of select ice species for the *first* of five solar approaches of comet Hale–Bopp with initially *interstellar* ice abundances, solar protons and UV, and additional sodium chemistry; Top: Abundances at first perihelion. Bottom: Abundances at first aphelion after starting point. The y-axis of each plot corresponds with the ice surface. The x-axis is the depth, from the surface, in terms of monolayers (ML) shown on the bottom and meters (m) shown on the top. Each column represents a different subset of species grouped based on size and relevance.

comet made from the Kuiper Belt to the projected position may not actually have a strong impact on the comet today.

4.4.1 Effects of UV and High Energy Protons

Like in Paper I, interstellar UV and GCRs have a significant impact on the chemistry and chemical makeup of the ice. While the UV penetrates to a depth of approximately

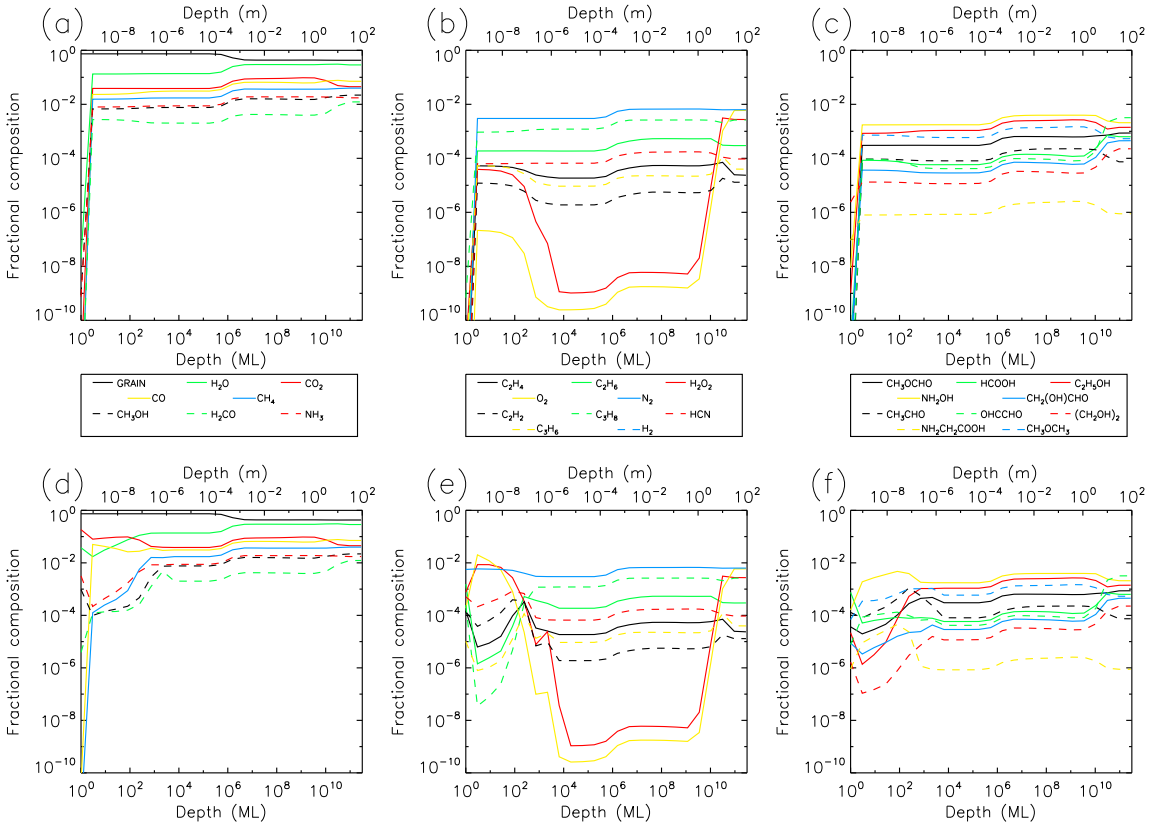

Figure 4.18: Fractional abundances of select ice species for the *second* of five solar approaches of comet Hale–Bopp with initially *interstellar* ice abundances, solar protons and UV, and additional sodium chemistry; Top: Abundances at second perihelion. Bottom: Abundances at third aphelion after starting point. The y-axis of each plot corresponds with the ice surface. The x-axis is the depth, from the surface, in terms of monolayers (ML) shown on the bottom and meters (m) shown on the top. Each column represents a different subset of species grouped based on size and relevance.

1 micron in significant doses before rapidly falling off, the GCRs reach down to ∼15 m. This ends up creating certain thresholds or regimes in the ice that are somewhat obvious in the various plots in §4.3.

What was not included in Paper I was the similar effects originating from the sun. Due to the much longer period of Comet Hale-Bopp, the effects were deemed negligible in that case. For a JFC like Comet 67P, this was not necessarily a valid assumption. Therefore, a component tracing the additional UV provided by the sun as

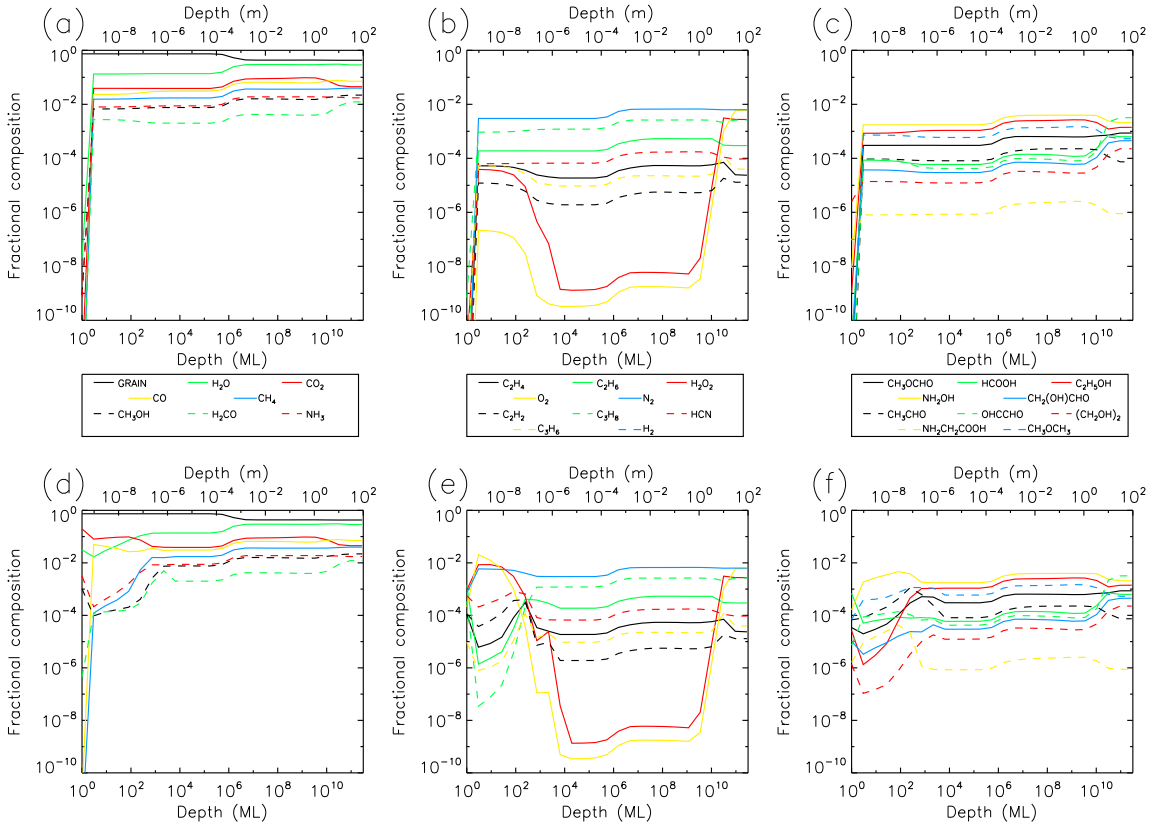

Figure 4.19: Fractional abundances of select ice species for the *fifth* of five solar approaches of comet Hale–Bopp with initially *interstellar* ice abundances, solar protons and UV, and additional sodium chemistry; Top: Abundances at fifth perihelion. Bottom: Abundances at fifth aphelion after starting point. The y-axis of each plot corresponds with the ice surface. The x-axis is the depth, from the surface, in terms of monolayers (ML) shown on the bottom and meters (m) shown on the top. Each column represents a different subset of species grouped based on size and relevance.

well as additional high energy protons from the sun was added to the model. Each of these components naturally were adjusted to change with heliocentric distance. While the solar UV addition could simply be added to the interstellar UV component, the same could not be done for the solar protons to the GCRs. Most solar protons would not reach the same high energies as the GCRs assumed for this model and therefore would not penetrate as deep into the comet. Measurements by Cooper et al. (2003) indicated that solar protons would only have a significant impact approximately on

the upper 1 micron. Therefore, somewhat coincidentally, we retain the same two thresholds at 1 micron and 15 m as before.

While the solar UV and solar proton components become largely negligible compared to the interstellar UV beyond ∼10 AU, they reach comparable or even higher values than the interstellar UV component at the closest perihelions. If we strictly consider the effects of these components on the chemical abundances, the addition of solar UV and solar protons overall has a minor but noticeable effect on the composition. However, even if we were to ignore the effects of solar protons, it would have a largely negligible effect on the results. If we consider the mass loss rates outlined in detail in §4.3.1, it is shown that the comet experiences a significant amount of mass loss. While the mass loss rate at around 5 AU and beyond is generally low enough that the production rate in the upper layers of other molecular species can outpace the mass loss, once the comet moves farther inwards, somewhere from 5–3 AU, the mass loss will spike, and eject more than 1 micron worth of mass.

As a result, any buildup of material caused by interstellar UV, solar UV, and solar protons, would have largely been lost by the time of our first observations in 1969, or shortly thereafter. Therefore, any long term effect observable in the modern day would be from far reaching effects such as the GCRs. As the GCR component does not depend on heliocentric distance, it therefore becomes largely irrelevant exactly what path Comet 67P took coming from the Kuiper Belt to its current position. Though if we were to have observed it several hundred years ago before it moved much closer to the sun, this may not have necessarily held true.

4.4.2 Initial Ice Composition

It is important to examine the importance of the initial ice abundance on the chemistry of the comet. In this work, two different initial ice compositions were modeled for these comets: a *simple* ice and an *interstellar* ice. In previous iterations of the model, a *simple* ice was implemented for ease of use. The breakdown of the initial ice compositions is shown in Fig. 4.1 with the "other" category only present in the *interstellar* ice composed of some definite combination of 266 other ice species not listed in the figure, but present in the model. Additional atoms not present in the *simple* ice such as Na are also included here.

Overall, the *interstellar* ice resulted in a very different composition than the *simple*. To begin with, the *interstellar* ice already begins with some significant fraction of COMs or other larger ice components. This seems to compound with the formation of new large ice species during the cold storage phase, resulting in higher abundances. As well, since the ice already starts with some amount of these larger ice species at every layer in the ice, anything lost as a result of mass loss is only replenished from deeper layers. For the *simple* ice on the other hand, any complexity formed in the upper layers, once lost, is only replaced with other simpler components. This becomes especially evident in the gap between the two thresholds of 1 micron and 15 m, where some ice species become depleted due to destruction caused by GCRs. Once the comet reaches the later stages of the active phase and experiences significant mass loss, the ice from the reservoir below the 15 m threshold begins to increase the abundances of those species above 15 m.

The initial complexity does not only serve to replenish lost material with fresh complex material, but also to increase retention. The *interstellar* ice model that

includes the solar UV and solar proton components (and the models before that) showed a significantly reduced mass loss rate than that of the *simple* ice models. Closer examination revealed a significant buildup on Na, NaH, and NaOH in the upper layers. This resulted in a blockage which significantly slowed the mass loss at the later stages of the solar approach. These sodium species had slowly been building up as a result of previous mass loss without being desorbed from the surface themselves. To test the importance of the sodium component specifically, a version of the *interstellar* ice model was run that had no sodium component. The result was a higher mass loss rate than before, but still had significantly reduced mass loss compared to the *simple* ice models. Instead, the other remaining large molecules, specifically larger hydrocarbon chains, served a very similar role to the sodium species. As a result, it would seem that while the sodium species served to limit the mass loss, it was not unique. Further modeling was done with a slightly more rigorous set of parameters for sodium species, resulting in the final model which restricted the mass loss further still.

The *simple* ice models were not able to build up this layer for a variety of reasons. First of all, there was no sodium component at any stage. The *simple* ice models never had any sodium to begin with, and therefore it was unable to help limit mass loss. However, as we have shown, sodium is not the only component to the blockage. It was also other larger hydrocarbons that helped create a surface blockage. So, the *simple* ice models were unable to build up a significant enough layer to protect the lower layers of the ice. This could be a result of the initial composition of the *interstellar* ice having significant enough abundances of larger ice species that the layer could form, or it could be that even when the more complex ices were lost in the upper layers, that since they were spread throughout the ice in the *interstellar* ice

model, that they could replace any lost material, while the *simple* ice model, which had very little complexity in the lower layers, could not.

4.4.3 Comparison of 67P

Drozdovskaya et al. (2019) made comparisons of observed bulk ice abundances within Comet 67P and compared them to interstellar ice abundances. The work found a notable similarity in abundances of ice species and when on to state that it was likely that comets inherit their ices directly from the interstellar or presolar phases, thus retaining complexity. The comparisons between both *simple* ice models and *interstellar* ice models allow us to test if it is necessary for interstellar inheritance or if the comet is able to retain abundances.

The two *simple* ice versions of the model experience large mass loss rates well above the supposed maximum. The great mass loss rate along with the initially simple ice results in all complexity being quickly expelled from the comet surface. This results in *simple* ice models being unable to replicate observed bulk ice abundances within Comet 67P. On the other hand, the five *interstellar* ice versions of the model had a much lower mass loss rate which falls below the expected maximum. This along with its already higher initial abundance and its ability to supply the upper layers with pristine ice should it lose any is significant. The upper layers of a comet may be significantly processed during the cold storage phase, but the active phase sheds some of those ice layers, revealing the more pristine ice.

Among the *interstellar* ice models, the addition of solar UV into the model had a relatively small but likely significant effect on the ice composition. The addition of solar protons added on top of that only had a small and hardly noticeable effect.

However, this is only in the context of both being applied to the same model. Ultimately, it would seem that solar protons would be negligible, however, they actually have a similar impact on the ice abundances as the solar UV. However, the two of them together makes it less noticeable. It could therefore be reasonable to ignore one component, either the solar UV or solar protons, if necessity dictated, but for a short period comet like Comet 67P, they should not generally be ignored.

The two models testing the importance of sodium chemistry and surface blockage, models six and seven, display an interesting effect on the ice. As previously mentioned, the initial complexity of the ice will slow any mass loss as the larger, non-volatiles accumulate on the surface. This occurs with or without the presence of sodium. Regardless, the *interstellar* ice models were the only ones to display this behavior.

Within these models, the oxygen abundances are specifically worth noting. Here, we combine the abundances of O_2 and H_2O_2, as the conversion ratio between the two has not been well constrained within the model. If we take this combined abundance to be our molecular oxygen abundance, then the *simple* ice model, having lost all its complexity, cannot come close to matching observational data. The *interstellar* ice model, on the other hand, begins to approach that expected value. Among the *interstellar* ice models, the one with the best fit to the upper layer molecular oxygen abundances is with the seventh model, which includes the additional solar UV and protons as well as better constrained sodium chemistry and a very limited mass loss.

Another factor that could fill in for the role that the sodium and other non-volatiles are playing on the surface is a dust layer. A certain amount of dusty material lacking in ice is expected to have built up on cometary surfaces. However, this model does not currently have the ability to model such effects or the effects of dust loss. It is possible then that a sufficiently built up dust layer might limit mass loss rates

enough to allow *simple* ice models to replicate certain COM abundances. However, this is left for future studies.

4.4.4 Comparison of Hale–Bopp

Models were run for Comet Hale-Bopp in addition to the ones for Comet 67P so as to compare results directly with those in Paper I. Three versions of the model, in line with some of those used for Comet 67P, were used. The first model tested the effects of adding the solar UV component to the model, while the second model additionally added the solar proton component. Both of these models used the *simple* ice for the initial abundance. The third and final model used the *interstellar* ice for the initial abundance along with the solar UV and proton components, as well as adjusted sodium chemistry.

The first two models ultimately have only marginal effects on the abundances and show little change from the results shown in Paper I. This further supports the assumption made that the solar UV and proton components could be ignored, made in Paper I. The third model, on the other hand, displayed significant deviations. This is similar to the results for Comet 67P and therefore somewhat expected. The initially more complex ice of the *interstellar* ice model caused a different result. The more complex species are resupplied from the reservoir below the ice layers and also slows mass loss in the top layers.

Likely as a result of those same conditions is the higher overall abundance of COMs, hydrocarbons, and significant levels of O_2 and H_2O_2. This is especially prevalent near perihelion where mass loss will have dropped significantly and where the ice may replenish some complexity in the upper layers. Another thing of note is how the

third model adjusts to the environment quicker than in previous versions. Results from Paper I showed that the abundance profiles remained relatively similar for similar time points following the second orbit. During the first two orbits, the comet was affected more drastically as it adjusted to the new physical parameters. However, in this new model, only the first orbit is notably different. The second orbit and beyond are now more similar to one another.

4.5 Conclusion

The model, *MAGICKAL* presented here represents the first cometary ice chemistry model which has been used to model Comet 67P/Churyumov–Gerasimenko. The model has been updated with additional capabilities necessary to model more complex orbits such as those of JFC like Comet 67P. Additional other factors also needed to be considered, such as the solar UV and solar protons, which were previously ignored. Short period comets spend much longer periods of time closer to the sun, and it was therefore no longer a valid assumption to ignore them.

Additional models tested the effect of varying the initial set of abundances by taking an initially *simple* ice, composed of a small set of small molecules, versus an ice inherited directly from an interstellar cloud model which already had some level of complexity. The results show that drastic mass loss rates from *simple* ice models do not allow for a sustainable complex ice mantle on Comet 67P. On the other hand, an initially *interstellar* ice model results in an early blockage of the upper ice layers, which significantly slows mass loss. Mass lost from the upper layers will only be replaced with pristine ice from below, so while mass lost in the *simple* ice model can only be replaced with simple ice species, the *interstellar* ice model can always be

replenished with complex species.

While the cold storage phase can largely serve to increase the complexity of cometary ices within the upper layers, the active phase is mostly a destructive phase. A comet like Comet 67p getting much closer than 5 AU will result in mass loss rates which exceed any production rates within the ice. Much of the material built up during the cold storage will eventually become stripped away, leaving only pristine ice behind. This ultimately should lend credence to the idea that the cometary ice was directly inherited from the interstellar source, as by the modern day, as those upper layers of ice will have likely long been stripped away.

Chapter Acknowledgements

This work was funded by the NASA Emerging Worlds Program, grant no. NNX17AE23G.
DAC thanks the NASA FINESST program for a graduate fellowship grant no. 80NSSC22K1328.

Chapter 5

Comet Chemistry with Extrasolar Events

5.1 Introduction

Comets are balls of ice and dust that formed along with the solar system. Following this, they spend millions to billions of year within the outer solar system, typically in the Kuiper Belt (Kuiper, 1951) or the Oort Cloud (Oort, 1950). The Kuiper Belt rests roughly from the orbit of Neptune (∼30 au) out to an outer radius of ∼50 au and has temperatures averaging ∼40 K (Hsieh and Jewitt, 2006). The Oort Cloud is somewhat more mysterious in its size. Typically it is assumed to have an inner radius of 3000 au, while its outer radius ranges somewhere from 50,000 au (Hsieh and Jewitt, 2006) to as much as 200,000 au (Duncan et al., 1987). As a result, the Oort Cloud has average temperatures of ∼10 K but can be as little as ∼5 K. It is for this reason that comets are considered as having pristine sources of ice. That is to say, the ices are minimally processed and thus are representative of the conditions of the early solar system.

Therefore, comets are prime targets of study not only for themselves but as windows into the solar systems past. Complex organic molecules (COMs) have also been detected in the comae of comets (e.g. Balsiger et al., 2007; Altwegg et al., 2016) in-

cluding the amino acid glycine. Comet 67P/Churyumov–Gerasimenko is one of the most well studied comets. It is a short period comet originating from the Kuiper Belt but is currently a Jupiter Family Comet (JFC) with an orbital period of 6-8 years. The ROSETTA mission launched in 2004 eventually made its way to the comets, becoming both the first to orbit and land on a comet. This mission resulted in a wealth of data, which is one of the reasons why this remains one of the most well studied comets. Various cometary models have also studied the chemistry in depth, both in the coma (e.g. Irvine et al., 1998) and the mantle (Chapter 4).

Comet Hale–Bopp is another well studied comet. Compared to comet 67P, it instead originates from the Oort Cloud and is a long period comet, with a current orbital period of ∼4400 years. While unlike Comet 67P there has not been a landing, there are many observational studies that have detected molecules in the coma (e.g. Bockelée-Morvan et al., 2000; Crovisier et al., 2004). Similarly, there have been computational studies for Hale–Bopp as well (Willis et al., 2024).

Despite the claim that comets are pristine, they are not chemically inert. Even the Oort Cloud has conditions sufficient for some amount of hydrogen diffusion among the ice. In addition, the surface is constantly irradiated by the interstellar UV field as well as galactic cosmic rays (GCRs). Gronoff et al. (2020) and Maggiolo et al. (2020) performed experimental studies examining the effects of GCRs on cometary ices. On top of this, a comet may enter an active phase, being perturbed from its cold storage orbit (such as the Kuiper Belt or the Oort Cloud) and moving much closer to the sun. This will naturally heat the comet and subject it to solar UV and high energy protons. Any of this can result in processing of the ice material to make it less pristine than it otherwise would be. However, the inner portions of the ice, beyond where the GCRs can penetrate, will likely remain mostly pristine.

Aside from this, certain external factors could also lead to further processing during the cold storage phase. Oort Cloud comets are typically perturbed into the inner solar system by gravitational influences outside the solar system such as passing stars. These same passing stars may be close enough to heat and irradiate portions of or the entire Oort Cloud. Statistical studies have predicted that at least one Type O star has passed within 5 parsecs of the solar system within the past 4 Gyrs, and an even higher likelihood for B and A type stars (Stern, 2003). Such encounters could potentially heat up the surfaces of Oort Cloud comets from its usual 5 K up to 30 K (Stern and Shull, 1988). On top of that, encounters with stars are relatively long, sometimes lasting on the order of hundreds of thousands of years, depending on the distance, speed, and size. This therefore leaves plenty of time for the star to affect the Oort Cloud comets.

Nearby supernovae are another source of external heating and irradiation. Within the past thousand years, at least four bright supernovae originating within our galaxy have been well documented: SN 1006, SN 1054, SN 1574, and SN 1604 (Hanslmeier, 2017). Stern (2003) predicted that approximately 30 supernova events have occurred within 20 pc of the solar system in the past 4 Gyr. Such events could have similarly heated the surfaces of Oort Cloud comets up to 60 K at each instance. While each individual supernova event is much more energetic than a passing hot star, they are also much shorter, usually lasting on the order of months. Therefore, while supernovae events will be much more drastic in heating the surface, the event duration of passing hot stars allows for heating much deeper into the ice. Supernovae and supernova remnants are major sources of energetic particles and photons (Bell, 1978; Kobayashi et al., 2004; Hillas, 2005), so in addition to the thermal heating produced by these events, the cosmic ray flux should also be augmented by additional energetic particles

during these events.

The chemical kinetics model *MAGICKAL* (Model for Astrophysical Gas and Ice Chemical Kinetics And Layering) was first presented in Garrod (2013a) and was used to model hot cores. In Garrod (2019) it was adapted to modeling cometary ices. Using the *MAGICKAL* model, we attempt to model the chemical effects that passing hot stars and nearby supernovae might have on cometary ices during cold storage as well as how well any changes are retained over time. §5.2 describes the additions to the physical and chemical models, including both general model capabilities and the ability to model hot stars and supernovae. §5.3 presents the results of passing hot star event and supernova event simulations, as well as our chemical model results. §5.4 examines physical and chemical effects on the comet compared to an unaffected comet as well as how well such effects are retained, followed by conclusions in §5.5.

5.2 Methods

The model used here builds off the work presented in Chapters 3 and 4. Here, we use the chemical kinetics model *MAGICKAL* for cometary ices originally presented in Garrod (2019) with various updates (see Jin and Garrod, 2020; Garrod et al., 2022; Willis et al., 2024) to the reaction mechanism, bulk diffusion, and the implementation of an active phase, among other things. Work from Chapter 4 also worked to fill in previous gaps by using a more complex starting ice as well as adding in a solar UV factor and a solar proton factor. The model used is the same as that presented in Chapter 4 unless otherwise noted, but the basic parameters will be outlined here.

A cometary ice is constructed by taking some initial abundances of ice species with an appropriate dust fraction determined at the start of the model. The initial

ice composition used is the same as the *interstellar* ice shown in Chapter 4. This set of fractional abundances is then distributed into 25 chemically distinct layers. Each layer is set up such that the topmost layer is one monolayer thick and each layer below that is three times thicker than the last. This results in an ice with a total thickness of ∼136 m. Below the bottom layer is a chemically inert reservoir composed of ice material with an identical fractional makeup as the initial ice. This reservoir therefore remains 'pristine' throughout all stages of the model. Here, pristine is taken to mean it is unaltered from when the comet was originally formed. Only atomic and molecular hydrogen are allowed to diffuse within the bulk layers. However, ice material may be lost into the gas phase. In this case, for the sake of the model, ice material is assumed to move up into the layer above such that the space is again filled. The layer fractional abundances are then recalculated such that the layer sizes remain the same. In this instance, when material is pulled from the reservoir below the bottom layer, the bulk ice may be replenished with pristine ice material, and leaves the reservoir unaffected.

5.2.1 Dust layer build-up and erosion

In our previous models, the dust grains initially present in the ice could become concentrated in the upper layers, due to ice loss through thermal and non-thermal desorption. The dust grains themselves were trapped within the structure, and the dust component of the upper layers of the comet could not exceed some maximum fractional value ($F_{\rm gr,max} \simeq 74\%$, based on Gauss' formula for close packing of identical spheres).

Here, we have implemented an adjustment to this treatment that allows (i) the

build-up of an outer layer, beyond the upper layer of ice/dust, composed purely of porous dust, and (ii) the erosion of this dust layer due to gas drag from sublimating molecules, especially during the solar approach phase when evaporative losses are high. This development is especially valuable because a large fraction of the mass-loss measured in comets is comprised of dust presumed to be lost in this way. Jewitt and Matthews (1999) found the dust mass-loss rate to be > 5 times larger than the mass-loss rate of water for Comet Hale-Bopp.

To achieve aspect (i), when desorption of icy material from the upper comet layer occurs, a fraction of the dust material (by volume) in that layer is considered to leave that surface layer of mixed ice and dust, to form part of a new outer dust layer that is contiguous with the ice-dust surface layer. The fraction that leaves is proportional to the fractional dust composition in the upper layer; if the dust composition in the upper ice-dust layer is at its maximum ($F_{\mathrm{gr,max}}$), dust leaves at the same proportional rate as the ice material. If the dust makes up less than its maximum value, the dust loss is scaled down by this amount.

The outer dust layer is assumed to be composed of closely packed grains, hence dust makes up $\sim$74% of the volume of this layer, with the rest being open void through which desorbing molecules may escape. The total amount of dust in this dust layer is tracked, allowing its thickness to be determined based on the assumed close packing of the grains.

The dust layer also contributes to the absorption of the impinging UV flux, thus as the dust gradually builds up, it helps to diminish the rates of photodissociation in the upper ice-dust layers. Its thickness is also considered in the depth of penetration of the solar protons, so that the ices are completely shielded from solar proton-driven dissociation once an outer dust layer of thickness 1 μ has built up.

Aspect (ii) of this dust-layer treatment involves its erosion by repetitive collisions of desorbing atoms and molecules. We assume that the process of dust loss occurs grain by grain, rather than atom by atom. To determine a rate, we consider that a grain is lost to space once enough mechanical work has been done on that grain. The amount of work required is based on its total binding energy with the contiguous grains to which it is bound by van der Waals interactions. This value may be arrived at by multiplying the pairwise atomic binding between dust-grain atoms by the number of atoms that are in contact with atoms in other grains. Taking a canonical value of 1 million surface atoms for a 0.1 μm radius grain, we estimate 10^4 surface atoms, or 1% of the total are bound to other grain atoms.

5.2.2 Passing Hot Stars and Nearby Supernovae

In order to simulate the effects of a passing hot star or a supernova on the chemistry of cometary ice, it was decided to simulate situations that would have the greatest effect. From there, it can be determined whether these events will significantly impact the composition of a comet and from there determine the maximum degree. The comet was first set far out in the Oort Cloud at 5×10^4 AU and allowed to evolve for 10^6 years. This distance is chosen in part to ensure that the comet remains outside of heliopause which may inhibit certain external effects. The comet then undergoes the event, either a passing hot star or a nearby supernova, and is then allowed to evolve again over 4.2×10^9 years to determine the retention of these events.

The passing star was set up as an O-type star. The star radius was set to be $15R_\odot$ and the surface temperature was set as 50,000 K. A minimum distance of 1 parsec from the comet was taken. An average star velocity of 30 kms^{-1} relative to the solar

system was used (taken from Stern and Shull, 1988) along with an encounter time of 5×10^5 years. The star was set to move perpendicular to the comet such that the midpoint (i.e. 2.5×10^5 years) would be its closest point to the comet, which was 1 pc in this case. Any point before and after this event period is assumed to be too far away to have any effect. The comet temperature and the UV flux from the star was calculated at each time point. Assuming the hot star is a perfect blackbody, a factor of $\sim 3.05 \times 10^2$ was calculated for the UV intensity of the hot star at 1 AU relative to the interstellar UV field. This factor was then scaled with distance to find the UV flux.

The supernova was set up to be a generic Type II-P supernova. The peak bolometric luminosity was taken to be $10^{44} ergs^{-1}$. The supernova is first assumed to exponentially rapidly ramp up from eight orders of magnitude below its maximum up to its maximum luminosity over a period of 80 days. Following this, there is a gradual decrease over the next several months and years, decreasing in absolute magnitude by 0.0075 $magday^{-1}$ (Doggett and Branch, 1985). This decrease continues for 10^3 years before being assumed as zero. In this case, the supernova is assumed to happen and remain at 10 pc from the comet. Treating the supernova explosion as a perfect blackbody, a factor of $\sim 2.58 \times 10^7$ was calculated for the UV intensity of the supernova at 1 AU relative to the interstellar UV field. This was then scaled out to 10 pc and then scaled based on the exponential increase and decay along with the luminosity, though it initially ramps up from fifteen orders of magnitude below the maximum to have a smooth transition from no additional UV to the addition of the supernova.

An additional factor taking into account the increase in the CR flux was also considered. For the purposes of the model, we ignore any delay in the arrival time

of the CRs and assume they arrive at the same time as the UV photons. Cosmic rays initially trapped in supernova remnants are initially trapped by the magnetic field. As the field expands, more cosmic rays are released starting from the highest energy (e.g. R. et al., 2020). Here, for simplicity, we assume that the total energy flux of the additional cosmic rays remains the same over a period of 10^5 years after the supernova explosion, as the number of CRs will increase with decreasing particle energy. Meaning that initially there will be fewer but higher energy particles, which gradually progresses to more but lower energy particles. We initially assume that the CR flux ramps up the same way as the luminosity, and after 10^5 years it will exponentially decay at the same rate before being assumed as zero. We assume that 10% of the total supernova shock energy is converted into CRs, where the total shock energy is taken to be 10^{51} ergs.

5.3 Results

First, we will discuss the features of the initial model including starting conditions and abundances. Then we will discuss model results which exclude hot stars and supernovae. Following this, model results for the hot star event will be shown and compared to the comet without the event. Next, the model results for the supernova event will be discussed and similarly compared to the comet without the event. Finally, we will briefly discuss the findings and interpretation in §5.4.

The first thing to notice within Fig 5.1 is the nearly horizontal line for each chemical species below ∼1 micron. This is representative of the initial abundances within *each* model at all ice layers. By this point, the upper micron has diverged from the initial values. Of the species listed, most have decreased in fractional abundance

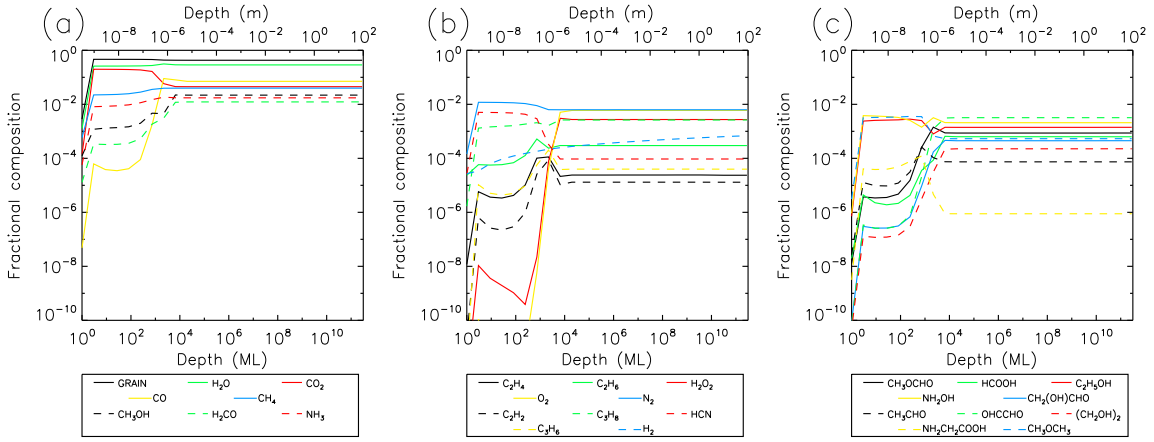

Figure 5.1: Fractional abundances of select ice species for a generic Oort Cloud comet cold storage at 10^6 years. The y-axis of each plot corresponds with the ice surface. The x-axis is the depth, from the surface, in terms of monolayers (ML) shown on the bottom and meters (m) shown on the top. Each column represents a different subset of species grouped based on size and relevance.

by this time from their initial values. Exceptions include, CO_2, N_2, HCN, CH_3OCH_3, and glycine (NH_2CH_2COOH) which have increased. Others such as C_2H_5OH and NH_2OH have remained largely the same or slightly increased, while H_2O has slightly decreased. On top of this, the grain content has started to increase near the surface. This is a result of the gradual mass loss of ice, allowing for dust grains to build up.

Once we get to Fig. 5.2, we can see another drastic change. Within the next 1 Myr, the ice abundances do not reach into the upper micron. This is an indication of a 1 micron thick dust layer that has covered the surface of the comet. Below this threshold, there is still some deviations in the upper layer ice composition. However, it is not until 4.5 Gyr that effects in the lower layers start to appear. Molecular hydrogen is the only exception to this, as it is almost linearly decreasing as it approaches the surface even at 1 Myr. By the endpoint, many of the upper layer abundances exhibit similar trends as before. O_2 and H_2O_2 are notable exceptions, as they have a significant drop initially and around 10^{-4} m, but then rise up significantly near the

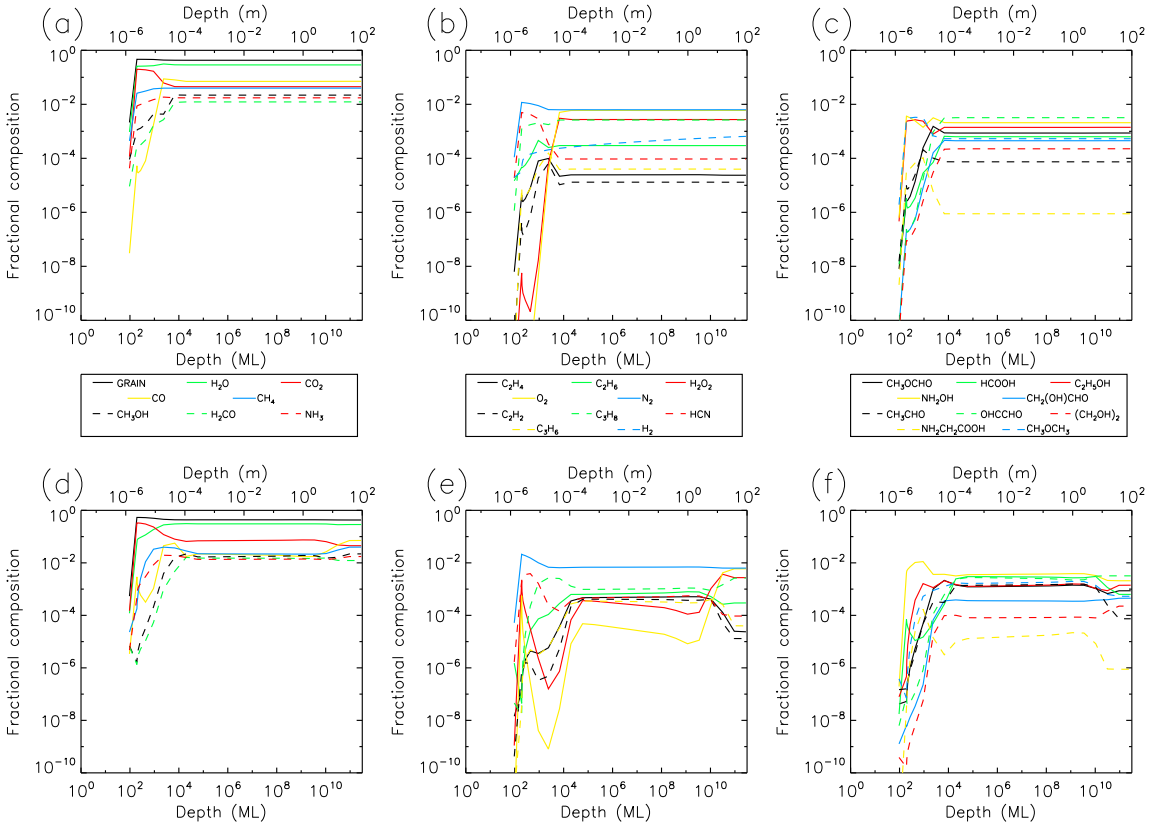

Figure 5.2: Fractional abundances of select ice species for a generic Oort Cloud comet during cold storage WITHOUT encountering a passing hot star or nearby supernova. Top: Top: Abundances at 10^6 years. Bottom: Abundances at 4.5×10^9 years. The y-axis of each plot corresponds with the ice surface. The x-axis is the depth, from the surface, in terms of monolayers (ML) shown on the bottom and meters (m) shown on the top. Each column represents a different subset of species grouped based on size and relevance.

top. Looking deeper into the ice as well indicates that these two species have been somewhat depleted over time throughout the whole ice, not just near the surface. Glycine as well, has an increase in abundance down to about 10 m.

Moving onto the passing hot star event shown in Fig. 5.3, the top row of panels is notably similar to the top row in Fig. 5.2 despite having experienced 2.5×10^5 years of the hot star up to this point and having reached the peak temperature. However, the lower panel does show some notable changes. Within the upper layers is a slight

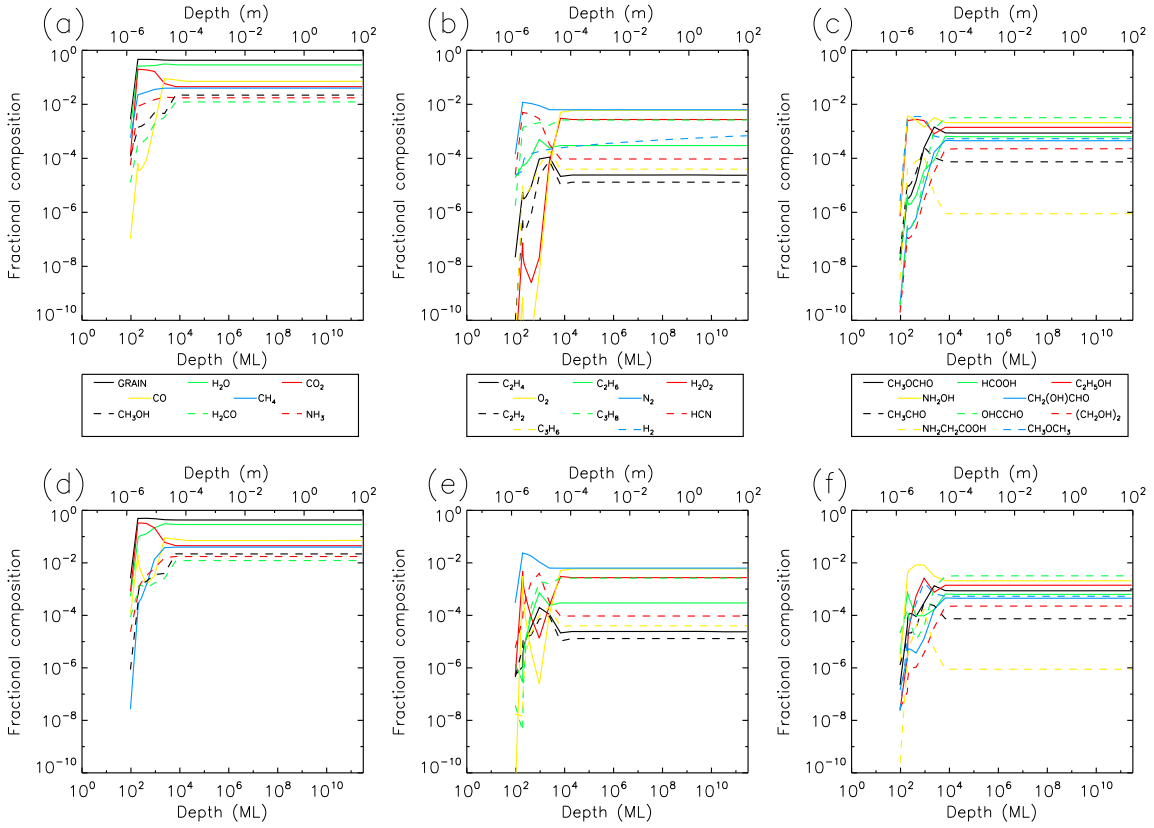

Figure 5.3: Fractional abundances of select ice species for a generic Oort Cloud comet DURING an encounter with a hot star passing within 1 parsec of the comet. Top: Abundances at 2.5×10^5 years, when the star is closest. Bottom: Abundances at 5×10^5 years, when the star is gone. The y-axis of each plot corresponds with the ice surface. The x-axis is the depth, from the surface, in terms of monolayers (ML) shown on the bottom and meters (m) shown on the top. Each column represents a different subset of species grouped based on size and relevance.

bump in the CO abundances. N_2 and NH_2OH also slightly increase while NH_3 slightly decreases. Then the abundances of O_2 and H_2O_2 are shown to have an overall increase in the upper layers as well. Once we examine Fig. 5.4 we can see many of the remnants of this time in the upper panels, 1 Myr after the encounter. Notable is the slight bump in the H_2 abundance in the upper ice layers that had entirely disappeared previously during the event. However, once we reach the endpoint shown in the bottom row, the results are quite similar to the bottom row of Fig. 5.2.

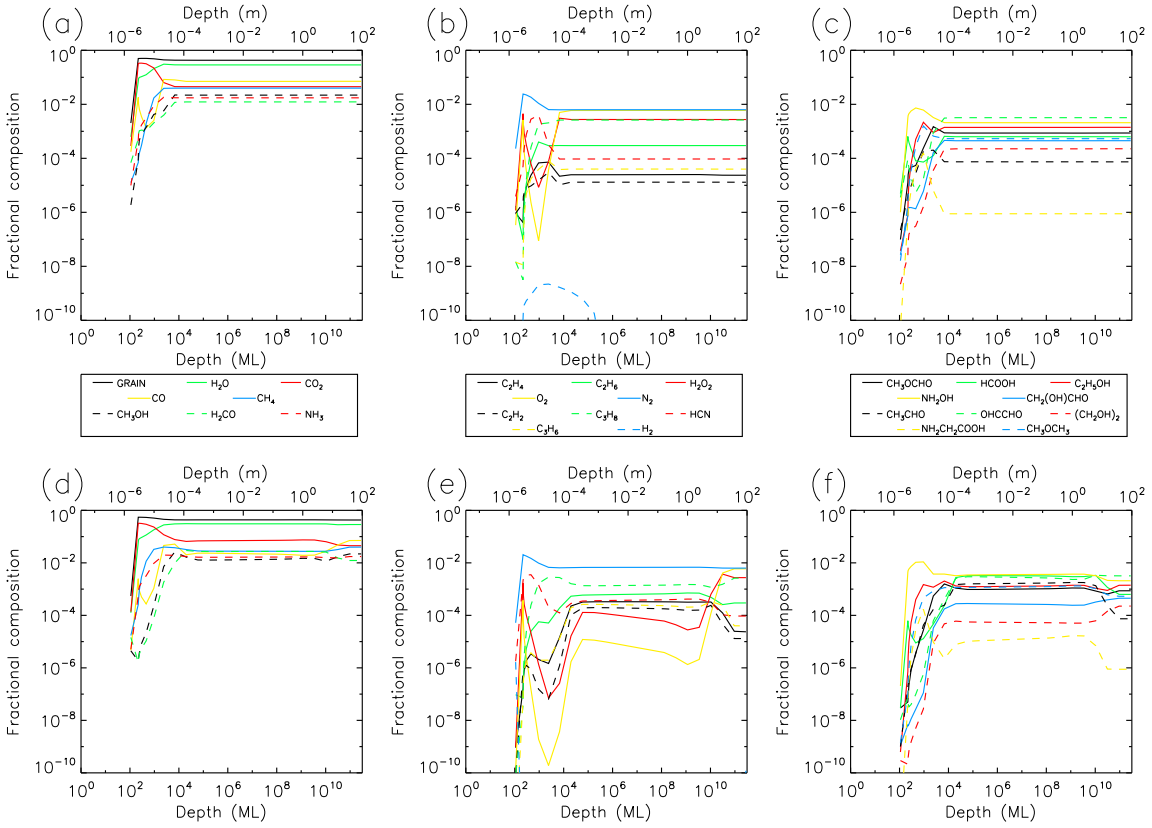

Figure 5.4: Fractional abundances of select ice species for a generic Oort Cloud comet AFTER an encounter with a hot star passing within 1 parsec of the comet. Top: Abundances at 10^6 years after the star has gone. Bottom: Abundances at 4.2×10^9 years after the star has gone. The y-axis of each plot corresponds with the ice surface. The x-axis is the depth, from the surface, in terms of monolayers (ML) shown on the bottom and meters (m) shown on the top. Each column represents a different subset of species grouped based on size and relevance.

Finally we come to the nearby supernova event shown in Fig. 5.5. Surprisingly, the abundances in the upper panels, 10 years after the supernova explosion, are quite similar to the bottom panel of Fig. 5.3, where the comet has been affected by the star for 50 kyrs. The notable differences are O_2 and H_2O_2 which are actually higher than in the previous case. Additionally, H_2 is also significantly depleted down to 10 m. By 1000 yrs, shown in the bottom panels, the O_2 and H_2O_2 abundances have slightly decreased and the H_2 has somewhat replenished. However, in Fig. 5.6, even in the

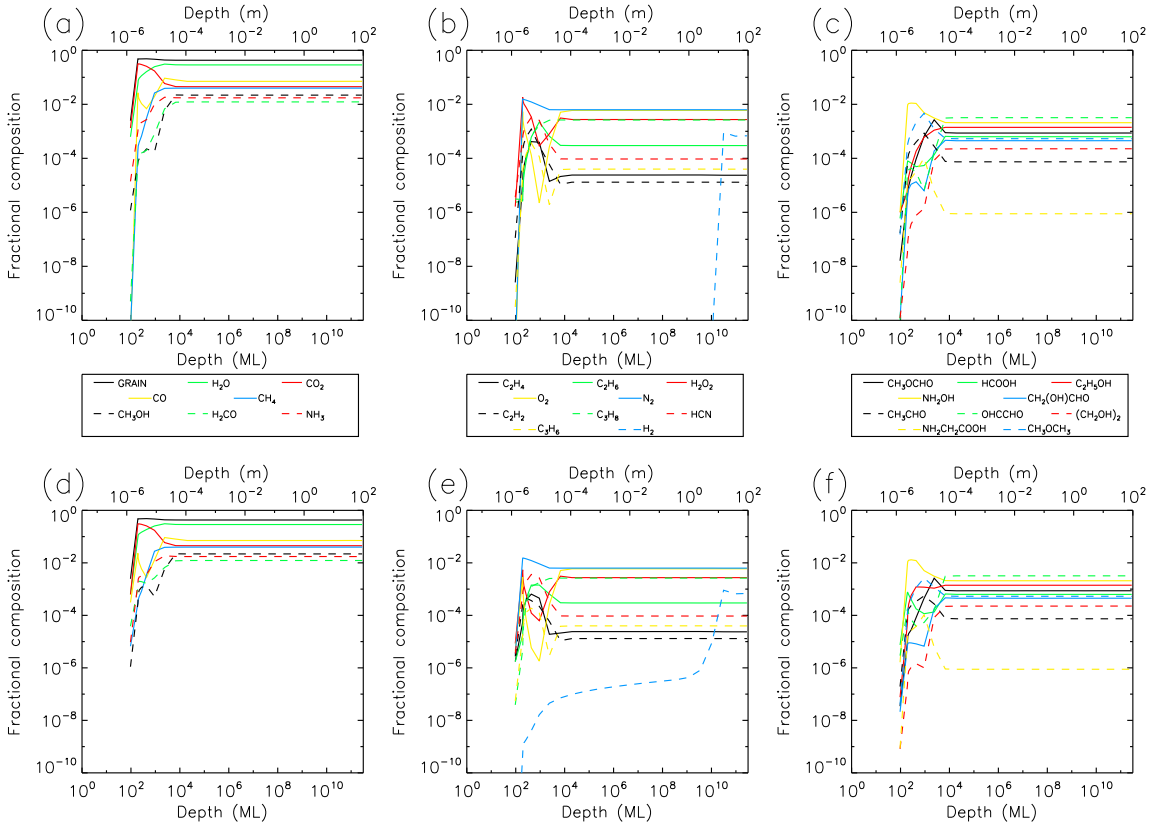

Figure 5.5: Fractional abundances of select ice species for a generic Oort Cloud comet DURING an encounter with a supernova 10 parsecs from the comet. Top: Abundances at 10 years after the supernova. Bottom: Abundances at 10^3 years after the supernova. The y-axis of each plot corresponds with the ice surface. The x-axis is the depth, from the surface, in terms of monolayers (ML) shown on the bottom and meters (m) shown on the top. Each column represents a different subset of species grouped based on size and relevance.

upper panels, 1 Myrs following the supernova explosion, the abundances are already almost identical to those in Fig. 5.2. By the endpoint of 4.5 Gyrs, the two sets of plots match even better.

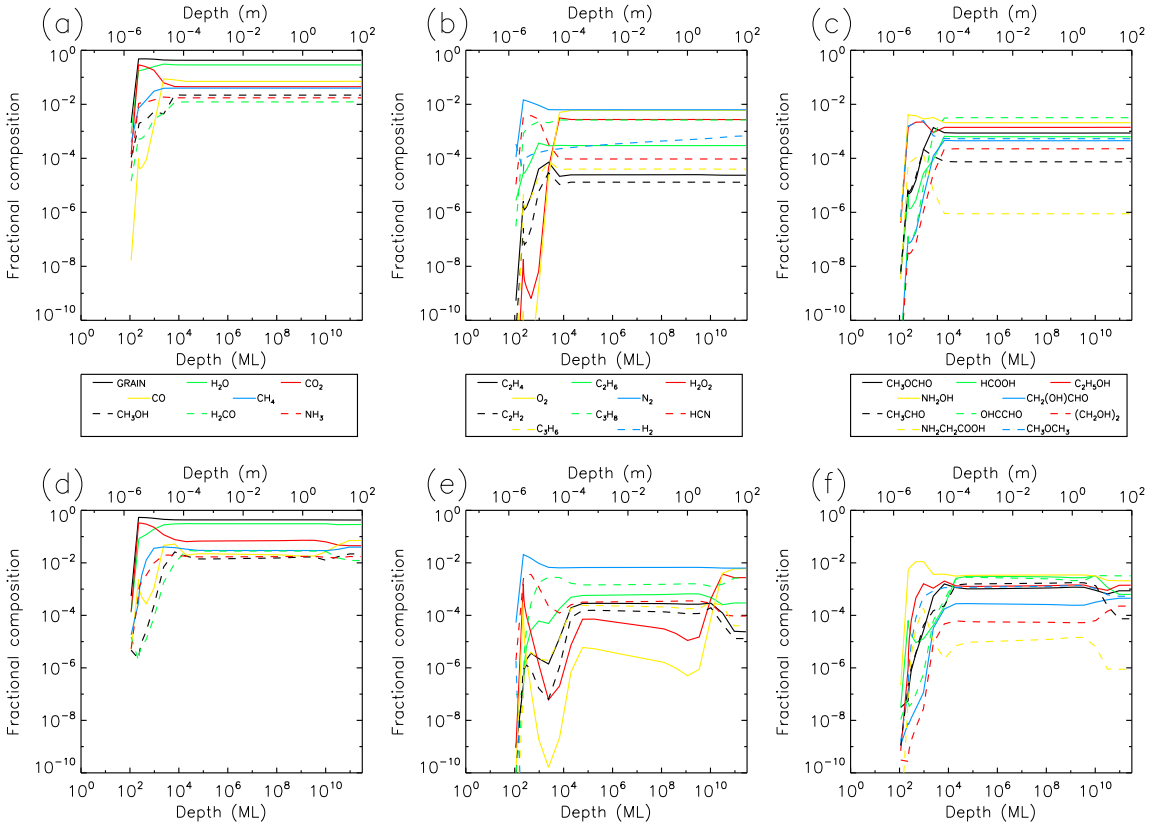

Figure 5.6: Fractional abundances of select ice species for a generic Oort Cloud comet AFTER an encounter with a supernova 10 parsecs from the comet. Top: Abundances at 10^6 years after the supernova. Bottom: Abundances at 4.2×10^9 years after the supernova. The y-axis of each plot corresponds with the ice surface. The x-axis is the depth, from the surface, in terms of monolayers (ML) shown on the bottom and meters (m) shown on the top. Each column represents a different subset of species grouped based on size and relevance.

5.4 Discussion

Overall we can see that the effects of the single hot star event are relatively minor, restricted to the upper layers of the ice. Though remnants of the event are still present after 1 Myr, they are all but gone by 4.5 Gyr, thus not surviving to the modern day. This is likely in part due to the micron thick dust layer that has built up on the surface. The additional UV from the hot star only penetrates about a micron deep,

therefore, with the layer already formed in the early stages, only the very top of the ice is affected by the UV and the rest is only affected by the temperature increase.

The single supernova event is a similar story. However, there are some minor effects reaching deeper into the ice due to the additional CRs. Additionally, the effects that we see are a bit more pronounced in the upper layers. This is likely a result of how powerful and violent an immediate effect the supernova has on the ice. However, conversely, the effects of this event disappear much quicker. Any remnant of the event has practically disappeared by 1 Myrs following the event. It would therefore seem that while supernova events may trigger a much more appreciable difference in the short term, after any significant length of time it will not be noticeable. Compared to hot star events, which are only slightly less significant, but last much longer. Ultimately, neither leave identifiable remnants up to the present day.

However, based on the statistical analysis of Stern (2003), there should be multiple such events occurring over the course of the cold storage phase. Only a singular Type-O star is likely to have occurred, but encounters with smaller stars in addition to this are statistically probable. It is therefore possible that the accumulation of these smaller events spread over the course of a comet lifetime might have some lasting effects. Similarly, the same statistical analysis predicted 30 supernova events within 4 Gyrs. With the higher immediate effects, perhaps this too would leave a mark on the comet ice composition.

Despite this, it is unlikely that these events would be frequent enough to have a noticeable effect. The results presented here are under conditions of being as close or even closer than is reasonably likely for a passing hot star or super nova event. It is more likely that the actual events that occur with any frequency will be much farther away and therefore have depreciated effects. On top of that, the effects of a

supernova event on the ice composition do not appear to last more than 1 Myr, and the effects of the hot star event don't seem to last that much longer overall. It is therefore more likely that the effects of any given hot star or supernova event will have disappeared long before the next one appears. The testing of this hypothesis is left to future work.

5.5 Conclusions

The model presented herein uses the first solid-phase chemical kinetics model adapted for cometary ices adapted to model the effects of passing hot star and nearby supernova events during the cold storage period of an Oort Cloud comet. This model, *MAGICKAL*, also exhibits additional capabilities in modeling a pure dust layer buildup in the upper layers of the comet. This can result in a shell of dust grains which can limit ice loss. Additionally, this pure dust layer was given the capability of losing grain material from the surface of the comet, which it was previously incapable of replicating.

A model of a single Type-O star passing within 1 pc of an Oort Cloud comet was run. Results show that the effects of this event can be retained up to and exceeding 1 Myr, but are completely lost by 4.5 Gyr. Another model of a single nearby Type II-P supernova event within 10 pc of an Oort Cloud comet was run. Results indicate that initially there is a greater impact on the ice chemistry of the comet. Noticeable effects are retained for at least 1000 yrs following the initial supernova explosion, but are not retained at all by 1 Myr.

It is possible, but unlikely, that multiple of each event, or each event used in tandem, might exhibit lasting effects. It is more likely, however, that the effects of

each event on the chemical abundances will have depreciated before a subsequent event can occur.

Chapter Acknowledgements

This work was funded by the NASA FINESST program for a graduate fellowship grant no. 80NSSC22K1328.

Chapter 6

Conclusions and Future Work

6.1 Concluding Remarks

The work presented in this thesis represents the culmination of the research I have performed over my graduate career. This work, within the field of astrochemistry, used multiple computational models of varying capabilities to model a selection of conditions. Earlier work, discussed in Chapter 2, used microscopic Monte Carlo methods to model interstellar dust grains. While a general set of shapes, sizes, conditions for interstellar dust grains are widely accepted, their more detailed structures are still hotly debated as well as their importance for detected gas-phase chemical abundances in interstellar clouds. Here, I have shown some chemical and physical variability that may occur when including or omitting high degrees of porosity within chemical models of dust grains.

Following this work, I began using rate-equations methods to model cometary ices, as discussed in Chapters 3–5. While gas-phase chemical kinetics models of the comae of comets are not uncommon, there were no chemical models on cometary ices prior to the one used here. Thus, this work emphasizes the ice chemistry over a comet lifetime. Different comets were examined over various phases, from cold storage to active phase. Over time, the existing model has been adapted, updated, and improved with new mechanisms and capabilities to better model cometary ices.

This was done in an effort to replicate observations which would then give insight into the lifetime of the comet as well as its origins and significant influences on any chemical variability. Here, I have shown that with our current models, we are able to replicate some observations of a comparable comet. In particular, this work finds importance in inheriting interstellar ices directly into the comet, supporting earlier work. I also particularly explore the significance that supernovae and hot stars in the solar vicinity play in the chemical evolution of cometary ices. This work shows that supernovae and hot stars can have significant short term effects, but are likely negligible on solar timescales.

The content of this thesis, as well as its related publications, was built off the work others have done in the past. It is also my hope that my research can be used as groundwork for more research in the future.

6.2 Future Work

In this section I will discuss both planned future research and some possible future directions for research that could derive from the work presented herein, either directly or indirectly. Of the planned research, one ongoing project is implementing the dust build layer described in §5.2.1 of Chapter 5 into a typical comet model that excludes the supernova and hot star additions. Following this, models for both Comet Hale-Bopp and Comet 67P will be run under different physical conditions, similar to what was done previously. This is meant to further refine the model in hopes of better matching observations and our understanding of comet lifetimes. This is a direct extension of work in Chapter 4 and is planned to be published along with data from that chapter.

Another planned continuation is an increase in parameter space examined in Chapter 5. Currently, only a supernova at 10 parsecs and a hot star approaching to 1 parsec at its closest were examined. Additional models of supernovae and hot stars at different distances will further support results. Currently, a range of minimum hot star distances of 1 to 5 parsecs are planned, and a range of supernova distances of 1 to 50 parsecs are planned. Current model results indicate that these are not promising contenders for long term effects. However, simulations of further distances will also be useful in examining the range of short term effects. Additionally, the model of a supernova set at 1 parsec could still yield long term effects on the comet ice, in this extreme case. Additionally, the current model considers cosmic rays to be released uniformly over a long period of time. Models assuming a different release profile, such as one that primarily releases most of the cosmic rays immediately before rapidly decaying, are also currently being examined for their viability. The increase in immediate cosmic ray flux will likely have a significant immediate effect on the deep layers of the ice. If these changes are drastic enough and deep enough, then it should be enough to retain this change over the comets cold storage lifetime.

While not currently planned, there are more possibilities that may be examined on the topic of the effects of supernovae and hot stars. Currently, the data presented is only based on single encounters with each and only at one distance each. However, in reality, multiple of such events could occur over the cold storage lifespan of a comet. It is possible that repeated events could cause the short term effects to last longer or be replenished enough to have a visible effect. Using a variety of distances, as well as including both supernovae and hot star encounters, in the same model will add to the already complex environment. While this would be difficult to model, this is worth examining. This, along with the previously mentioned differing cosmic

ray release rates, may be able to drastically affect the conclusions of this work. The current models also focus on Oort Cloud comets. While it is expected that the effects these events have on Kuiper Belt comets will be notably less significant, it would nonetheless be interesting to see to what degree they can be affected. Further, using a variety of methods such as modeling the motion of stars in the galaxy as well as searching for geological traces of increased cosmic ray flux could result in a list of likely encounters to test specifically for our solar system. Under ideal circumstances, this would lead to the most accurate results.

Currently, the only comets that have been directly examined with the *MAGICKAL* model are Comet Hale-Bopp and Comet 67P. While there are certainly improvements that should be made, and are currently being implemented, to further improve the accuracy of these models, it would nevertheless be worthwhile to examine other comets of interest. This could be more famous comets such as Comet Halley as well as other comets with direct close observations or return samples such as Comet Wild 2 and Comet Hartley 2 among others. Examining other comets could not only help expand the range of models of cometary ice chemistry but also help drive the progression and improvements of the current model by simulating different conditions.

There is also plenty of room to work with the *MIMICK* model. The range of models examined in Chapter 2 is rather limited. While results indicate that the dust grain size shouldn't significantly impact the ice composition, with the limited number of sizes examined, this could be confirmed with further studies. However, a pathway that may be more productive would be either further varying the porosity, or changing the dust grain shape. The results presented only tested two porosities, one being not porous at all, for a grain of approximately the same size. Further examinations of

the degree of porosity could reveal a crossover point in the degree of porosity that begins to display the effects presented in the chapter, or some gradient across them. Additionally, modeling different types of porosity, such as having large structures with large voids as opposed to smaller voids with more spindly grain material, could also lead to different results. As for the shape, the only grain shape examined was approximately spherical. While spherical is the canonical grain shape, realistically, they can be quite different. It would be interesting indeed to find physical or chemical differences that can result from different grain shapes.

Beyond the current scope of the models would be to model both the ice chemistry and gas chemistry of a comet. This is a very computationally expensive prospect with the current models. However, if made reasonable by future models, it would be very useful for making comparisons to observations which are most often taken from coma observations. This would also better outline the contribution that ice chemistry plays in observations as opposed to chemistry during the gas phase. Simpler models may also attempt to make use of the model results within this thesis in conjunction with their own gas phase model in an attempt to replicate this outcome.

One of the conclusions of Chapter 4 was that inheriting ice from the interstellar or protostellar phase was important for replicating observations. This was done in this thesis by running an interstellar cloud model and incorporating those results into the initial comet ice. While ambitious, this could be taken a step further by adding in additional steps such as running a protoplanetary disk model. With how drastic a change exhibited from the two different ice compositions examined in this chapter, differences resulting from going through all the intermediate steps could change it further. This would most effectively be accomplished through a concerted effort of specialized models suited for each stage passing along results for other models to start

their models with, similar to what was done within the research group here.

These are only some of the many possibilities for research related to the work presented in this thesis. Many creative individuals will take the work of the past and make something unique and informative to further elucidate the mysteries of the universe. I will continue building on my previous work as I advance my career, and I also encourage others to use what I have done to advance their own work as well to improve our understanding of science.

Bibliography

Accolla, M., Congiu, E., Manicò, G., Dulieu, F., Chaabouni, H., Lemaire, J.L., Pirronello, V., 2013. Morphology of the solid water synthesized through the pathway D + O_2 studied by the sensitive TPD technique. Month. Noti. Royal Astro. Soc. 429, 3200–3206. doi:10.1093/mnras/sts578.

Acharyya, K., Hassel, G.E., Herbst, E., 2011. The effects of grain size and grain growth on the chemical evolution of cold dense clouds. Astrophys. J. 732, 15. doi:10.1088/0004-637X/732/2/73.

Agarwal, J., Müller, M., Grün, E., 2007. Dust environment modelling of comet 67p/churyumov-gerasimenko. Spa. Sci. Rev. 128, 79–131. doi:10.1007/s11214-006-9139-1.

Altwegg, K., 2022. Cometary chemistry. Physics Today 75, 34–41. doi:10.1063/PT.3.4920.

Altwegg, K., Balsiger, H., Bar-Nun, A., Berthelier, J.J., Bieler, A., Bochsler, P., Briois, C., Calmonte, U., Combi, M.R., Cottin, H., De Keyser, J., Dhooghe, F., Fiethe, B., Fuselier, S.A., Gasc, S., Gombosi, T.I., Hansen, K.C., Haessig, M., Jäckel, A., Kopp, E., Korth, A., Le Roy, L., Mall, U., Marty, B., Mousis, O., Owen, T., Rème, H., Rubin, M., Sémon, T., Tzou, C.Y., Waite, J.H., Wurz, P., 2016. Prebiotic chemicals-amino acid and phosphorus in the coma of comet 67P/Churyumov-Gerasimenko. Science Advances 2, 1–6. doi:10.1126/sciadv.1600285.

Altwegg, K., Balsiger, H., Hänni, N., Rubin, M., Schuhmann, M., Schroeder, I., Sémon, T., Wampfler, S., Berthelier, J.J., Briois, C., Combi, M., Gombosi, T.I., Cottin, H., De Keyser, J., Dhooghe, F., Fiethe, B., Fuselier, S.A., 2020. Evidence of ammonium salts in comet 67p as explanation for the nitrogen depletion in cometary comae. Nature Astronomy 4, 533–540. doi:10.1038/s41550-019-0991-9.

Altwegg, K., Combi, M., Fuselier, S.A., Hänni, N., De Keyser, J., Mahjoub, A., Müller, D.R., Pestoni, B., Rubin, M., Wampfler, S.F., 2022. Abundant ammonium hydrosulphide embedded in cometary dust grains. Monthly Notices of the Royal Astronomical Society 516, 3900–3910. doi:10.1093/mnras/stac2440.

Bacmann, A., Taquet, V., Faure, A., Kahane, C., Ceccarelli, C., 2012. Detection of complex organic molecules in a prestellar core: A new challenge for astrochemical models. Astronomy and Astrophysics doi:10.1051/0004-6361/201219207.

Balsiger, H., Altwegg, K., Bochsler, P., Eberhardt, P., Fischer, J., Graf, S., Jäckel, A., Kopp, E., Langer, U., Mildner, M., Müller, J., Riesen, T., Rubin, M., Scherer, S., Wurz, P., Wüthrich, S., Arijs, E., Delanoye, S., De Keyser, J., Neefs, E., Nevejans, D., Rème, H., Aoustin, C., Mazelle, C., Médale, J.L., Sauvaud, J.A., Berthelier, J.J., Bertaux, J.L., Duvet, L., Illiano, J.M., Fuselier, S.A., Ghielmetti, A.G., Magoncelli, T., Shelley, E.G., Korth, A., Heerlein, K., Lauche, H., Livi, S., Loose, A., Mall, U., Wilken, B., Gliem, F., Fiethe, B., Gombosi, T.I., Block, B., Carignan, G.R., Fisk, L.A., Waite, J.H., Young, D.T., Wollnik, H., 2007. Rosina - Rosetta orbiter spectrometer for ion and neutral analysis. Space Science Reviews doi:10.1007/s11214-006-8335-3.

Bar-Nun, A., Dror, J., Kochavi, E., Laufer, D., 1987. Amorphous water ice and its ability to trap gases. Phys. Rev. B. 35, 2427–2435. doi:10.1103/PhysRevB.35.2427.

Bell, A.R., 1978. The acceleration of cosmic rays in shock fronts - ii. Monthly Notices of the Royal Astronomical Society 182, 443–455. doi:10.1093/mnras/182.3.443.

Bergin, E.A., Tafalla, M., 2007. Cold Dark Clouds: The Initial Conditions for Star Formation. Annu. Rev. Astron. Astrophys. 45, 339–396. doi:10.1146/annurev.astro.45.071206.100404, arXiv:0705.3765.

Bergner, J.B., Öberg, K.I., Garrod, R.T., Graninger, D.M., 2017. Complex Organic Molecules toward Embedded Low-mass Protostars. The Astrophysical Journal doi:10.3847/1538-4357/aa72f6, arXiv:1705.05338.

Berné, O., Mulas, G., Joblin, C., 2013. Interstellar c60+. Astronomy & Astrophysics 550, 5. doi:10.1051/0004-6361/201220730.

Biver, N., Bockelee-Morvan, D., Colom, P., Crovisier, J., Davies, J.K., Dent, W.R.F., Despois, D., Gerard, E., Lellouch, E., Rauer, H., Moreno, R., Paubert, G., 1997. Evolution of the outgassing of comet hale-bopp (c/1995 o1) from radio observations. Science 275, 1915–1918. doi:10.1126/science.275.5308.1915.

Bockelée-Morvan, D., Lis, D.C., Wink, J.E., Despois, D., Crovisier, J., Bachiller, R., Benford, D.J., Biver, N., Colom, P., Davies, J.K., Gérard, E., Germain, B., Houde, M., Mehringer, D., Moreno, R., Paubert, G., Phillips, T.G., Rauer, H., 2000. New molecules found in comet C/1995 O1 (Hale-Bopp): Investigating the link between cometary and interstellar material. Astronomy and Astrophysics 353, 1101–1114.

Boogert, A.C.A., Gerakines, P.A., Whittet, D.C.B., 2015. Observations of the icy universe. Annu. Rev. Astron. Astrophys. 53, 541–581. doi:10.1146/annurev-astro-082214-122348.

Brown, D.E., George, S.M., Huang, C., Wong, E.K., Rider, K.B., Smith, R.S., Kay, B.D., 1996. H2O condensation coefficient and refractive index for vapor-deposited ice from molecular beam and optical interference measurements. Journal of Physical Chemistry doi:10.1021/jp952547j.

Brownlee, D., Tsou, P., Aléon, J., O'D Alexander, C.M., Araki, T., Bajt, S., Baratta, G.A., Bastien, R., Bland, P., Bleuet, P., Borg, J., Bradley, J.P., Brearley, A., Brenker, F., Brennan, S., Bridges, J.C., Browning, N.D., Brucato, J.R., Bullock, E., Burchell, M.J., Busemann, H., Butterworth, A., Chaussidon, M., Cheuvront, A., Chi, M., Cintala, M.J., Clark, B.C., Clemett, S.J., Cody, G., Colangeli, L., Cooper, G., Cordier, P., Daghlian, C., Dai, Z., D'Hendecourt, L., Djouadi, Z., Dominguez, G., Duxbury, T., Dworkin, J.P., Ebel, D.S., Economou, T.E., Fakra, S., Fairey, S.A., Fallon, S., Ferrini, G., Ferroir, T., Fleckenstein, H., Floss, C., Flynn, G., Franchi, I.A., Fries, M., Gainsforth, Z., Gallien, J.P., Genge, M., Gilles, M.K., Gillet, P., Gilmour, J., Glavin, D.P., Gounelle, M., Grady, M.M., Graham, G.A., Grant, P.G., Green, S.F., Grossemy, F., Grossman, L., Grossman, J.N., Guan, Y., Hagiya, K., Harvey, R., Heck, P., Herzog, G.F., Hoppe, P., Hörz, F., Huth, J., Hutcheon, I.D., Ignatyev, K., Ishii, H., Ito, M., Jacob, D., Jacobsen, C., Jacobsen, S., Jones, S., Joswiak, D., Jurewicz, A., Kearsley, A.T., Keller, L.P., Khodja, H., Kilcoyne, A.L., Kissel, J., Krot, A., Langenhorst, F., Lanzirotti, A., Le, L., Leshin, L.A., Leitner, J., Lemelle, L., Leroux, H., Liu, M.C., Luening, K., Lyon, I., MacPherson, G., Marcus, M.A., Marhas, K., Marty, B., Matrajt, G., McKeegan, K., Meibom, A., Mennella, V., Messenger, K., Messenger, S., Mikouchi, T., Mostefaoui, S., Nakamura, T., Nakano, T., Newville, M., Nittler, L.R., Ohnishi, I., Ohsumi, K., Okudaira, K., Papanastassiou, D.A., Palma, R., Palumbo, M.E., Pepin, R.O., Perkins, D., Perronnet, M., Pianetta, P., Rao, W., Rietmeijer, F.J., Robert, F., Rost, D., Rotundi, A., Ryan, R., Sandford, S.A., Schwandt, C.S., See, T.H., Schlutter, D., Sheffield-Parker, J., Simionovici, A., Simon, S., Sitnitsky, I., Snead, C.J., Spencer, M.K., Stadermann, F.J., Steele, A., Stephan, T., Stroud, R., Susini, J., Sutton, S.R., Suzuki, Y., Taheri, M., Taylor, S., Teslich, N., Tomeoka, K., Tomioka, N., Toppani, A., Trigo-Rodríguez, J.M., Troadec, D., Tsuchiyama, A., Tuzzolino, A.J., Tyliszczak, T., Uesugi, K., Velbel, M., Vellenga, J., Vicenzi, E., Vincze, L., Warren, J., Weber, I., Weisberg, M., Westphal, A.J., Wirick, S., Wooden, D., Wopenka, B., Wozniakiewicz, P., Wright, I., Yabuta, H., Yano, H., Young, E.D., Zare, R.N., Zega, T., Ziegler, K., Zimmerman, L., Zinner, E., Zolensky, M., 2006. Comet 81P/wild 2 under a microscope. Science doi:10.1126/science.1135840.

Burke, D.J., Brown, W.A., 2010. Ice in space: surface science investigations of the thermal desorption of model interstellar ices on dust grain analogue surfaces. Physical Chemistry Chemical Physics 12, 5947. doi:10.1039/b917005g.

Calmonte, U., Altwegg, K., Balsiger, H., Berthelier, J.J., Bieler, A., Cessateur, G.,

Dhooghe, F., van Dishoeck, E.F., Fiethe, B., Fuselier, S.A., Gasc, S., Gombosi, T.I., Hässig, M., Le Roy, L., Rubin, M., Sémon, T., Tzou, C.Y., Wampfler, S.F., 2016. Sulphur-bearing species in the coma of comet 67p/churyumov-gerasimenko. Monthly Notices of the Royal Astronomical Society 462, S253–S273. doi:10.1093/mnras/stw2601.

Cernicharo, J., Marcelino, N., Roueff, E., Gerin, M., Jiménez-Escobar, A., Muñoz Caro, G.M., 2012. Discovery of the methoxy radical, CH3O, toward B1: Dust grain and gas-phase chemistry in cold dark clouds. Astrophysical Journal Letters doi:10.1088/2041-8205/759/2/L43.

Chaabouni, H., Bergeron, H., Baouche, S., Dulieu, F., Matar, E., Congiu, E., Gavilan, L., Lemaire, J.L., 2012. Sticking coefficient of hydrogen and deuterium on silicates under interstellar conditions. Astron. Astrophys. 538, A128. doi:10.1051/0004-6361/201117409, arXiv:1202.2473.

Chang, Q., Herbst, E., 2014. Interstellar Simulations Using a Unified Microscopic-Macroscopic Monte Carlo Model with a Full Gas-Grain Network Including Bulk Diffusion in Ice Mantles. The Astrophysical Journal 787, 135. doi:10.1088/0004-637X/787/2/135, arXiv:1405.0840.

Christianson, D.A., Garrod, R.T., 2021. Chemical kinetics simulations of ice chemistry on porous versus non-porous interstellar dust grains. Frontiers 8, 26. doi:10.3389/fspas.2021.643297.

Clements, A.R., Berk, B., Cooke, I.R., Garrod, R.T., 2018a. Kinetic Monte Carlo simulations of water ice porosity: extrapolations of deposition parameters from the laboratory to interstellar space. Physical Chemistry Chemical Physics 20, 5553–5568. URL: http://xlink.rsc.org/?DOI=C7CP05966C, doi:10.1039/C7CP05966C.

Clements, A.R., Berk, B., Cooke, I.R., Garrod, R.T., 2018b. Kinetic monte carlo simulations of water ice porosity: extrapolations of deposition parameters from the laboratory to interstellar space. Phys. Chem. Chem. Phys. 20, 5553–5568. doi:10.1039/C7CP05966C.

Cooper, J.F., Christian, E.R., Richardson, J.D., Wang, C., 2003. Proton irradiation of centaur, kuiper belt, and oort cloud objects at plasma to cosmic ray energy. Earth, Moon, and Planets 92, 261–277. doi:10.1023/B:MOON.0000031944.41883.80.

Crovisier, J., Bockelée-Morvan, D., Biver, N., Colom, P., Despois, D., Lis, D.C., 2004. Ethylene glycol in comet C/1995 O1 (Hale-Bopp). Astronomy and Astrophysics doi:10.1051/0004-6361:20040116.

Cuppen, H.M., Morata, O., Herbst, E., 2006. Monte Carlo simulations of H_2 formation on stochastically heated grains. Month. Noti. Royal Astro. Soc. 367, 1757–1765. doi:10.1111/j.1365-2966.2006.10079.x, arXiv:astro-ph/0601554.

Cuppen, H.M., Walsh, C., Lamberts, T., Semenov, D., Garrod, R.T., Penteado, E.M., Ioppolo, S., 2017. Grain surface models and data for astrochemistry. Spa. Sci. Rev. 212, 1–58. doi:10.1007/s11214-016-0319-3.

Curdt, W., Brekke, P., Feldman, U., Wilhelm, K., Dwivedi, B.N., Schühle, U., Lemaire, P., 2001. The sumer spectral atlas of solar-disk features. Astronomy and Astrophysics 375, 591–613. doi:10.1051/0004-6361:20010364.

Doggett, J.B., Branch, D., 1985. A comparative study of supernova light curves. The Astrophysical Journal 90, 2303–2311. doi:10.1086/113934.

Douglas, A.E., Herzberg, G., 1941. Ch+ in interstellar space and in the laboratory. The Astrophysical Journal 94, 381. doi:10.1086/144342.

Drozdovskaya, M.N., van Dishoeck, E.F., Rubin, M., Jørgensen, J.K., Altwegg, K., 2019. Ingredients for solar-like systems: protostar iras 16293-2422 b versus comet 67p/churyumov-gerasimenko. Monthly Notices of the Royal Astronomical Society 490, 50–79. doi:10.1093/mnras/stz2430.

Duncan, M., Quinn, T., Tremaine, S., 1987. The formation and extent of the solar system comet cloud. The Astronomical Journal doi:10.1086/114571.

Dupuy, J.L., Lewis, S.P., Stancil, P.C., 2016. A Comprehensive Study of Hydrogen Adsorbing to Amorphous Water ice: Defining Adsorption in Classical Molecular Dynamics. Astrophys. J. 831, 54. doi:10.3847/0004-637X/831/1/54, arXiv:1608.05158.

Ellsworth, K., Schubert, G., 1983. Saturn's icy satellites: Thermal and structural models. Icarus doi:10.1016/0019-1035(83)90242-7.

Elsila, J.E., Glavin, D.P., Dworkin, J.P., 2009. Cometary glycine detected in samples returned by Stardust. Meteoritics and Planetary Science doi:10.1111/j.1945-5100.2009.tb01224.x.

Fernández, Y.R., 2000. The nucleus of comet Hale-Bopp (C/1995 O1): size and activity. Earth, Moon, and Planets 89, 3.

Ferrero, S., Zamirri, L., Ceccarelli, C., Witzel, A., Rimola, A., Ugliengo, P., 2020. Binding Energies of Interstellar Molecules on Crystalline and Amorphous Models of Water Ice by Ab Initio Calculations. Astrophys. J. 904, 11. doi:10.3847/1538-4357/abb953, arXiv:2009.09763.

Fixsen, D.J., 2009. The temperature of the cosmic microwave background. The Astrophysical Journal 707, 916–920. doi:10.1088/0004-637X/707/2/916.

Garrod, R.T., 2008. A new modified-rate approach for gas-grain chemical simulations. Astron. Astrophys. 491, 239–251. doi:10.1051/0004-6361:200810518.

Garrod, R.T., 2013a. a Three-Phase Chemical Model of Hot Cores: the Formation of Glycine. The Astrophysical Journal 765, 60. URL: http://stacks.iop.org/0004-637X/765/i=1/a=60?key=crossref.4dbc2fde1b07a0ed3c73ff6b72b68840, doi:10.1088/0004-637X/765/1/60.

Garrod, R.T., 2013b. Three-dimensional, off-lattice monte carlo kinetics simulations of interstellar grain chemistry and ice structure. Astrophys. J. 778, 14. doi:10.1088/0004-637X/778/2/158.

Garrod, R.T., 2013c. Three-dimensional, Off-lattice Monte Carlo Kinetics Simulations of Interstellar Grain Chemistry and Ice Structure. The Astrophysical Journal 778, 158. URL: http://adsabs.harvard.edu/abs/2013ApJ...778..158G{%}5Cnhttp://adsabs.harvard.edu/cgi-bin/nph-data{_}query?bibcode=2013ApJ...778..158G{&}link{_}type=ARTICLE, doi:10.1088/0004-637X/778/2/158;, arXiv:1310.2512.

Garrod, R.T., 2013d. A three-phase chemical model of hot cores: The formation of glycine. Astrophys. J. 765, 29. doi:10.1088/0004-637X/765/1/60.

Garrod, R.T., 2019. Simulations of Ice Chemistry in Cometary Nuclei. The Astrophysical Journal doi:10.3847/1538-4357/ab418e, arXiv:1909.03366.

Garrod, R.T., Belloche, A., Müller, H.S., Menten, K.M., 2017. Exploring molecular complexity with ALMA (EMoCA): Simulations of branched carbon-chain chemistry in Sgr B2(N). Astronomy and Astrophysics doi:10.1051/0004-6361/201630254.

Garrod, R.T., Jin, M., Matis, K.A., Jones, D., Willis, E.R., Herbst, E., 2022. Formation of Complex Organic Molecules in Hot Molecular Cores through Nondiffusive Grain-surface and Ice-mantle Chemistry. The Astrophysical Journal Supplement Series 259, 1. doi:10.3847/1538-4365/ac3131, arXiv:2110.09743.

Garrod, R.T., Pauly, T., 2011. On the Formation of CO_2 and Other Interstellar Ices. Astrophys. J. 735, 15. doi:10.1088/0004-637X/735/1/15, arXiv:1106.0540.

Garrod, R.T., Pauly, T., 2011. on the Formation of Co2 and Other Interstellar Ices. The Astrophysical Journal 735, 15. URL: http://stacks.iop.org/0004-637X/735/i=1/a=15?key=crossref.65bc73761508a748b372c3453f91a7f6, doi:10.1088/0004-637X/735/1/15, arXiv:1106.0540.

Garrod, R.T., Wakelam, V., Herbst, E., 2007. Non-thermal desorption from interstellar dust grains via exothermic surface reactions. Astron. Astrophys. 467, 1103–1115. doi:10.1051/0004-6361:20066704, arXiv:astro-ph/0703188.

Garrod, R.T., Widicus Weaver, S.L., Herbst, E., 2008. Complex Chemistry in Star-forming Regions: An Expanded Gas-Grain Warm-up Chemical Model. The Astrophysical Journal 682, 283–302. doi:10.1086/588035, arXiv:0803.1214.

Ghesquière, P., Ivlev, A., Noble, J.A., Theulé, P., 2018. Reactivity in interstellar ice analogs: Role of the structural evolution. Astronomy and Astrophysics doi:10.1051/0004-6361/201732288.

Gillespie, D.T., 1976. A general method for numerically simulating the stochastic time evolution of coupled chemical reactions. J. Comput. Phys. 22, 403–434. doi:10.1016/0021-9991(76)90041-3.

Glavin, D.P., Dworkin, J.P., Sandford, S.A., 2008. Detection of cometary amines in samples returned by Stardust. Meteoritics and Planetary Science doi:10.1111/j.1945-5100.2008.tb00629.x.

Gould, R.J., Salpeter, E.E., 1963. The interstellar abundance of the hydrogen molecule. i. basic processes. Astrophys. J. 138, 393. doi:10.1086/147654.

Gronoff, G., Maggiolo, R., Cessateur, G. ; Moore, W.B., Airapetian, V., De Keyser, J., Dhooghe, F., Gibbons, A., Gunell, H., Mertens, C.J., Rubin, M., Hosseini, S., 2020. The effect of cosmic rays on cometary nuclei. i. dose deposition. The Astrophysical Journal 890, 8. doi:10.3847/1538-4357/ab67b9.

Guilbert-Lepoutre, A., Jewitt, D., 2011. Thermal shadows and compositional structure in comet nuclei. Astrophysical Journal doi:10.1088/0004-637X/743/1/31.

Hales, T.C., 2005. A proof of the kepler conjecture. Annals of Mathematics 162, 1065–1185. doi:10.4007/annals.2005.162.1065.

Hanslmeier, A., 2017. Supernovae, our solar system, and life on earth. Handbook of Supernovae 1, 2489. doi:10.1007/978-3-319-21846-5_114.

Hasegawa, T.I., Herbst, E., Leung, C.M., 1992a. Models of gas-grain chemistry in dense interstellar clouds with complex organic molecules. Astrophys. J. 82, 167. doi:10.1086/191713.

Hasegawa, T.I., Herbst, E., Leung, C.M., 1992b. Models of gas-grain chemistry in dense interstellar clouds with complex organic molecules. The Astrophysical Journal Supplement Series 82, 167–195. URL: http://adsabs.harvard.edu/abs/1992ApJS...82..167H{%}5Cnhttp://adsabs.harvard.edu/cgi-bin/nph-data{_}query?bibcode=1992ApJS...82..167H{&}link{_}type=ARTICLE, doi:10.1086/191713.

He, J., Acharyya, K., Vidali, G., 2016a. Binding Energy of Molecules on Water Ice: Laboratory Measurements and Modeling. Astrophys. J. 825, 89. doi:10.3847/0004-637X/825/2/89, arXiv:1603.02191.

He, J., Acharyya, K., Vidali, G., 2016b. Sticking of Molecules on Nonporous Amorphous Water Ice. Astrophys. J. 823, 56. doi:10.3847/0004-637X/823/1/56, arXiv:1602.06341.

He, J., Clements, A.R., Emtiaz, S., Toriello, F., Garrod, R.T., Vidali, G., 2019. The Effective Surface Area of Amorphous Solid Water Measured by the Infrared Absorption of Carbon Monoxide. Astrophys. J. 878, 94. doi:10.3847/1538-4357/ab1f6a, arXiv:1905.00969.

Heays, A.N., Bosman, A.D., van Dishoeck, E.F., 2017. Photodissociation and photoionisation of atoms and molecules of astrophysical interest. Astronomy and Astrophysics 602, 62. doi:10.1051/0004-6361/201628742.

Herbst, E., Klemperer, W., 1973. The formation and depletion of molecules in dense interstellar clouds. The Astrophysical Journal 185, 505–534. doi:10.1086/152436.

Herman, G., Podolak, M., 1985. Numerical simulation of comet nuclei I. Water-ice comets. Icarus doi:10.1016/0019-1035(85)90107-1.

Herman, G., Weissman, P.R., 1987. Numerical simulation of cometary nuclei. III. Internal temperatures of cometary nuclei. Icarus doi:10.1016/0019-1035(87)90108-4.

Hillas, A.M., 2005. Topical review: Can diffusive shock acceleration in supernova remnants account for high-energy galactic cosmic rays? Journal of Physics G: Nuclear and Particle Physics 31, R95–R131. doi:10.1088/0954-3899/31/5/R02.

Hollenbach, D., Salpeter, E.E., 1971. Surface Recombination of Hydrogen Molecules. Astrophys. J. 163, 155. doi:10.1086/150754.

Hsieh, H.H., Jewitt, D., 2006. A population of comets in the main asteroid belt. Science 312, 561–563. doi:10.1126/science.1125150.

Huynh, L., Violi, A., 2008. Thermal decomposition of methyl butanoate: Ab initio study of a biodiesel fuel surrogate. J. Org. Chem. 73, 94–101.

Irvine, W.M., Bergin, E.A., Dickens, J.E., Jewitt, D., Lovell, A.J., Matthews, H.E., Schloerb, F.P., Senay, M., 1998. Chemical processing in the coma as the source of cometary HNC. Nature 393, 547–550. URL: http://adsabs.harvard.edu/cgi-bin/nph-data{_}query?bibcode=1998Natur.393..547I{&}link{_}type=EJOURNAL{%}5Cnpapers3://publication/doi/10.1038/31171, doi:10.1038/31171.

Jewitt, D., Matthews, H., 1999. Particulate mass loss from comet hale-bopp. The Astronomical Journal 117, 1056–1062. doi:10.1086/300743.

Jin, M., Garrod, R.T., 2020. Formation of Complex Organic Molecules in Cold Interstellar Environments through Nondiffusive Grain-surface and Ice-mantle Chemistry. The Astrophysical Journal Supplement Series 249, 26. doi:10.3847/1538-4365/ab9ec8, arXiv:2006.11127.

Jones, A.P., Ysard, N., Köhler, M., Fanciullo, L., Bocchio, M., Micelotta, E., Verstraete, L., Guillet, V., 2014. The cycling of carbon into and out of dust. Farad. Discuss. 168, 313. doi:10.1039/C3FD00128H.

Keane, J.V., Tielens, A.G.G.M., Boogert, A.C.A., Schutte, W.A., Whittet, D.C.B., 2001. Ice absorption features in the 5-8 μm region toward embedded protostars. Astron. Astrophys. 376, 254–270. doi:10.1051/0004-6361:20010936.

Kobayashi, T., Komori, Y., Yoshida, K., Nishimura, J., 2004. The most likely sources of high-energy cosmic-ray electrons in supernova remnants. The Astrophysical Journal 601, 340–351. doi:10.1086/380431.

Kouchi, A., Yamamoto, T., Kozasa, T., Kuroda, T., 1994. Conditions for condensation and preservation of amorphous ice and crystallinity of astrophysical ices. ASTRONOMY AND ASTROPHYSICS -BERLIN- .

Kouchi, A., Yamamoto, T., Kozasa, T., Kuroda, T., Greenberg, J.M., 1994. Conditions for condensation and preservation of amorphous ice and crystallinity of astrophysical ices. Astron. Astrophys. 290, 1009–1018.

Krolikowska, M., 2003. 67p/churyumov-gerasimenko – potential target for the rosetta mission. Acta Astronomica 53, 195–209. doi:10.48550/arXiv.astro-ph/0309130.

Kuiper, G.P., 1951. On the Origin of the Solar System. Proceedings of the National Academy of Science 37, 1–14. doi:10.1073/pnas.37.1.1.

Lis, D.C., Bockelée-Morvan, D., Güsten, R., Biver, N., Stutzki, J., Delorme, Y., Durán, C., Wiesemeyer, H., Okada, Y., 2019. Terrestrial deuterium-to-hydrogen ratio in water in hyperactive comets. Astronomy & Astrophysics 625, 8. doi:10.1051/0004-6361/201935554.

Maggiolo, R., Gronoff, G., Cessateur, G., Moore, W.B., Airapetian, V.S., De Keyser, J., Dhooghe, F., Gibbons, A., Gunell, H., Mertens, C.J., Rubin, M., Hosseini, S., 2020. The effect of cosmic rays on cometary nuclei. ii. impact on ice composition and structure. The Astrophysical Journal 901, 13. doi:10.3847/1538-4357/abacc3.

Mannel, T., Bentley, M.S., Boakes, P.D., Jeszenszky, H., Ehrenfreund, P., Engrand, C., Koeberl, C., Levasseur-Regourd, A.C., Romstedt, J., Schmied, R., Torkar, K., Weber, I., 2019. Dust of comet 67p/churyumov-gerasimenko collected by rosetta/midas: classification and extension to the nanometer scale. Astron. Astrophys. 630, 14. doi:10.1051/0004-6361/201834851.

Marsden, B.G., 1997. Orbit determination and evolution of comet c/1995 o1 (hale-bopp). Earth, Moon, and Planets 79, 3–15. doi:10.1023/A:1006268813208.

Mason, C.G., Gehrz, R.D., Jones, T.J., Woodward, C.E., Hanner, M.S., Williams, D.M., 2001. Observations of Unusually Small Dust Grains in the Coma of Comet Hale-Bopp C/1995 O1. The Astrophysical Journal doi:10.1086/319039.

Mathis, J.S., 1996. Dust models with tight abundance constraints. Astrophys. J. 472, 643. doi:10.1086/178094.

Mathis, J.S., Rumpl, W., Nordsieck, K.H., 1977. The size distribution of interstellar grains. Astrophys. J. 217, 425–433. doi:10.1086/155591.

McKellar, A., 1940. Evidence for the Molecular Origin of Some Hitherto Unidentified Interstellar Lines. Publications of the Astronomical Society of the Pacific 52, 187–192. doi:10.1086/125159.

Mezger, P.G., 1990. The Interstellar Radiation Field and its Interaction with the Interstellar Matter, in: Bowyer, S., Leinert, C. (Eds.), The Galactic and Extragalactic Background Radiation, p. 63.

Minissale, M., Dulieu, F., Cazaux, S., Hocuk, S., 2016. Dust as interstellar catalyst. I. Quantifying the chemical desorption process. Astron. Astrophys. 585, A24. doi:10.1051/0004-6361/201525981, arXiv:1510.03218.

Mumma, M.J., Charnley, S.B., 2011. The Chemical Composition of Comets—Emerging Taxonomies and Natal Heritage. Annual Review of Astronomy and Astrophysics 49, 471–524. doi:10.1146/annurev-astro-081309-130811.

Navarro-Ruiz, J., Sodupe, M., Ugliengo, P., Rimola, A., 2014. Interstellar h adsorption and h2 formation on the crystalline (010) forsterite surface: a b3lyp-d2* periodic study. Phys. Chem. Chem. Phys. 16, 17447–17457. URL: http://dx.doi.org/10.1039/C4CP00819G, doi:10.1039/C4CP00819G.

Oba, Y., Miyauchi, N., Hidaka, H., Chigai, T., Watanabe, N., Kouchi, A., 2009. Formation of Compact Amorphous H_2O Ice by Codeposition of Hydrogen Atoms with Oxygen Molecules on Grain Surfaces. Astrophys. J. 701, 464–470. doi:10.1088/0004-637X/701/1/464.

Oort, J.H., 1950. The structure of the cloud of comets surrounding the Solar System and a hypothesis concerning its origin. Bulletin of the Astronomical Institutes of the Netherlands 11, 91–110.

Ormel, C.W., Paszun, D., Dominik, C., Tielens, A.G.G.M., 2009. Dust coagulation and fragmentation in molecular clouds. i. how collisions between dust aggregates alter the dust size distribution. Astron. Astrophys. 502, 845–869. doi:10.1051/0004-6361/200811158.

Ossenkopf, V., 1993. Dust coagulation in dense molecular clouds : the formation of fluffy aggregates. Astron. Astrophys. 280, 617–646.

Pantaleone, S., Enrique-Romero, J., Ceccarelli, C., Ugliengo, P., Balucani, N., Rimola, A., 2020. Chemical Desorption versus Energy Dissipation: Insights from Ab Initio Molecular Dynamics of HCO · Formation. Astrophys. J. 897, 56. doi:10.3847/1538-4357/ab8a4b, arXiv:2004.11758.

Pauly, T., Garrod, R.T., 2016. The effects of grain size and temperature distributions on the formation of interstellar ice mantles. Astrophys. J. 817, 16. doi:10.3847/0004-637X/817/2/146.

Pauly, T., Garrod, R.T., 2018. Modeling co, co_2, and h_2o ice abundances in the envelopes of young stellar objects in the magellanic clouds. Astrophys. J. 854, 16. doi:10.3847/1538-4357/aaa96a.

Pirronello, V., Liu, C., Shen, L., Vidali, G., 1997. Laboratory Synthesis of Molecular Hydrogen on Surfaces of Astrophysical Interest. Lab. Synth. Mol. Hydrogen Surf. Astrophys. Int. 475, L69–L72. doi:10.1086/310464, arXiv:astro-ph/9611022.

Potapov, A., Jäger, C., Henning, T., 2020. Ice coverage of dust grains in cold astrophysical environments. Phys. Rev. Lett. 124, 221103. doi:10.1103/PhysRevLett.124.221103.

Prialnik, D., Sarid, G., Rosenberg, E.D., Merk, R., 2008. Thermal and Chemical Evolution of Comet Nuclei and Kuiper Belt Objects. Space Science Reviews 138, 147–164. doi:10.1007/s11214-007-9301-4.

Pätzold, M., Andert, T.P., Hahn, M., Barriot, J.P., Asmar, S.W., Häusler, B., Bird, M.K., Tellmann, S., Oschlisniok, J., Peter, K., 2019. The nucleus of comet 67p/churyumov-gerasimenko - part i: The global view - nucleus mass, mass-loss, porosity, and implications. Monthly Notices of the Royal Astronomical Society 483, 2337–2346. doi:10.1093/mnras/sty3171.

R., B., M., P., I., S., O., O.P., , T., K., 2020. Cosmic-ray acceleration and escape from post-adiabatic supernova remnants. Astronomy & Astrophysics 634, 11. doi:10.1051/0004-6361/201936567.

Raut, U., Fama, M., Teolis, B.D., Baragiola, R.A., 2007. Characterization of porosity in vapor-deposited amorphous solid water by methane adsorption. J. Chem. Phys. 127, 204713. doi:10.1063/1.2796166.

Rhodes, B.C., 2011. PyEphem: Astronomical Ephemeris for Python. arXiv:1112.014.

Russell, H.W., 1935. PRINCIPLES OF HEAT FLOW IN POROUS INSULATORS. Journal of the American Ceramic Society doi:10.1111/j.1151-2916.1935.tb19340.x.

Sandford, S.A., Allamandola, L.J., 1990. The volume- and surface-binding energies of ice systems containing CO, CO $_2$ and H $_2$O. Icarus 87, 188–192. doi:10.1016/0019-1035(90)90028-8.

Schmidt, M., Lipson, H., 2009. Distilling free-form natural laws from experimental data. Science doi:10.1126/science.1165893.

Schmidt, M., Lipson, H., 2014. Eureqa (Version 0.98 beta).

Senevirathne, B., Andersson, S., Dulieu, F., Nyman, G., 2017. Hydrogen atom mobility, kinetic isotope effects and tunneling on interstellar ices (I_h and ASW). Mol. Astrophys. 6, 59–69. doi:10.1016/j.molap.2017.01.005.

Shingledecker, C.N., Vasyunin, A., Herbst, E., Caselli, P., 2019. On Simulating the Proton-irradiation of O 2 and H 2 O Ices Using Astrochemical-type Models, with Implications for Bulk Reactivity . The Astrophysical Journal doi:10.3847/1538-4357/ab16d5, arXiv:1904.04143.

Stern, S.A., 2003. The evolution of comets in the Oort cloud and Kuiper belt. Nature 424, 639–642. URL: http://adsabs.harvard.edu/abs/2003Natur.424..639S, doi:10.1038/nature01725.

Stern, S.A., Shull, J.M., 1988. The influence of supernovae and passing stars on comets in the Oort cloud. URL: http://www.nature.com/doifinder/10.1038/332407a0, doi:10.1038/332407a0.

Swings, P., Rosenfeld, L., 1937. Considerations regarding interstellar molecules. The Astrophysical Journal 86, 483–486. doi:10.1086/143879.

Vincent, J.B., Kruk, S., Fanara1, Lida Birch, S., Jindal, A., 2021. Automated detection of surface changes on comet 67p. doi:10.5194/epsc2021-525. european Planetary Science Congress 2021.

Waggoner, A.R., Cleeves, L.I., 2022. Classification of x-ray flare-driven chemical variability in protoplanetary disks. The Astrophysical Journal 928, 14. doi:10.3847/1538-4357/ac549f.

Wakelam, V., Bron, E., Cazaux, S., Dulieu, F., Gry, C., Guillard, P., Habart, E., Hornekær, L., Morisset, S., Nyman, G., Pirronello, V., Price, S.D., Valdivia, V., Vidali, G., Watanabe, N., 2017a. H_2 formation on interstellar dust grains: The viewpoints of theory, experiments, models and observations. Mol. Astrophys. 9, 1–36. doi:10.1016/j.molap.2017.11.001, arXiv:1711.10568.

Wakelam, V., Loison, J.C., Mereau, R., Ruaud, M., 2017b. Binding energies: New values and impact on the efficiency of chemical desorption. Mol. Astrophys. 6, 22–35. doi:10.1016/j.molap.2017.01.002, arXiv:1701.06492.

Weingartner, J.C., Draine, B.T., 2001. Dust grain-size distributions and extinction in the milky way, large magellanic cloud, and small magellanic cloud. Astrophys. J. 548, 296–309. doi:10.1086/318651.

Weinreb, S., Barrett, A.H., Meeks, M.L., Henry, J.C., 1963. Radio observations of oh in the interstellar medium. Nature 200, 829–831. doi:10.1038/200829a0.

Weissman, P., Morbidelli, A., Davidsson, B., Blum, J., 2020. Origin and Evolution of Cometary Nuclei. doi:10.1007/s11214-019-0625-7.

Whipple, F.L., Huebner, W.F., 1976. Physical Processes in Comets. Annual Review of Astronomy and Astrophysics doi:10.1146/annurev.aa.14.090176.001043.

Whittet, D.C.B., Gerakines, P.A., Hough, J.H., Shenoy, S.S., 2001. Interstellar Extinction and Polarization in the Taurus Dark Clouds: The Optical Properties of Dust near the Diffuse/Dense Cloud Interface. Astrophys. J. 547, 872–884. doi:10.1086/318421.

Willis, E.R., Christianson, D.A., Garrod, R.T., 2024. Ice chemistry modeling of active phase comets: Hale–bopp. Icarus 416, 22. doi:10.1016/j.icarus.2024.116097.

Willis, E.R., Garrod, R.T., 2017. Kinetic Monte Carlo Simulations of the Grain-surface Back-diffusion Effect. The Astrophysical Journal 840, 61. URL: http://stacks.iop.org/0004-637X/840/i=2/a=61?key=crossref.d9af7f08a4a65de6ffd7ee440d34b24a, doi:10.3847/1538-4357/aa6ea7.

Willis, E.R., Garrod, R.T., Belloche, A., Müller, H.S., Barger, C.J., Bonfand, M., Menten, K.M., 2020. Exploring molecular complexity with ALMA (EMoCA): Complex isocyanides in Sgr B2(N). Astronomy and Astrophysics 636. doi:10.1051/0004-6361/201936489.

Appendices

Appendix A

Additional Context for Chapter 3

A.1 Kinetic Monte Carlo simulations of reaction rates in bulk-ice layers

Kinetic Monte Carlo simulations of diffusive reactions were carried out to determine the degree of back-diffusion affecting bulk-ice reactions of H or H_2. The model is broadly similar to that described in Section 3.2.3, except that when diffusers meet (i.e. hop into the same site) they are assumed to react, ending that particular simulation and triggering the next to begin. These simulations may be considered to be specifically representative of the $H + H \rightarrow H_2$ reaction system.

The simulations must continue until a reaction occurs, even if a diffuser has attempted to cross an upper or lower boundary of the ice layer. Thus, when a diffuser does cross a boundary, an action must be taken to conserve the total number of diffusers in the ice. Two separate sets of simulations were run to take account of these cases in different ways: (i) if a boundary is crossed, then that hop is ignored, the particle is replaced in its previous position, and it is allowed to move again in a different, random direction; (ii) the ice is treated as fully periodic, so that the crossing of a boundary places the diffuser into the other end of the ice layer, which could lead directly to a reaction. Case (i) may be considered to be closer to the interstellar

dust-grain situation, in which the lower bound of the ice is blocked by the grain itself. Case (ii) is closer to the picture presented in the comet model, in which a diffuser may leave the ice layer in question (while preserving the total number of diffusers), while diffusers might also enter from another adjacent ice layer.

Fig. A.1 shows the reactive back-diffusion factor, ϕ, as determined for case (ii), as a function of the inverse of the degree of occupation of sites ($N_{\mathrm{M}}/N_{\mathrm{d}}$), following the same method of representation as used by Willis and Garrod (2017). Occupation is highest toward the left, while the rightmost point for each color indicates the case where only two diffusers/reactants are present in that ice layer. Different colors show the results for different ice-layer thicknesses, with values chosen to coincide with the layer thicknesses actually used in the comet model (except for $N_{\mathrm{th}} = 30$, which is simply the thickest ice tested). For all thicknesses other than $N_{\mathrm{th}} = 1$ and 3, the back-diffusion factor ranges between 1 and $\sim$1.5, with the $N_{\mathrm{th}} = 3$ models also coming very close to this behavior. The true exception is $N_{\mathrm{th}} = 1$, which corresponds to a single layer in which any upward or downward diffusion is technically counted as a hop, while not leading to an actual change of position. This has the effect of artificially inflating the number of hops by a factor of 1.5 (= 6/4) for all $N_{\mathrm{M}}/N_{\mathrm{d}}$ values.

Fig. A.2 shows the results for case (i), in which no diffusion across the boundaries is allowed, using a slightly wider ice ($N_{\mathrm{lat}} = 25$) and a slightly lower maximum thickness ($N_{\mathrm{th}} = 20$). For $N_{\mathrm{th}} = 1$ the anomalous factor of 1.5 is removed, while the greatest back-diffusion factor – corresponding, as usual, to the presence of two diffusers/reactants – is still fairly small at around 2.25. The particular case of two reactants on a surface was studied in more detail by Willis and Garrod (2017), and they derived an expression for ϕ that was dependent on the number of sites, N_{M} (see

their Table 2). Their expression for a flat surface morphology returns a value $\phi = 2.23$ for $N_{\rm lat} = 25$, matching the data shown in Fig. A.2. The same expression (multiplied by a factor 1.5) may also be used to reproduce the most extreme ϕ-value for $N_{\rm th} = 1$ shown in Fig. A.1.

The same expression may be used to extrapolate the most extreme result of the simulations to a surface of a size appropriate to a comet, as indeed is done in the comet model to determine the back-diffusion factor for the surface reaction rates. Adopting a (square) comet surface of 1 km $\times$ 1 km, a total of $\phi \simeq 18$ would be expected. While this is not insignificant, it represents a value even higher than would be achieved in the first bulk-ice layer ($N_{\rm th} = 3$), as judged by Fig. A.1, while the $N_{\rm th} = 9$ layer beneath it would be expected to converge to values in the range 1 – 1.5 for all $N_{\rm M}/N_{\rm d}$ values. These ϕ-values are all minuscule compared with the back-diffusion factor for transfer between layers (instead of reaction).

Thus, while the Monte Carlo simulations cannot be used to calculate directly the degree of three-dimensional back-diffusion affecting diffusive reaction rates in bulk-ice layers of sizes appropriate to comets (i.e. $N_{\rm lat} \gg 25$), the limits placed on the most extreme cases indicate that the effect is likely small enough to ignore. Judging by the results for $N_{\rm th} > 1$ in Fig. A.2, the effect of back-diffusion on bulk-ice reaction rates in the *interstellar-grain* case is also more or less negligible, and will always be substantially less than the factor of $\sim$5 found for surface reactions ($N_{\rm th} = 1$), both here and in Willis and Garrod (2017).

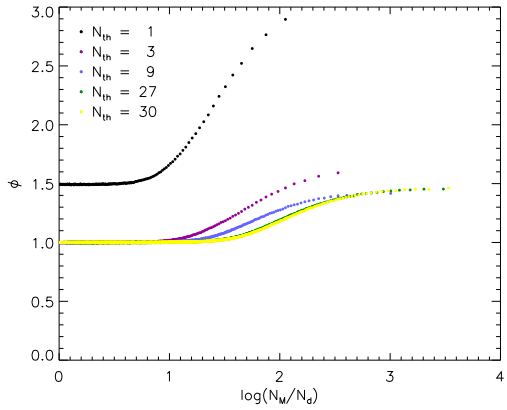

Figure A.1: Back-diffusion factor, ϕ, affecting the rates of diffusive reactions in bulk-ice layers of various thicknesses, N_{th}, based on kinetic Carlo Models with full periodic boundary conditions. Results are shown as a function of the degree of occupation of sites ($N_{\mathrm{M}}/N_{\mathrm{d}}$). Details of the models are described here and in Section 3.2.3.

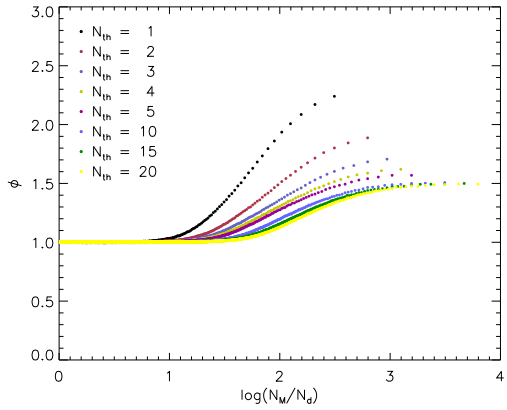

Figure A.2: As Fig. A.1, but using a model in which boundary-crossing is not allowed and is not counted in the total number of hops.

Appendix B

Additional Figures for Chapter 3

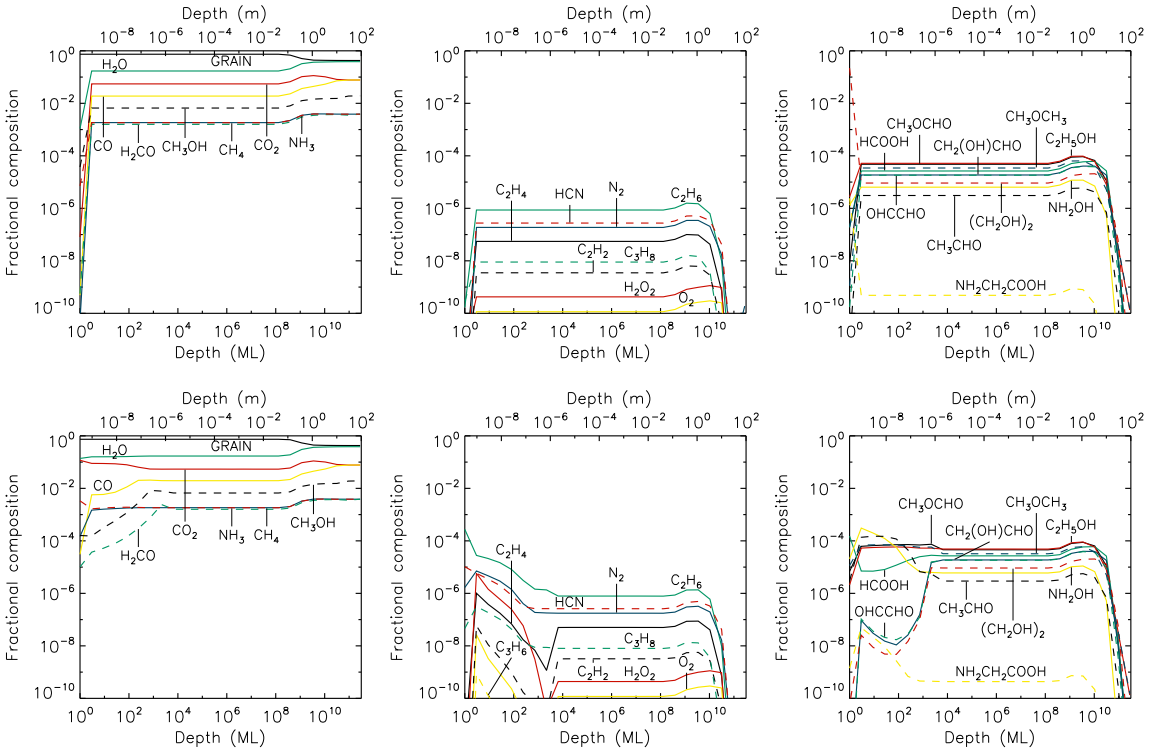

Figure B.1: Fractional abundances of select ice species for the third of five solar approaches in terms of monolayers of material per ice layer. The y-axis of each plot corresponds with the ice surface. When material is lost, the surface position moves such that the ice surface is always at 0. The x-axis is the depth, from the surface, in terms of monolayers (ML) shown on the bottom and meters (m) shown on the top. Each column represents a different subset of species grouped based on size and relevance. Top: Abundances at first perihelion. Bottom: Abundances at first aphelion after starting point.

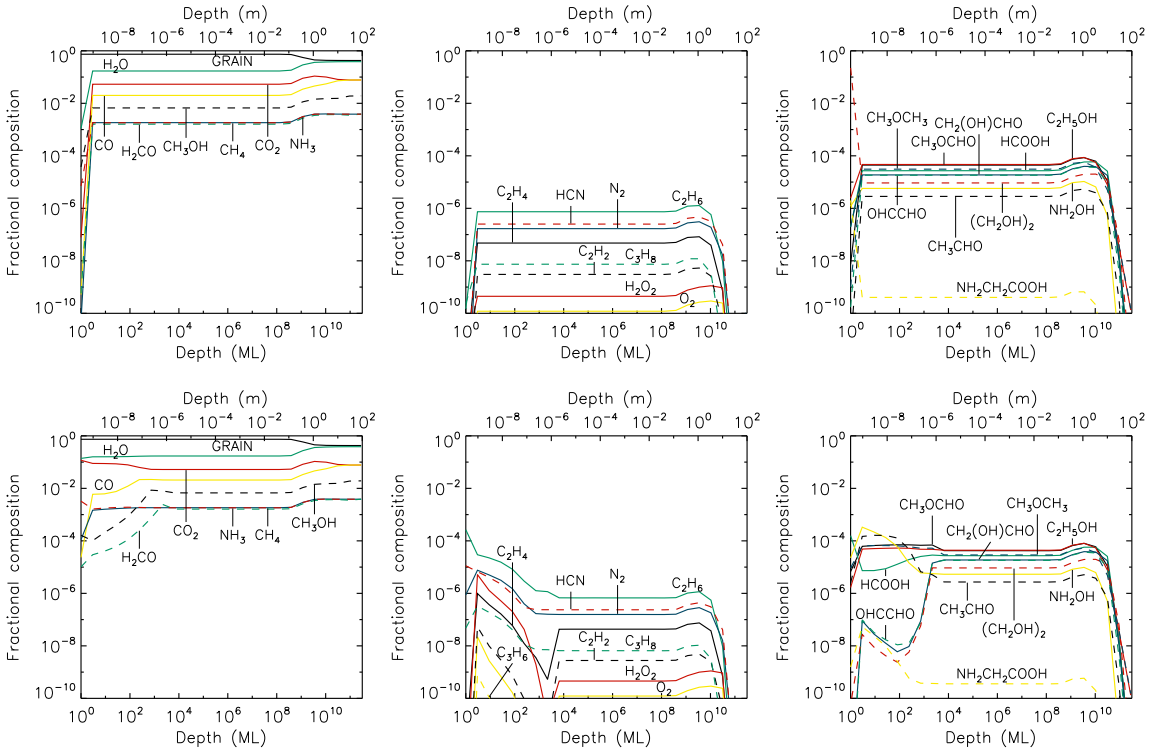

Figure B.2: Fractional abundances of select ice species for the fourth of five solar approaches in terms of monolayers of material per ice layer. The y-axis of each plot corresponds with the ice surface. When material is lost, the surface position moves such that the ice surface is always at 0. The x-axis is the depth, from the surface, in terms of monolayers (ML) shown on the bottom and meters (m) shown on the top. Each column represents a different subset of species grouped based on size and relevance. Top: Abundances at first perihelion. Bottom: Abundances at first aphelion after starting point.

Appendix C

Additional Figures for Chapter 4

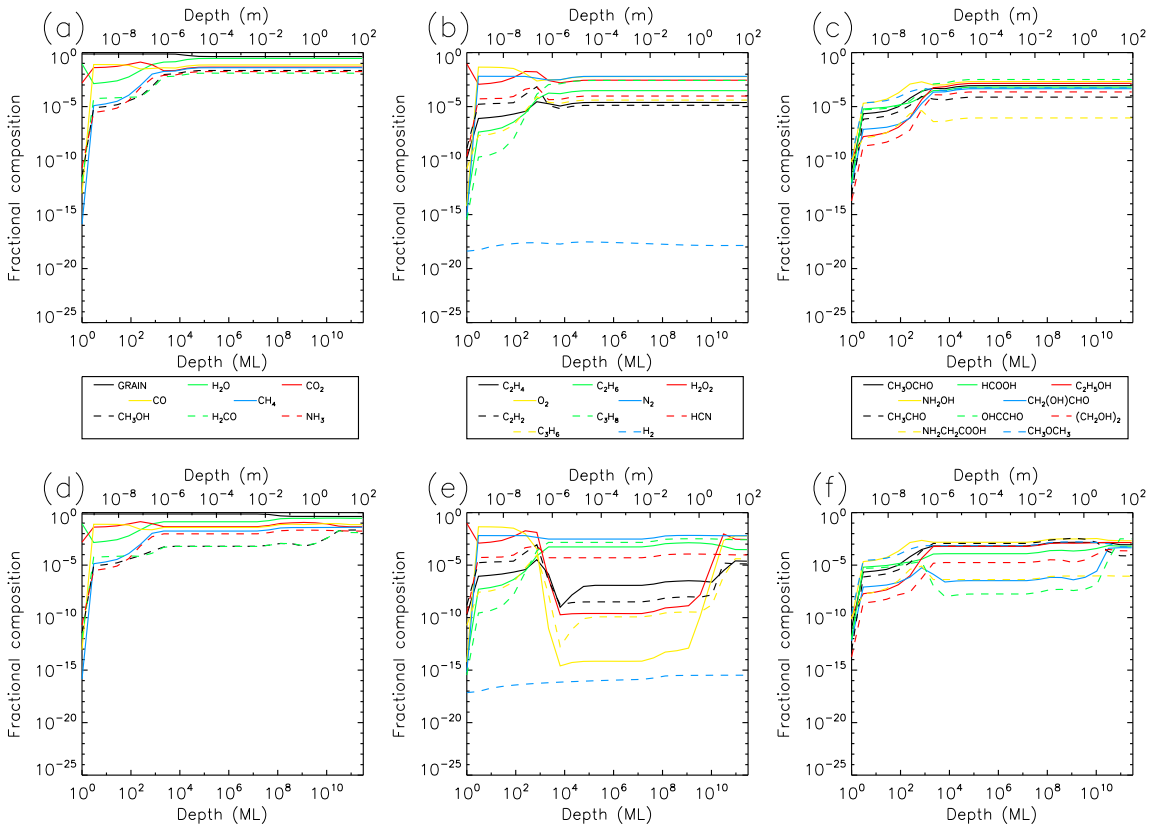

Figure C.1: Fractional abundances of select ice species for the cold storage of comet 67P with initially *interstellar* ice abundances and solar UV; Top: Abundances at 10^6 years. Bottom: Abundances at 4.5×10^9 years. The y-axis of each plot corresponds with the ice surface. The x-axis is the depth, from the surface, in terms of monolayers (ML) shown on the bottom and meters (m) shown on the top. Each column represents a different subset of species grouped based on size and relevance.

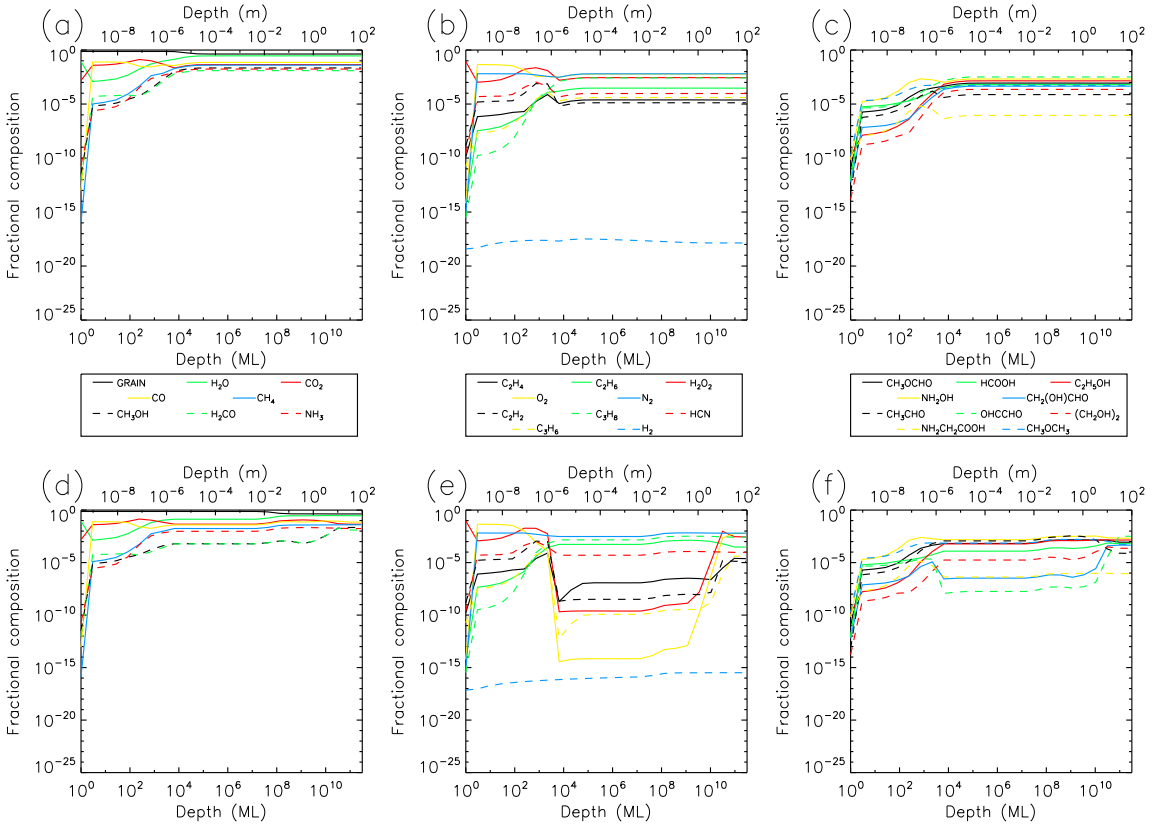

Figure C.2: Fractional abundances of select ice species for the cold storage of comet 67P with initially *interstellar* ice abundances and solar protons and UV; Top: Abundances at 10^6 years. Bottom: Abundances at 4.5×10^9 years. The y-axis of each plot corresponds with the ice surface. The x-axis is the depth, from the surface, in terms of monolayers (ML) shown on the bottom and meters (m) shown on the top. Each column represents a different subset of species grouped based on size and relevance.

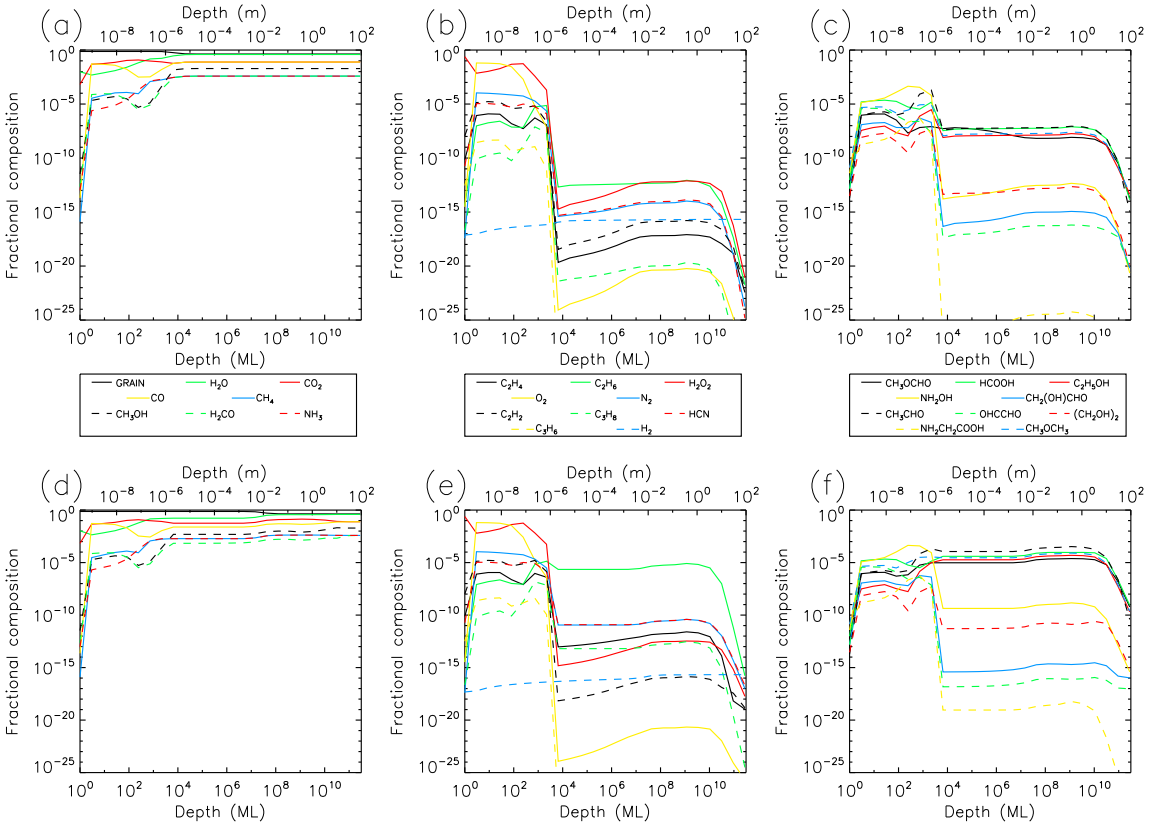

Figure C.3: Fractional abundances of select ice species for the cold storage of comet 67P with initially *simple* ice abundances and solar protons and UV; Top: Abundances at 10^6 years. Bottom: Abundances at 4.5×10^9 years. The y-axis of each plot corresponds with the ice surface. The x-axis is the depth, from the surface, in terms of monolayers (ML) shown on the bottom and meters (m) shown on the top. Each column represents a different subset of species grouped based on size and relevance.

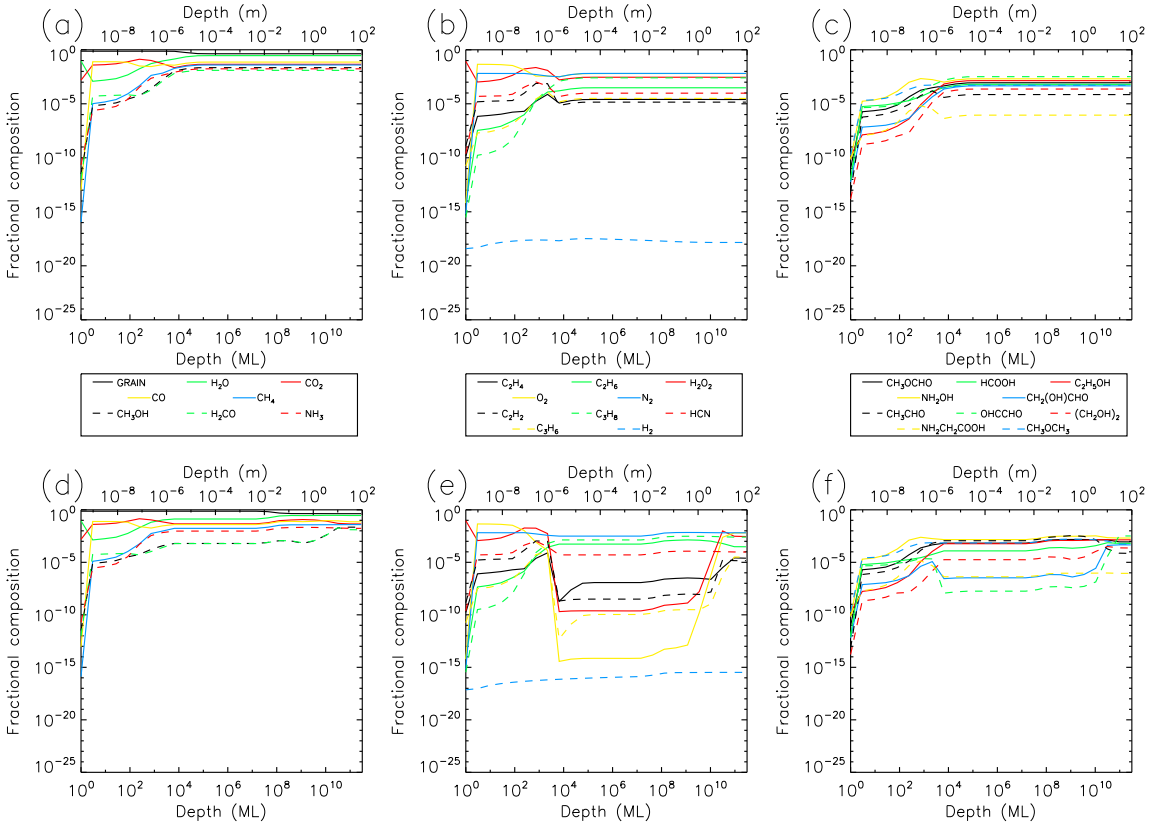

Figure C.4: Fractional abundances of select ice species for the cold storage of comet 67P with initially *interstellar* ice abundances, solar protons and UV, and sodium content removed; Top: Abundances at 10^6 years. Bottom: Abundances at 4.5×10^9 years. The y-axis of each plot corresponds with the ice surface. The x-axis is the depth, from the surface, in terms of monolayers (ML) shown on the bottom and meters (m) shown on the top. Each column represents a different subset of species grouped based on size and relevance.

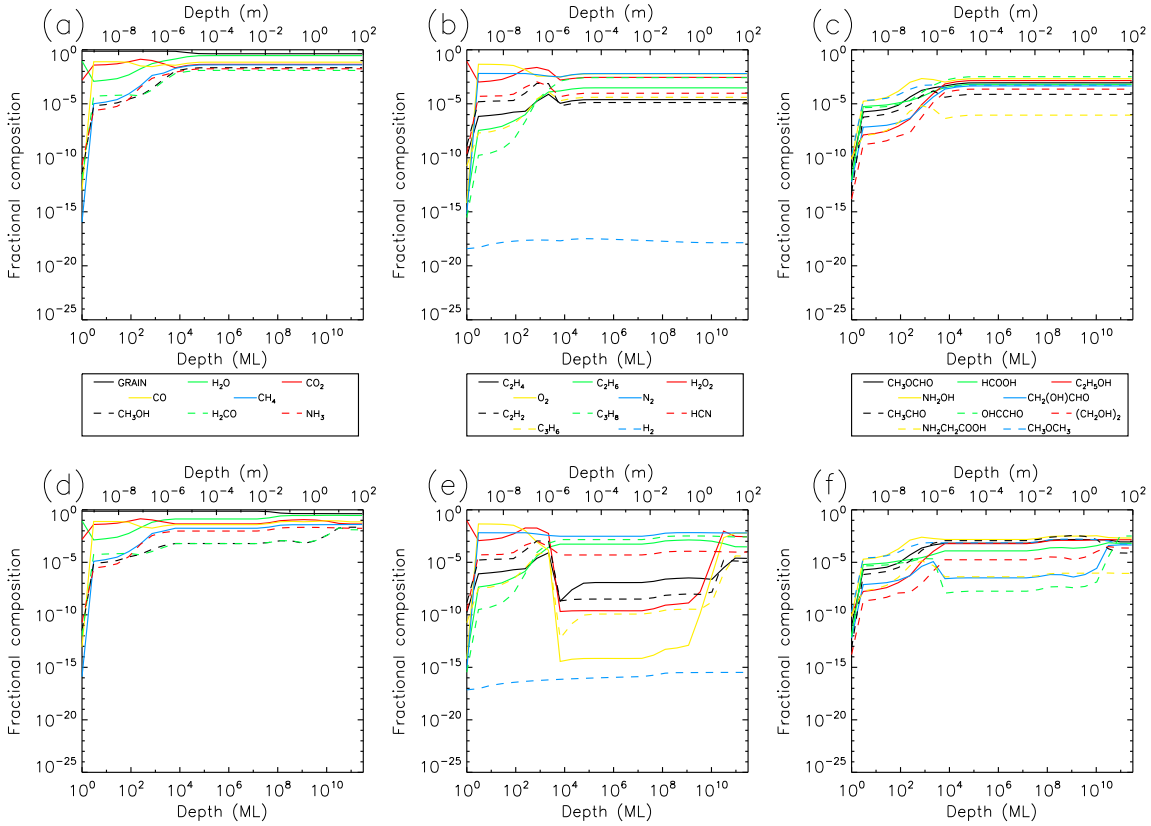

Figure C.5: Fractional abundances of select ice species for the cold storage of comet 67P with initially *interstellar* ice abundances, solar protons and UV, and additional sodium chemistry; Top: Abundances at 10^6 years. Bottom: Abundances at 4.5×10^9 years. The y-axis of each plot corresponds with the ice surface. The x-axis is the depth, from the surface, in terms of monolayers (ML) shown on the bottom and meters (m) shown on the top. Each column represents a different subset of species grouped based on size and relevance.

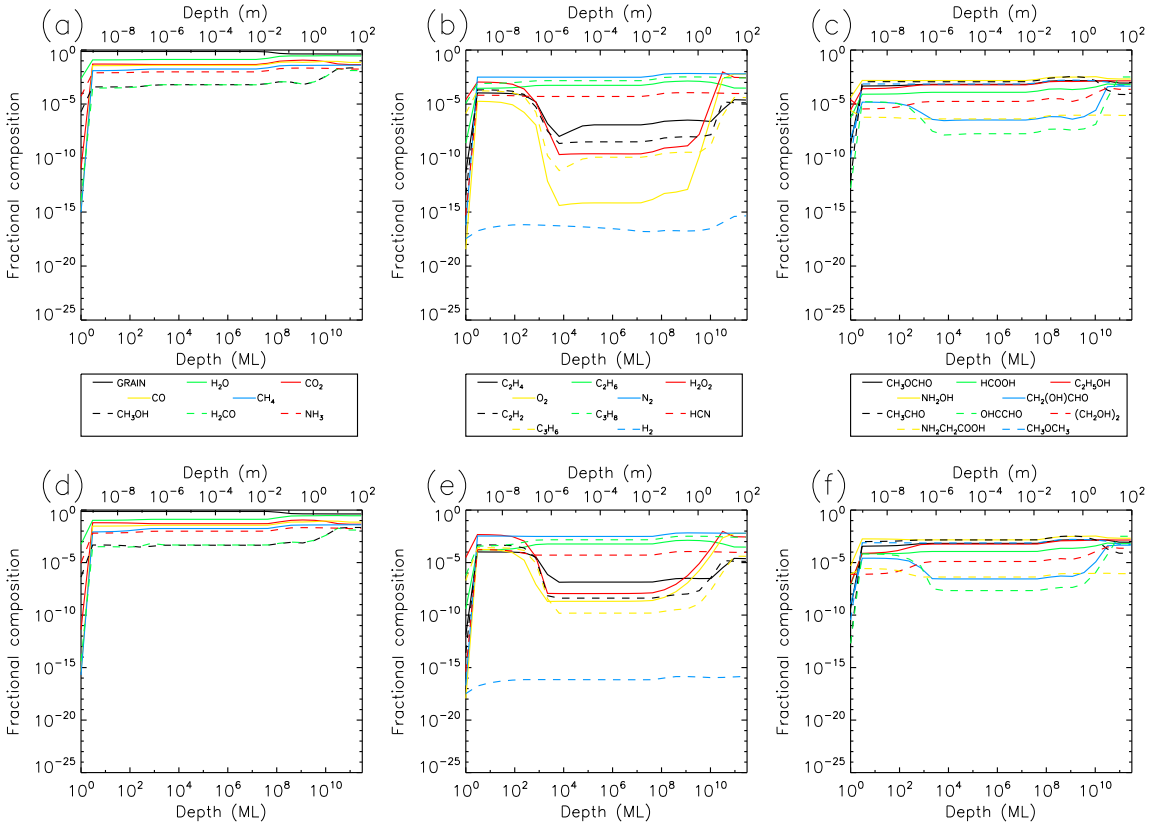

Figure C.6: Fractional abundances of select ice species for the transition phase (Top) and active phase (Bottom) of comet 67P with initially *interstellar* ice abundances and solar UV. The y-axis of each plot corresponds with the ice surface. The x-axis is the depth, from the surface, in terms of monolayers (ML) shown on the bottom and meters (m) shown on the top. Each column represents a different subset of species grouped based on size and relevance.

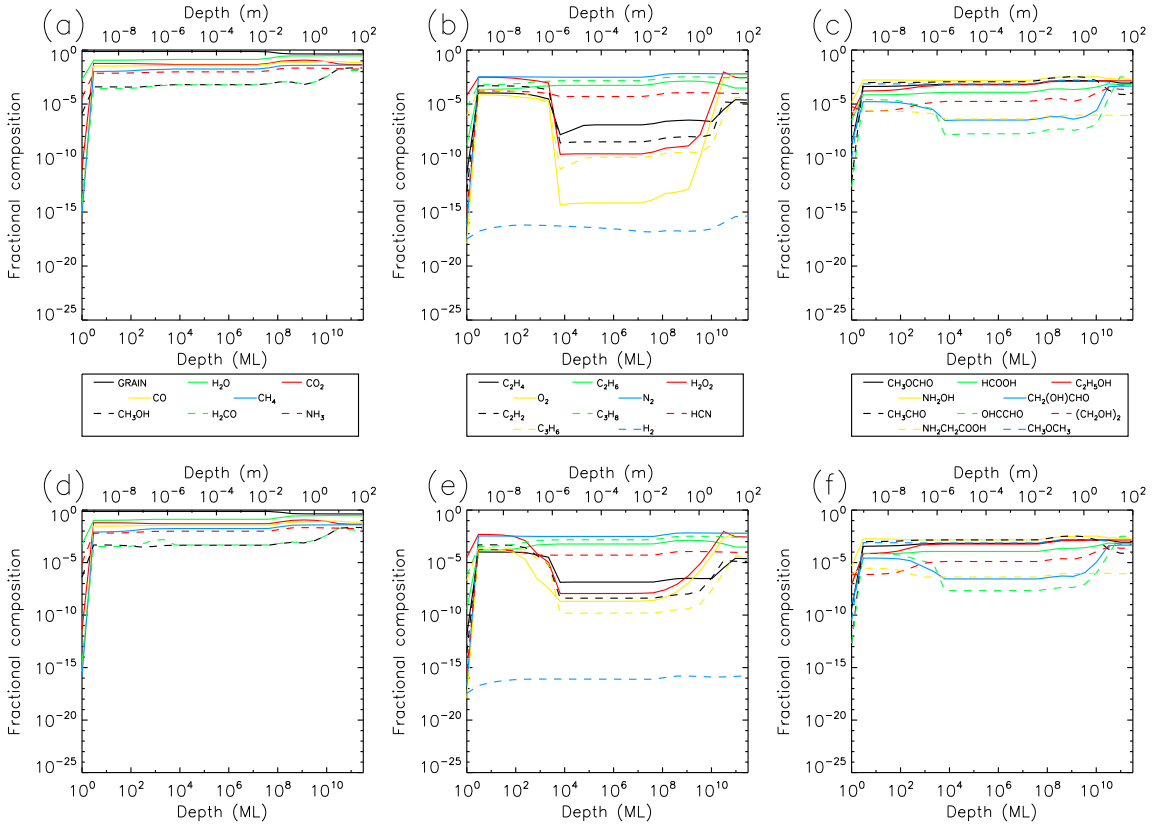

Figure C.7: Fractional abundances of select ice species for the transition phase (Top) and active phase (Bottom) of comet 67P with initially *interstellar* ice abundances and solar protons and UV. The y-axis of each plot corresponds with the ice surface. The x-axis is the depth, from the surface, in terms of monolayers (ML) shown on the bottom and meters (m) shown on the top. Each column represents a different subset of species grouped based on size and relevance.

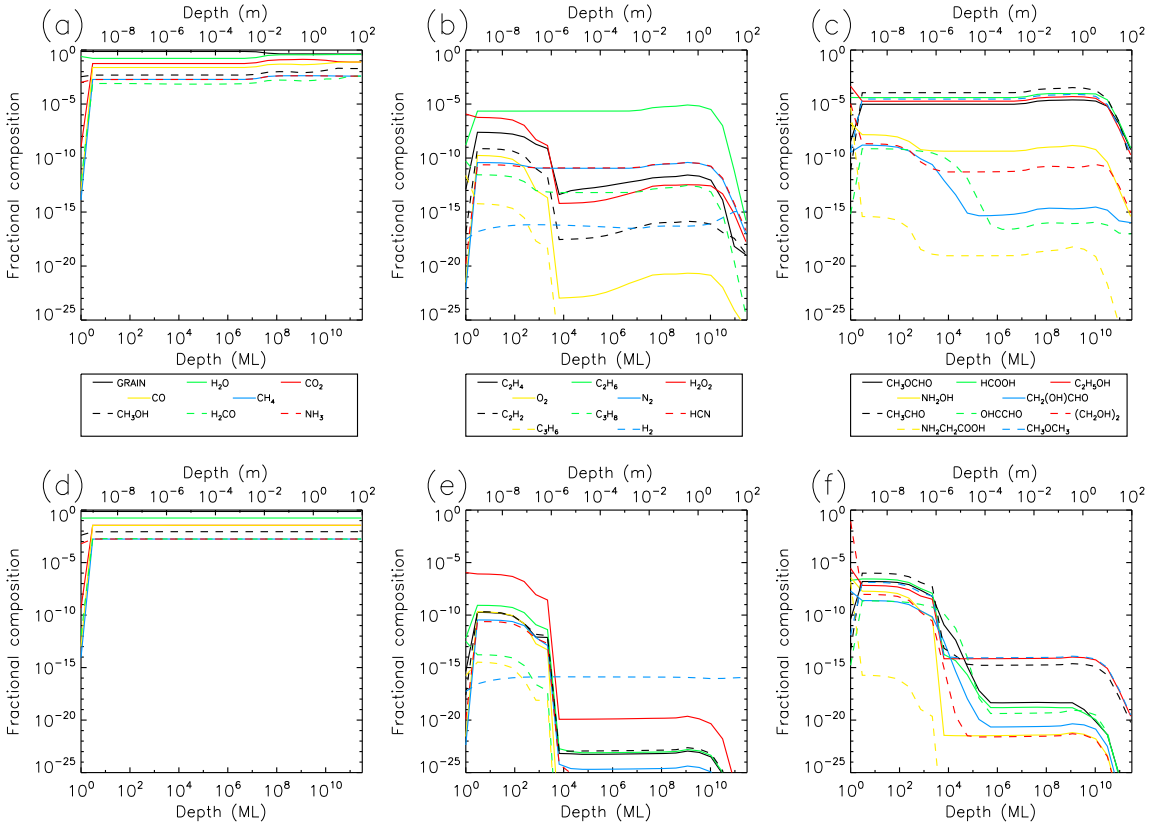

Figure C.8: Fractional abundances of select ice species for the transition phase (Top) and active phase (Bottom) of comet 67P with initially *simple* ice abundances and solar protons and UV. The y-axis of each plot corresponds with the ice surface. The x-axis is the depth, from the surface, in terms of monolayers (ML) shown on the bottom and meters (m) shown on the top. Each column represents a different subset of species grouped based on size and relevance.

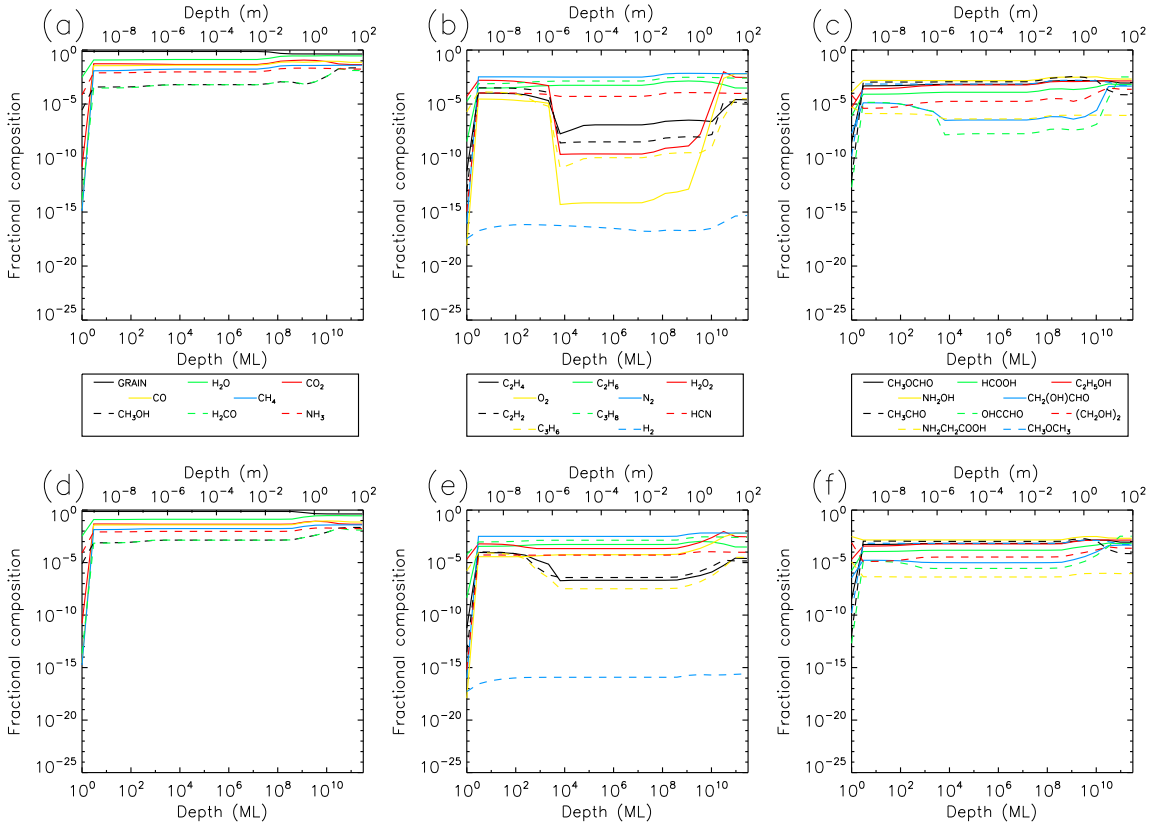

Figure C.9: Fractional abundances of select ice species for the transition phase (Top) and active phase (Bottom) of comet 67P with initially *interstellar* ice abundances, solar protons and UV, and sodium content removed. The y-axis of each plot corresponds with the ice surface. The x-axis is the depth, from the surface, in terms of monolayers (ML) shown on the bottom and meters (m) shown on the top. Each column represents a different subset of species grouped based on size and relevance.

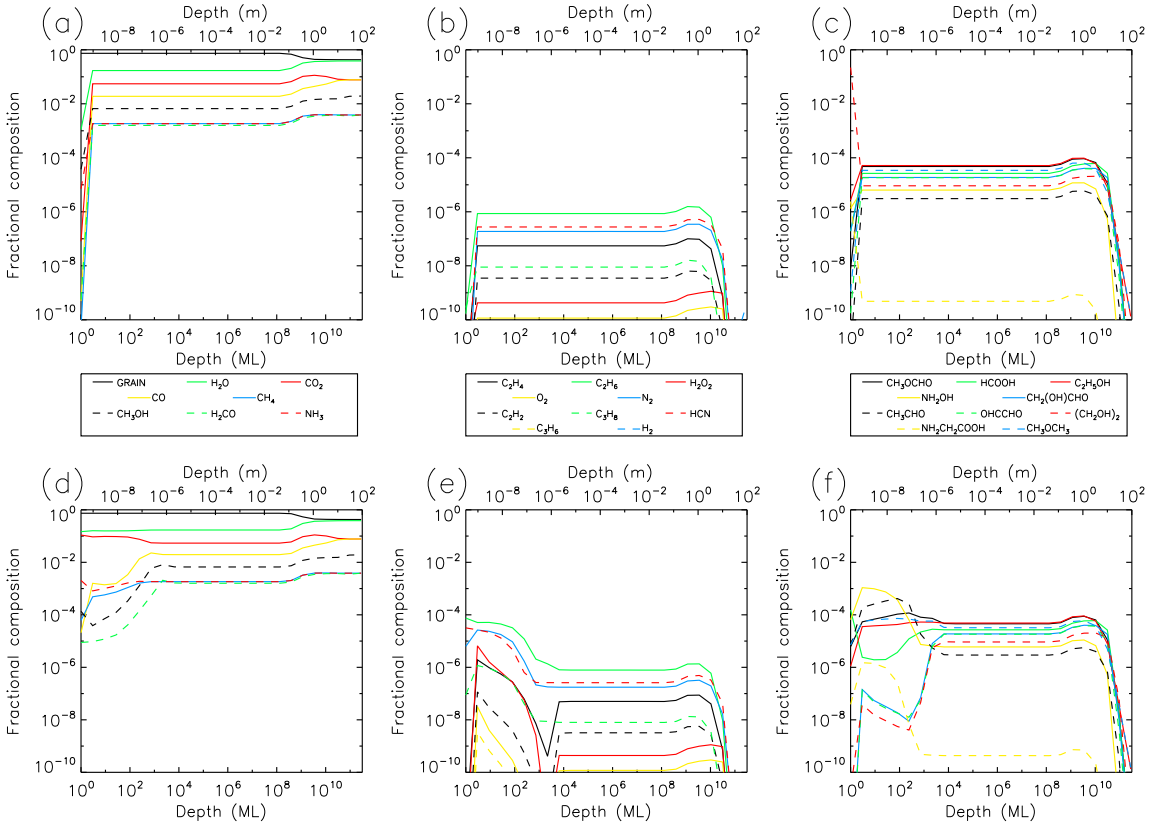

Figure C.10: Fractional abundances of select ice species for the *third* of five solar approaches of comet Hale–Bopp with initially *simple* ice abundances and solar UV; Top: Abundances at third perihelion. Bottom: Abundances at third aphelion after starting point. The y-axis of each plot corresponds with the ice surface. The x-axis is the depth, from the surface, in terms of monolayers (ML) shown on the bottom and meters (m) shown on the top. Each column represents a different subset of species grouped based on size and relevance.

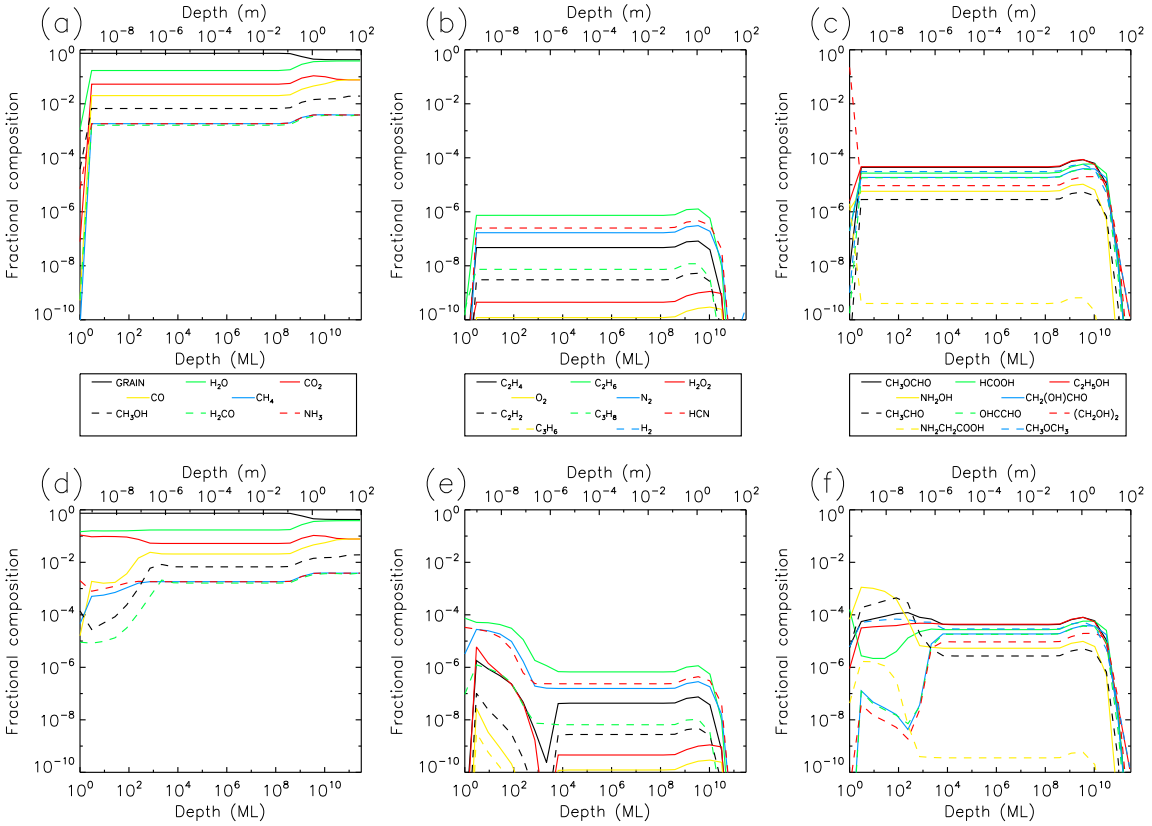

Figure C.11: Fractional abundances of select ice species for the *fourth* of five solar approaches of comet Hale–Bopp with initially *simple* ice abundances and solar UV; Top: Abundances at fourth perihelion. Bottom: Abundances at fourth aphelion after starting point. The y-axis of each plot corresponds with the ice surface. The x-axis is the depth, from the surface, in terms of monolayers (ML) shown on the bottom and meters (m) shown on the top. Each column represents a different subset of species grouped based on size and relevance.

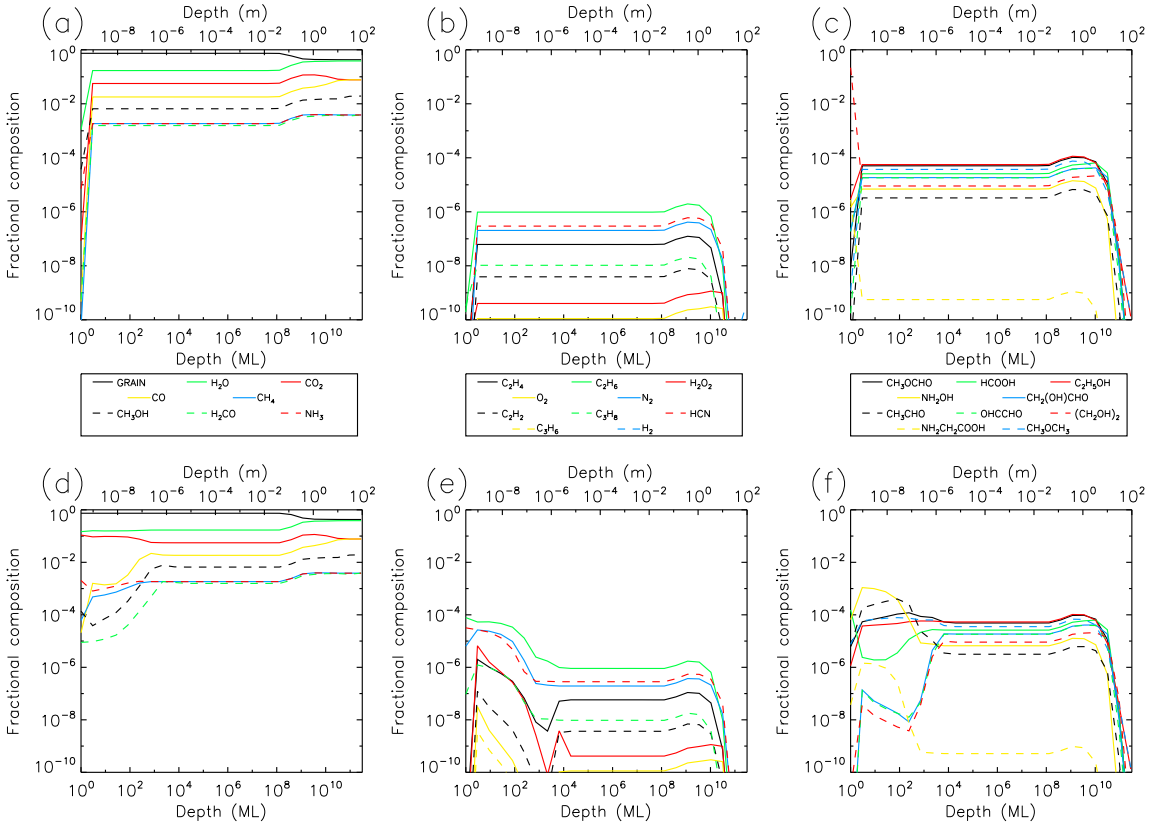

Figure C.12: Fractional abundances of select ice species for the *third* of five solar approaches of comet Hale–Bopp with initially *simple* ice abundances and solar protons and UV; Top: Abundances at third perihelion. Bottom: Abundances at third aphelion after starting point. The y-axis of each plot corresponds with the ice surface. The x-axis is the depth, from the surface, in terms of monolayers (ML) shown on the bottom and meters (m) shown on the top. Each column represents a different subset of species grouped based on size and relevance.

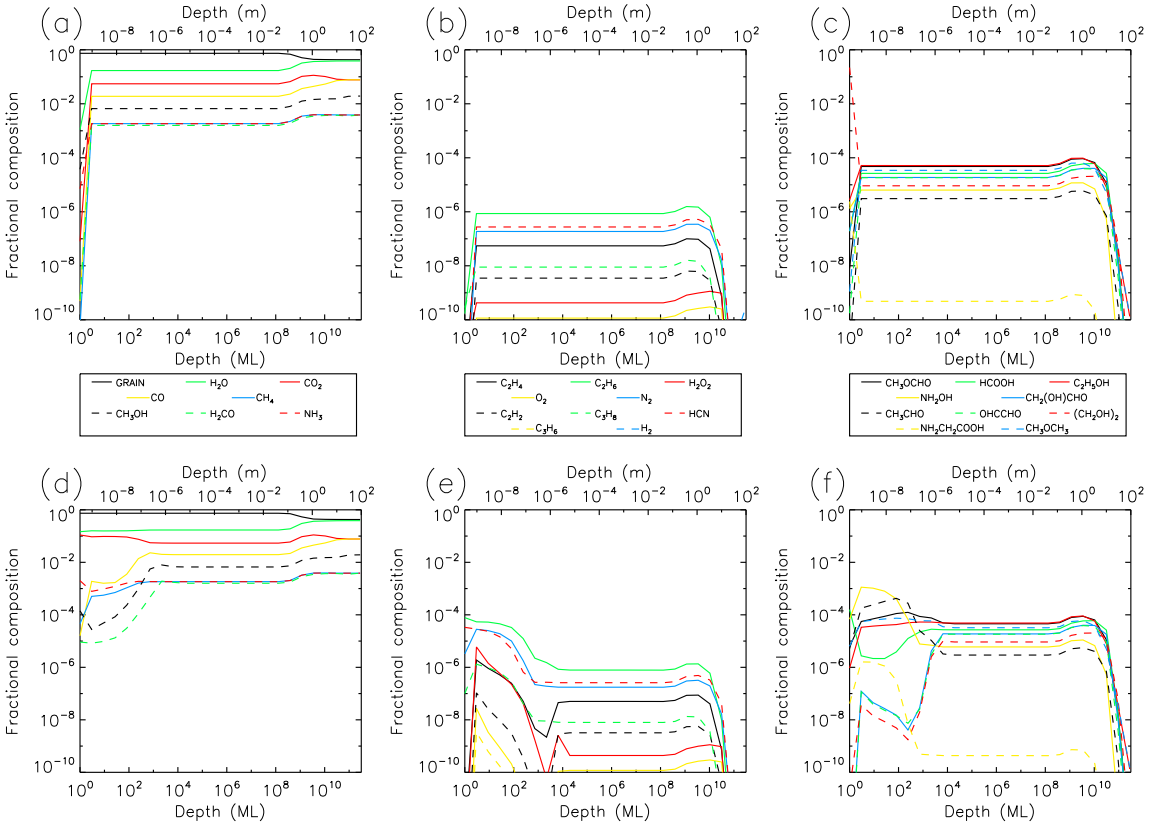

Figure C.13: Fractional abundances of select ice species for the *fourth* of five solar approaches of comet Hale–Bopp with initially *simple* ice abundances and solar protons and UV; Top: Abundances at fourth perihelion. Bottom: Abundances at fourth aphelion after starting point. The y-axis of each plot corresponds with the ice surface. The x-axis is the depth, from the surface, in terms of monolayers (ML) shown on the bottom and meters (m) shown on the top. Each column represents a different subset of species grouped based on size and relevance.

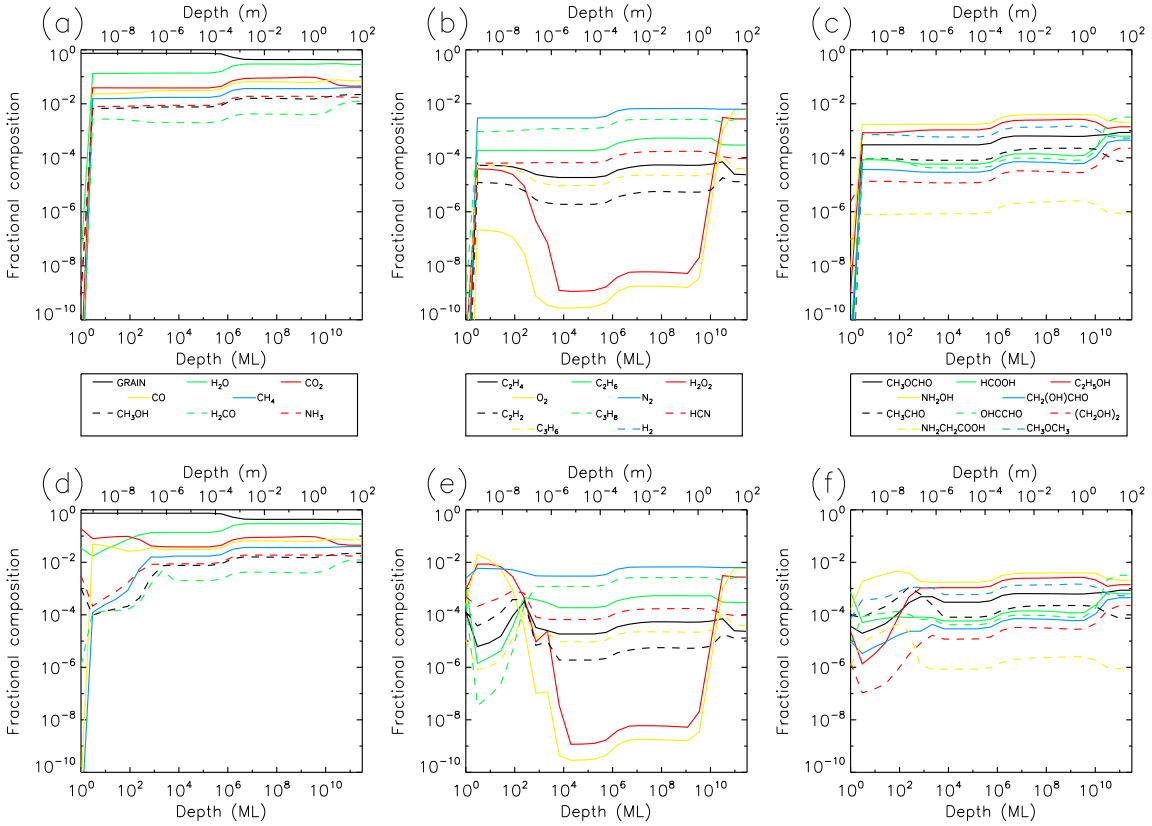

Figure C.14: Fractional abundances of select ice species for the *third* of five solar approaches of comet Hale–Bopp with initially *interstellar* ice abundances, solar protons and UV, and additional sodium chemistry; Top: Abundances at third perihelion. Bottom: Abundances at third aphelion after starting point. The y-axis of each plot corresponds with the ice surface. The x-axis is the depth, from the surface, in terms of monolayers (ML) shown on the bottom and meters (m) shown on the top. Each column represents a different subset of species grouped based on size and relevance.

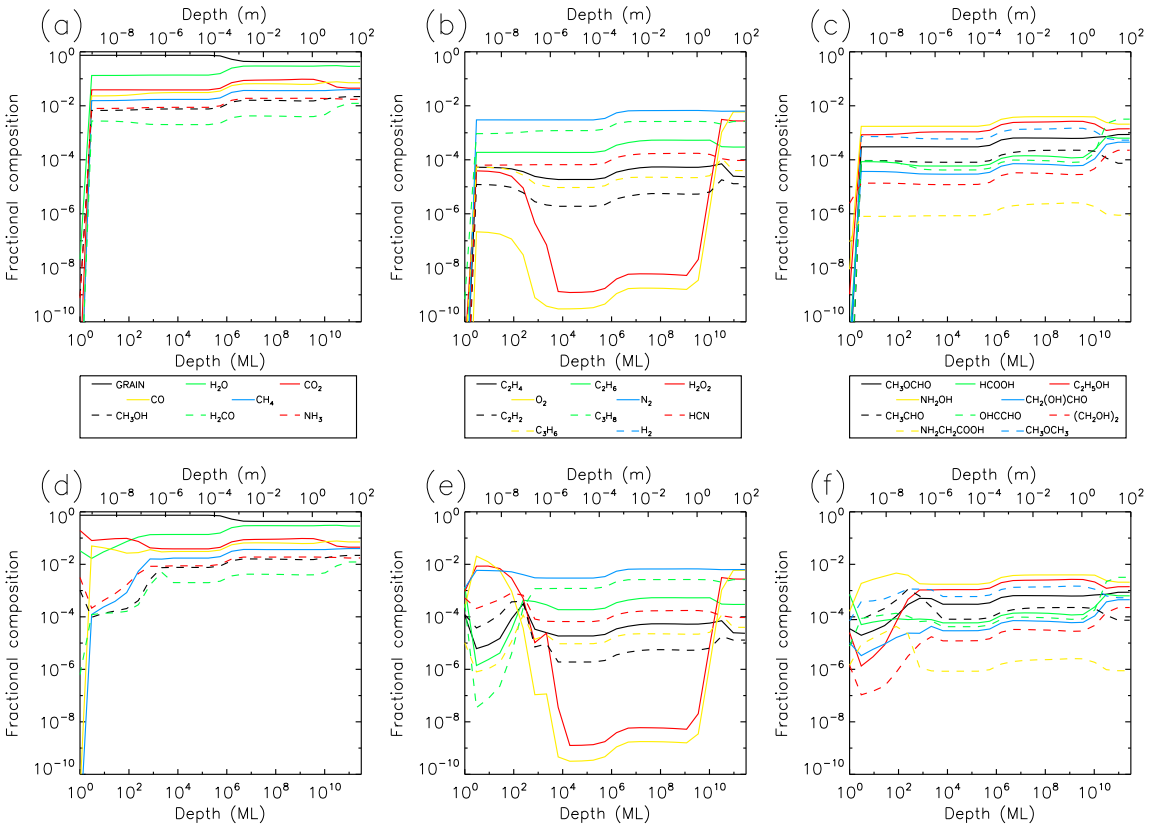

Figure C.15: Fractional abundances of select ice species for the *fourth* of five solar approaches of comet Hale–Bopp with initially *interstellar* ice abundances, solar protons and UV, and additional sodium chemistry; Top: Abundances at fourth perihelion. Bottom: Abundances at fourth aphelion after starting point. The y-axis of each plot corresponds with the ice surface. The x-axis is the depth, from the surface, in terms of monolayers (ML) shown on the bottom and meters (m) shown on the top. Each column represents a different subset of species grouped based on size and relevance.